STRUCTURE AND PROPERTIES OF ARC SPRAYED STEEL COATINGS

BY

CAMERON LINDSAY JOHNSTON

A Thesis
submitted for the
Degree of
Doctor of Philosophy
to
The University of Aston in Birmingham

May 1985

THE UNIVERSITY OF ASTON IN BIRMINGHAM

STRUCTURE AND PROPERTIES OF ARC SPRAYED STEEL COATINGS

Submitted by CAMERON LINDSAY JOHNSTON
for the degree of Doctor of Philosophy

1985

SUMMARY

A review of thermal spraying processes and coating materials is followed by a detailed description of arc spraying. The basic principles involved in the production and deposition of spray droplets are discussed together with gas/metal reactions and the formation of oxides. Published literature relating to the measurement of adhesion and cohesion, bonding mechanisms, the development and measurement of residual stress and mechanical properties of sprayed coatings is reviewed.

Three commercially available coatings were investigated, mild steel, a 1% carbon 2% chromium steel and a 13% chromium steel. Process variables were spraying distance, deposition rate, arc voltage and atomising pressure. The coatings were characterised by optical metallography, scanning electron microscopy and micro-analysis, gas and chemical analysis. A collar type shear adhesion test, employing a mild steel substrate, was used to assess bonding of coating to substrate. Residual stress was determined from dimensional changes of the collar. Adhesion arose mainly from mechanical interlocking and was generally increased with hot, large particles and ranged from 10-155 MPa. With a cylindrical substrate the shrinkage stress developed during cooling markedly contributed to adhesion, it ranged from 0 - 188 MPa and was material dependent.

Considerable amounts of oxidation (up to 7.0 wt%), the majority of which occurred after deposition, and elemental loss (up to 70% alloying additions) occurred and is related directly to deposition parameters.

Coating mechanical properties are shown to be influenced by particle composition, grain size, oxides and other dispersed compounds. These features are related to the mechanisms involved in the creation, flight and impingement of the particles. Oxide content and porosity controls tensile properties. Quantitative relationships are proposed to enable properties to be calculated from process variables.

The study demonstrates how parameters affect adhesion, coating composition and constitution and that it is possible to determine directly the cohesive properties of a coating given prior knowledge of the deposition parameters.

KEY WORDS: Sprayed steel coatings, Electric arc spraying, Coating adhesion testing, Sprayed coating formation, Sprayed coating properties.

CONTENTS

LIST OF FIGURES

LIST OF TABLES

CHAPTER I - INTRODUCTION

The flexibility in design afforded by the use of thermal spraying is widely accepted. Mechanical engineers have used sprayed coatings extensively for more than 50 years; initially to reclaim engineering components and subsequently to enhance performance by providing improved wear resistance, thermal conductivity, etc. In recent years the use of sprayed coatings has increased considerably. This is due to the availability of a large number of coating materials which have the ability to impart a wide range of, sometimes unique, properties and the development of several versatile processes which produce denser, stronger and more adherent coatings. A wide selection of pure metals, alloys, ceramics and composites are used as sprayed coatings in industry. The versatility is further extended by the availability of several spraying techniques, the main areas being combustion, arc and plasma. The trend now is movement towards more economic automated spraying systems which produce coatings of improved consistency.

The electric arc process offers the capability of producing strong, well bonded deposits of almost all the common engineering alloys. Combined with the potential for high deposition rates this process is rapidly gaining acceptance for engineering applications. Yet different coating properties will be achieved from a given material depending on the spraying parameters employed. With the development of new approaches to producing engineering components for example, Flexible Manufacturing Systems, the use of thermal spraying could be significantly increased. However, a considerable constraint on expansion, or use, is the lack of reliable quantitative design data, particularly concerning strength and

adhesion. Even that which has been published is of limited value due to inadequate specification of spraying parameters or test methods; and there is a lack of confidence in adhesion understanding even though quite a lot of work has been carried out in recent years. In consequence processing parameters are frequently based on economic considerations tempered by service experience. Reliance is placed on careful preparation of the surface of the basis material. Adhesion is frequently judged by the appearance of the sprayed deposit and by a variety of qualitative confirmatory tests. Designers adopt a cautious approach to the specification of sprayed coatings and reliance is often placed on practical, performance tests rather than published results.

The writer was given the opportunity of undertaking a research project utilising the experience and expertise of an industrial concern specialising in arc spraying. With this arrangement it was also possible to combine personal, practical, shop floor observations with scientific studies at a University. The project was undertaken to determine the influence of deposition parameters on the adhesive, mechanical and chemical properties of arc sprayed deposits, with a view to being able to match (select) and control spraying parameters to suit the properties required for a particular application. The coatings mainly studied represent those of major interest in ferrous engineering applications. It is expected that the use of arc spraying is likely to increase rapidly once greater knowledge and confidence of coating properties is established.

CHAPTER II

LITERATURE SURVEY

2.1 Thermal Spraying

Thermal spraying was introduced in Switzerland over 75 years ago by a Dr. Schoop [1]. The idea of mechanically passing a metal through a high temperature gas flame, atomising the resultant molten metal by compressed air, and then propelling it on to the surface to be coated was first put to commercial use in Britain in the 1920's. Initially it was restricted to the deposition of low melting point materials, such as zinc, onto iron and steel to provide resistance against atmospheric corrosion.

Since then the process has spread throughout the industrial world and the original gas gun has been supplemented by other types of spraying equipment. More recent processes enabled the spraying of much higher melting point engineering materials such as bronzes and carbon and stainless steels used for reclaiming mis-machined and worn engineering components. Metal spraying has now developed into a flexible design tool, for example, by imparting specific properties to surfaces in selected positions in an assembly to withstand the severe localised working conditions. Very hard, abrasion resistant materials such as metal carbides and nitrides, and heat resistant ceramics such as aluminium oxide can be applied to the surface of a component. Metal and ceramic coatings are applied to various materials, including; metal, glass, concrete, plastic, wood, paper and fabric [2] to impart a variety of physical, mechanical and decorative properties.

At present there are four principal energy sources used to convert materials into a spray, see Fig. 1., namely oxy/fuel gas combustion, electric arc, plasma and detonation.

Oxy-fuel gas (acetylene, propane or hydrogen) flame spraying is used for most general engineering applications. The coating material is fed into the flame as powder, wire or solid rod. Large pistols are capable of depositing up to 9 kg of steel per hour. The main restrictions of the flame process are the low deposition rate and the maximum temperature available: the hottest combustion flame which can be used is a neutral flame of oxygen and acetylene which attains temperatures in the region of 3000 K [1].

In the detonation gun a fuel gas mixture containing the coating powder is ignited and the energy released and shock waves created heat the powder and project it along the barrel of the gun onto the work surface. Oxides, carbides and high melting point metals can be applied, the high velocity and temperature of the stream of particles results in very hard, dense, adherent coatings for use under extreme conditions of temperature and abrasion.

This study was centred on the arc spraying system which was developed because of the need for higher deposition rates and automation for certain applications such as the factory coating of rolled strip, and the reclamation of large worn machine parts. The electric-arc gun is somewhat similar in external appearance to the gas gun and is also highly portable. The heat source is an electric arc which is struck between two consumable wires. The wires enter through insulating tubes

FIGURE 1 Thermal Spraying Processes

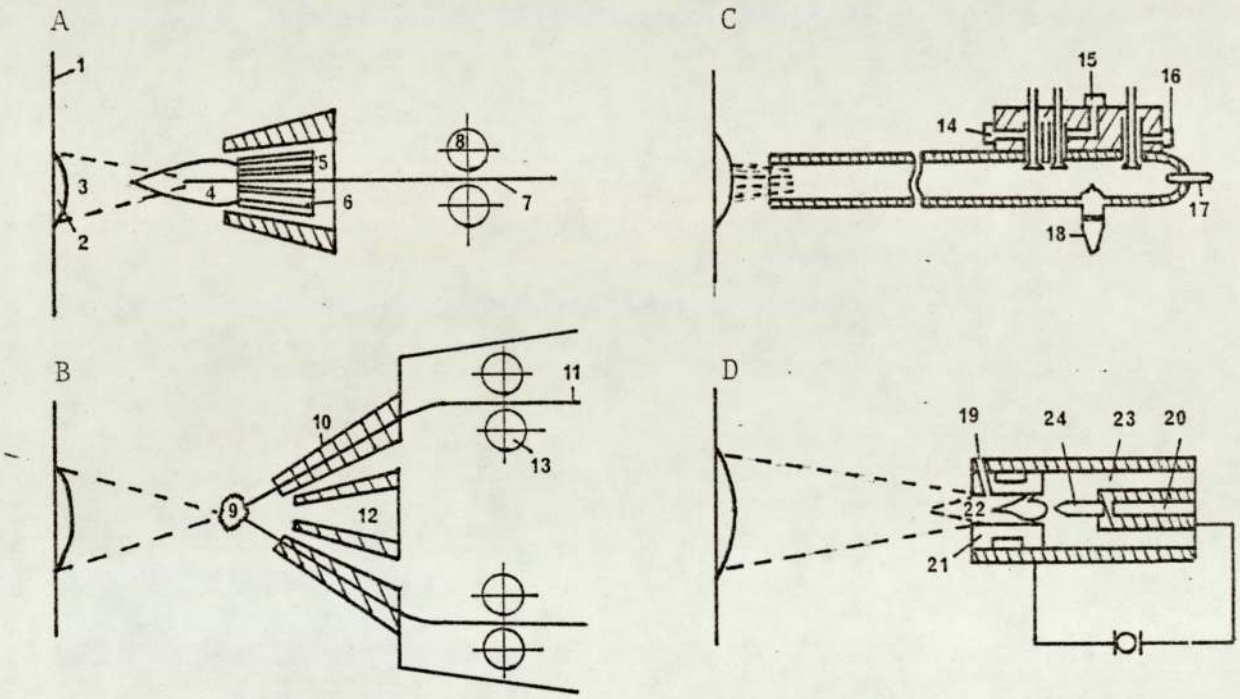

A) Flame Spraying

1) Base material; 2) Sprayed coating; 3) Spray jet;
4) Gas flame; 5) Compressed air; 6) Gas mixture;
7) Coating wire; 8) Wire drive.

B) Electric Arc Spraying

9) Electric Melting Arc; 10) Wire guides and current supply;
11) Coating wire; 12) Compressed air; 13) Wire drive

C) Detonation Spraying

14) Oxygen; 15) Acetylene; 16) Carrier Gas;
17) Coating powder; 18) Ignition

D) Plasma Spraying

19) Coating powder entry; 20) Cooling water;
21) Copper anode; 22) Plasma flame;
23) Plasma gas; 24) Tungsten cathode.

from feed tubes and are gripped and driven forward by feed rolls, through two conducting feed tubes, to approach the arc point at a slight angle each side of the centre line of the gun head. The arc produces a small but intensely hot area, up to 5000[3] - 6000[4] K in temperature, in which both wires melt. The molten metal is projected from the gun nozzle by a compressed air jet. Deposition rates of up to 35 kg of steel per hour can be achieved. Particle velocities (80-180 ms^{-1}) [4] are generally higher than those produced by flame spraying. The arc temperature imparts a higher thermal energy in the particles which results in a better bond to the substrate and higher cohesive strength of the coating. The arc process unlike the flame spraying process is limited to materials which are electrically conductive and available in wire form.

The temperatures produced in a free arc range from 5000-6000 K. An increase in power is known to only slightly raise the temperature [3] since the gas can expand laterally and this limits any increase in enthalpy. To produce higher temperatures it is necessary to increase the current density and enthalpy. This is achieved in Plasma spraying by passing the arc through an anode nozzle the diameter of which is smaller than that of the natural arc. A plasma is formed by the action of the arc upon a gas (generally argon) whereby electrons are stripped from gas atoms. It consists of neutral atoms, molecules, electrons and ions. The electrons are the most important carriers of energy [5]. They recombine with the liberation of intense heat on leaving the pressure zone surrounding the arc. Very high temperatures (15,000-20,000 K)

are produced, sufficient to melt most known materials. The consequent rapid expansion of the gas dramatically increases the velocity of the gases issuing from the nozzle[6] and particle velocity can be up to 610 ms^{-1} [7].

The plasma process was created to meet certain special needs and supplement other methods. It is usually employed for spraying high melting point metals, refractory oxides and carbides and is used particularly in the aerospace industry.

2.2 Properties of the Deposit

In theory any material that can be melted without decomposition can be formed into a spray. In practice there are more than 150 coating materials available. The main types and applications are shown in Table 1 [2]. These range from low melting point metals such as aluminium and zinc (atmospheric corrosion resistance), Babbit metals (high speed bearings) and tin alloys (radio frequency shielding), to ceramic oxides and carbides which resist wear, particle erosion, high temperatures, a certain amount of chemical attack, and thermal shock. Common metals such as steels and bronzes are used to produce coatings with engineering properties or to reclaim and repair mis-machined or worn parts. It is also possible to produce coatings with unique properties; for example, high temperature alloys of nickel, cobalt and chromium can be blended with hard carbides and nitrides to resist the combined effects of abrasion and corrosion at elevated temperatures.

TABLE 1

THERMAL SPRAY COATING MATERIALS [2]

Broad Description	Environmental Applications
FERROUS	
Carbon Steels 0.1-1.2% C	Good wear resistance in lubricated conditions. Some coatings machinable.
Various Stainless Steels	Good corrosion resistance. Some coatings machinable and workhardening.
NICKEL AND COBALT BASE*	
Ni-Cr, Ni-Cr-W, Ni-Cr-Al	Resist oxidising and corrosive gases.
Co-Cr-Ni-W	Resists abrasion and erosion.
Exothermic Ni-1 materials, including self-bonding one-step coatings. May contain molybdenum or copper-aluminium composites.	Many coatings are self-bonding: used as undercoats for ceramics: resistant to medium or high temperature, thermal shock, abrasion, corrosion, oxidation also used for reclamation.
SELF-FLUXING (for fusion)	
Fused coatings of Ni-Cr alloys with Si and B additions	Hard facing uses; some coatings machinable. Resist abrasion/corrosion, erosion, cavitation, pore-free.
Fused CW-Co aggregates in Ni-Cr matrix: 30-75% WC-Co	Dense, pore-free coating to resist corrosion, abrasion, erosion, fretting and high temperature.
CERAMIC OXIDES	
Aluminium Oxide Chromium Oxide	Resist abrasive wear, high temperature, molten metal, chemical attack, cavitation and erosion.
Zirconium Dioxide Magnesium Zirconate Mixtures of Oxides	Resist erosion and thermal shock at high temperature (up to 900°C)
CARBIDES	
WC-Co composite	Resist wear, particle erosion, fretting, thermal shock, low-medium temperatures.
Cr_2C_3	Resists wear and oxidation at high temperatures.
WC-Fe-Cr	Resist wet abrasion.
CERMETS	
Boron Nitride - Al-Ni-Cr	Clearance control coatings at high temperatures.
Magnesium Zirconate - Ni-Cr	Thermal barrier coatings.
Nickel-graphite Aluminium-alloy-graphite	Abradable seal coatings in gas turbines
Oxides blended with nickel-aluminium	Hard, resistant to thermal shock and abrasion.
REFRACTORY METALS	
Molybdenum	Self-bonding, hard, low-friction coatings. Resist scuffing, resist arc erosion; excellent bond coat.
Tungsten	Dense, heat resistant coatings; bond readily. Resists molten copper and zinc.
Tantalum	Resists high temperatures; self-bonding to steel.

continued...

TABLE 1 (CONTINUED)

Broad Description	Environmental Applications
NON-FERROUS	
Pure Aluminium: Al-Si alloys	Resist atmostpheric and sea-water corrosion, and slightly acid environments. Resist oxidation at temperatures up to 900°C.
Pure Zinc	Resists atmospheric and water corrosion and alkaline environments.
Pure Tin; Sn-Zn alloys	Protecting food vessels; radio frequency shielding; solid shapes for moulds and dies.
Tin-based Babbitt	High-speed bearings
Pure Lead	Acid and fume resistance.
Pure Copper	Electrical conductivity, thick or thin coatings.
Aluminium-bronze	Bond coating. Resists low temperature fretting, corrosion and cavitation. Machines well.
Phosphor-bronze	Resists oxidation and wear.
Pure Nickel	Corrosion resistant.
Nickel-copper alloy (Monel)	Resists chemical attack, fretting and arc erosion.
Nickel-aluminium alloy	Excellent bond coat. Resists corrosion.

Metallographic examination of a typical coating reveals an undulating, lamellar structure formed by the successive impact and spreading of extremely plastic particles. A metal coating contains oxide and porosity. The high solidification rates which are similar to those in splat quenching promote a very small grain size within the flattened particles.

The properties of the sprayed layer are understandably different from the cast or wrought condition of the material. Usually the lamellae exhibit a high strength as a result of the fine grains caused by the cooling rate, however the bulk tensile strength, elastic modulus, hardness and density of sprayed material are generally lower than for cast material.

The importance of adhesion of coatings to a substrate and cohesion within a coating is obviously of importance, particularly in relation to engineering applications of coatings.

2.3 Measurement of Adhesion Strength

The tests [8-13] commonly used to assess the integrity of the bond are qualitative; for example, bending, chiselling, resonance and heating. These tests are inadequate for a scientific type of study. A variety of quantitative tests [14-21] have been used and discussed in published literature, these involve shear, bending, torsion, tensile and fracture mechanics approaches to testing. The most widely accepted tests prove to be the bond tensile strength test and the bond shear strength test.

The tensile test involves bonding a suitable "dummy" substrate to a deposit with a resin, after which the deposit is pulled from its substrate in a tensile manner, see Fig. 2.

For the shear test a coating is deposited onto a rotating cylindrical rod. Rings are then machined from the deposit. The shear bond strength is determined when the rod is forced through a hardened steel die which has a hole larger in diameter than the rod but smaller than that of the rod plus coating, as illustrated in Fig. 3. The coating is detached and the adhesion strength R is determined from the formula:-

$$R = \frac{P}{\pi ds}$$

P = load to cause failure
d = diameter of cylindrical rod
s = width of ring of deposit

Despite extensive use of the tensile test wide scatter appears in results obtained, many of these are due to the use of an adhesive. The following aspects are of concern:-

a) The tensile strength of the adhesive must be greater than that of the coating.

b) The curing temperature for the adhesive can affect the adhesion of the coating by reducing residual stress or even promoting diffusion between coating and substrate materials.

c) Specimens must be mounted axially during the curing process to ensure the tensile force applied during testing is at right angles to the interface between coating and substrate.

FIGURE 2 Bond Tensile Test Specimen
(dimensions in mm)

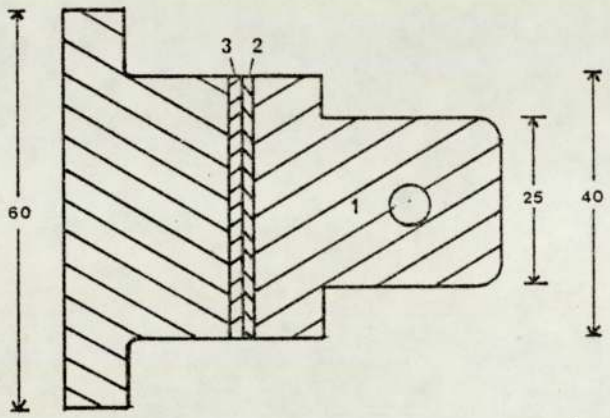

1) Test Specimen; 2) Sprayed Layer
3) Adhesive

FIGURE 3 Bond Shear Strength Test Specimen
(dimensions in mm)

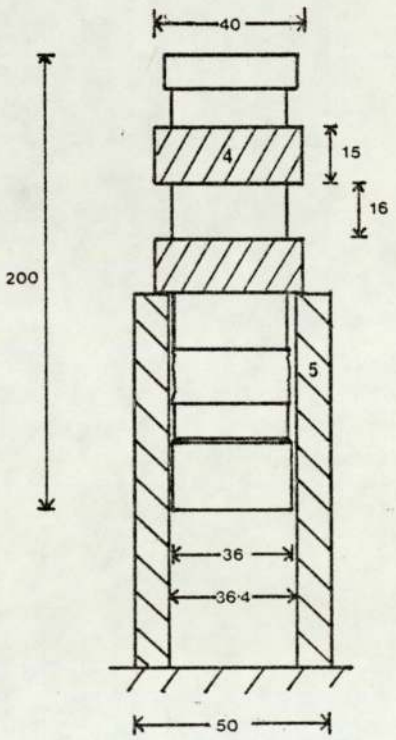

4) Sprayed Layer; 5) Die

d) In the ideal case fracture should occur at the interface between coating and substrate. However, partial fracture can occur at the interface between the adhesive and coating. In this event the area of the "torn-off" coating is measured and used as the area supporting the tensile force. However, this additional operation again leads to inaccuracies.

e) The resin may penetrate to the substrate/coating interface. It is possible to control by the use of various sealants, however in each case the fracture faces should be assessed visually.

The extent that a coating is stressed during service depends on the type of coating and its particular use [22-24]. Materials such as aluminium, zinc or tin, used for atmospheric and aqueous corrosion resistance, and radio frequency shielding, would be expected to be subject to little external stress. Ceramic oxides such as Zirconium Dioxide or Magnesium Zirconate or cermets such as Magnesium Zirconate-Ni-Cr however are used as thermal barriers and will be subject to the stress induced by thermal gradients, cycling, and shock. Oxides of chromium and aluminium and carbides of chromium and tungsten are subject to the stresses induced by impact and shock loading produced by abrasion.

Engineering type steels are of particular interest to the author. They are generally used to restore mis-machined or worn components to their original dimensions, they impart wear resistance and act as a hard oil retaining coating.

Specific examples of areas of use are:- crankshaft journals, steel mill roll journals, paper mill roll faces, brake discs and drums, and impeller shafts. Although a certain degree of tensile stress may be developed within the coating due to the centrifugal force due to the rotation of a shaft this is minimal especially with thin coatings compared to the shear and compressive forces induced by rubbing or sliding contact.

In the author's opinion, a shear type of test would provide the more useful, practical and probably more consistent information, with regard to the adhesive properties of engineering steels.

2.4 Arc-Spraying Process

This process involves the creation of an electric arc between two continuously fed consumable wire electrodes. The energy of the arc is sufficient to melt the electrodes, the molten material is continuously atomised and projected by compressed air emanating from a nozzle situated between and behind the two electrodes.

The process can be conveniently examined on three aspects, namely: the production of molten droplets, the transfer of droplets to the substrate and the formation of a coating. In the following pages each aspect is considered singularly, particular reference is made to arc welding in which similar effects can occur.

2.4.1 Production of Molten Droplets

An electric arc is produced by the passage of an electric current through an ionised or partially ionised gas. Initially the ionised gas is created as the two wires advance to an

intersecting point. Due to the high density of the electric current, extreme heat is generated at the contact surface, fusing these portions of the metal wires and ionising the surrounding gas, therefore creating a localised plasma [25]. The plasma established between the two wires provides a reasonably low resistance path for the flow of an electric current, this ionised state is maintained by the high current density.

Positive gas ions flow from the anode to cathode, which is intensely heated by the impact. The anode is usually cooler than the cathode. There is a high velocity flow of atomising gas and the melting of the electrodes occurs as shown in Figure 4. The gap between the two electrodes widens in the direction of the flow of atomising gas. The anode is seen to be extended more, in the direction of the workpiece, than the cathode and therefore is heated at a slower rate. Due to the cooler nature of the anode, the particles formed are larger than those formed by the cathode. Anode particles are in the form of fine droplets while at the cathode there exists a finer spray type droplet formation. This is a continuous process and as the arc melts a length of wire back from the tip more solid wire is fed into the arc region.

The material at this stage is in the most thermally active and fluid state of the whole process. It is in the form of very hot, large, extended, irregular shaped particles. Temperatures encountered within the metal are dependent on the environment, they have been measured within the region of 5000-6000 K [26,27]

FIGURE 4 Diagrammatic representation of the electric arc spraying process

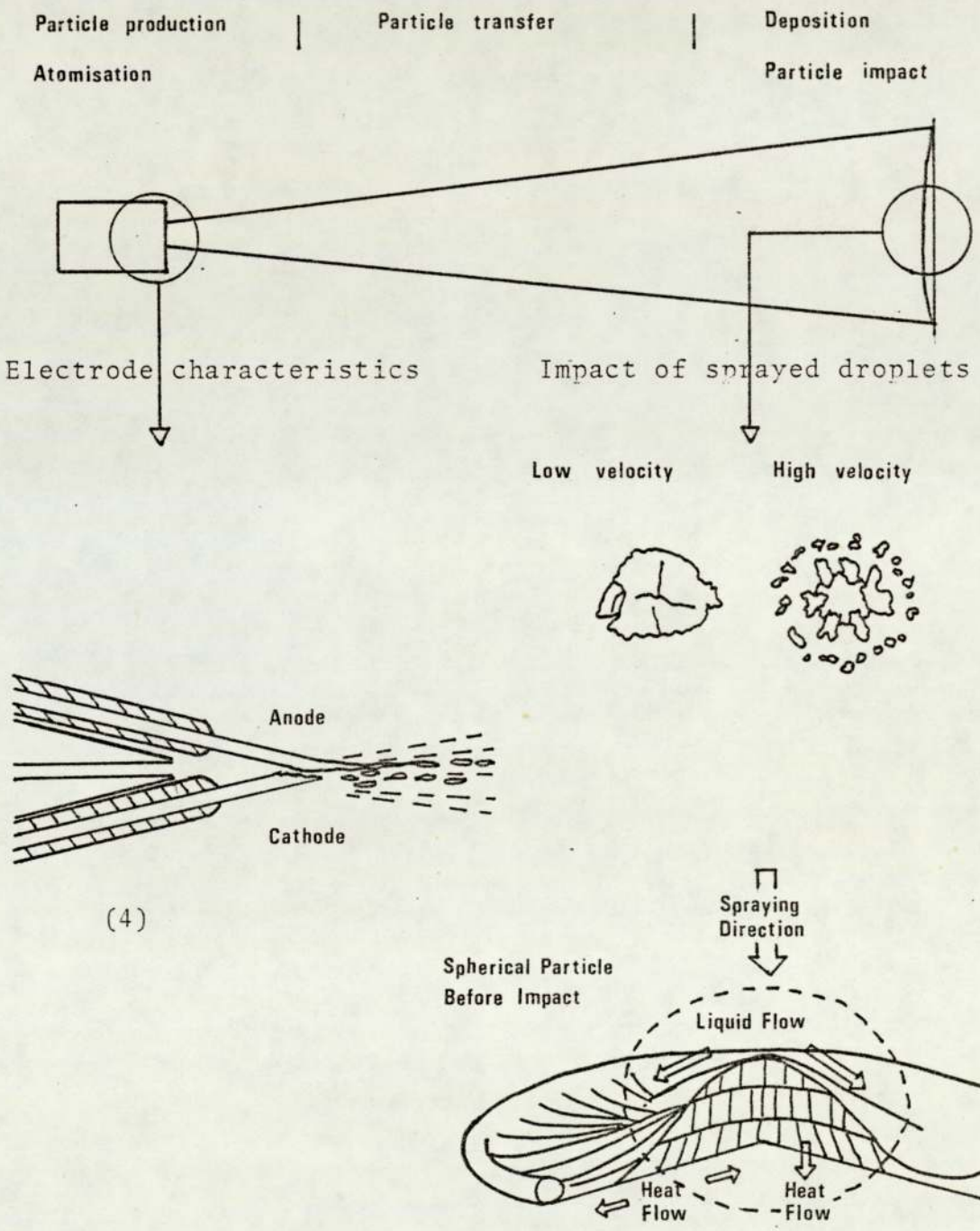

(4)

(143)

in air, however temperatures as high as 10,000 K [28], have been recorded.

Several direct and indirect measurements of arc and weld pool temperatures have been taken. Early work by Cobine [29] reported that metal in the central core of the arc column reached a temperature of 11,000 K. Christensen and Chipman [30] measured the weld pool temperature of pure iron at 2200 K, by passing the arc directly over a W-Mo thermocouple with an exposed hot junction.

Later work performed by Christensen and Gjermundsen [31] utilised a W/W Rhenium thermocouple introduced through a hole in the welded plate or into the weld pool from above. It was concluded that extreme temperatures of 2800 K prevailed in the arc plasma only. The temperature in the main body of the weld pool, during the welding of mild steel, ranged from the liquidus to about 2500 K. Belton et al [32] used the same method and measured temperatures of 2200 - 2500 K. In general the conclusion is that temperatures in the region of 2000 - 2500 K is representative of the weld pool temperature during the welding of steel.

It is reasonable to assume then that the temperatures obtained within molten droplets produced by arc spraying are initially within this temperature range.

Under these conditions the kinetics of high temperature processes must be taken into consideration regarding the material in the arc zone. Rapid processes of diffusion and reaction occur between sprayed metal and gases, this is

considered by Steffens [27] to influence particle composition, surface tension, spreading and wetting ability. Due to the complex nature of high temperature processes, the kinetics of reactions in the arc zone are not fully characterised.

It is generally recognised that, for example, during the spraying of steel elemental loss of carbon, chromium, manganese and silicon is greatest in the arc zone [33,34].

2.4.1.1 Absorption of the Carrier Gas

Gas retention in arc welding rather than spraying is discussed due to the limited amount of available information relating to this aspect of the spraying process. However, the two processes are essentially similar and a parallel can be drawn between the two. Gas retention and reaction is likely to be higher during the spraying process, not because higher temperatures are expected but as a result of the much greater solidification rates which can be 10^4 times greater than welding. It may also be enhanced by the very large surface area exposed by the spray droplets to the atomising/carrier gases.

In an electric arc the electrical energy applied to the electrodes is largely converted to heat between them. Electrons emitted from the cathode reach high levels of kinetic energy, and collisions with atoms and molecules of gas cause ionisation and in diatomic gases [3] dissociation. The atomising and carrier gas generally used in arc spraying is compressed air which may contain a certain amount of water and hydrocarbon vapour, in addition to the nitrogen, oxygen and hydrogen.

The superheated condition of the metal at the arc position in welding or spraying and the presence of gas in the atomic form ensures the absorption and reaction of a relatively large amount of gas. Absorption is accelerated by the electro-magnetic stirring action in the weld pool which has been observed [35]. This action transports saturated liquid metal to cooler regions of the pool, and exposes a new liquid surface to the environment. Salter, Howden and Milner [36,37] have shown that the rate of reaction and distribution of the reacting elements is influenced by transport processes within the molten weld pool. The solidification rates imposed by welding and especially spraying will not accommodate equilibrium desorption of the gases, therefore a retention in excess of the equilibrium quantity is expected after solidification.

Iron combines with oxygen to form FeO which is soluble in molten iron to about 0.2 wt% [38], see Fig. 5 [39]. Solidification reduces the equilibrium solubility limit to 0.03-0.05 wt%. This may be increased in steels with alloying elements such as Cr, Mn and Si which have a strong affinity for oxygen. The oxygen content of solidified iron after bare wire welding may be as high as 0.30% [39], which corresponds to 1.4 wt% FeO.

The theoretical solubility of nitrogen in iron at 1870 K and 1 atmosphere of pressure is 0.045 wt%, see Fig. 6. Under the conditions of arc welding at this temperature and pressure Uda et al [28] recorded 20 times the expected nitrogen content and Kobayashi [40] 3-4 times the content.

FIGURE 5 Oxygen content of liquid iron saturated with liquid iron oxide

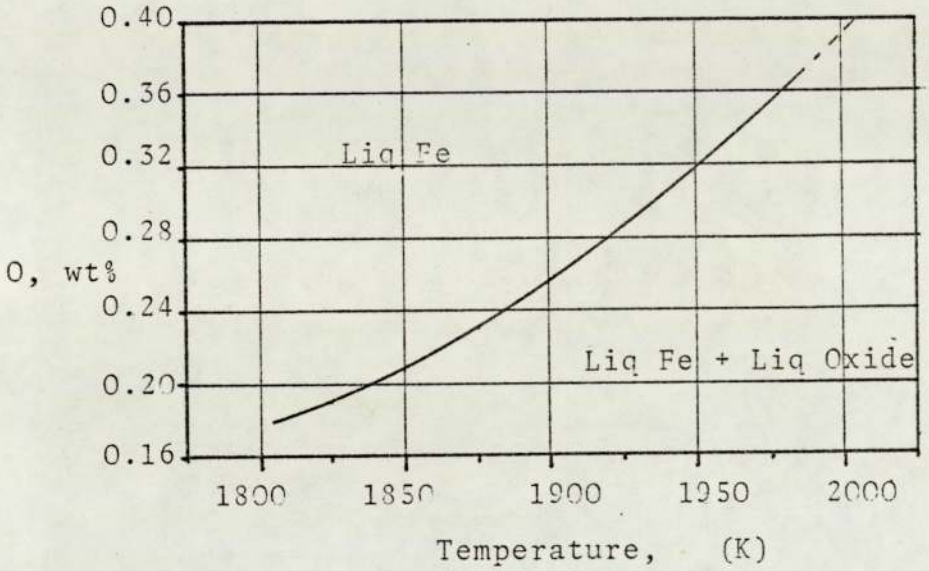

FIGURE 6 Solubility of nitrogen in liquid iron alloys at 1 Atm pressure and 1873 K

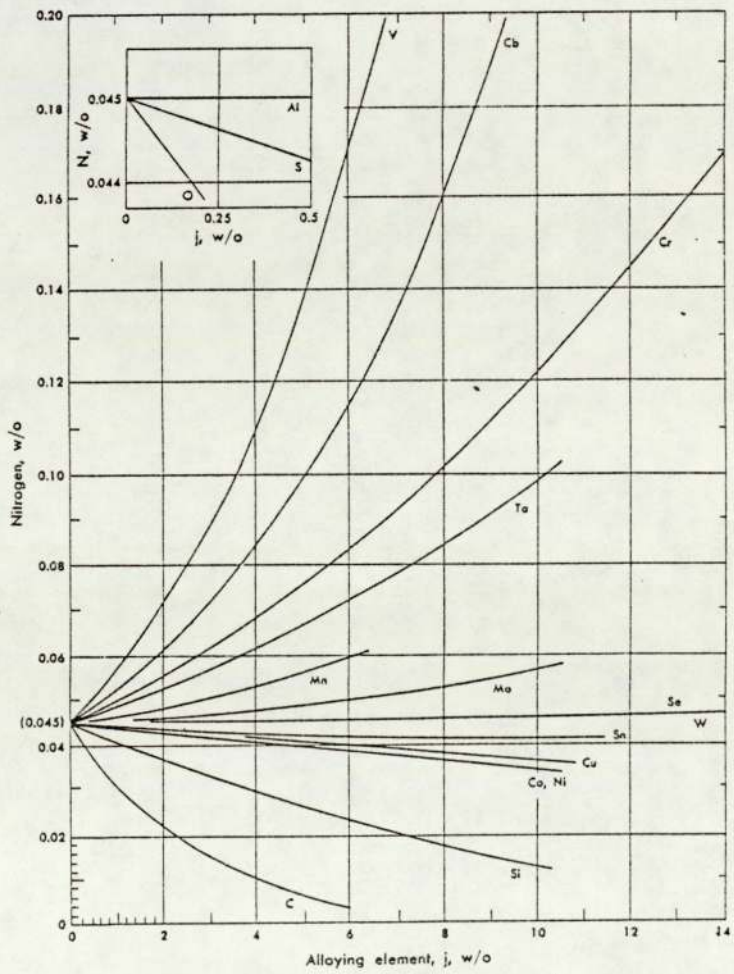

Uda et al [41] studied the effect of oxygen content on the solubility levels of nitrogen. In the range 200-600 p.p.m. oxygen within the iron 3-8 times the solubility is recorded, this level of absorption of nitrogen is only observed in arc melting and canot be explained using thermodynamic data. The explanation for this anomalous nitrogen absorption involves the formation of FeO on the surface. Nitrogen is mainly absorbed through the arc atmosphere which is in a highly activated state and has a high chemical potential of nitrogen, the rate of evolution of the gas as the metal cools is suppressed by surface active elements such as FeO. The solubility of nitrogen is also increased in alloyed steels due to the affinity of elements such as chromium and manganese [28,40], see Fig. 6.

In general the hydrogen content of arc melted iron is only slightly higher than expected. Howden and Milner [37] determined that the hydrogen content is 1.4 times greater than the hydrogen content at its melting point and roughly equal to the theoretical solubility at 2370 K. The smaller increase in retained hydrogen as compared to oxygen and nitrogen is attributed to the greater mobility of atomic hydrogen. They state that the initial absorption rate is approximately proportional to the square root of the hydrogen partial pressure, however there is evidence of atomic hydrogen and that gas is being absorbed at a greater rate than would be expected in contact with hydrogen alone. They also state that the rate of loss of gas from a cooling specimen is remarkably high although the desorption rate is lower than the absorption rate.

Alloying elements such as chromium and manganese slightly increase the solubility of hydrogen, Fig. 7 [39].

2.4.2 Transfer of Droplets to the Substrate

It is generally considered that relatively large metal drops leave the arc zone in a super-heated state [27]. Atomisation continues and the final diameter of the particles ranges from 1-100 μm, although the mean particle diameter is dependent on spraying parameters. This is discussed in more detail later. Particles are accelerated in the transfer region by the jet of compressed air, however the final impact velocity of the particles is, of course, related to factors such as particle size and spraying distance. Typically, particles reach a velocity of 90 ms^{-1} [34] during arc spraying. Due to the considerable increase in surface area gas/metal reactions become particularly significant. Matting [34] makes reference to Soviet literature which records the formation of a solid shell of oxide surrounding a liquid core during transfer of steel particles. He regards this as unlikely due to the fact that the melting points of ferric oxides are similar to that of pure iron. Oxide splashing on impact is described by a number of authors [27,42] including Matting, indicating that oxide is forming and it is still molten during transfer, although the formation of a complete shell may be the exception rather than the rule. Steffens [27] records that no firm oxide film can be expected during the spraying of steel but has observed the complete oxidation of particles after deposition.

The molten particles are subject to a certain degree of cooling during transfer, however the majority still maintain a tempera-

FIGURE 7 Solubility of Hydrogen in Iron-j alloys at 1 Atm pressure and 1873 K

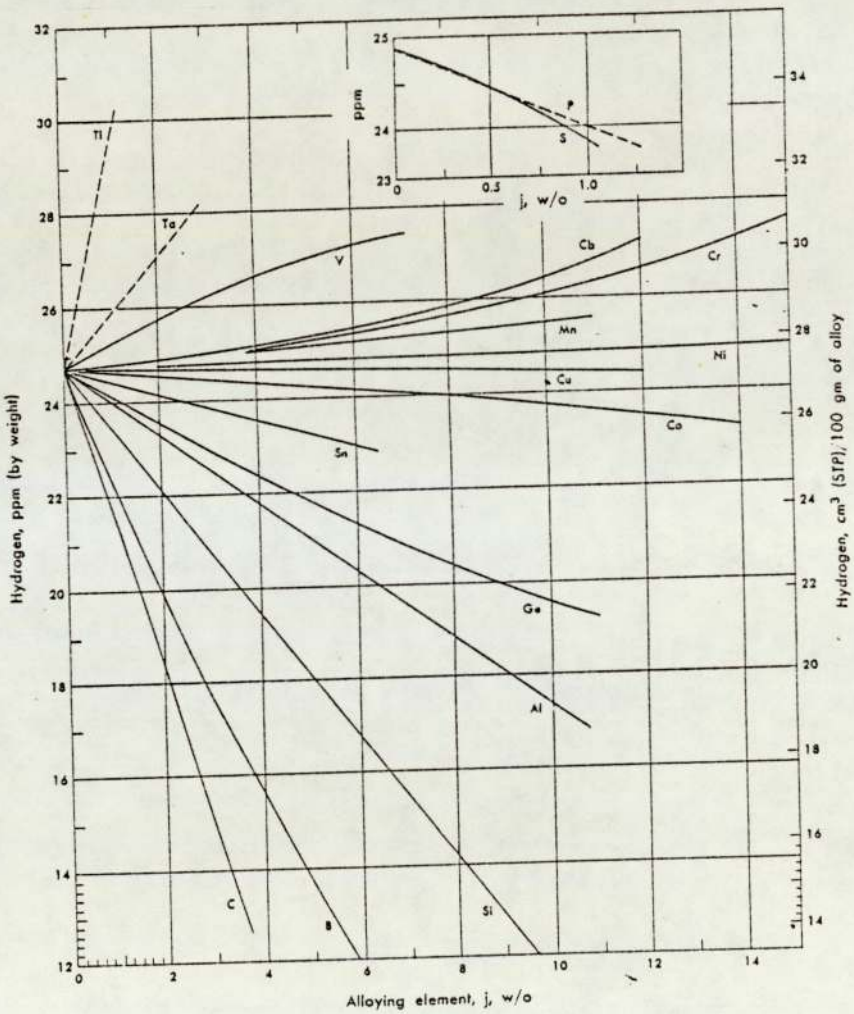

ture in excess of the melting point, illustrated by the flow characteristics and the amount of splashing which can be observed on impact with a substrate.

2.4.3 Coating Formation

The microstructure of a typical coating produced by spraying depends on the manner in which individual particles, which are molten or in a highly plastic state, flatten and solidify on impact. The main factors controlling the microstructure are particle velocity, temperature and diameter [42].

On impingement with the substrate surface the particles lose their kinetic energy and undergo severe deformation. The kinetic energy can be transformed into heat. Dallaire [43] recorded a rise of 270° in lamellae during plasma spraying.

The final shape of the flattened particle is dependent on its original size, which, linked with the viscosity will determine the amount of substrate area covered. The direction and degree of flow will also be affected by surface roughness. Classical theory [44] states that the final equilibrium shape of a drop on impact with a flat surface is determined by static surface tension forces. Generally a flat disc is produced, however at high velocities this becomes unstable and the radially flowing thin sheet becomes unstable and disintegrates at the edge into many small droplets, illustrated in Fig. 4. This has been observed during spraying [45] and is reported as detrimental to the integrity of the coating.

The situation with droplets in the spraying process is more complex since the substrate surface is rough. This introduces components of motion normal to the plane of the surface. The particles are in various thermal conditions and solidification is initiated on impact. The rate of heat extraction from an impinging droplet will rapidly increase as it flattens against the substrate and as the surface area available for heat transfer increases. Soldification of droplets striking the substrate takes place extremely rapidly, the rate is related to particle thermal content, shape after impact, the extent and nature of intimate contact with the substrate, substrate temperature and the thermal conductivity of particle and substrate.

The rate of freezing of each particle is of the order 10^4 - 10^7 Ks^{-1} [42,45]. A very fine grained structure is produced with a grain size of the order of several microns.

The coating is built up in a lamellar form particle by particle. During the time it takes for one particle to solidify Zaat [45] postulates that about 50-100 particles arrive onto one square metre, and the time of arrival on the same spot takes about 0.1 seconds, about 10^6 times greater than the freezing time. He considered that the process of removal of the heat content from one particle will not be influenced by another particle. However each lamella will be subject to a thermal cycle every 0.1 seconds as heat is absorbed from the next impacting particle.

For this period of 0.1 seconds the lamella exposes a large surface area to the environment. Any oxide formed on the particle during transfer is probably disrupted and clean metal is exposed, again there is the opportunity for gas/metal reaction. It is probably during this period that lamellar oxides are formed.

2.4.3.1 Formation of Oxides During the Deposition of Engineering Steels

Pfeil [46] showed that carbon steels exposed to oxygen at high temperatures for an appreciable time produced scale consisting of layers of three types of oxide. The innermost layer is wüstite (FeO), the middle layer is magnetite (Fe_3O_4) and the thin outermost layer is hematite (Fe_2O_3). The thickness of the oxide depends on both temperature and time of oxidation and proceeds approximately according to the parabolic law $x^2 = kt$, where x is the increase in weight, k is a temperature dependent constant and t is the time. The relative thickness of the various types of oxide generally depends on the temperature of formation [47].

Paidassi [48] determined the thickness of the oxides of iron formed between 970 and 1520 K in air. The relative thicknesses remain constant at 1% hematite, 4% magnetite and 95% wüstite.

At temperatures below 840 K FeO is unstable and decomposes to Fe_3O_4 and iron (Fe). Matting and Steffens [34] observed that most of the oxide formed in a sprayed steel consisted of Fe_3O_4 and that FeO formed an extremely thin film.

The decomposition of FeO however is influenced by cooling rates and it is possible that complete breakdown of FeO will not occur after deposition. Thus, it is reasonable to assume that the iron oxides produced in a sprayed carbon steel are non-stoichiometric FeO and/or Fe_3O_4.

2.5 Adhesion of Coatings

The indispensable property of a sprayed coating to be used in engineering applications is good adherence to the substrate. A dense and coherent coating which spalls from the surface on which it has been deposited is not useful. Similarly an adherent coating that is highly stressed and lacks coherent strength is equally useless.

It is general knowledge amongst researchers that the adhesion of a deposit is material dependent, however it is also influenced by process and other factors, namely surface preparation, spraying practice and component design. The importance of surface preparation with regard to adhesion has been evaluated and discussed to great depth by several authors [49-51]. For the experimental programme surface preparation was required to be optimum and non-variable. Thus it is not intended to discuss this aspect in great depth.

The substrate surface should be free from contaminants which may be detrimental to adhesion and is preferably prepared prior to spraying by some surface roughening process to promote mechanical interlocking. Spraying ideally is performed directly after surface preparation whilst the surface is still active. Studies [42] on the adhesion of droplets on impact with a surface show that not all particles adhere or wet the

surface and that the degree of adhesion is influenced markedly by the size, temperature and velocity of a droplet. Several authors [40,43] have noted that the real area of contact between individual lamellae within the coating and between lamellae and substrate is much less than the apparent area because of adsorbed and entrapped gas, oxide films or other contamination.

Generally particles with greater thermal and kinetic energy exhibit an increase in adhesion due to better flow characteristics, improving contact with the surface of the substrate and interparticle contact, and possibly resulting in less stress raising pores. Spraying practice that produces high velocity, hot, large particles should increase adhesion. These spraying conditions however could also prove to be detrimental. High velocities produce splashing, as previously mentioned, which is considered to reduce the strength of the coating. Also, it is known [3] that these conditions tend to increase residual stress which may cause the formation of micro-cracks [42] in brittle materials. In addition to the micro-stresses a pattern of macro-stresses may also be developed because of the mismatch [54] of thermal expansion between coating and substrate due to thermal gradients or differences in the co-efficient of thermal expansion. This is discussed in greater detail later, it is evident that component design now becomes important and stress raising areas must be minimised.

Mechanisms of adhesion have been categorised by several authors [34,55]. Matting and Steffens used three main headings:-

a) Mechanical interlocking of the metal-metallic oxide mixture of particles with the irregularities of the roughened substrate surface.

b) Physical adhesion of the spray/substrate materials which are brought into intimate contact such that the two types of atoms are within the lattice constant distance.

c) Metallurgical interactions between the spray particles and substrate material.

Mechanical bonding essentially involves shrinkage of metallic lamellae around and onto the projections of an irregular substrate surface. Prior to spraying, a substrate surface is roughened by means ranging from acid pickling, through grit or shot blasting to coarse machining. This also improves adhesion by increasing the surface area available for contact and by removing any detrimental surface contaminants. It also creates a high energy surface by micro cold work.

Matting and Becker [56] suggest that individual particles at the interface are joined by mechanical interlocking and local cold welding, and make parallels with this to cold pressure welding. Ballard [57] states that the surface tension of the spray particles is primarily responsible for the establishment of adhesive forces. He explains that surface tension exerts a

force which counteracts the forces on the metal particles which cause splatter on impact. He describes how the projections of the roughened surfaces are enveloped and interlock with the sprayed metal layer. He stated that metals of low heat content adhere better since solidification occurs immediately the favourably acting surface tensions achieve their maximum value, whereas those with high heat content tend to burst into several single droplets on impact forming small areas of adhesion separated by voids. Matting and Steffens [4,55] consider mechanical interlocking a local effect and can therefore only be expected to play a part in the adhesion.

Physical adhesion presupposes that both spray and substrate materials have approximately the same lattice constant The fundamental mechanism [55] is considered to be due to Van der Waal's forces (dispersion forces). This is a weak attractive force which involves fluctuations and surges of electronic charge in individual atoms [58]. It is temperature independent and does not require an activation energy, it assumes intimate contact between substrate and coating. Matting and Steffens estimated, from theoretical considerations, the adhesion due to Van der Waal's forces and came to the conclusion that they would only contribute a small part of the total bond strength.

A metallurgical bond assumes sharing of electrons across the substrate coating interface. Much of the research preceeding 1960 resulted in the conclusion that a metallurgical bond

between coating and substrate could not exist, due to the very fast cooling of the spray droplets[59]. However research into solid phase welding has since shown that a true metallurgical bond can be formed even at room temperature, for example in cold pressure welding and explosive welding[60]. Van der Waal's forces are also thought to be present.

More recent research has identified regions of metallurgical bonding which is especially highlighted using coatings of aluminium and molybdenum. Giersten[61], Baxter and Reiter[18], and Stanton[62] observed partial welding between substrate and aluminium. Electron probe microanalysis positively identified interdiffusion of the aluminium and ferrous substrate. It also indicated the presence of intermetallic compounds such as Al_5Fe_2. The reactions occurring at the substrate surface provided visible evidence of thermal oxygen transfer processes in areas where residual ferrous oxides were known to be present.

Steffens et al[63] reported the possibility of the formation of an intermediate compound Fe_7Mo_6 during the spraying of molybdenum onto a ferrous substrate. Birchon[64] also reported evidence of this intermetallic compound at the coating interface. Overs[65] however observed no such alloying except after a post-spraying heat-treatment at 1370 K.

Using a nitrogen carrier gas, Steffens[4] observed epitaxial growth of fine subgrains perpendicular to the boundary layer in a steel/steel system. The metallic connection being interrupted in several regions by oxides or other foreign substances.

Several mechanisms are likely to contribute to the bond formed in the spraying process. The degree that each mechanism contributes depends on the type of material and the spraying conditions used. In certain sprayed systems, such as aluminium onto steel, a metallurgical bond can dominate due to a "thermit" type of reaction occurring on deposition. The exothermic reaction promotes diffusion and the formation of intermetallic compounds. Generally when a secondary reaction does not occur the formation of a metallurgical bond is the exception rather than the rule. This view is supported by Farrow [66] who performed electron microscopy on steel droplets after impact with a polished steel surface and observed infrequent metallurgical bonding. The dominant mechanism for adhesion in this case is probably mechanical interlocking due to the shrinkage of sprayed lamellae around the projections on the roughened surface. Although a contribution to the bond by localised welding and cold welding due to deformation and intimate contact cannot be dismissed.

2.6 Residual Stress

Surface preparation and cleanliness followed by good spraying practice is necessary to produce acceptable adhesion of a deposit to a substrate and cohesion within the deposit itself. Of equal importance however is the control, or at least knowledge, of the shrinkage stress developed within the coating both during and after spraying.

The production of a mechanical bond involves the shrinkage of the resultant sprayed lamellae onto and around the roughened surface of the substrate. This shrinkage process develops micro-stresses in the lamella. The successive deposition of droplets results in the development of macro-stresses within the bulk coating.

In some cases the residual contraction stresses may contribute to the apparent bond strength, in others residual stress may cause failure and exfoliation. Stanton [67] described the fractures likely to occur if the developed stresses are too high. Failure of coatings deposited on flat or internal surfaces invariably commence at the exposed interface edges. When spraying onto outside diameters he observed cracks extending through the deposit to the basis metal. Failure may also occur within the coating itself if the cohesive strength is insufficient to withstand the effects of shrinkage induced during spraying.

The development of residual stress, however, is not always detrimental and can be advantageous with regard to the adhesion of a coating. Haddleton [68] performed several heat treatments, see below, on shear adhesion strength type specimens and tested both mild steel and 13% chromium steel coatings.

(i) 920 K for 1 hour (stress relieving temperature)

(ii) 1220 K for 2 hours (to promote diffusion, grain boundary growth)

(iii) 1400 K for 1 hour (to promote rapid diffusion, grain growth and oxide solution).

All heat treatments were performed in a vacuum induction furnace at 13 x 10^{-3} Pa. After stress relief the shear bond strength of the coatings was reduced, in the case of the 13% chromium steel by 30-35% and by a relatively smaller amount for mild steel. The other heat treatments which induced diffusion increased the bond strength from this new stress relieved level.

The conclusion was that a significant proportion of the bond strength of the coatings, especially the 13% chromium steel, deposited on this type of test piece, was a direct result of residual shrinkage stress.

The development of a residual stress system within a thermally sprayed deposit can affect both the adhesive and cohesive strength of the coatings, and thus control the overall mechanical performance. This will be explained in greater detail later.

Residual stresses can be induced in a coating in several ways:-

(i) due to the variation of temperature and temperature gradients which lead to differences in shrinkage. The material subject to the higher temperature contracts more than all other areas on cooling, this contraction is restrained by underlying cooler layers, which may even be expanding at the same time.

(ii) the effect described in (i) is further complicated by differences in the co-efficient of thermal expansion of substrate and coating.

(iii) phase transformations involving a dimensional change, occurring at the substrate surface and within the coating.

(iv) the difference in modulus of elasticity of the substrate and coating.

Due to the complex nature of formation of a sprayed deposit the residual stress is difficult to determine or model.

Several authors [54,69-73] have produced models which predict residual stress magnitude and patterns within individual systems under certain boundary conditions. Generally a number of assumptions have to be made and the model is limited to particular coating and substrate materials and dimensions and specific spraying parameters, varying degrees of success are obtained.

Lee [69,70] used finite element analysis to determine the temperature and stress distribution within a substrate (nickel) and a sprayed deposit (copper) as a function of deposition time, in a low pressure plasma deposition process. He reduced the problem to a one dimensional conduction analysis and computed temperature profiles which were in reasonable agreement with experimental data. Using the same model the temperature profile in the substrate and deposit was then obtained for a more complicated three layer super alloy composite.

Then, by using the computed temperature profiles, the thermal stress developed during spraying and thermal cycling of the more complicated layered system was analysed, using the same type of analysis. The maximum tensile and compressive radial stresses during heating or cooling were shown to develop in the middle of each layer not at the interface of adjacent materials.

Marynowski [54] theoretically determined the stresses induced during the plasma spraying of a 2.5 mm thick coating of titanium carbide on metal substrates (iron and copper). In these systems the substrate has a co-efficient of thermal expansion greater than that of the coating. The theoretical experiments were designed to produce information from a range of temperature gradients produced by combinations of traverse speed and cooling periods. An infinite slab approximation was used to calculate the temperature distribution throughout the test-piece, assuming that the coating was thin compared with the area heated by the plasma gun, and that the stresses induced did not exceed elastic limits.

For the model, the assumption was made that the individual molten particles were impacted on the surface, flattened, frozen and quenched to the temperature of the surface without contributing any significant internal stress to the coating. The stresses induced were calculated considering the coating to be sprayed onto a water cooled substrate and the entire piece brought down to room temperature.

The thermal distribution during spraying is shown in Fig. 8a, a small temperature gradient exists through the substrate and a steeper temperature gradient occurs across the coating. Marynowski explained that when cooled down to room temperature the substrate tends to contract to a greater extent than the coating at the interface, inducing a state of compression within the coating at the interface, and the surface of the coating which was hottest during spraying, goes through the greatest contraction. Figure 8b depicts the strain pattern in the system when the entire structure is cooled down to room temperature. Provided complete bonding at the interface and elastic behaviour for both the coating and substrate are assumed, the stress distribution will be similar to that shown in Fig. 8c. It is evident that the surfaces of the substrate and coating are in states of residual tension and residual compression respectively and that the free surface of the coating is in tension. The interfacial stresses tend to cause adhesive failures and the tensile stress at the free surface of the coating tend to produce micro-cracks and a cohesive failure in the coating. If the values of these stresses are greater than the bond strength between the coating and the substrate, failure of the coating will occur, which has been observed by Marynowski.

Induced stresses at the interface of 5.0 - 132.0 MPa (in compression) and tensile stresses of 54.0 - 344.0 MPa were calculated. The tensile strength of TiC is approximately 206 MPa, therefore in most cases examined by Marynowski the tensile strength of the coating was exceeded and it should exhibit micro or macro-cracks.

FIGURE 8a Thermal distribution through coating and substrate

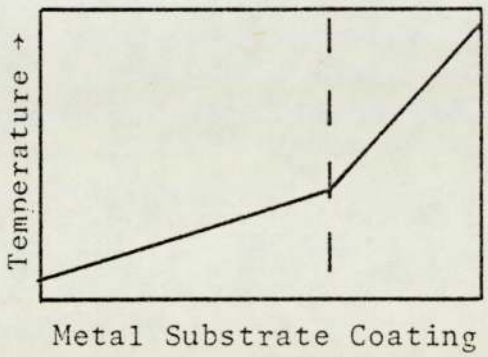

FIGURE 8b Strain produced by cooling to room temperature

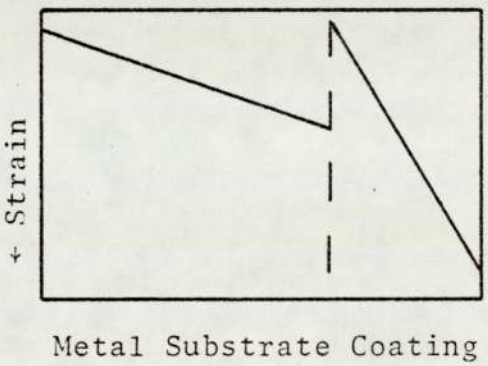

FIGURE 8c Stress distribution within sprayed system at room temperature

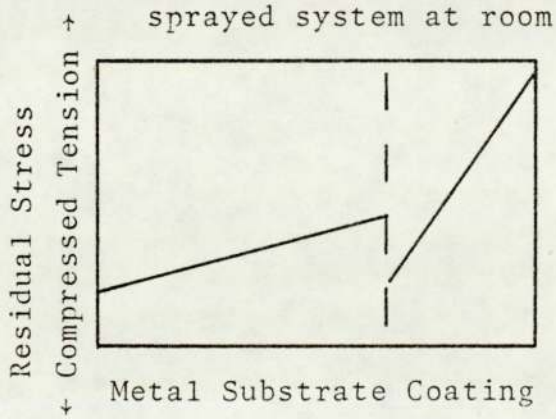

Marynowski concluded that a reduction in interfacial stress resulted when using a high conductivity substrate, however this simultaneously produced an increase in the surface tensile stress. Also, that great variations in stress levels can result from seemingly insignificant changes in the spraying process.

The model devised assumes elastic behaviour and does not take into account the initial expansion of the substrate layers at the interface caused by the sudden increase in temperature when particles impinge and solidify. It certainly can be used to indicate the large values of residual stress theoretically possible, however it gives little information about the existing stress distribution.

Keshtvartzi (71) based an analysis of stress on Timoshenko's equations of bi-metallic thermostat (see Appendix 1). Experimental procedure involved spraying molybdenum onto cylinders and flat strips of mild steel. The substrate is described as being subject to the following thermal history. The top layer expands due to the initial thermal input by the impinging particles, this expansion is restrained by the cooler inner layers, the outer layers are therefore in a state of compression, Fig. 9. It is possible that the temperature at the surface of the substrate is sufficient to significantly reduce the yield stress and allow plastic deformation to take place. During the cooling process if yielding has occurred then the top layers experience a state of residual tension, and the core compression.

Keshtvartzi also considered the consequences of the formation of martensite within the surface of the substrate, this would produce two distinct layers with opposite stress configurations.

FIGURE 9 Temperature and thermal stress distribution during the spraying of a round bar

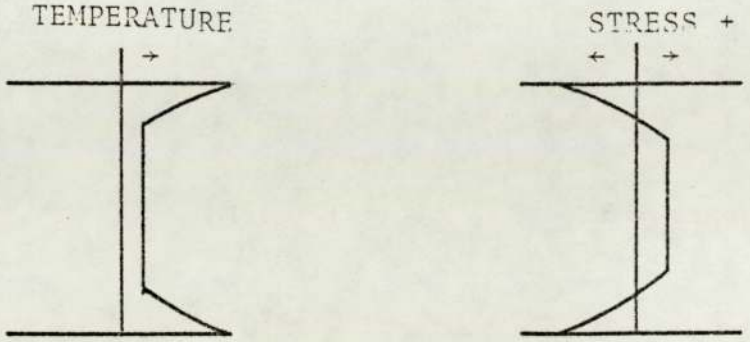

Temperature and residual stress distribution after cooling down

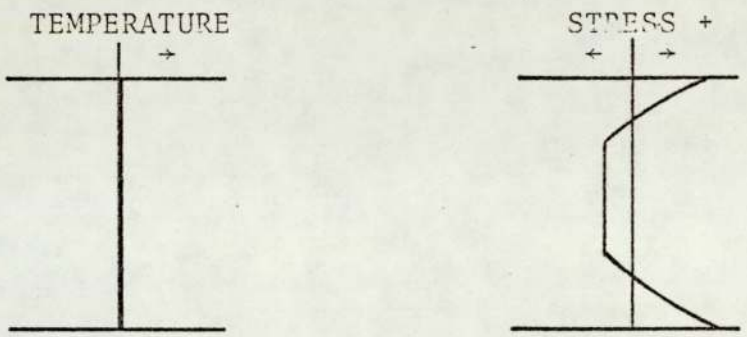

FIGURE 10 Stresses existing within a round bar resulting from martensitic transformation occurring in surface layers

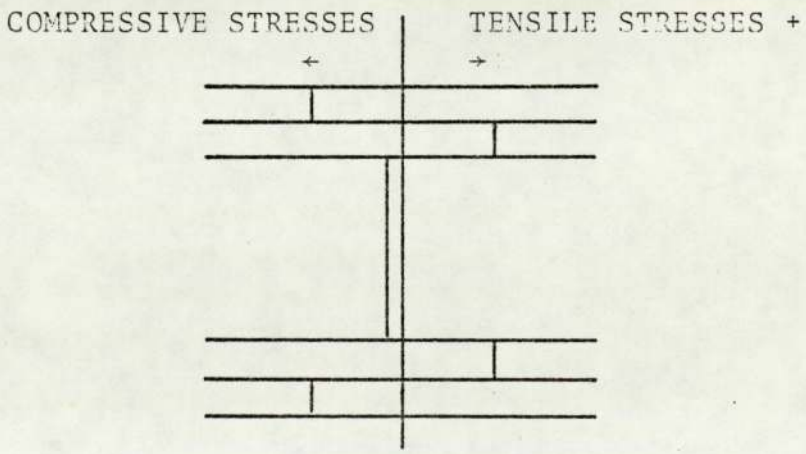

The formation of martensite involves a volume increase of the order of 4%, creating a state of compression in the outer layers. The inner layers are cooled from below the transformation temperature and are therefore placed under tension due to thermal contraction, Fig. 10.

Keshtvartzi then considered a relatively thin coating of molybdenum bonded to a thick steel substrate, he assumed elastic behaviour and a shallow temperature gradient across the coating. The stress distribution within the system is modified, Fig. 11. The particles of the coating cool and contract immediately on impact with the substrate, the top layers of the substrate expand. At the interface the strain difference produces compression in the surface of the substrate and tension in the thin coating, the magnitude of stress increases until thermal equilibrium is reached. At this stage the coating and substrate cool and contract together reducing the magnitude of the compressive and tensile stresses, Fig. 11.

Keshtvartzi states that the only way the coating can be left under compression with respect to the top layers of the substrate upon cooling to room temperature, is for the substrate to contract more than the coating. This could occur if the substrate is pre-heated to a higher temperature prior to spraying, or the interfacial stresses are relieved by a mutual yielding of substrate and coating before the structure begins to cool. Marynowski confirms this with theoretical calculations of the stress existing within a coating of tungsten carbide sprayed onto a copper substrate during cooling, after the substrate was pre-heated to a temperature of 730 K. The compressive stress existing within the coating would theoretically reach 690 MPa.

FIGURE 11 Thermal distribution and stress pattern across the coating and substrate

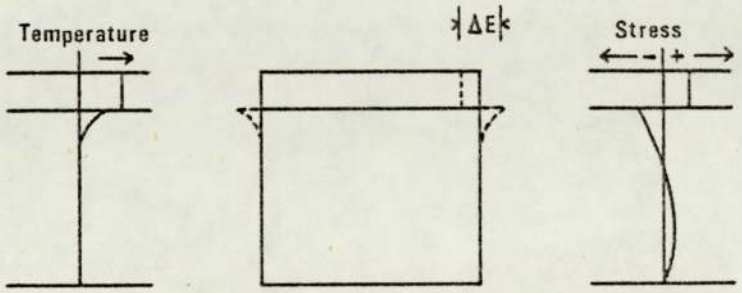

a) Before thermal equilibrium at the interface

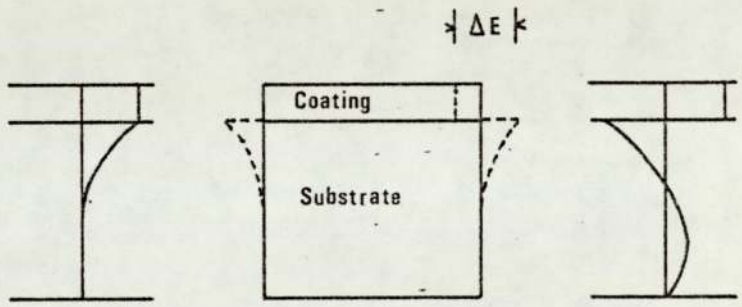

b) At thermal equilibrium

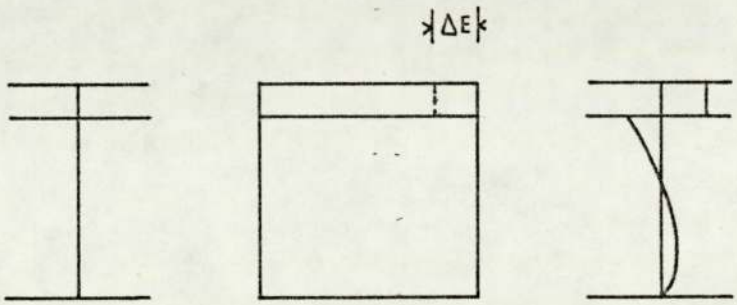

c) After cooling to room temperature

Theoretical calculations, using Timoshenko's equations of bi-metallic thermostat and assuming elastic conditions, confirmed the above theories. However, the magnitude of stress calculated by Keshtvartzi is extremely high,+2850 MPa within the coating and -1440 MPa within the substrate. These values are impossible to reach within this system, the yield stress of the substrate being approximately 260 MPa and the fracture stress of a typical molybdenum coating is 50 MPa [72].

In practice the opposite stress distributions were found to exist, the stress patterns remaining in the test pieces indicated that the coating was under compression and the substrate tension. Keshtvartzi proposed that the large calculated stresses and opposite observed stress patterns were due to the assumption that elastic behaviour exists within the system, as explained earlier plastic deformation within the substrate can produce tensile stresses at the surface. He proposed that at some early stage during the heating part of the thermal cycle, whilst the coating is cooling down and the substrate is still heating up, stresses of the same magnitude of the fracture stress were achieved. It is calculated that at an increase in substrate temperature of 20^{o} would produce a stress equal to that of the fracture stress of sprayed molybdenum. Under more arduous conditions, the coating no longer acts as an effective constraint on the expansion of the substrate, and during cooling, because of the relative difference in the coefficient of contraction, the coating would be placed in compression and subject the substrate surface to a corresponding tension.

A further paper was published by Keshtvartzi in conjunction with Reiter[73] which shows that the peak stress distribution can be considerably modified (but not changed in sign) by spraying a self-fusing grade of molybdenum which has a solidification temperature of 1000 degrees less than that of pure molybdenum. Using the same experimental techniques and spraying aluminium they produced a reversal of the stress pattern, a coating in tension and a substrate in compression. They attributed this reversal to the larger co-efficient of thermal expansion of aluminium than steel. In this case thermal expansion of each material is the major cause of the stresses induced during spraying, however, the overall controlling factor is thermal input.

Several other authors[72-76] have determined experimentally the residual stress induced in a variety of thermally sprayed materials using a number of techniques. Engineering steels of interest to the writer have been investigated and are included in the following section, the results are also discussed.

Barbinok[74] determined experimentally the residual stress in plasma coatings of aluminium and boron nitride and the effect of variation of certain spraying parameters. The coating was deposited on the internal surfaces of steel rings using an underlayer (bond-coat) of nickel aluminide. After deposition the change in diameter of the ring was measured during continuous electrolytic etching, in this way the stress distribution was recorded duirng continuous removal of the

sprayed layer. This technique was performed on "as sprayed" samples and on samples which were subjected to thermal cycling. As illustrated in Figure 12, all samples exhibited tensile stresses throughout the deposit thickness balanced by compressive stresses within the substrate. The levels of residual stress were reduced particularly within the bond-coat, after thermal cycling.

Barbinok also investigated the effect of some spraying parameters on residual stress. An increase in power of the plasma arc (ie.thermal input to the deposit) increased the magnitude of tensile residual stress. An increase of spraying distance from 100 mm to 160 mm reduced the maximum level of residual tensile stresses by a factor of approximately 1.3. Sand blasting, which was used as a surface preparation for the rings, resulted in the formation of compressive stresses in the surface layer of the rings, this was generally removed by subsequent spraying, due to the thermal stress relief.

Barbinok is in agreement with Keshtvartzi [71] in that he considers the tensile residual stress to be due to the sprayed layer contracting to a greater extent than the surface layer of the substrate on cooling. Residual tensile stresses consequently appear in the sprayed layer. The increase in stress due to the increase in power of the plasma arc or reduction in spraying distance is considered to be related to the increase in the thermal stress state of the process. The more severe this state, the higher the magnitude of residual tensile stresses. Barbinok considers the reduction in tensile residual stress due to thermal cycling as a consequence of diffusion processes and recrystallisation.

FIGURE 12 Distribution of residual stresses in the 70%Al + 30%BN sprayed layer, in the underlayer of nickel aluminide, and in the substrate after one (crosses), five (open circles) and ten (triangles) cycles, filled in circles designate the initial specimen.

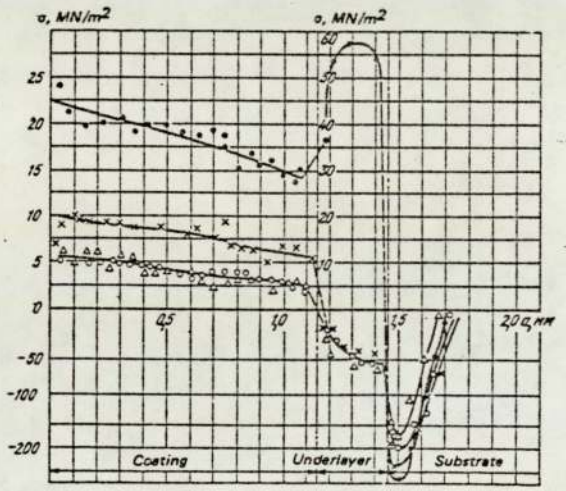

FIGURE 13 Distribution of residual stresses in arc sprayed hollow cylinders with different material combinations. Base material, mild steel, (σ_U: peripheral stresses, σ_L: axial stresses)

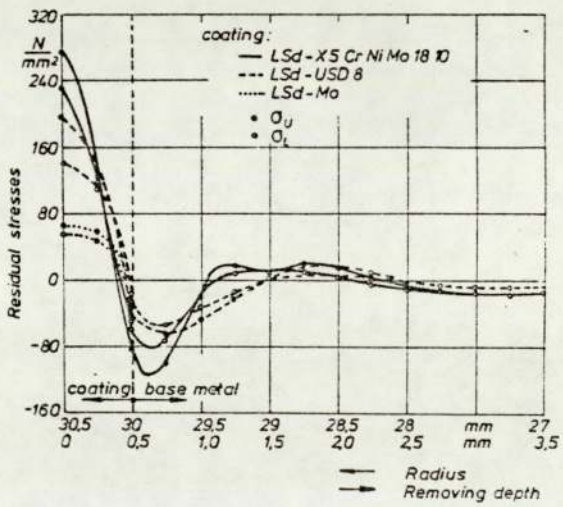

Szieslo [75] determined and compared the stress distributions in a number of ferrous and non-ferrous sprayed materials, Fig. 13. The procedure involved arc and flame spraying the outside of hollow steel cylinders to a certain thickness. The stress distribution was determined by measuring the changes in dimensions of the cylindrical testpiece as the coating was removed layer by layer using a boring or lathing method. Dimensional changes were determined using strain gauges.

Materials investigated:-

1. Molybdenum (LSd-Mo)

2. Unalloyed spraying wire (plain carbon steel) (LSd-USD8)

3. C- 1.10%, Cr - 1.80%, Ti - 0.25%, steel (LSd - 110 Mn Cr Ti 8)

4. C - 0.07%, Mn - 2.00%, P - 0.04%, S - 0.03%, Si - 1.00%, Cr - 17.00%, Ni - 12.5%, Mo - 2.25%, Steel (LSd - X5CrNiMo18 10).

5. C - 0.15%, Mn - 6.50%, Cr - 19.00%, Ni - 8.50%, steel (LSd - X15 CrNiMn18 8).

1. Molybdenum

The molybdehum sprayed deposit and substrate exhibited relatively low tensile and compressive stresses as compared to steel deposits. Szieslo attributed this to distinctly lower sample temperatures immediately after spraying, which is probably linked to the method and/or rate of deposition of molybdenum.

The production of tensile residual stress within the coating is contrary to that observed by Keshtvartzi. One explanation for this contradiction could be the fact that Keshtvartzi used a coating thickness of 0.2 mm for most of his experimental work, and results published by Szieslo, Fig. 13, indicate that very small compressive stresses exist at a distance 0.1 mm below the surface of the coating (at distances greater than 0.1 mm a tensile stress completely dominates). It is possible that Keshtvartzi is measuring these initial values of stress. However, the values of compressive stress produced are of several orders of magnitude higher than those recorded by Szieslo.

The tensile residual stresses produced in plain carbon steel coatings were an order of magnitude greater than those produced in molybdenum coatings. The tensile stresses abruptly changed to compressive stresses at the coating boundary with the substrate. Szieslo attributed the tensile stresses to thermal effects, differential expansion and contraction due to thermal gradients, which is in agreement with the theory postulated by Keshtvartzi.

The high carbon steel coatings could exhibit either a compressive or tensile stress depending on coating thickness. Thicknesses of less than 1.0 mm induced tensile stresses of the same order as mild steel coatings, Fig. 14. As the coating thickness is increased the tensile stresses reduce and revert to compressive stresses across the cross-section.

FIGURE 14 Distribution of residual stress in arc sprayed hollow cylinders with different coating thicknesses. Material combination LSd - 110 MnCrTi8/Mild Steel.

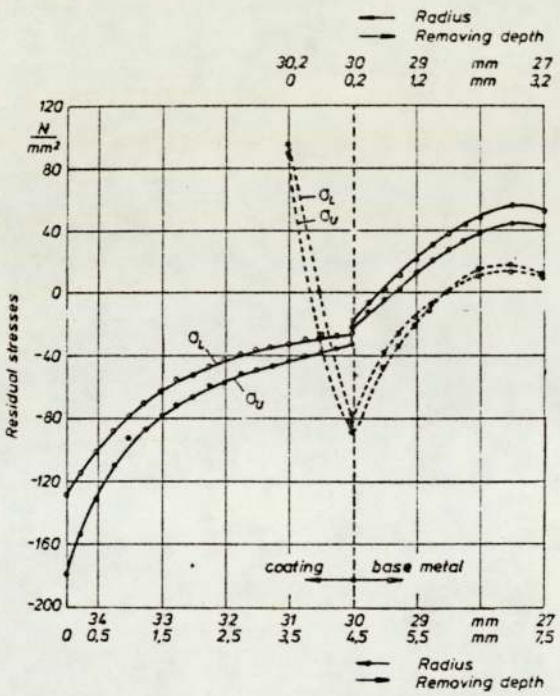

Szieslo considers that the formation of compressive stresses is a result of the volume expansion within the coating due to the occurrence of a martensitic transformation. At small coating thickness however the sample temperatures are low and due to the high carbon content a large amount of austenite is retained. He considers that at greater thicknesses transformation stresses dominate, and as the thickness decreases, thermal stresses dominate.

The tensile residual stress produced in the 17% Cr - 12% Ni stainless steel were the highest of the materials tested, of the order of 270 MPa. This is attributed to the differences in co-efficient of thermal expansion between substrate and coating, (10.8 and 16.0 x 10^{-6}/K, 290-570 K respectively). At room temperature the tensile residual stresses are higher due to coating shrinkage, about 30% more than the substrate.

Harris et al [76] used essentially the same techniques to determine the stress distribution in a number of sprayed steel systems. Research was also carried out to measure the stress existing in sprayed flat steel plates. In each case the flat steel strip plus coating deflected so that the specimen became concave on the coating side. The deflection at the mid-point of the mild steel strip was measured at intervals of 0.1 mm thickness to a maximum of 0.6 mm.

The concave shape of the specimens suggests that all the coatings were in tension, the substrate, due to the thermal input on the coating side would attempt to deflect in the opposite direction.

Harris recorded an increase in tensile residual stress levels throughout the materials in the following order, as determined from flat steel specimens:

Residual stress increase (Harris):

65E - C - 1.05, Si - 0.23, Mn - 0.73, P - 0.03, S - 0.03, Cr - 1.50, Mo - 0.21, Ni - 0.23 steel

60E - C - 0.24, Si - 0.30, Mn - 0.47, P - 0.01, Cr - 13.30, Mo - 0.03, Ni - 0.20, Cu - 0.23 steel

30E - C - 0.18, Si - 0.20, Mn - 0.22, P - 0.02, S - 0.03 steel

80E - C - 0.02, Si - 0.71, Mn 1.92, Cr - 18.6, Ni - 9.40 steel

This work generally agrees with the results obtained by Szieslo and the order of the materials in terms of magnitude of stress previously mentioned is essentially the same. But there are some differences. The high carbon steel does not exhibit compressive stresses, however it does exhibit the lowest tensile stresses. The position of 60E is variable within the order, analysis of the results illustrates that the use of spraying conditions such as low arc voltages and high atomising air pressures can induce stresses within 60E that are higher than 80E. It appears that the stress system formed in 60E is inherently more sensitive to changes in spraying parameters than the other materials.

The layer removal method performed by Harris produces some interesting results; in all materials tested the residual stress within the coatings up to thicknesses of 0.5 mm is tensile, at greater thicknesses they become compressive.

These results are opposite to those recorded by Szieslo and also seem to contradict the results produced by the flat plate specimens.

The literature reviewed illustrates that different and even opposite stress sytems can be determined within the same or similar deposition materials of equal thickness.

This variation is probably due to one or a combination of the following factors:-

a) the technique used for measuring residual stress.
It is evident that different techniques for the measurement of residual stress can produce different results from identical deposit and substrate materials. This is illustrated by Harris's work involving a deflection and a layer removal technique. In this case it is probably due to the different substrate dimensions and volume used in each technique, as compared to the volume of material deposited.

The layer removal technique can produce conflicting results. The method, when applied to a certain thickness of coating, may record stress levels which are not indicative of the levels existing at the same thickness during the deposition stage of the process. In fact, the residual stress at a certain thickness can be modified by further deposition.

This may be one factor that accounts for the contradicting results obtained by Keshtvartzi and Szieslo for the deposition of molybdenum, and is illustrated in Szieslo's

own work when determining the stress within high carbon steel coatings. Using the same technique residual stress of both signs can be determined at the same thickness of deposited material during layer removal due to the influence of the initial thickness of coating.

b) spraying system and practice. Each system has a unique thermal input to deposit and substrate. An example is flame spraying which can, under certain conditions, involve a much higher thermal input than arc spraying. This could lead to the development of high stress, especially if the two materials have significantly different coefficients of thermal expansion. But to counter this effect the whole component is likely to reach an equilibrium temperature at an early stage and cool uniformly.

Producing a coating by arc spraying generally involves high droplet temperatures, but with minimum thermal input to the substrate. This gives rise to steep thermal gradients and high residual stress compared to flame sprayed coatings.

Again the details of spraying practice are important, namely, deposition rate, traverse speed, position of the gun with reference to the substrate, cooling intervals (if any). Each of these will contribute to the magnitude and distribution of thermal input to the workpiece.

c) substrate and coating materials. The combination of materials can also influence residual stress. Materials with similar co-efficients of expansion and conductivity are unlikely to be as highly stressed as those with dissimilar properties, after deposition.

d) size and shape of substrate and thickness of coating. It is evident that the thickness of deposit unfluences residual stress. The size and shape of the substrate will also be an influence by acting as a restraint or by contributing to contraction or expansion.

2.7 Mechanical Properties

A design engineer may consider the mechanical properties of a sprayed component to be split into three categories, that of:-

(i) the composite of substrate and coating
(ii) the interface between substrate and coating
(iii) the coating itself.

the properties of the substrate are likely to be well documented. Depending on the particular application of a component the relative importance of each aspect would have to be considered.

As already discussed the adhesion of sprayed materials to various substrates has been entensively researched using a variety of techniques. The properties of a substrate and coating acting as a composite have also been studied, for example, research into the fatigue of metal sprayed components [63]. However there is little published data relating to the mechanical

properties of deposits (although some information from compression tests [77] is available). This is partly due to the problem of producing suitable test-pieces from sprayed material. In many cases considerable difficulties arise when attempting to build up thick coatings to give sufficient volume to machine test-pieces. A widely practised approach is to build up a deposit on a relevant substrate and treat it as a composite. Using this method, Harris and Cobb [76] determined the Young's modulus of arc sprayed mild steel as close to that of wrought mild steel, namely 200 G.Pa.

Overs [65] also determined the modulus (E) of composites of sprayed materials on steel substrates. He measured the modulus of a composite of 13% Chromium steel on steel as 123 G.Pa.

Using the rule of mixtures:-

$$E_c = E_m V_m + E_f (1-V_m)$$

where E_c = modulus of elasticity of coating and substrate,

E_m = modulus of elasticity of substrate alone,

E_f = modulus of elasticity of coating alone,

V_m = volume fraction of substrate,

and assuming $V_m = 0.55$; the modulus of sprayed 13% Chromium steel can be calculated as 33 G.Pa.

Overs considered the value of Young's modulus determined by this method to be surprisingly low. It is evident then that widely different values of modulus can be obtained by this method.

Farrow [66] however determined the tensile strength and modulus of arc sprayed 13% Chromium steel using a test piece machined from a coating and obtained the modulii shown in Table 2. These values of (E) appear to be more realistic, when comparing the structure of a sprayed material to that of a wrought material of similar composition. A coating can be described as a composite of metallic lamellae, oxide particles and films, and voids and is subject to the related stress raising defects.

It it generally accepted [4,42] that ineffective contact between metallic particles arising from porosity and from oxide films is one of the dominant features affecting mechanical properties.

2.7.1 Influence of Oxides on Mechanical Properties

Tylecote [78] determined the tensile strength of wüstite (FeO) and haematite (Fe_2O_3) over a range of temperatures, and refers to recent Soviet work [79] to assess the tensile properties of wüstite, haematite and magnetite (Fe_3O_4). The conclusion is that wüstite is far weaker than haematite and magnetite and that it has some degree of plasticity. At lower temperatures the tensile strength of the oxides is of the order 7 MPa, and elongation to fracture of metal oxides in general is negligible. The Soviet work suggests E = 20 G.Pa as being representative of metal oxides.

An increase in strength was observed for slower loading rates at lower temperatures. This was related to the inherent brittleness of oxides at lower temperatures, and high sensitivity to shock loading. Tylecote also investigated the

TABLE 2

MECHANICAL PROPERTIES OF 60E [66]

Test piece No	(Fracture stress) (MPa)	E (GPa)
1	177.53	110.91
2	171.00	121.60
3	164.90	105.08

adherence of iron oxide to iron and the related influence of impurities. Oxidation of iron containing 0.15% Mn failed to give adherent films in either air or oxygen in the range 770-1470 K. It is reported that although no obvious spalling of oxide occurred, micro-examination always showed a gap between the oxide and metal and that smooth interfaces were obtained with no grain boundary penetration.

Tylecote records that with pure iron there was an apparent improvement in adhesion of oxide. Peters and Engell [80] have shown that impurities which form oxides with higher free energies of formation than iron itself tend to reduce the adherence of oxide on iron. Thus silicon, aluminium and manganese reduce adherence. This is also observed by Matting and Steffens [54] for aluminium, chromium, silicon and manganese. Tylecote also states that increase in the level of other impurities such as copper, sulphur, phosphorous and carbon also produce a decrease in adherence.

It is concluded that the lack of adhesion of oxides formed in the 770-1470 K range is due to differential contraction, see Table 3, and that the increase in adherence with increasing purity is more likely to be connected with the general level of purity than any specific element. The research performed by Tylecote involved oxide thicknesses far in excess of those observed in sprayed coatings, it would be unwise to directly relate the work to phenomena occurring in a sprayed deposit. However, the temperature ranges considered are similar to those experienced by lamellae during deposition. It would therefore seem unlikely to expect the oxide within a coating to be

TABLE 3

LINEAR EXPANSION OF METALS AND OXIDES

Metal	Temperature range K	Coefficient x 10^{-6}	
Fe	273-1170	15.3	(82)
Cr	273-1270	9.5	(78)
FeO	370-1270	12.2	(81)
Cr_2O_3	370-1270	7.3	(81)

strongly bonded. The probable low adhesion strength of oxides linked with the low fracture stress of oxides leads to the conclusion that the contribution of the oxide to the strength of the deposit may be negligible and even detrimental. This does not mean that the oxide content could not improve other engineering properties such as wear resistance.

2.7.2 Influence of Porosity on Mechanical Properties

The mechanical properties of sintered steel powder compacts are controlled mainly by porosity and its morphology. It is useful to draw a comparison between sintered compacts and sprayed material. Both are particulate masses containing a certain amount of porosity, and involve only partial bonding between particles. The structure of a sintered steel powder compact is somewhat less complicated than that of a sprayed material in that oxides and other contaminants are not normally present, however essentially they are similar and a comparison is valid.

Many researchers have expressed the properties of sintered materials as a function of their total porosity. It is apparent that percentage total porosity or density is not the sole controlling factor. Pore shape, size, spacing and orientation with respect to stress, also influence mechanical properties.

The importance of pore morphology is illustrated by work on cast irons [83-88], in which it was assumed that graphite flakes or nodules could not transmit tensile stresses and were essentially equivalent to voids. It was determined that, with graphite in the

form of nodules, the modulus was proportional to the volume of the metallic phase present. An equivalent proportion of graphite in the form of flakes reduced the modulus. This effect was associated with the stress concentration effect which induced localised plastic deformation at the ends of flakes.

Although it cannot be assumed that the oxide within a sprayed material does not contribute to some extent to tensile properties, this is a useful comparison. The notches and stress raising areas produced by the inherent porosity and between oxide and metallic lamella within sprayed material must be, at least as effective in reducing mechanical properties, as those existing in sintered material.

Two relationships between Young's modulus and porosity have been determined empirically by Phol [89] and McAdam [90]. Pohl obtained the relationship:-

$$E = 1 - k\varepsilon$$

E = Young's Modulus

ε = Fractional Porosity

k is a factor which is related to the stress distributions in the matrix.

McAdam produced a relationship that represented the elastic modulus of sintered steel E_n as:-

$$E_n = E(1-\varepsilon)^{3.4}$$

This is produced from best fit relationships from computed data and is fitted reasonably well by moduli determined by Farrow [91] for low alloy steels, see Table 4. Farrow states that the modulii of sintered materials increases exponentially with density due to large elastic displacements occurring in a matrix with high porosity. The yield stress of sintered materials increases with increasing density, the rate of increase becoming slightly greater at higher density levels. As density increases the interaction of particles progressively inhibits displacement, resulting in a disproportionate stiffening of the material.

A Young's modulus of 200 G.Pa for arc-sprayed mild steel determined by Harris and Cobb [76] is considered to be too high. An arc-sprayed deposit generally contains 5-10% porosity, neglecting the influence of oxide and stress concentration effects this alone would infer a modulus of 190-200 G.Pa.

If McAdam's formula is used, which takes into consideration the stress concentration effects, then the expected modulus is 146-176 G.Pa.

These calculations do not take into account the presence of oxide which will undoubtedly reduce the modulus even further, although a reduction to the level of modulus obtained by Overs [65] is unlikely. These results introduce doubt as to the validity of properties determined using composite techniques.

TABLE 4

RELATIONSHIP BETWEEN POROSITY, YOUNG'S MODULUS, YIELD STRESS AND FRACTURE STRESS OF SINTERED STEEL POWDER COMPACTS (91)

Density Mgm^{-3}	6.40	6.48	6.57	6.65	6.71	7.01	7.87
Fractional Porosity	0.191	0.181	0.170	0.160	0.146	0.114	0
Young's Modulus GPa	94	101	108	118	120	136	207
Y.S. MPa	200	220	230	240	260	320	-
Max. S. MPa	245	280	310	320	330	360	-

CHAPTER III - EXPERIMENTAL PROCEDURE

3.1 Plan of Experiments

The intention was to study in detail the relationsips between process parameters and shear adhesion strength of three widely used steel coatings deposited onto a mild steel substrate. To validate the test procedure it was considered necessary to first study a range of coating and substrate materials. The experimental plan is shown in Fig. 15.

The plan of the supplementary study in which coating microstructure, mechanical properties and composition were characterised is illustrated in Fig. 16.

FIGURE 15

EXPERIMENTAL PLAN

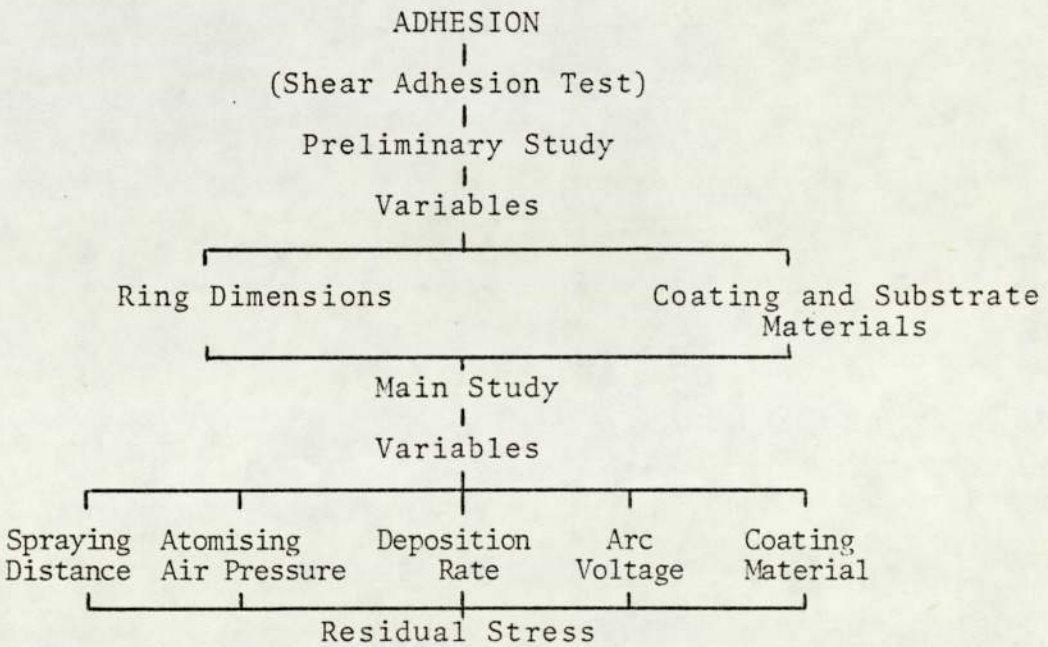

FIGURE 16

SUPPLEMENTARY STUDY

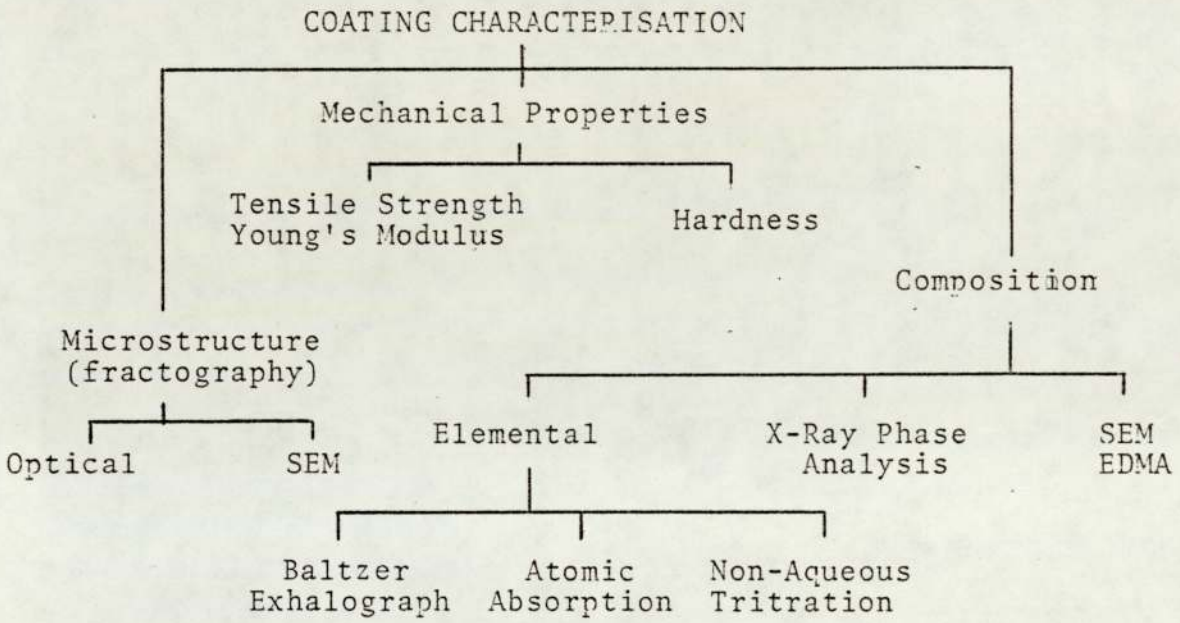

3.2 Adhesion

The service performance of a coated component is often strongly dependent on the strength of adhesion of the coating to the substrate. The shear strength adhesion test was chosen for the assessment of the degree of adhesion for this study because it possessed the qualities required, namely:-

(i) that with respect to engineering, load bearing materials, the coating shape and morphology are similar to those widely encountered in engineering applications,

(ii) the method of testing induced forces and fracture modes similar to those experienced in practice, that is, shear rather than tensile or peel,

(iii) the non-involvement of adhesives,

(iv) the simplicity of manufacture.

3.2.1 Preliminary Study

In recent years a variety of test-piece designs have been used to determine the shear adhesion strength and results described in published literature [9,65]. Although a standard [21] has been produced it is not widely recognised [93].

A preliminary study was therefore performed in order to determine the test-piece dimensions best suited for this particular investigation. From the outset, a decision was made, in consultation with the industrial advisor, to use a bar substrate of 25.4 mm diameter. In addition the study was designed to assess the sensitivity of the test to material variables.

In the preliminary study all specimens were supplied by Metallisation Limited, of Dudley; the specimens used in the main study were prepared by the author, using a similar technique.

3.2.1.1 Spraying Equipment and Parameters

The pistol used was a commercially available, twin-wire, electric arc model, Metallisation 375. It was fitted with an open-arc head, Fig. 24, when using 1.6 mm diameter wires to deposit steel and aluminium bronze, and a constricted arc nozzle for the 2.0 mm diameter wires to deposit aluminium and zinc.

The constricted arc nozzle was originally designed for spraying aluminium which required a more concentrated atomising air flow and is now adopted for aluminium and zinc.

The pistol specifications are given in Table 5.

TABLE 5

SPECIFICATIONS OF ARCSPRAY 375 PISTOL

Weight:	2.68 kg	Dimensions:	0.27 x 0.09 x 0.23 m
Comp. Air:	18.8×10^{-3} $m^3 s^{-1}$ (@ 550 KN/m^3)	Power:	440 v, 50 Hz, 3 phase
Throughput:	$1.4 - 4.2 \times 10^{-3}$ kg s^{-1}		

Substrate bars were rotated to produce a constant substrate surface velocity of 0.2 ms^{-1} throughout the spraying period and the pistol aligned with the axis of the bar, fixed at a range of 150 mm; deposition rate was 2.8×10^{-3} kg s^{-1}. The

voltage used was the minimum needed to produce a fine "sputter-free" spray which was understood, from experience, to be desirable. To prevent overheating of the deposit a spraying cycle of 5 seconds spray, 10 seconds cool using compressed air, was repeated.

The collar shear tests were performed on an Instron type 1197 50 tonne capacity tensile testing machine, see Fig. 17. A cross-head displacement rate of 8.3×10^{-6} m s^{-1} was maintained throughout the testing programme. For each test a load/ displacement curve was plotted on a Bryans 29000 XY recorder. The maximum load was recorded and the shear adhesion strength (R) calculated using:-

$$R = \frac{P}{\pi d s}$$

P = load to cause fracture

d = diameter of cylindrical rod

s = width of ring of deposit.

The geometry of the test-piece and the position of the die ensured that fracture initiated at the interface between coating and substrate, see Fig. 17.

3.2.1.2 Manufacture of Test-pieces

Details of the test-piece are given in Fig. 18. Each substrate bar was 25.4 mm diameter mild steel or aluminium. Surface preparation involved a grit blasting treatment which was carried out to the standard outlined in section 3.2.2.1. The bars were sprayed with mild steel, aluminium bronze, aluminium or zinc, as described below.

FIGURE 17 Shear Testing Machine

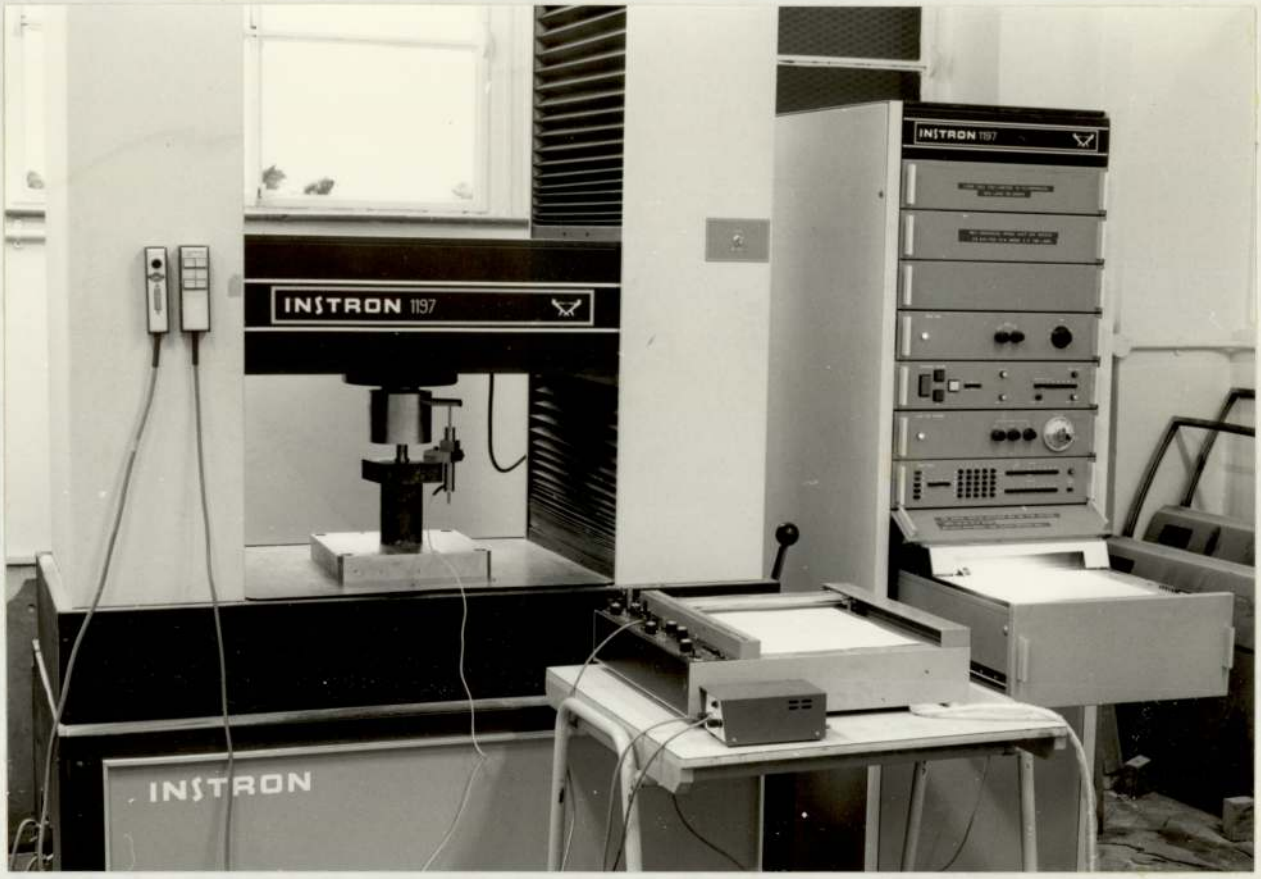

Diagrammatic Representation

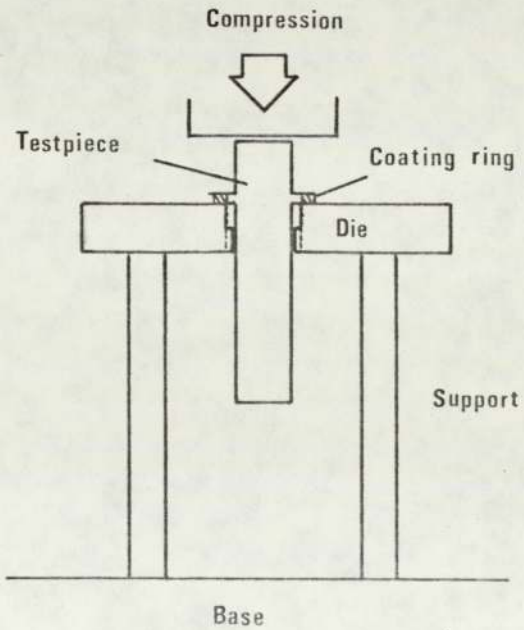

FIGURE 18 Shear Adhesion Strength test-piece
(dimensions in mm)

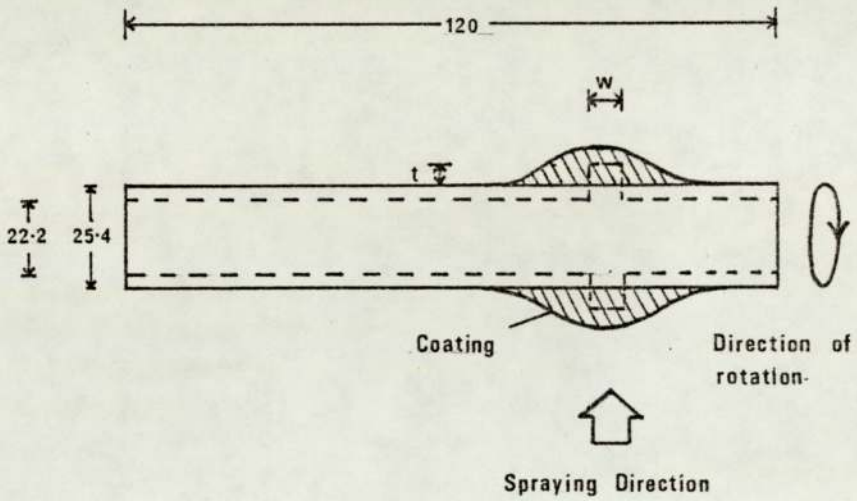

Complete lines : original dimensions

Dotted lines : test-piece dimensions

A 120 mm length of bar was held in a chuck and rotated in front of the fixed pistol and a coating built up as shown in Fig. 19. A collar was then machined from the central portion of the deposit to a dimensional tolerance of $\pm$ 0.02 mm.

3.2.1.3 Approach

On the advice of the industrial collaborator, a longitudinal cut was sawn in each collar of the 96 test-pieces prepared for this part of the study. This was considered to be necessary to relieve circumferential residual stress developed during the spraying process. For comparative purposes, however, a further 16 test-pieces were tested with uncut collars. Subsequently the effects of residual stress in a coating became a major aspect of the study.

A factorial design of experiment was adopted and the data was laid out in the following style, see Table 6; a triplicated experiment with four variables, three having two levels and one having four levels.

TABLE 6 FACTORIAL DESIGN OF EXPERIMENT

		C_1						C_2					
		D_1			D_2			D_1			D_2		
A_1	B_1	M	M	M	M	M	M	M	M	M	M	M	M
	B_2	M	M	M	M	M	M	M	M	M	M	M	M
A_2	B_1	M	M	M	M	M	M	M	M	M	M	M	M
	B_2	M	M	M	M	M	M	M	M	M	M	M	M
A_3	B_1	M	M	M	M	M	M	M	M	M	M	M	M
	B_2	M	M	M	M	M	M	M	M	M	M	M	M
A_4	B_1	M	M	M	M	M	M	M	M	M	M	M	M
	B_2	M	M	M	M	M	M	M	M	M	M	M	M

FIGURE 19 : Arc Spraying of Shear Test-Pieces (Protective ultraviolet radiation shield removed)

A

B

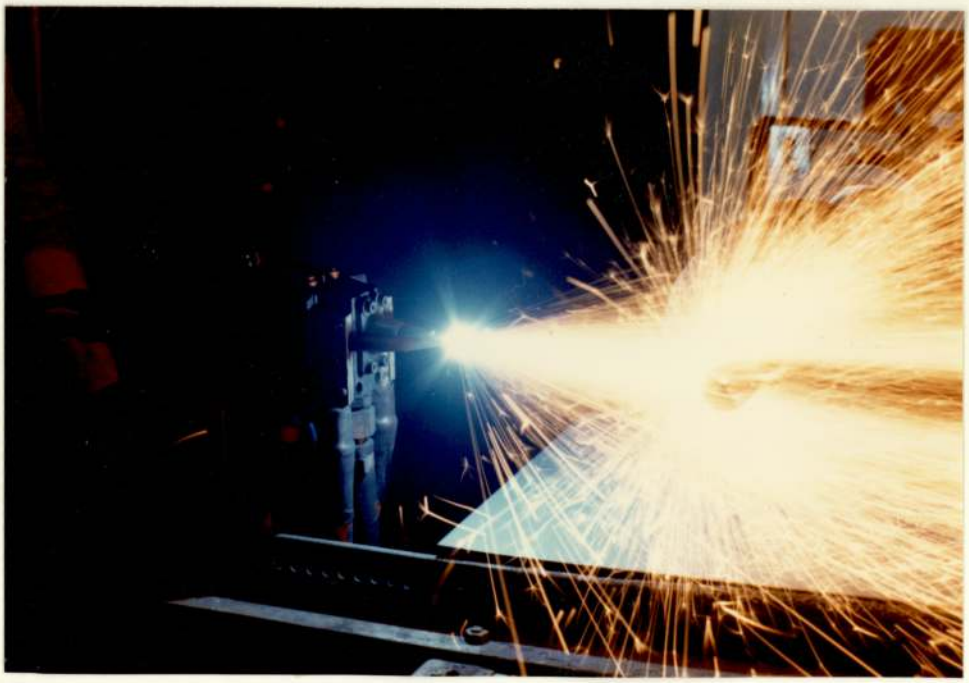

The influence of the following variables on the response variable (shear adhesion strength) was assessed at the levels indicated.

1) A : Coating : A_1 (Carbon steel)
A_2 (Zinc)
A_3 (Aluminium)
A_4 (Aluminium Bronze)

2) B : Coating thickness (t): B_1 (4 mm)
B_2 (2 mm)

3) C : Substrate : C_1 (Carbon steel)
C_2 (Aluminium)

4) D : Coating width (w) : D_1 (10 mm)
D_2 (5 mm)

An analysis of variance was carried out using a statistical package facility on a Hewlett Packard 2000 main-frame computer. In this way the effect on the shear adhesion strength of each variable, singularly, and in multiple interaction, was assessed. Also the influence of test-piece geometry on the scatter was assessed by using the relationship

$$\text{Error } \% = \frac{\text{scatter}}{\text{mean}} \times 100$$

for each geometry combination. Although this is not a standard statistical method of representing error, it was considered to be appropriate for the small number of results obtained for each particular set of variables.

3.2.2 Main Study

Having established the test-piece dimensions likely to yield the most consistent results, the test was used to determine the effect small variations in spraying parameters have on adhesion of a coating.

3.2.2.1 Pre-treatment of Surface Prior to Spraying

The surface preparation of a substrate prior to spraying is critical to the adhesion of a deposit. Throughout the study it was necessary to use a method which would produce both a maximum degree of adhesion and allow sufficient control to maintain a consistent surface preparation. This is important because variation in adhesion due to inconsistencies in surface preparation may mask the effect of small variations in spraying parameters.

Each test-piece was degreased by immersion in acetone and then grit blasted in a Guysen Blast Clean cabinet, Model S2, incorporating a 4 mm diameter nozzle. As specified, the surface was blasted until a uniform, clean appearance was obtained, as assessed by visual inspection by the operator. The final finish was produced by a further blast period of a length equal to one third of the original blasting time. The medium used was G.24 chilled iron grit.

Blasting was maintained at an air pressure of 585×10^3 Pa, at an angle of 90° to, and a distance of 0.18 m from, the substrate surface. The grit was regularly checked by eye for wear and/or contamination and replaced as soon as deterioration was observed. To avoid erroneous results which may

be produced by contamination and surface degradation, which has been well documented by Apps [49,51], the spraying process was performed within 30 minutes of blasting. Talysurf graphical results are illustrated in Fig. 20, describing the condition of the surface before and after blasting, the relevant centre line average values are recorded. Scanning electron microscope photographs of the grit blasted surface are shown in Fig. 21.

3.2.2.2 Coating and substrate Materials

The substrate material was bright finished mild steel bar to B.S.970 specification, namely, Carbon: 0.25 - 0.30%, Manganese: 0.70 - 0.90%.

Table 7 records the composition of the wires used to form the coatings, obtained by wet analysis. The three coating steels chosen for the study, although commercially available, offered the range of properties and compositions required. For convenience the commercial designations shown in Table 7 will be used for future reference.

TABLE 7

CHEMICAL ANALYSIS OF WIRES

Code Name	Composition (%)						
	C	Si	Mn	Cr	Ni	Cu	Fe
65E	1.10	0.44	1.63	1.82	0.11	0.51	Balance
60E	0.24	0.49	0.41	13.30	0.17	0.23	Balance
30E	0.08	0.88	1.45	0.03	0.03	0.15	Balance

FIGURE 20 Talysurf Recordings on substrate surface

A) As-received (cold finished)

C.L.A. = 0.45 microns

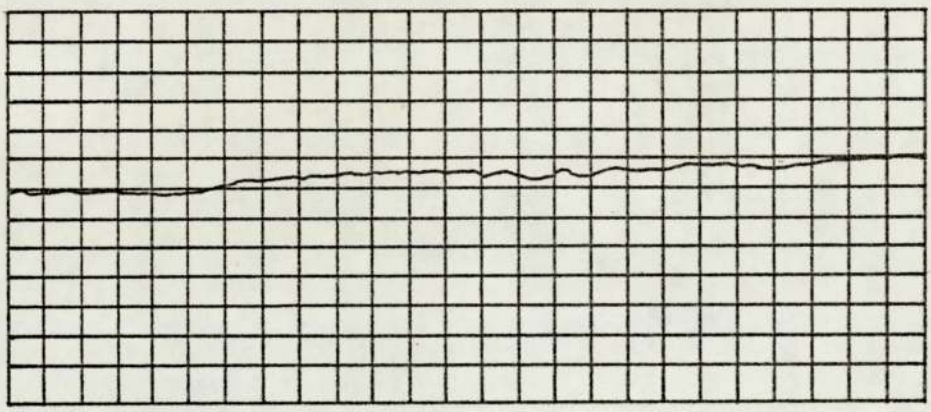

B) After grit blasting

C.L.A. = 4.50 microns

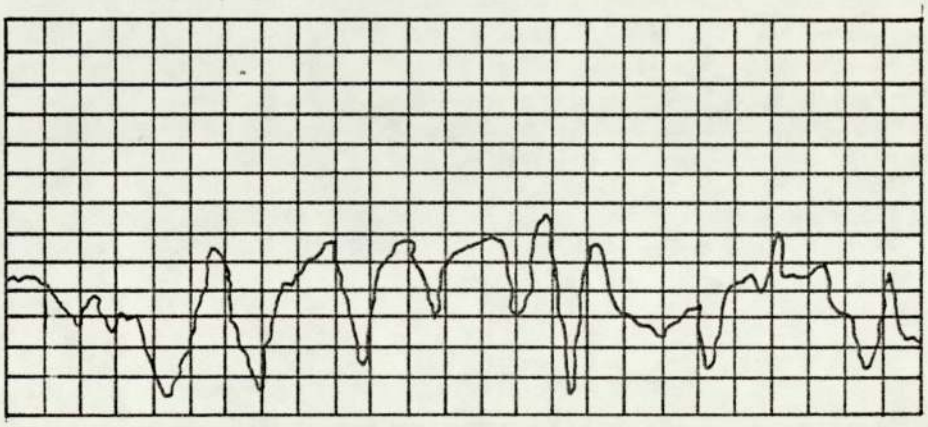

FIGURE 21 : Grit Blasted Substrate Surface

A

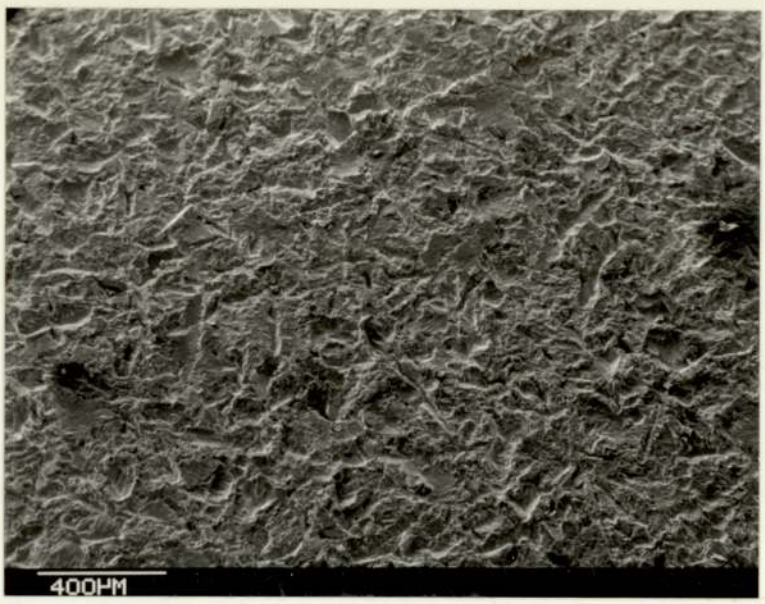

B

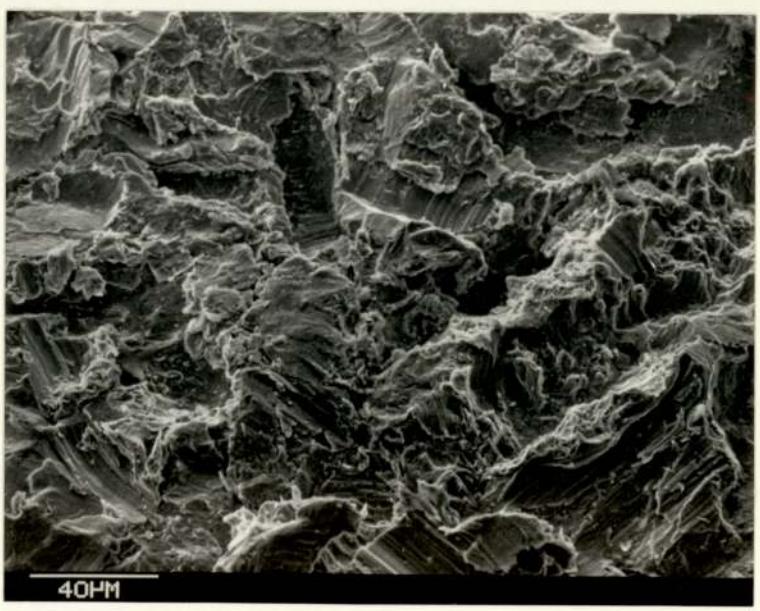

3.2.2.3 Equipment and Spraying Parameters

The arc spraying system for producing shear test-pieces is shown in Figs. 22 and 23. A Metallisation 375 pistol, illustrated in Fig. 24, was used with an open-head arc 1.6 mm diameter wire, in conjunction with a Metallisation 400 power supply, shown in Fig. 25, for the deposition of all three steels.

The spraying and testing technique was identical to that used in the preliminary study with one exception. To accommodate work at very small spraying distances and high deposition rates the spraying and cooling cycle was amended to a 2 seconds spray and 5 seconds cool.

From this point onwards the spraying voltages used will be expressed in the form X/Y, v. X is the voltage obtained before the commencement of wire feed and Y is the voltage during spraying.

3.2.2.4 Test-piece Manufacture

The test-piece was essentially the same design as that used in the preliminary study, dimensions w and t were 5 mm and 2 mm respectively. This study involved the use of much harder coating materials than the preliminary study, in the case of the high carbon steel coating the deposits were impossible to machine by normal means and therefore had to be ground and spark machined. The same dimensional tolerances were imposed.

FIGURE 22 : Arc Spraying System

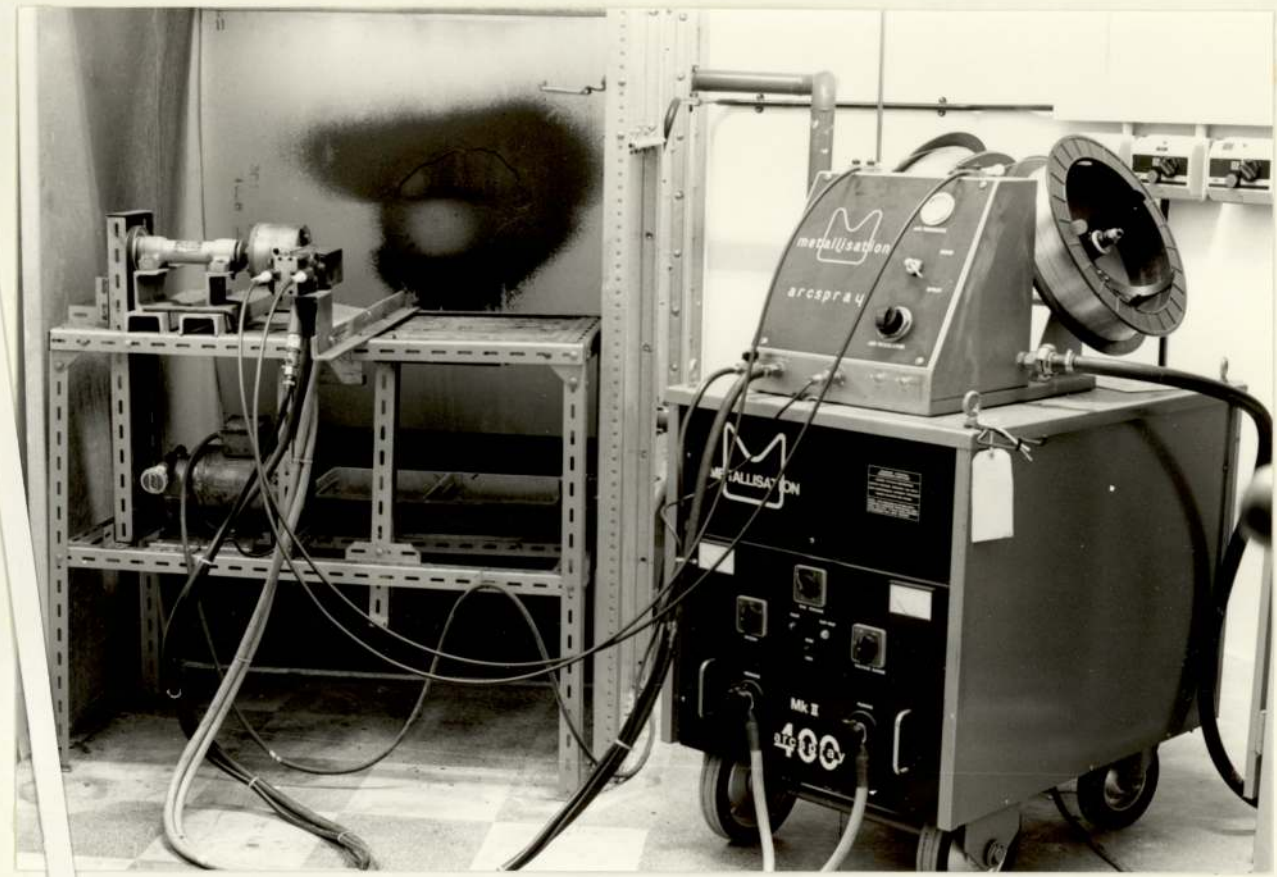

FIGURE 23 : Arc Spray Gun in Position to Spray Shear Test-Pieces

FIGURE 24 : Arc Spray Pistol 375

1) Drive Unit
2) Wire Feed Unit
3) Spraying Head
4) Compressed Air Nozzle
5) Rear Wire Guides
6) Contact Tubes
7) Remote Control Extensions

FIGURE 24 : Arc Spray Pistol Model 375

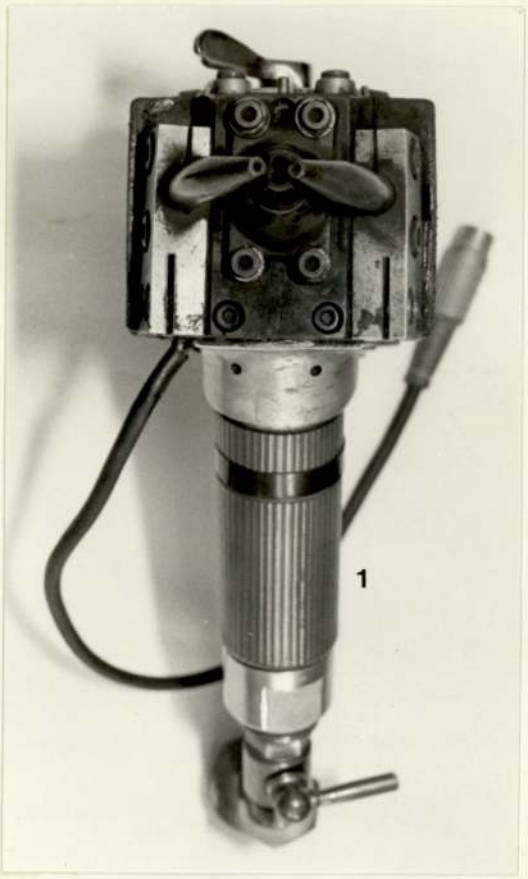

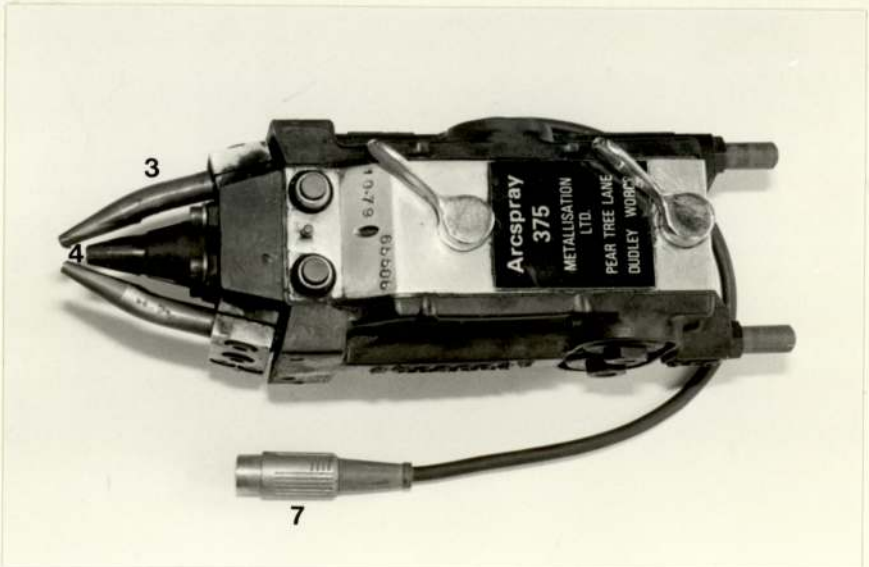

FIGURE 25 : Metallisation Power Supply
Model 400 Mk. II

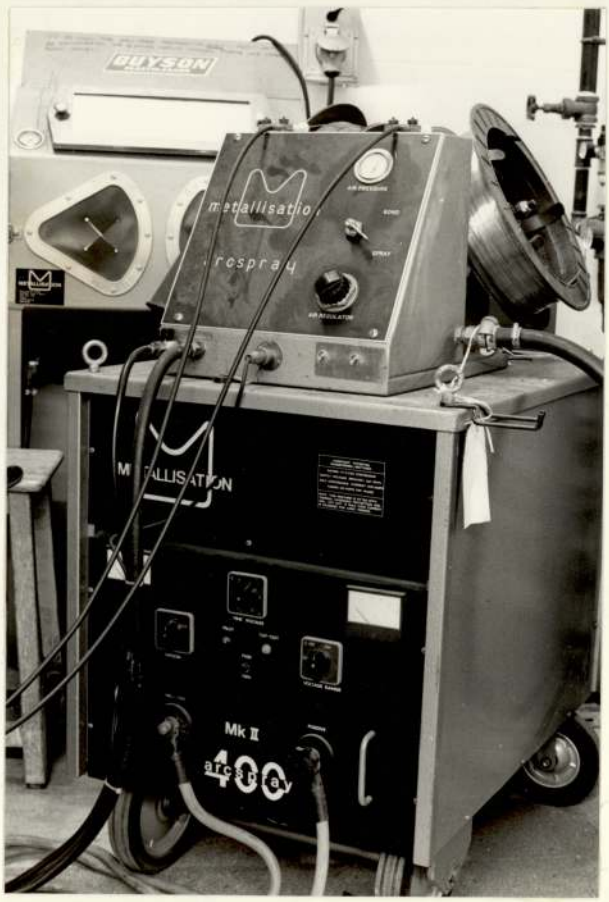

3.2.2.5 Approach

A classical approach to experimentation was adopted to study the effect of the following variables on shear adhesion strength:-

a) Spraying distance
b) Deposition rate
c) Arc voltage
d) Atomising air pressure.

Three-fold replication was employed for each particular set of spraying parameters.

3.3 Residual Stress

The work performed by Haddleton [68] showed that the residual stress developed during the spraying and cooling of the shear type of test-pieces may make a major contribution to the measured shear adhesion strength. This study therefore required knowledge of the residual stress existing within each test-piece.

The literature survey highlights the difficulties in developing a theoretical model which would reflect the residual stress developed during the spraying of even a simple component. A simple method which would directly quantify the residual stress within each of the sprayed rings was required.

A widely practised method of measuring the residual stress in a ring or tube is to cut through the wall and measure the resulting gap or change in diameter. In the circumstances it was considered that measurements of residual stress should be

attempted using this type of technique, even though generally the dimension w, see Fig. 18, of the ring is larger than that of the shear rings. The outcome suggests that the results are realistic.

Two methods of slitting the sprayed rings were tried. The first, which in most cases was performed on two of the three rings produced under the same spraying conditions, involved spark machining a slit in the ring, when in the displaced position after shear testing. The second, which was carried out on the remaining rings from each set, involved pushing the ring clear of the bar using the testing machine. This action invariably resulted in a single fracture through the ring cross-section. In both cases the change in diameter was measured to an accuracy of $\pm$ 0.005 mm using a micrometer.

In certain cases the above procedure could not be followed due to the highly stressed nature of some of the rings produced by "high energy input" spraying conditions, such as short ranges or high deposition rates. In these cases cross-sectional fracture occurred simultaneously with interfacial shear during testing.

The circumferential residual stress was calculated using the following equation [94,95]:

$$\sigma_{circ} = E.t \left(\frac{1}{d_1} - \frac{1}{d_2}\right)$$

E = Young's modulus

t = thickness of coating

d_1 and d_2 are the ring diameter measurements illustrated in Fig. 26.

FIGURE 26 Coating ring diameter before (d_1) and after (d_2) slitting

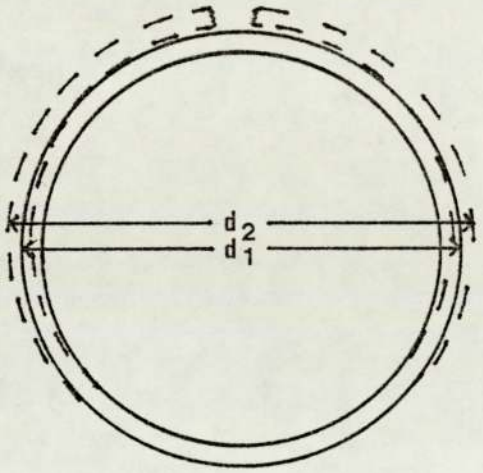

FIGURE 27 Tensile test-piece dimensions (mm)

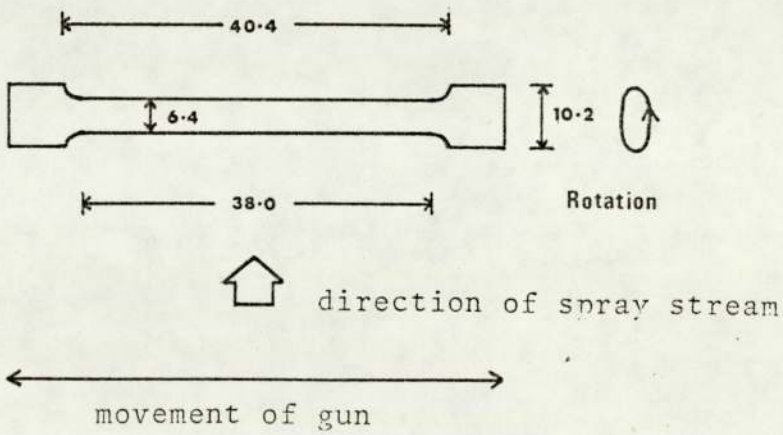

As a control, six shear test samples, three of 30E and three of 60E, were given a stress relieving heat treatment at 920 K for 1 hour in a vacuum furnace at a pressure of 13×10^{-3} Pa. The residual stress was then determined in the same manner.

3.4 Mechanical Properties

3.4.1 Tensile Strength and Elastic Modulus of 30E and 65E

The Young's modulus and tensile strength of 60E were determined by Farrow [66], a colleague in the research group. He used test-pieces prepared from a monolith of sprayed material, due to the lack of confidence in the composite test-piece commonly used. The results were encouraging and essentially the same method of test-piece manufacture was adopted by the writer.

3.4.1.1 Manufacture of Test-piece

A flat layer of deposit was produced by spraying onto a thick mild steel plate, which was in a "bright finished" condition and thoroughly degreased by immersion in acetone. The deposit was separated from the plate and thin strips of section 2 x 2 mm and length 80 mm were spark machined from it.

The corners of the strips were rounded by grinding and degreased in acetone with ultrasonics prior to surface blasting using high purity alumina. A strip was rotated in a chuck positioned ahead of the pistol and sprayed to a diameter of about 12 mm, which permitted a test-piece to be machined from the resultant bar.

Fixed spraying conditions were used for all test-pieces, namely:-

(i) Spraying distance : 100 mm

(ii) Deposition rate : 2.8×10^{-3} kg.s^{-1}

(iii) Voltage : 29/26 v

(iv) Atomising pressure : 586×10^{3} Pa

Test-piece dimensions are shown in Fig. 27; three test-pieces were produced for each of the materials 30E and 65E.

3.4.1.2 The Tensile Test

Two strain gauges were attached to the test-piece at opposite ends of the cross-section diameter, to reduce discrepancies arising from gauge alignment.

Strain gauge specifications are recorded in Table 8.

TABLE 8

STRAIN GAUGE SPECIFICATIONS

Manufacturer	Tokyo Sukki Kenkyujo Co.Ltd.
Type	FLA-10-11
Gauge length	10 mm
Gauge Sensitivity	120 $\pm$ 0.3 Ω
Gauge Factor	2.12
Lot No.	179811
Adhesive Manufacturer	Tokyo Sukki Kenkyujo Co. Ltd.
Adhesive Type	TML-EA-2

An Instron model TTCM 1000 kg capcity tensile testing machine was used, with a cross-head displacement rate of 8.3×10^{-6} $m.s^{-1}$. The strain registered by the gauges was measured by a direct strain transducer meter connected in an unbalanced bridge circuit, see Appendix II. Strain and load outputs were recorded by an X-Y plotter.

Each test-piece was loaded up to approximately half the yield stress, based on the results of Farrow [66], and repeatedly loaded and unloaded until it had "settled" into position within the grips. The modulus was then determined from the average of the slopes of the traces recorded from the two strain gauges.

The tensile strength of the test-pieces was ultimately measured. The cross-head speed used during testing was the same as that during modulus determinations.

3.4.2 Hardness Determinations

Micro- and macro-hardness surveys were performed using pyramidal diamond type indentation machines. Macro-hardnesses were carried out using a standard Vickers Machine, micro-hardness using an M41 Photoplan microscope with a Vickers micro-hardness facility. Unless otherwise stated loads of 30 kg were used for macro-hardness and 100 gms used for micro-hardness. All hardness determinations were positioned on the through thickness cross-section of the coatings, previously prepared for metallographic examination. Each value recorded in the tables presented in "Results" is a mean value of six hardness readings.

3.5 Coating Microstructure

3.5.1 Optical and Electron Metallography

Sections which had been cut in the through thickness direction were prepared for optical microscopy. The specimens were mounted in conducting thermosetting resin and ground by hand on successively fine silicon carbide papers. Each grinding operation was limited in time to minimise dragging-out of weakly bonded particles. Due to the considerable variation in hardness within the section of deposit, vibratory polishing, using aThorn-Bendix Type M14 metallurgical vibratory polisher, proved to be the best method for final polishing using 1 μm diamond paste.

The specimens were examined in the unetched and etched conditions. Nital (2% nitric acid in alcohol) proved to be the most successful etchant for 30E, Alcoholic ferric chloride (5 g $FeCl_3$, 15 ml HCl, 95% methanol) for 60E, Vilella's reagent (5 ml HCl, 1 g picric acid, 100 ml ethanol) for 65E.

Electron microscopy was used both for fractography of the faces produced during shear and tensile testing and metallographic study of heavily etched surfaces.

3.5.2 Heat Treated Coatings

For interest, the metallographic structure of each coating after the various heat treatments applied during the study of residual stress effects was also observed, (for treatments see Section 2.6 . The heat treatments revealed features which were not normally observed in the "as-sprayed" structure.

3.6 Coating Composition

The review of published literature shows that volatilisation and oxidation of elements is inherent to "airborne" spraying processes. Oxidation is accentuated during arc spraying due to the use of compressed air as an atomising medium. It is inevitable that oxide is an important constituent of coatings.

To study oxide content, chemical loss and their relationship with spraying parameters, bulk elemental analysis, S.E.M. micro-analysis, oxygen analysis and X-ray phase analysis were performed.

3.6.1 Oxygen Content of Coatings

Oxygen can be present in the coating in three forms:

a) in combination as oxide,
b) in solution in the metal, and
c) as gas in closed pores.

The total weight percentage of oxygen within 30E, 60E and 65E was determined using a Baltzer Exhalograph. The Exhalograph is not capable of analysing separately the three forms of oxygen. A total oxygen content is obtained. The sample is introduced into a graphite crucible and evacuated to a pressure of 13×10^{-3} Pa, this removes oxygen in inter-connected pores and adsorbed on the surfaces. The sample is then melted under the same degree of vacuum and the temperature raised to 2070 K.

At this point it is useful to consider the free energy diagram[96], see Fig.28. Consider the line of carbon monoxide, below 870 K neither water vapour nor ferrous oxide can be reduced by carbon under standard conditions. Above 1870 K it is clear from the diagram that all the iron oxides and the oxides associated with chromium, manganese and silicon can be reduced by carbon.

The oxygen analyses were performed at a pressure of 13×10^{-3} Pa. At this reduced pressure the stability of the oxides decreases and therefore the free energy/temperature oxide line will be raised, additionally the carbon monoxide line will be lowered.

At a temperature of 2070 K and a pressure of 13×10^{-3} Pa it is safe to assume that the oxides likely to be present in the three steels are reduced by the graphite crucible to form CO which is then analysed by infra-red means by the Exhalograph.

Three samples were analysed for each set of spraying parameters, the samples were weighed to an accuracy of $\pm 10^{-5}$ of a gramme. This accuracy was required due to the small sample size used. The size was restricted to the order of 0.01 g due to the relatively high oxygen content of the coatings. Due to the inhomogeneity of the coatings a certain scatter of results was expected because of the small sample size. In one respect however the small size is advantageous, as it is likely to ensure that the pores within the structure are completely evacuated[80], and that the wt% oxygen originated from the combined and dissolved state, as opposed to free oxygen which may be trapped in pores.

FIGURE 28 Free energy of formation of various oxides, based on the original diagram by Ellingham

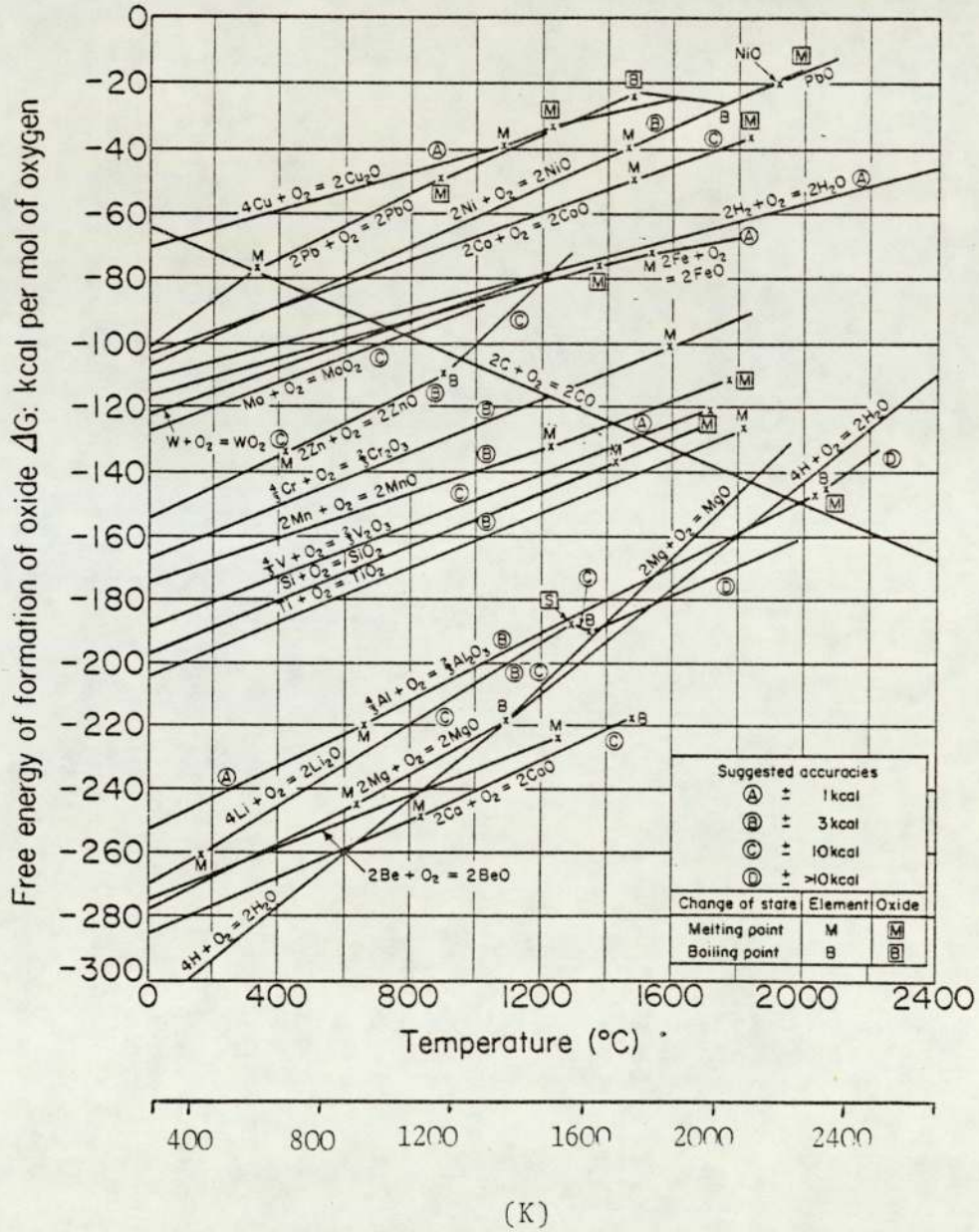

3.6.2. Energy Dispersive X-Ray Micro-Analysis

A Link System 960 Series 2, micro-analytical system in conjunction with a Cambridge Stereoscan S150 was used for micro-analysis of metallographic features. The equipment permitted analysis of individual oxides and metallic particles within the coating matrix.

Characteristic X-rays are produced, along with secondary electrons and back-scattered electrons, by interaction of the S.E.M. beam with the specimen. The Link System can provide quantitative elemental analysis by comparing the characteristic X-ray peak intensities with a known standard. It uses a computational process to overcome inter-element effects arising from multi-element analysis. The inter-actions are basically ionisation penetration and back-scatter (Z), absorption (A) and fluorescence (F). The analysis is known as ZAF and was used throughout the study.

Elements such as carbon, oxygen, nitrogen and hydrogen could not be measured using the equipment available, the wave-lengths generated by these elements being too large for penetration of the berylium window used in the detection system.

Oxygen analysis showed there to be a large amount of oxygen present with the sprayed matrix, to accommodate this a 'one element by difference' option was utilised on the Link System. As the term implies, the amount of oxygen is determined by difference.

The analyses were performed at magnifications between 2K and 5K. The samples were prepared by preferential etching of the metallic areas, oxides remained unetched and remained proud, providing relief for S.E.M. analysis.

The scanning electron microscope was also used to produce X-ray maps and line concentration profiles of particular elements on various coating sections.

3.6.3 X-Ray Diffractometry

X-ray diffractometry was performed on all three materials, to determine:-

a) the phases present within each coating,
b) if a texture existed.

The goniometer used was a Phillips PW1050 controlled by a Canberra computer interface. The surface of each specimen was irradiated with a beam of 40 KV, 20 mA, monochromatic, molybdenum K_α radiation (λ = 0.7093 Å). The data output was in the form of reflection intensity peaks at 2θ reflection angles (range 10^o-95^o), additionally after each step of 0.25^o the computer system printed the integrated area below the trace.

By applying the Bragg equation $n\lambda = 2d\sin\theta$ the interplanar spacing (d) can be calculated. The interplanar spacing used in conjunction with the relative intensity of the peak can be subsequently identified by comparison with standard reference patterns [98].

The samples were prepared in a "button" form of 12 mm diameter, by slicing up a bar sprayed and manufactured by the same technique as that used for tensile test-pieces. The surface of each specimen was electrolytically etched in a 5% perchloric acid solution to remove the surface layer which could have developed a texture during preparation.

Metallographic study of 65E indicated the presence of a significant amount of austenite. For this particular material the volume fraction of austenite was calculated. Although the occurrence seemed unlikely, traces were taken to detect the existence of any preferred orientation in the sprayed material. This was because any departure from complete randomness in the crystallographic orientation can lead to erroneous results [99] when calculating volume fractions of phases.

A trace was taken using diffraction from the (111) plane. No preferred orientation was observed in any of the three materials, therefore the structure was assumed to be isotropic.

Volume fractions of phases are calculated on the basis that the X-ray intensity diffracted from each phase is proportional to the volume fraction of that phase.

When Mo radiation is employed Miller[99] suggests the use of 220 austenite and 311 austenite peaks, and the 211 martensite peak located between them. The volume fraction of austenite (V_A) was then calculated using:-

$$V_A = \frac{1.4\ I_A}{I_M + 1.4\ I_A}$$

where $I_A = \frac{1}{2}\left[I_A^{220} + I_A^{311}\right]$

and $I_M = I_M^{211}$

I_A and I_M are the measured integrated intensities of the austenite and martensite lines used, which have been corrected for the inherent background integrated intensity.

3.6.4 Bulk Analysis

Bulk analysis of the elements carbon, chromium, manganese and silicon in each of the three coating materials was carried out externally by a commercial organisation. A 3 g sample mass was used for each analysis, and one sample was analysed for each particular set of spraying conditions. The method used for analysis of chromium, manganese and silicon was atomic absorption and that for carbon, non-aqueous titration.

CHAPTER IV - RESULTS

4.1 Coating Characteristics

4.1.1 General

Detailed metallographic examinations were made on each coating, after sectioning in the through thickness direction. A general characteristic of all the coatings was the 'wavy' lamellar structure, resulting from the layering of lenticular shaped particles. The lamellae were essentially parallel to the substrate surface. Other general features were porosity, oxides, fissures and spherical refrozen particles. These general features are exhibited in macrostructures shown in Figs.29-32. Oxides were observed in four forms; namely,as finely dispersed greyish black specks or globules within the metallic particles, as partial shells surrounding metallic particles, as thin lamellae separating metallic lamellae or as discrete spherical particles. These features are best illustrated in scanning electron microscope photographs of heavily etched sections, see Figs.29 A, B, C.

Montages are presented in Figs.30-32, these illustrate visually the effect of spraying parameters on coating macrostructure. It is apparent from these montages that lamella size is influenced to a large extent by arc voltage,atomising pressure and spraying distance, and to a lesser extent by deposition rate. An increase in voltage or spraying distance or a decrease in pressure or deposition rate results in a marked decrease in lamella size.

It is apparent that these four parameters also control oxide content. It can be seen that an increase in deposition rate or voltage, or a decrease in spraying distance or atomising pressure reduces oxide content. The composition of the

FIGURE 29 : S.E.M. Photographs, Heavily Etched (60E) (showing oxide morphology and defect radius)

A

B

FIGURE 29 continued

C

FIGURE 30 Influence of spraying distance and deposition rate on coating macro-structure (60E)
(constant arc voltage and atomising pressure)

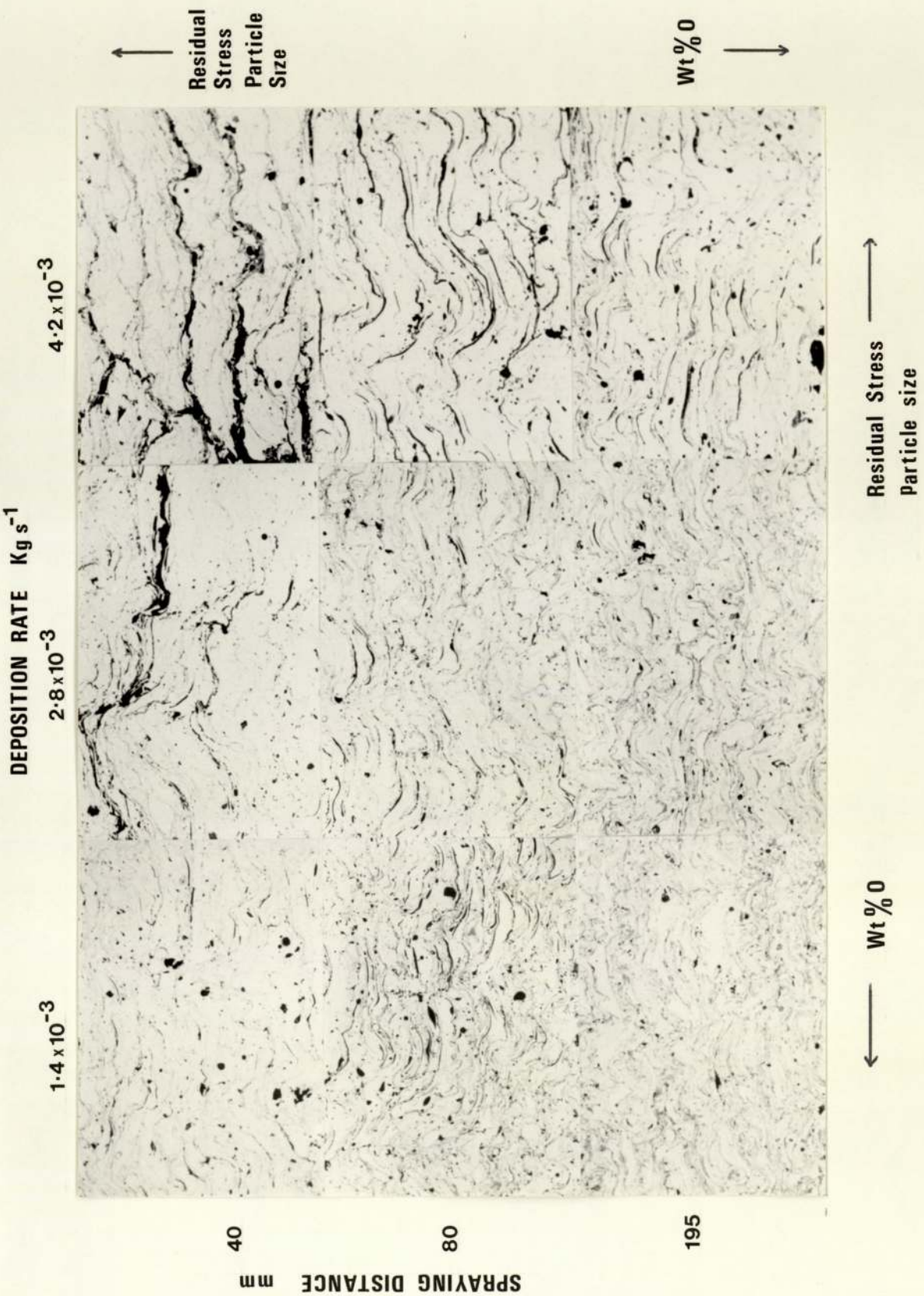

FIGURE 31 Influence of spraying distance and deposition rate on coating macro-structure (65E)
(constant arc voltage and atomising pressure)

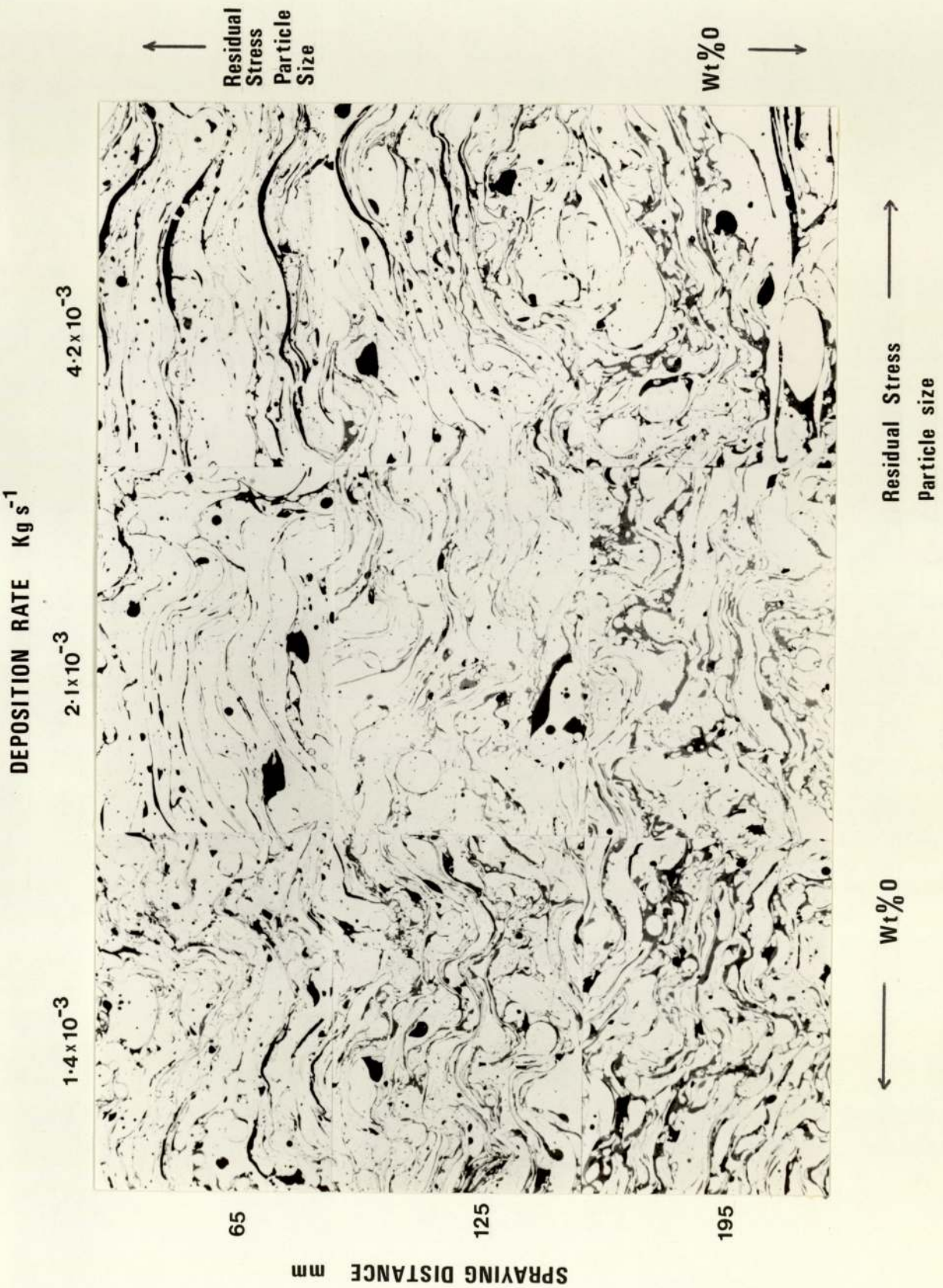

FIGURE 32 Influence of arc voltage and atomising pressure on macrostructure (65E) (constant spraying distance and deposition rate)

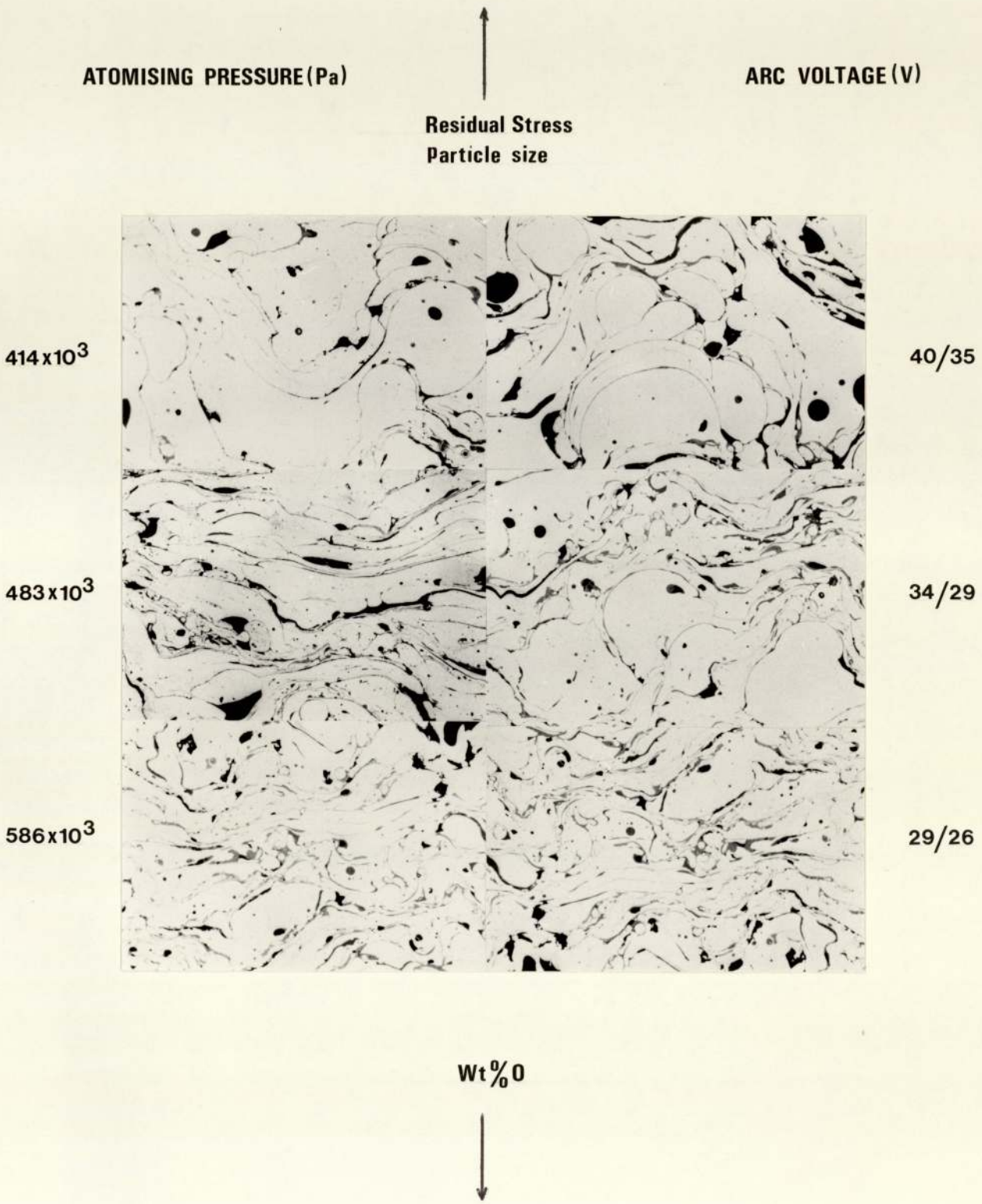

sprayed steel also affects oxide content, a larger proportion was observed in 65E than 30E or 60E.

4.1.2. Micro-structure

As a consequence of the high cooling rates, and the presence of impurities which act as grain boundary anchors, micro-structures with a grain size of the order of less than a micron and up to five microns are typical. The smallest grain sizes were difficult to determine because even at the highest magnification of the optical microscope areas within lamellae were unresolvable. However, it seems certain that grain sizes of the order of a fraction of a micron are present. A variation of grain shape was seen within individual coatings. Some contained collumnar grains, others, irrespective of composition, were composed of equi-axed, randomly orientated grains, pthers contained a mixture of the two, See Figs.33-35. The structures of the coatings are, broadly, ferritic in 30E, Fig.33 A-D, martensitic/ferritic in 60E, Fig.34 A-D, and martensitic/austenitic, in 65E, Fig.35 A-D. The micro-structure of the more highly alloyed 60E and 65E also exhibited a fine, sometimes unresolvable dispersion of other phases within the metallic lamallae.

The three heat treatments applied to the coatings when studying residual stresses, resulted in a general coarsening of the structure, involving the coalescence of the thin oxide lamallae and the growth of the finely dispersed phases or precipitates, Fig.36-39. A more striking effect was the formation and growth of iron nitride needles in 30E, Figs.40-43. The iron nitride needles are best illustrated in scanning electron micro-scope photographs, see Fig.44 A and B. This confirms the presence of nitrogen in the coatings since the heat treatment was performed under vacuum.

FIGURE 33 : 3OE, General
Etchant : Nital

A

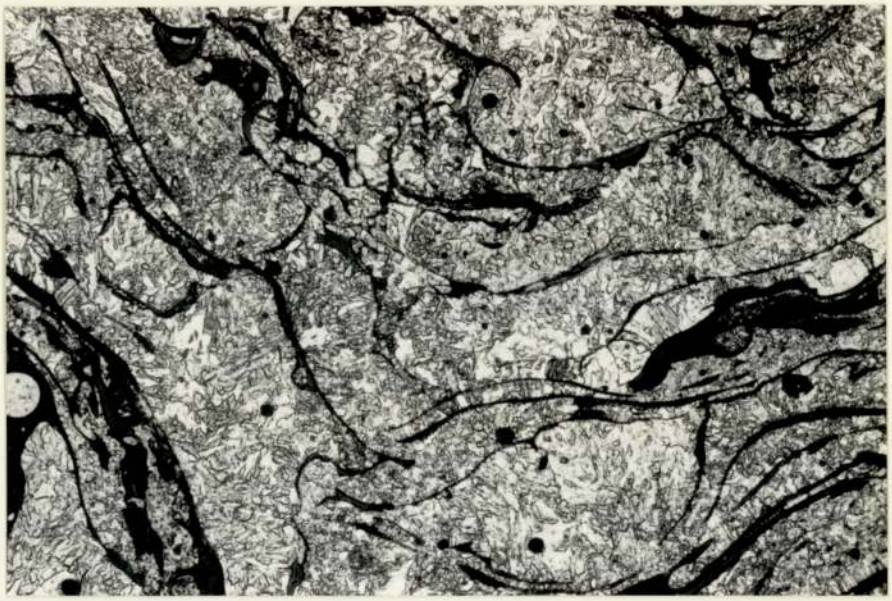

Magnification x840

B

Magnification x840

FIGURE 33 : 3OE, General
Etchant : Nital

C

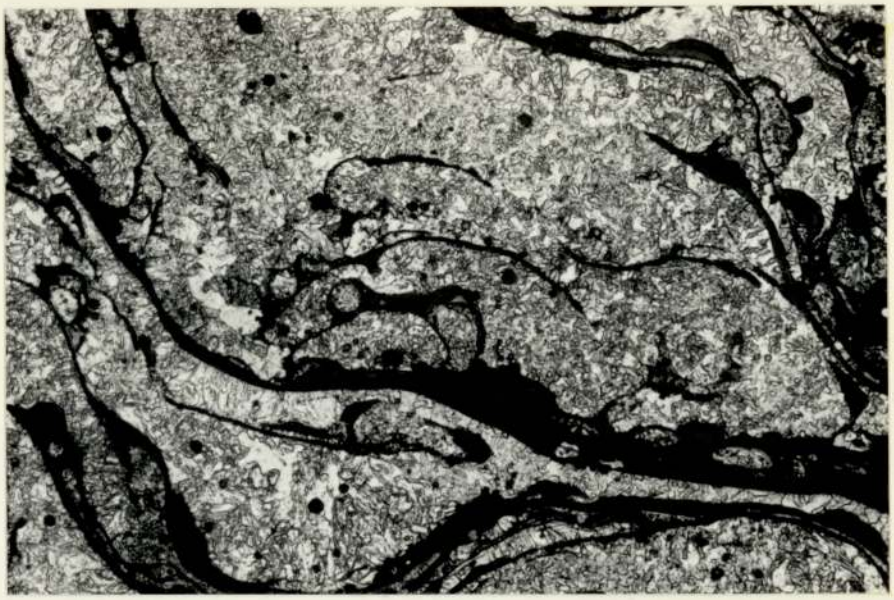

Magnification x840

FIGURE 33D : 3OE, Heat Treated, 920 K

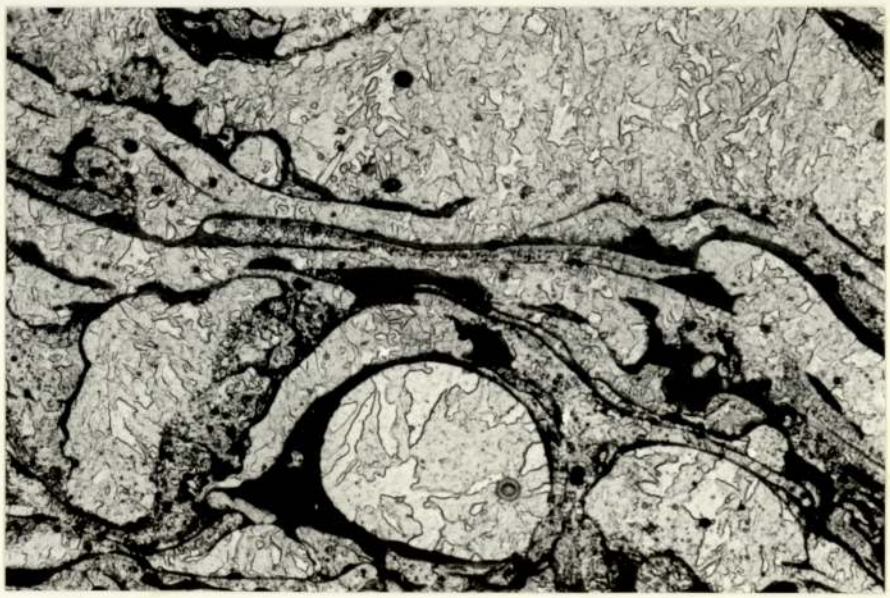

Magnification x840

FIGURE 34 : 60E, General
Etchant : Alcoholic Ferric Chloride

A

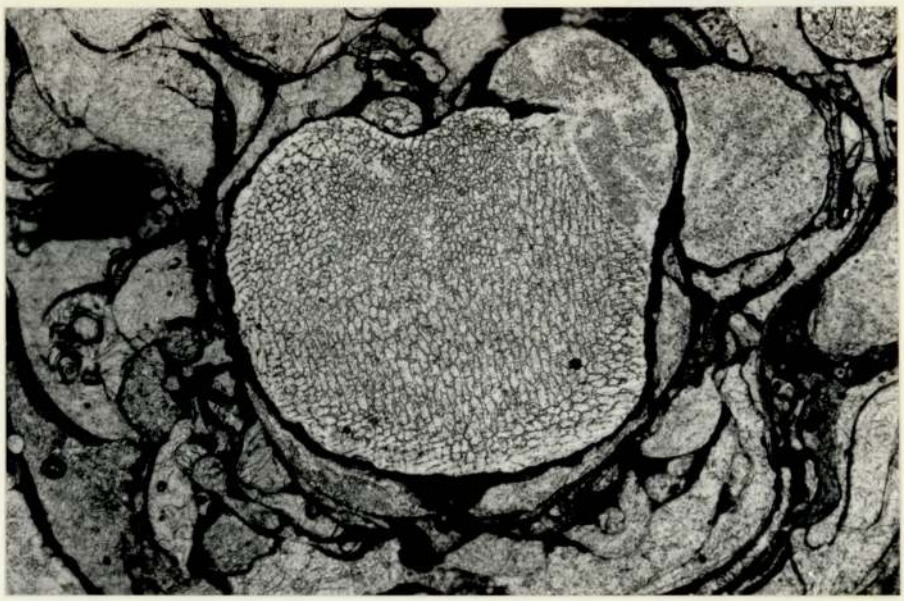

Magnification x840

B

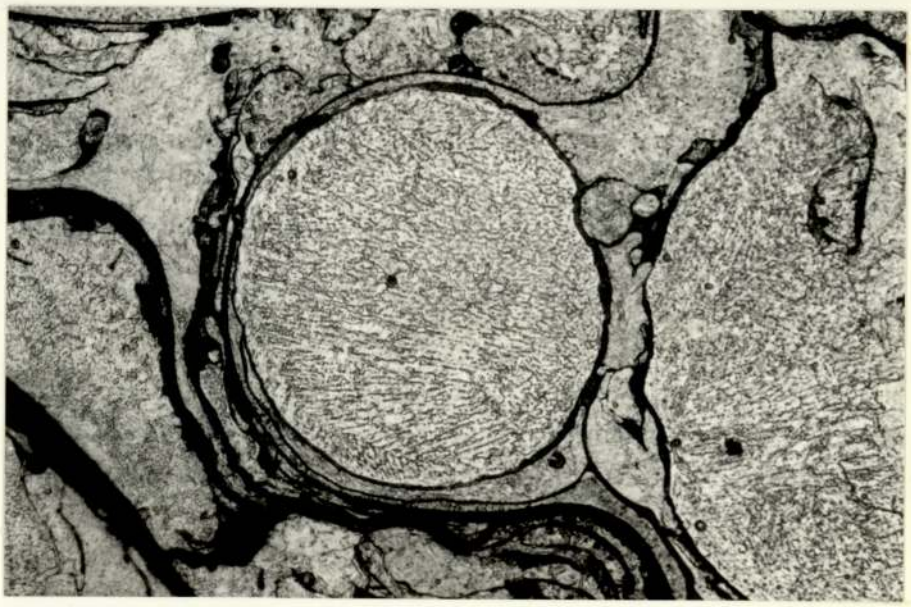

Magnification x840

FIGURE 34 : 60E, General
Etchant : Alcoholic Ferric Chloride

C

Magnification x840

D

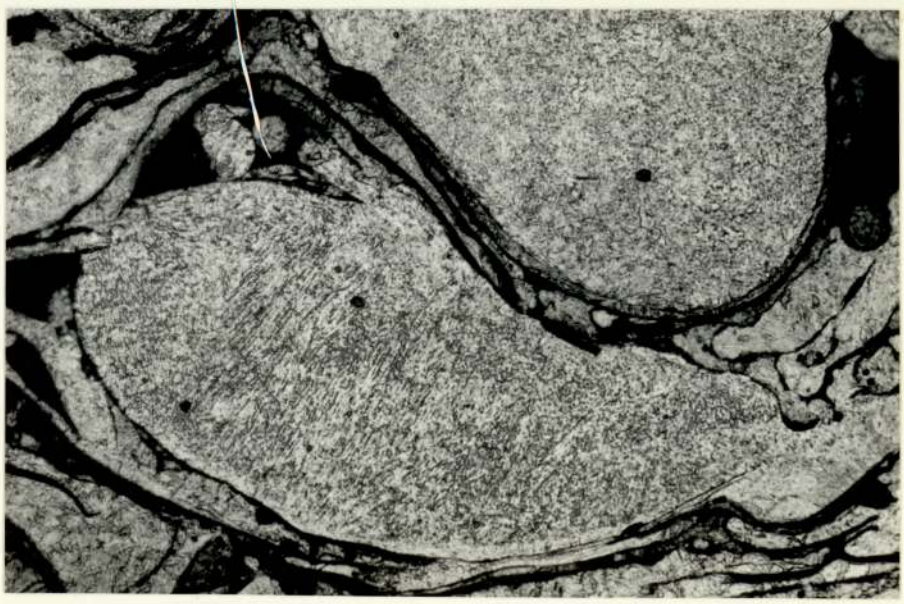

Magnification x840

FIGURE 35 : 65E, General
Etchant : Vilella's Reagent

A

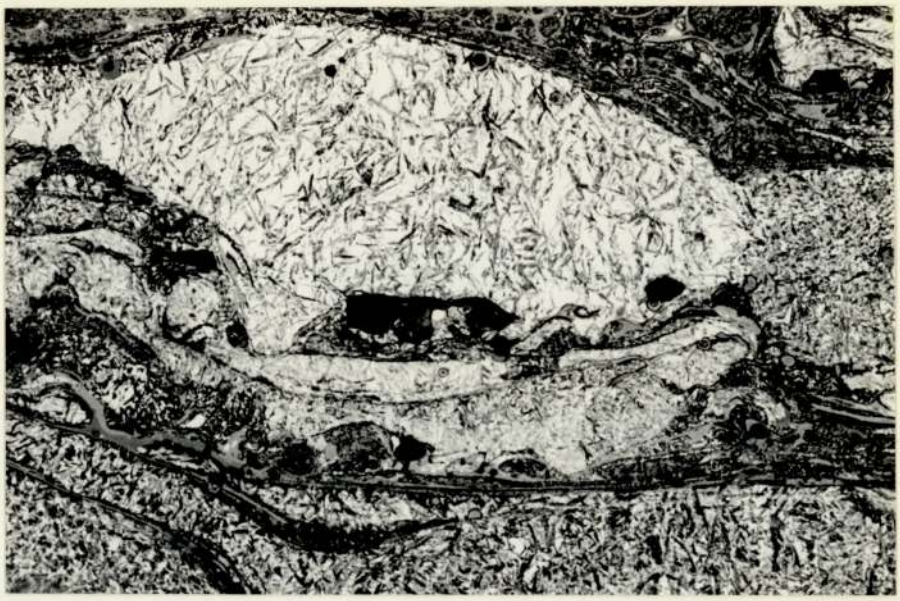

Magnification x420

B

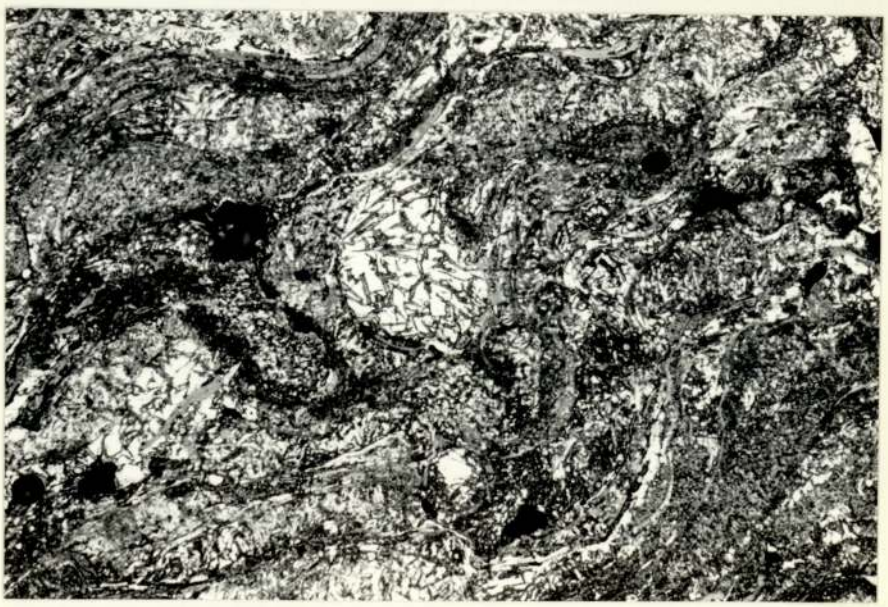

Magnification x420

FIGURE 35 : 65E, General
Etchant : Vilella's Reagent

C

Magnification x420

D

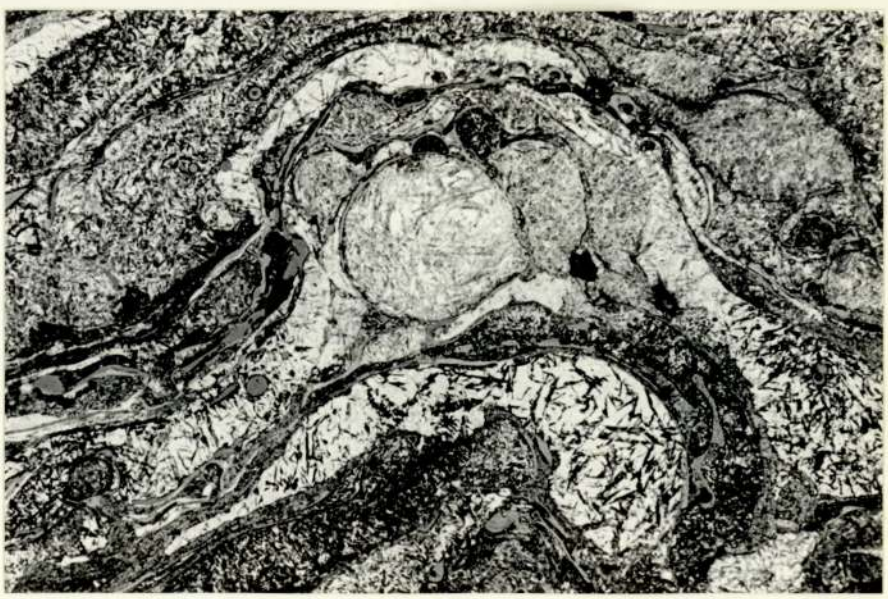

Magnification x420

FIGURE 36 : 60E, As Sprayed
Etchant : Alcoholic Ferric Chloride

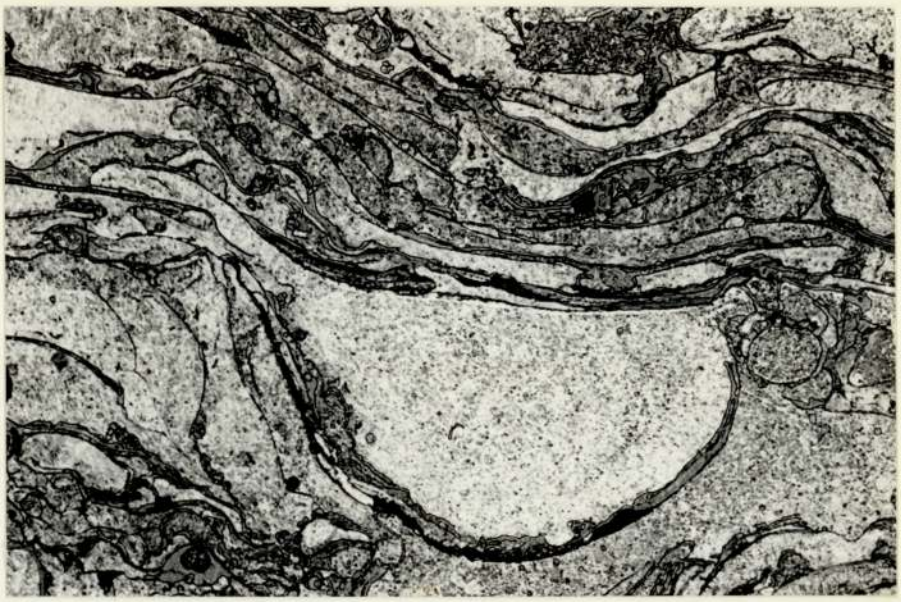

Magnification x420

Magnification x840

FIGURE 37 : 60E, Heat Treated, 920K
Etchant : Alcoholic Ferric Chloride

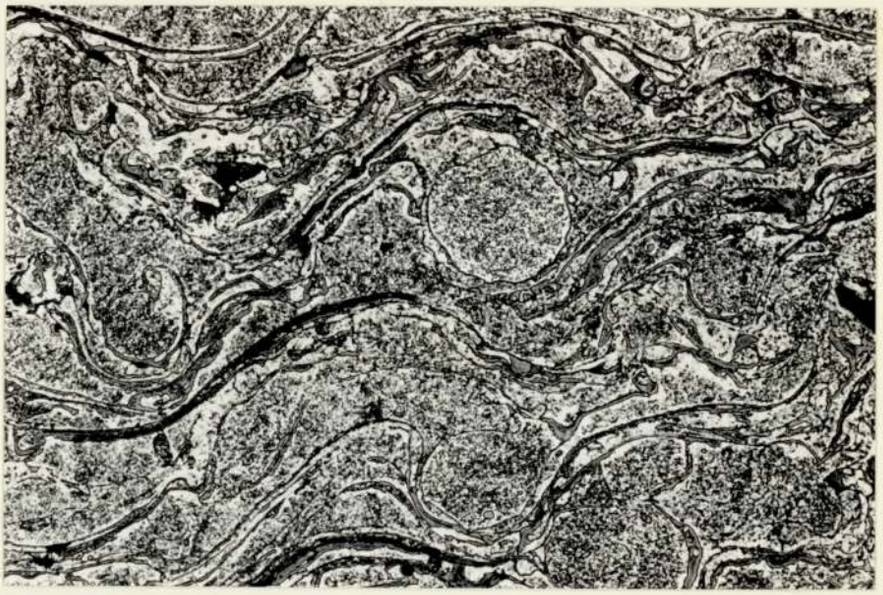

Magnification x420

Magnification x840

FIGURE 38 : 60E, Heat Treated, 1220K
Etchant : Alcoholic Ferric Chloride

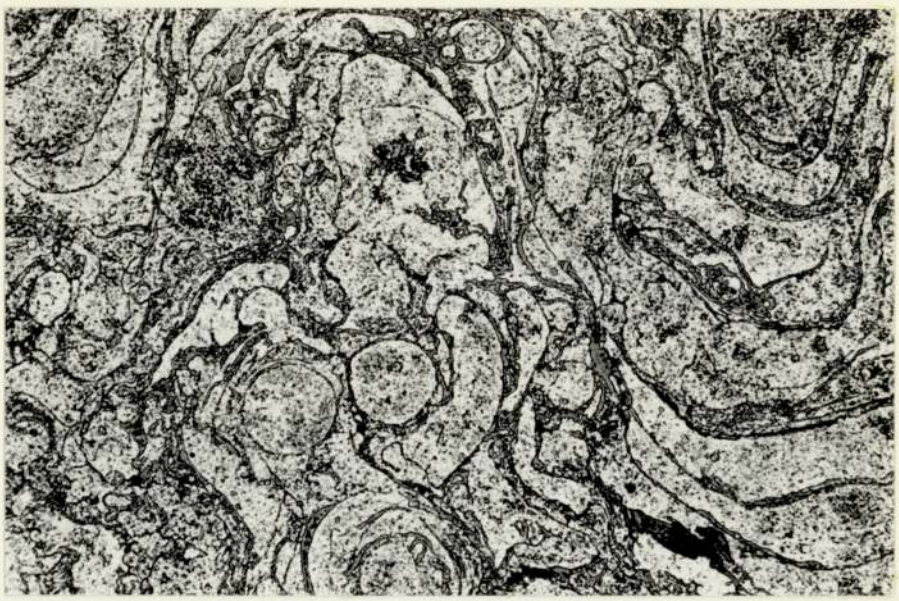

Magnification x420

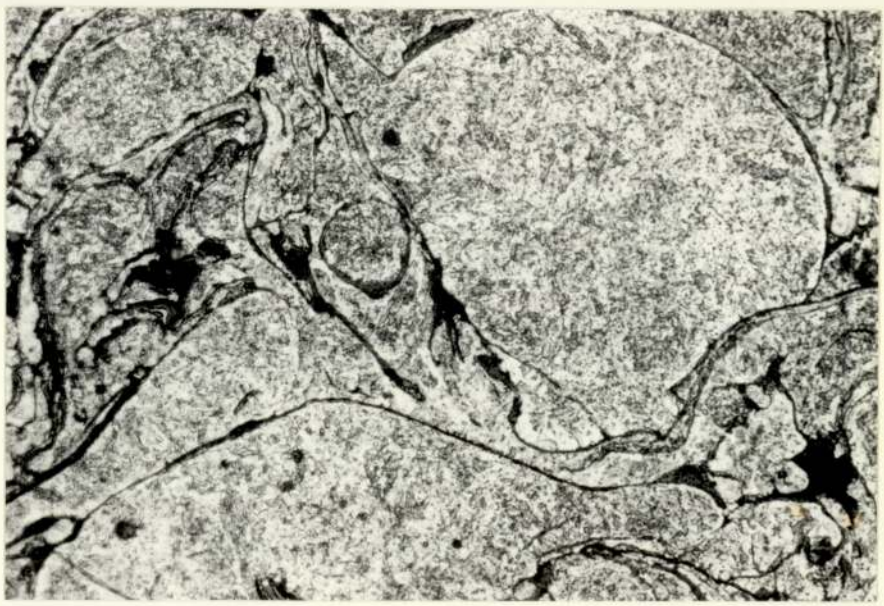

Magnification x840

FIGURE 39 : 60E, Heat Treated, 1420K

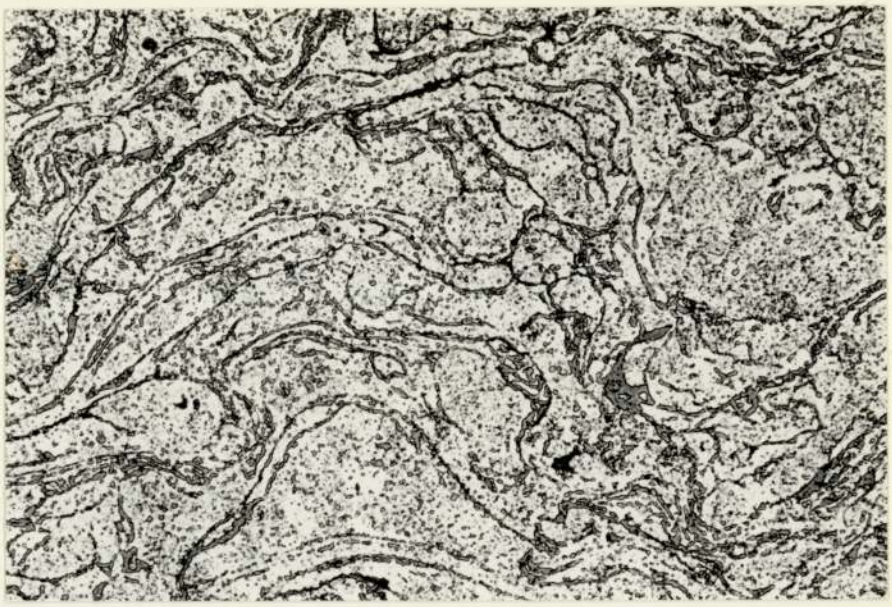

Magnification x420

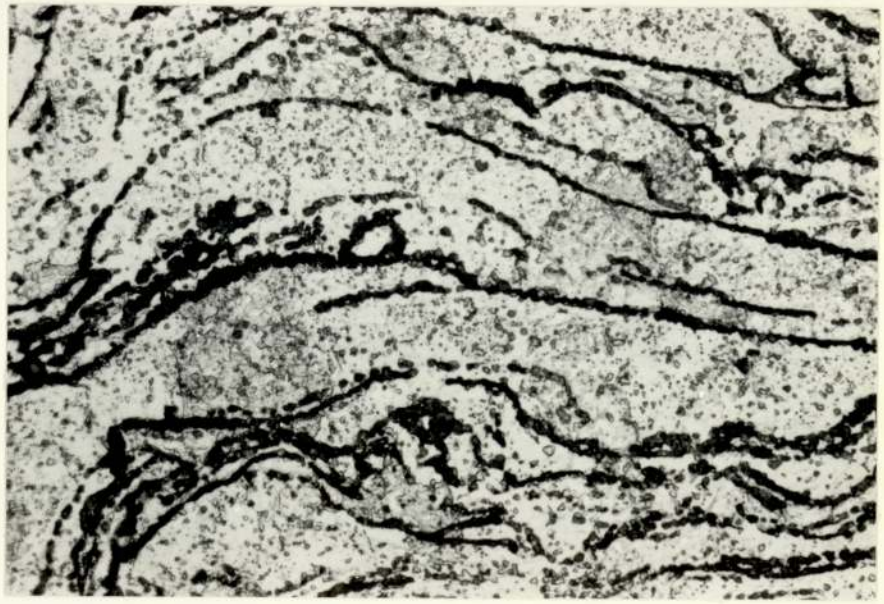

Magnification x840

FIGURE 40 : 30E, As Sprayed. Etchant : Nital

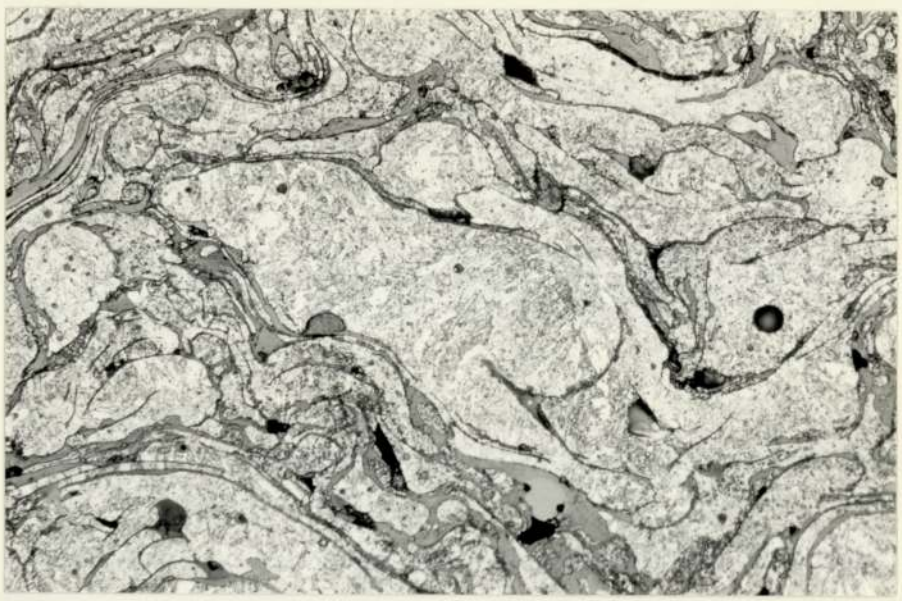

Magnification x 420

FIGURE 41 : 30E, Heat Treated, 920K,
Etchant : Nital

Magnification x 420

FIGURE 42 : 30E, Heat Treated, 1220K
Etchant : Nital

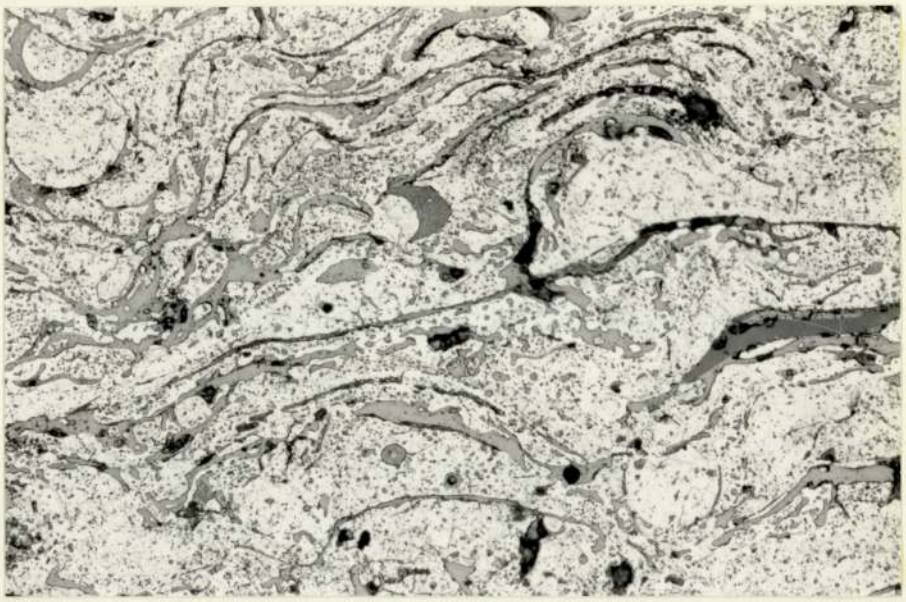

Magnification x840

FIGURE 43 : 30E, Heat Treated, 1420K
Etchant : Nital

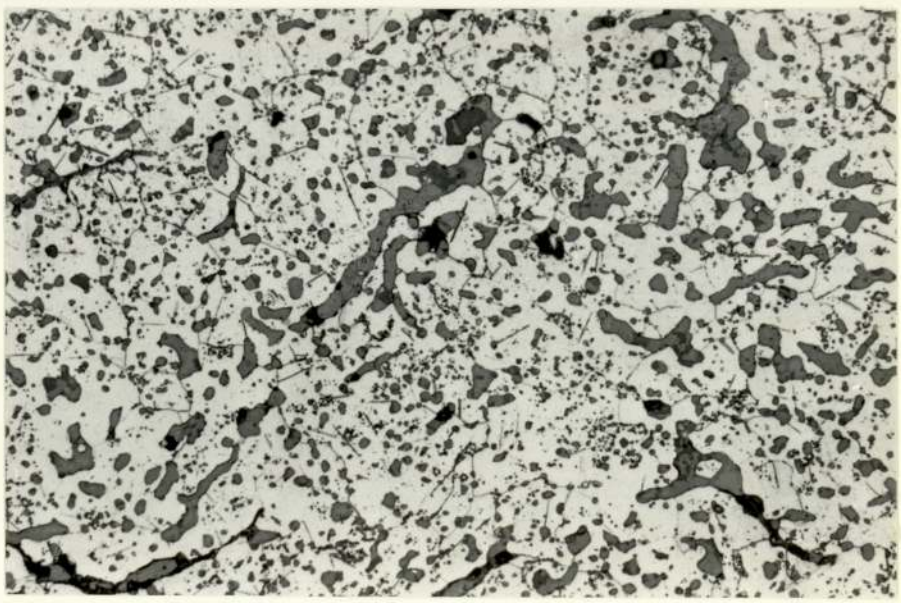

Magnification x420

FIGURE 44 : 30E, S.E.M. Photographs,
Iron Nitride Needles

A

B

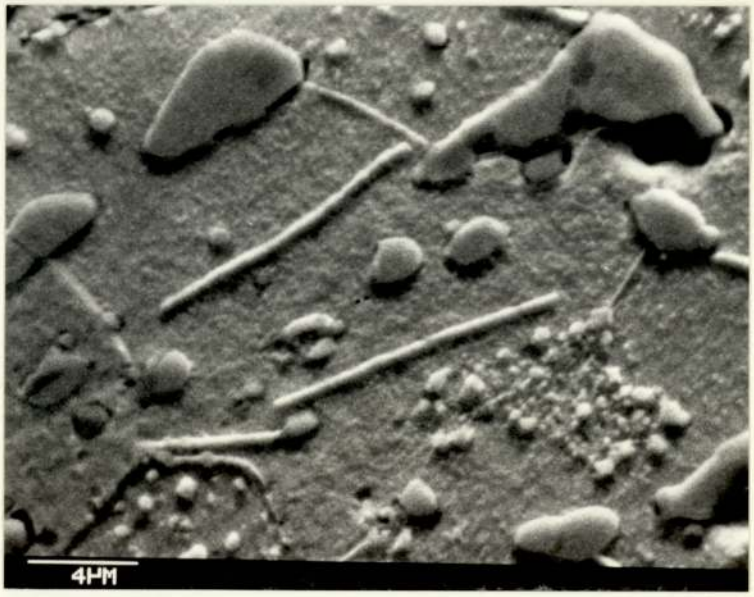

4.1.3 Elemental Composition of Coating Particles

The compositional micro-variations within selected examples of each coating were studied using energy dispersive micro-analysis and a Z.A.F. programme.

Although the Z.A.F. system offers quantitative analysis the results obtained from coatings suffered from recognised errors. For example, elements with an atomic number of less than 11 could not be detected. Thus carbon and nitrogen known to be present were not accounted for by the correction system used by the Z.A.F. programme, when using oxygen in the element by difference programme. Additionally, in the mode used, the electron beam penetrated below the surface of the sample. The depth of penetration is related to acceleration voltage and the material being examined. The depth expected from this analysis was of the order of 5 μm. Lamellar thickness was of the order of 2-20 μm, and each flattened particle varied in cross-sectional thickness. Thus the beam may have penetrated some of the constituents being examined, so that elements in the constituent underneath would be included.

The sensitivity of the technique is low, so analyses are only approximate. However, there is still considerable value in obtaining a rough guide to the micro-distribution of elements within coating structures.

Significant variations in composition were detected in metallic and oxide particles, the results of several analyses of selected oxide and metallic particles in 60E, 30E and 65E are presented in Table 9. The results presented are "raw",

TABLE 9

ENERGY DISPERSIVE MICRO-ANALYSIS OF
30E, 60E AND 65E DEPOSITS

MATERIAL: 60E					
Particle Type	Metallic	Metallic	Oxide	Oxide	Oxide
Element	Wt% Element Detected				
Fe	83.9	82.9	60.7	43.2	40.8
Cr	12.1	12.0	18.9	33.5	37.0
Mn	0.2	0.4	0.5	0.6	0.7
Si	0.3	0.4	0.5	0.3	0.5
Ni	0.1	0.1	0.0	0.1	0.2
Cu	0.3	0.1	0.1	0.1	0.1
O	3.1	4.1	19.3	22.2	20.7
(By difference)					
MATERIAL: 30E					
Fe	96.9	96.6	46.6	65.4	78.2
Mn	0.1	0.0	9.9	3.7	2.3
Si	0.2	0.2	13.2	0.8	0.2
Cu	0.2	0.1	0.2	0.3	0.1
O	2.6	3.1	30.1	29.8	19.2
(By difference)					
MATERIAL: 65E					
Fe	89.0	87.0	71.0	62.0	65.1
Cr	2.4	1.9	3.3	5.0	4.7
Mn	1.4	1.0	3.6	4.8	3.4
Si	0.4	0.4	1.1	1.8	0.9
Ni	0.2	0.4	0.0	0.1	0.0
Cu	0.5	0.3	0.2	0.3	0.6
O	6.1	9.0	20.8	26.0	25.3
(By difference)					

as produced by the Z.A.F. programme, however, the number of possible interactions may in this case reduce the accuracy of the analysis.

The compositional variation throughout coating sections is also illustrated both by X-ray maps (see Figs. 45-48, which show the distribution of chromium, silicon, and manganese) and chromium line concentration profiles (see Figs. 49 and 50). The distribution of these elements is far from uniform and they are especially concentrated within oxides.

4.1.4 X-Ray Diffractometry

X-ray diffractometry was used to investigate the crystal structure of the phases existing within selected representative examples of the three coating materials. The d-spacing is recorded as a logarithm and related to intensity, see Fig. 51.

A number of reflections were obtained which could relate to oxides, nitrides, carbides and intermetallic compounds. However, identification of the individual compounds was not possible. In the majority of cases only the most intense lines were present due to the small amounts of these compounds, and in many instances the peaks were masked due to coincidence with more intense lines. However, the traces obtained for 30E and 60E were typical of a ferritic and mixed ferritic/martensitic structures respectively.

Reflections occurred in 60E at the austenitic (311) and (220) d-spacings, however since there was no metallographic evidence for the existence of austenite these are more likely to be due

FIGURE 45 : 60E, S.E.M. Photograph for Elemental Distribution

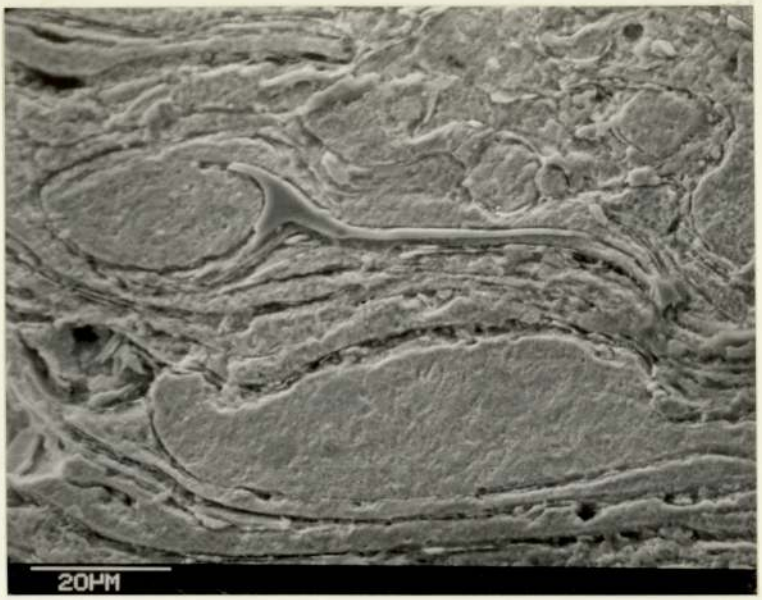

FIGURE 46 : 60E, X-Ray Map, Chromium Distribution

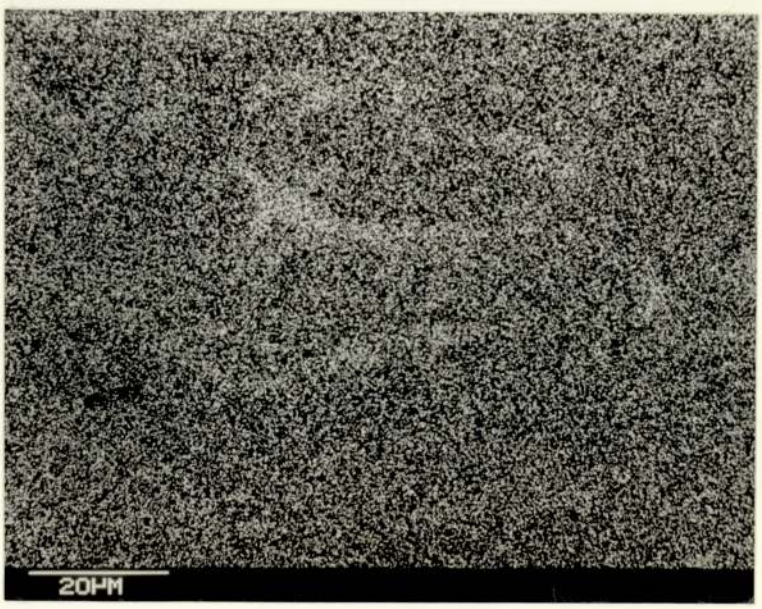

FIGURE 47 : 60E, X-Ray Map, Silicon Distribution

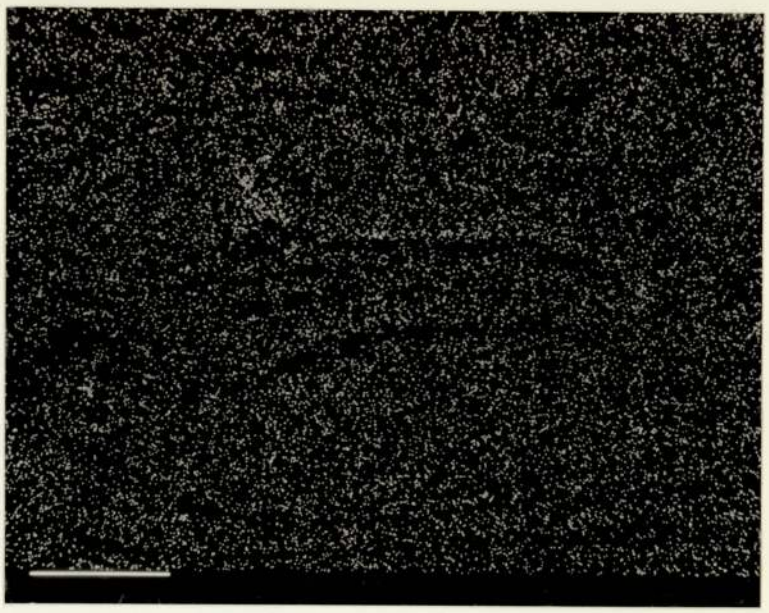

FIGURE 48 : 60E, X-Ray Map, Manganese Distribution

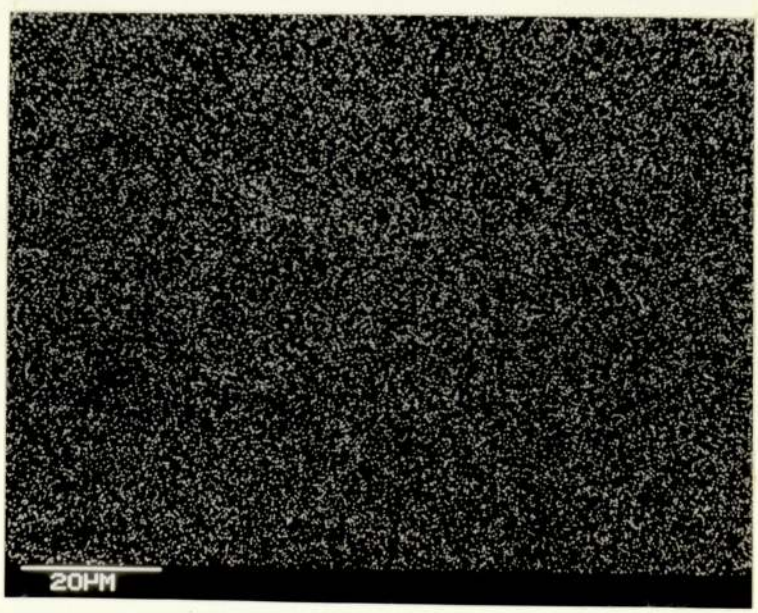

FIGURE 49 : Chromium Line Concentration Profile (60E)

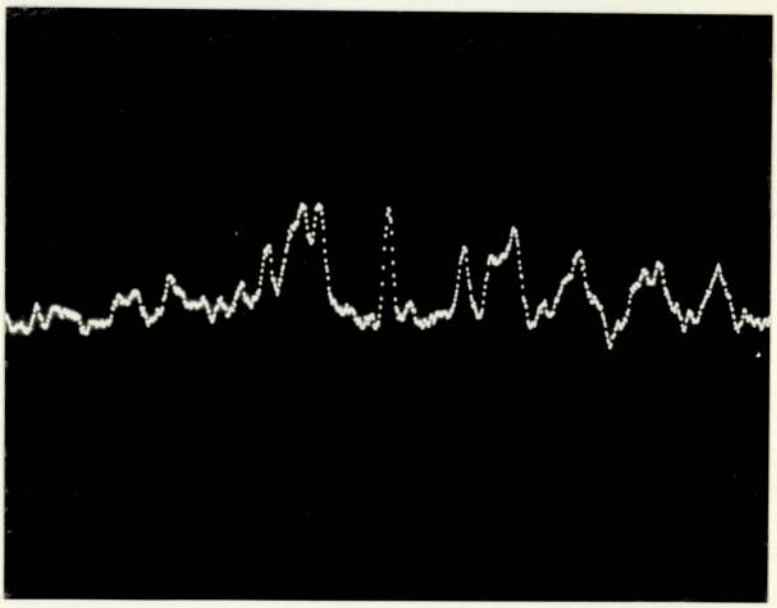

FIGURE 50 : Chromium Line Concentration Profile (60E)

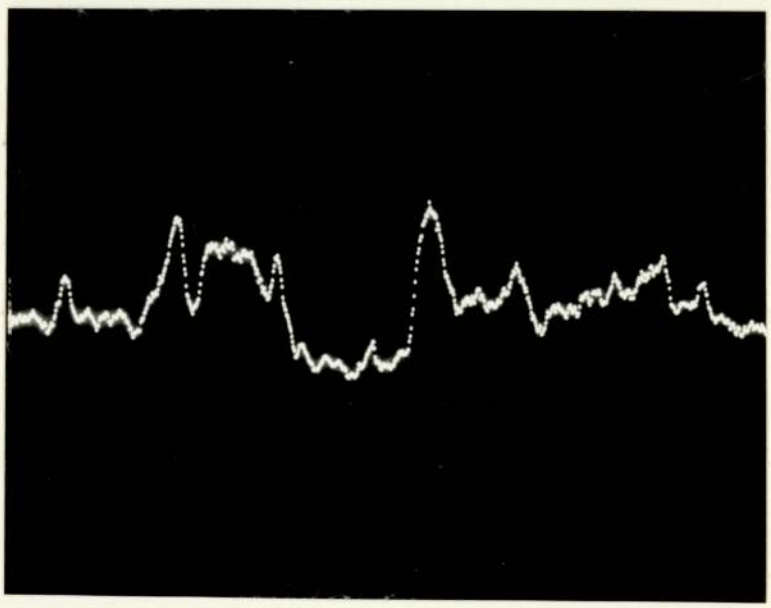

FIG. 51 X-RAY DIFFRACTION PATTERN DATA
RELATIVE INTENSITY VERSUS LOG INTERPLANAR
(d) SPACING.

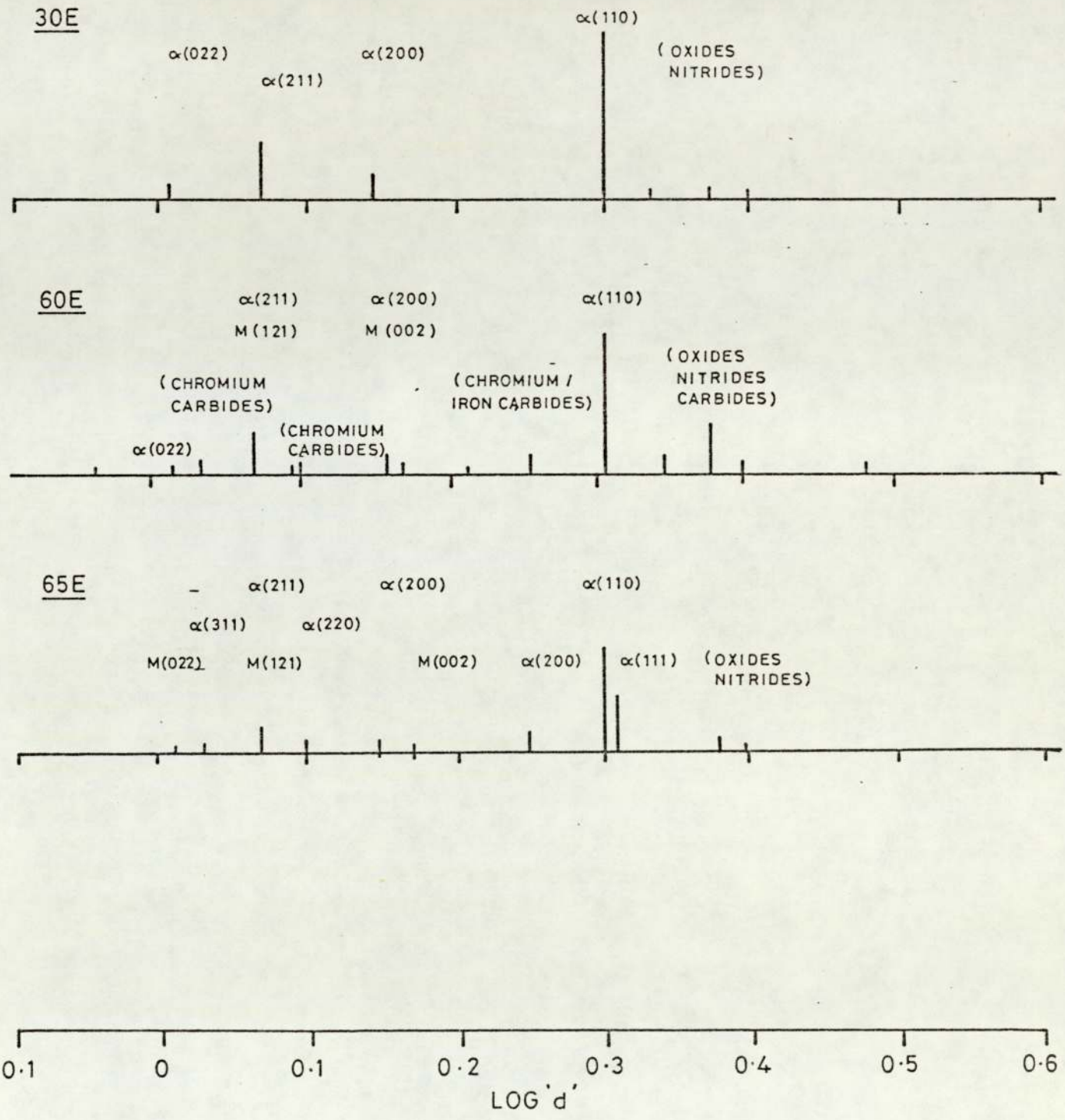

TABLE 10

INTERFERENCE OF ALLOY CARBIDE LINES WITH AUSTENITE AND MARTENSITE LINES

Austenite and Martensite 'd' Spacings	Fe_3C	M_6C	V_4C_3	Mo_2C or W_2C	WC	$Cr_{23}C_6$	Cr_7C_3
(200)γ 1.80Å	clear	clear	clear	clear	clear	strong overlap	strong overlap
(200)α 1.43Å	clear	strong overlap	clear	clear	weak overlap	weak overlap	weak overlap
(220)γ 1.27Å	weak overlap	strong overlap	weak overlap	strong overlap	weak overlap	medium overlap	clear
(211)α 1.17Å	strong overlap	clear	clear	weak overlap	weak overlap	weak overlap	medium overlap
(311)γ 1.08Å	weak overlap	medium overlap	clear	weak overlap	clear	strong overlap	clear

to chromium carbides, the reflections from which give peaks in similar positions [100], see Table 10.

A typical martensitic/austenitic trace was obtained for 65E. The volume fraction of austenite was estimated using Miller's [101] equation. Account was taken of the possible influence of chromium carbides on the integrated peak area of the austenitic peaks ($\gamma_{(220)}$ and $\gamma_{(311)}$) used. The results are presented in Table 11.

TABLE 11 - INTEGRATED PEAK AREAS

Peak	Total Area	Average Background	Integrated Peak Area
$\alpha(211)$	50492	32036	18456
$\gamma(311)$	25405	20557	4848
$\gamma(220)$	32756	28129	4627

Using:- Retained Austenite $(V_A) = I_M + \frac{1.3\ I_A}{1.3\ I_A}$

$$I_A = \tfrac{1}{2}\left[I_A^{220} + I_A^{311}\right]$$

$$I_M = I_M^{211}$$

The constant recommended for use in Miller's equation for low alloy steel is 1.3 [101].

$$(V_A)65E = 25\%$$

The volume fraction of austenite is approximately 25% which is in reasonable agreement with the amounts observed metallographically which can be estimated at about 20%, see Fig. 35.

4.2 Elemental Loss During Spraying

The extent of loss of each of the four main elements, namely

carbon, chromium, manganese and silicon, which occurred during spraying was studied. The effect of spraying distance, deposition rate, arc voltage and atomising pressure on elemental loss is shown in graphical form in Figs. 52-59. Most of the relationships are drawn on the basis of the results of three analyses. The full analysis results are recorded in Appendix III.

4.2.1 Carbon

A 30% loss of carbon content occurred at short spraying distances which increased to 50% loss at the largest distance in 60E and 65E. The carbon level in 30E wire was almost unchanged in conversion to a coating. An increase in atomising pressure had no effect on carbon loss, in all three materials a consistent loss of 40% was recorded at each setting of pressure. Thus the loss is related only to the spraying distance of 125 mm.

An increase in arc voltage from 26-35 v had a similar effect to increasing spraying distance from 40-195 mm in 65E. Carbon losses of 30-50% occurred in 65E, 30E and 60E were almost unchanged.

In general the influence of deposition rate on the retention of carbon is the most significant of the remainder of the parameters with 65E. In this case an increase in deposition rate resulted in a 20% decrease in the loss of carbon.

4.2.2 Manganese and Silicon

A loss of 15-50% each of manganese and silicon was shown to occur in 65E and 30E for an increase in spraying distance from 40-195 mm. However, at 195 mm the losses of these elements from 60E wire was as high as 80%.

FIGURE 52

Influence of spraying distance on wt% carbon content of 30E, 60E and 65E coatings

CARBON

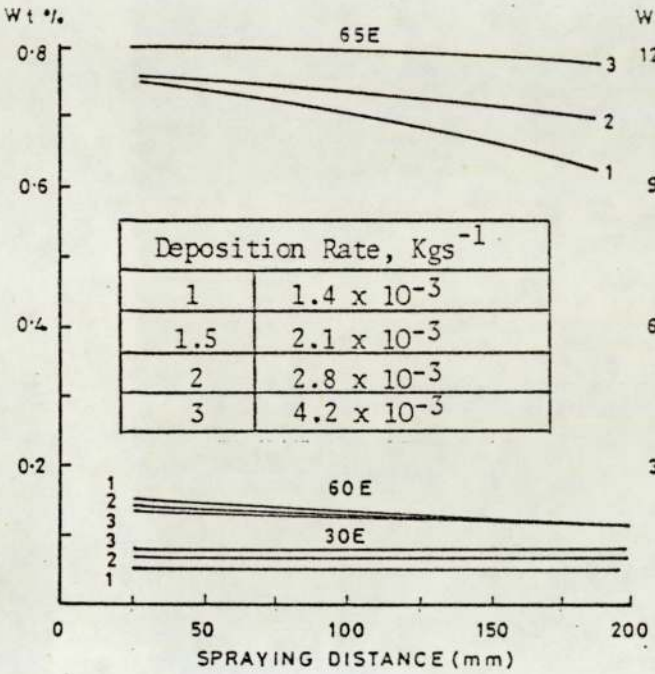

FIGURE 53

Influence of spraying distance on wt% chromium content of 60E and 65E coatings

CHROMIUM

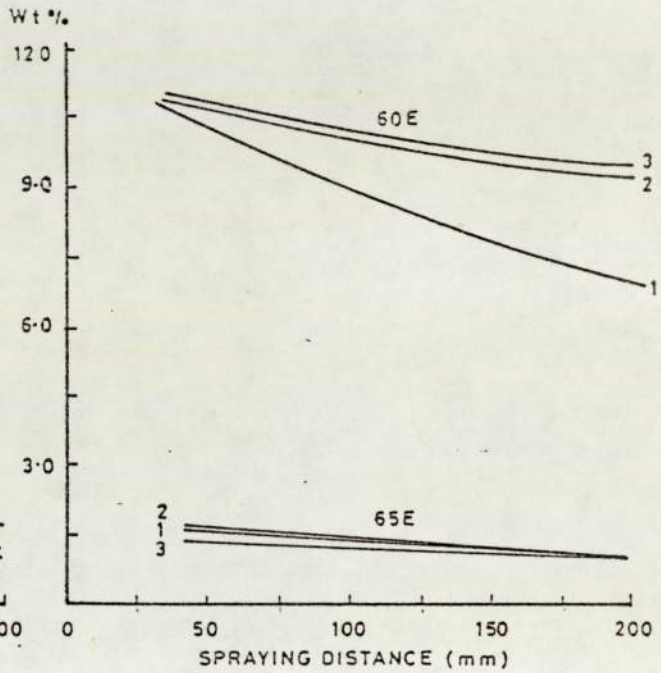

FIGURE 54

Influence of spraying distance on wt% manganese content of 30E, 60E and 65E coatings

MANGANESE

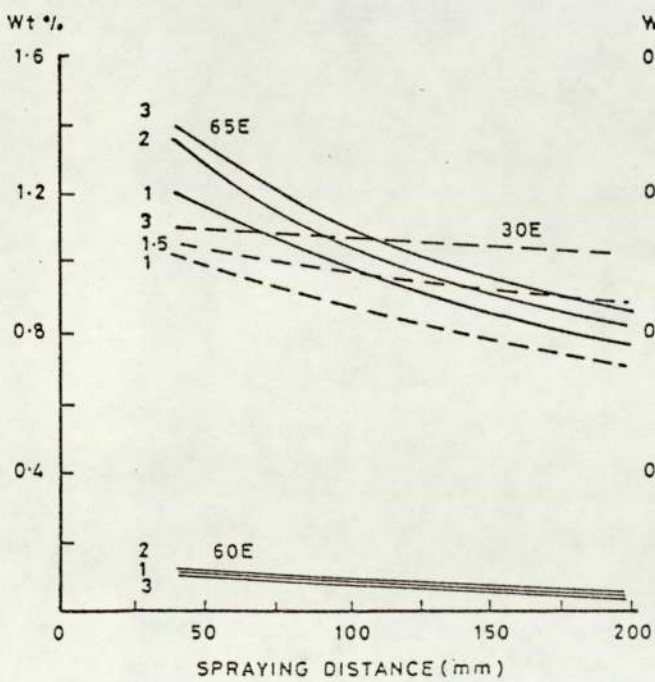

FIGURE 55

Influence of spraying distance on wt% silicon content of 30E, 60E and 65E coatings

SILICON

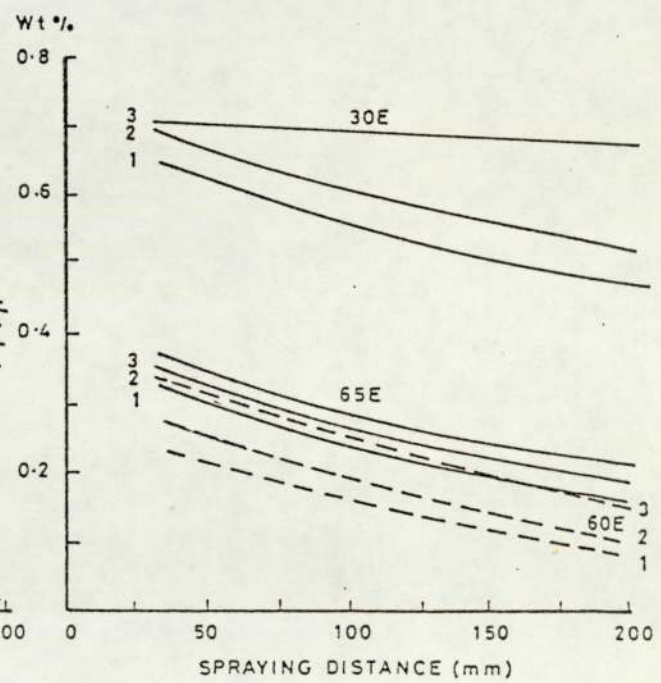

FIGURE 56 Influence of atomising pressure and arc voltage on the wt% chromium content of 60E and 65E coatings

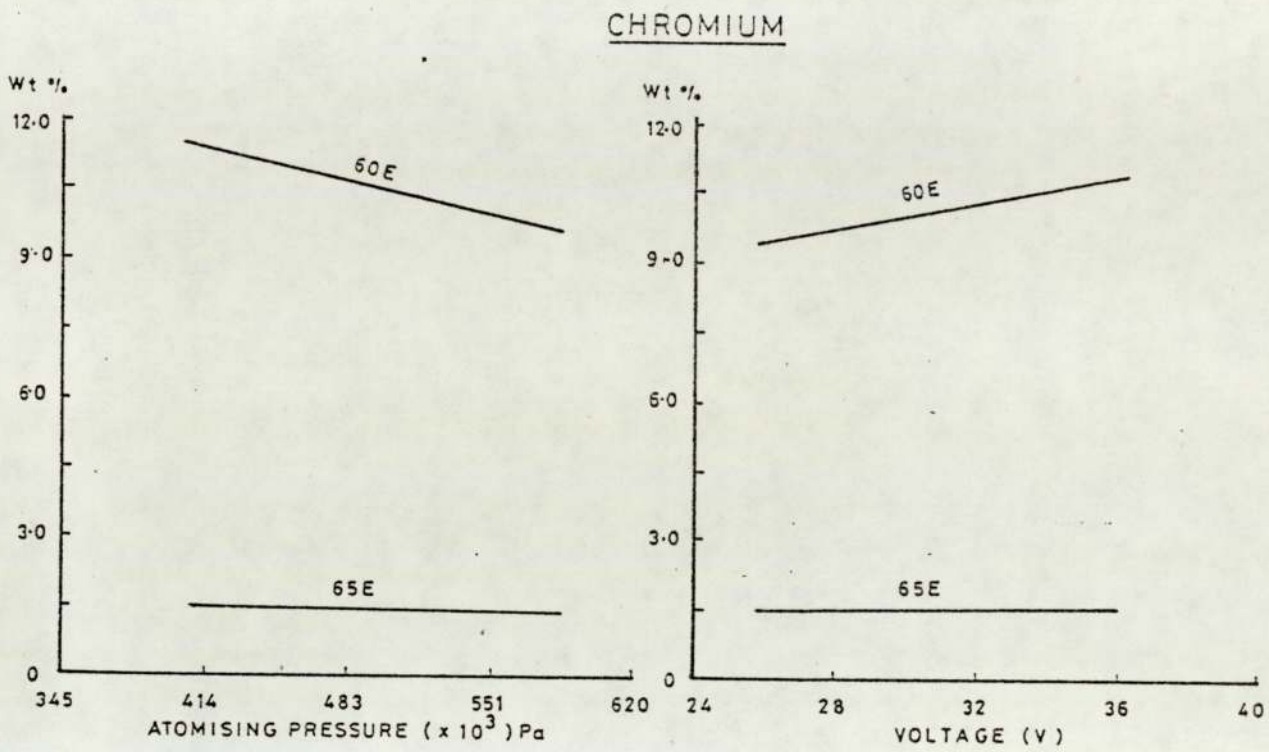

FIGURE 57 Influence of atomising pressure and arc voltage on the wt% carbon content of 30E, 60E and 65E coatings

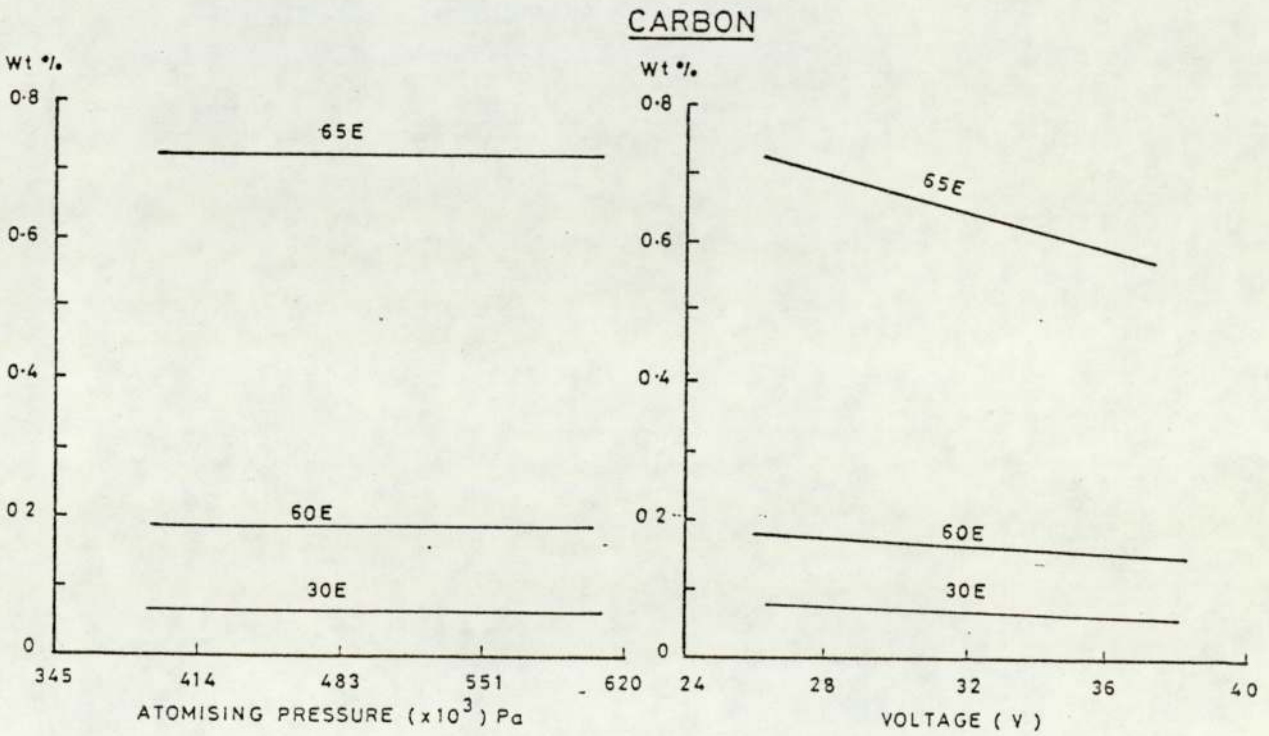

FIGURE 58 Influence of atomising pressure and arc voltage on the wt% manganese content of 30E, 60E and 65E coatings

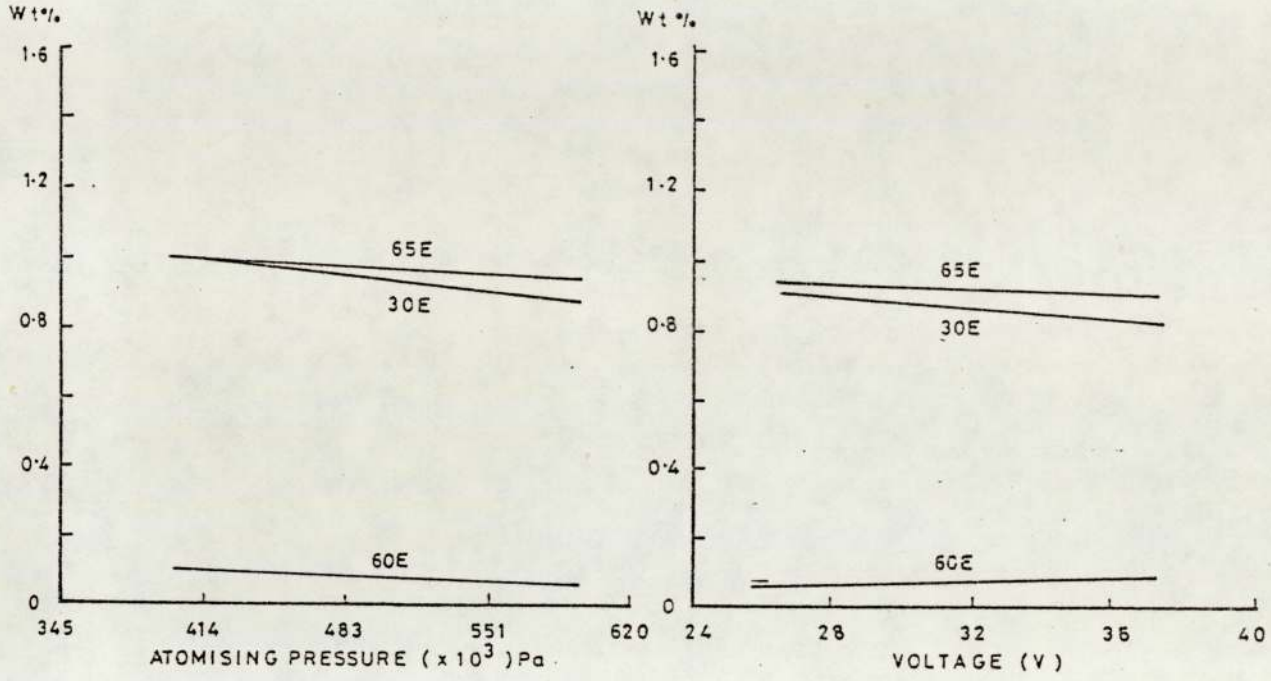

FIGURE 59 Influence of atomising pressure and arc voltage on the wt% silicon content of 30E, 60E and 65E coatings

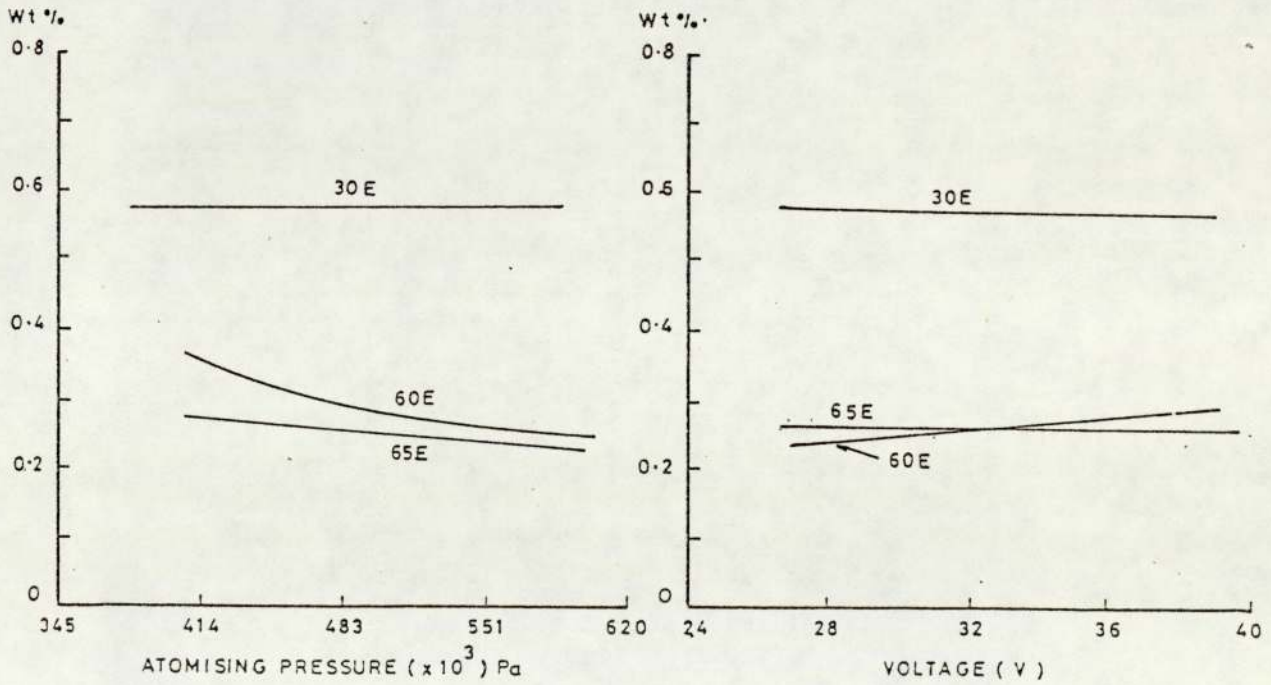

In general, increase in arc voltage and atomising pressure produced a small increase in elemental loss in excess of that due to the effect of spraying distance alone. The exception was 60E, where an increase in voltage slightly aided the retention of manganese and silicon.

4.2.3 Chromium

A loss of 25-50% and 10-45% occurred from 60E and 65E respectively, for an increase in spraying distance from 40-195 mm. Voltage and atomising pressure had no effect on chromium content loss, a consistent loss in 65E, a consistent loss related to the spraying distance was recorded.

The same trend with regard to the effect of voltage was exhibited by 60E. An increase in atomising pressure increased the loss of chromium and an increase in voltage had the opposite effect. This phenomenon has also been observed by James [33].

4.3 Oxygen Content

The oxygen content of the coating materials was determined using a Balzer Exhalograph. The effect of a variation in spraying distance, deposition rate, atomising pressure and spraying voltage on the oxygen content of samples of coatings was examined. The results are presented in Figs. 60 to 64. A linear relationship between oxygen content and the variable appeared to exist in each case. For convenience of data analysis, gradient (m) and intercepts (c) were determined and recorded in Table 12. In general, coatings of the more highly alloyed steels (65E and 60E) contained higher levels of oxygen than those of 30E.

FIGURE 60 Relationship between spraying distance and wt% O content of 30E coatings at deposition rates of 1.4 - 4.2 x 10^{-3} Kg s^{-1}

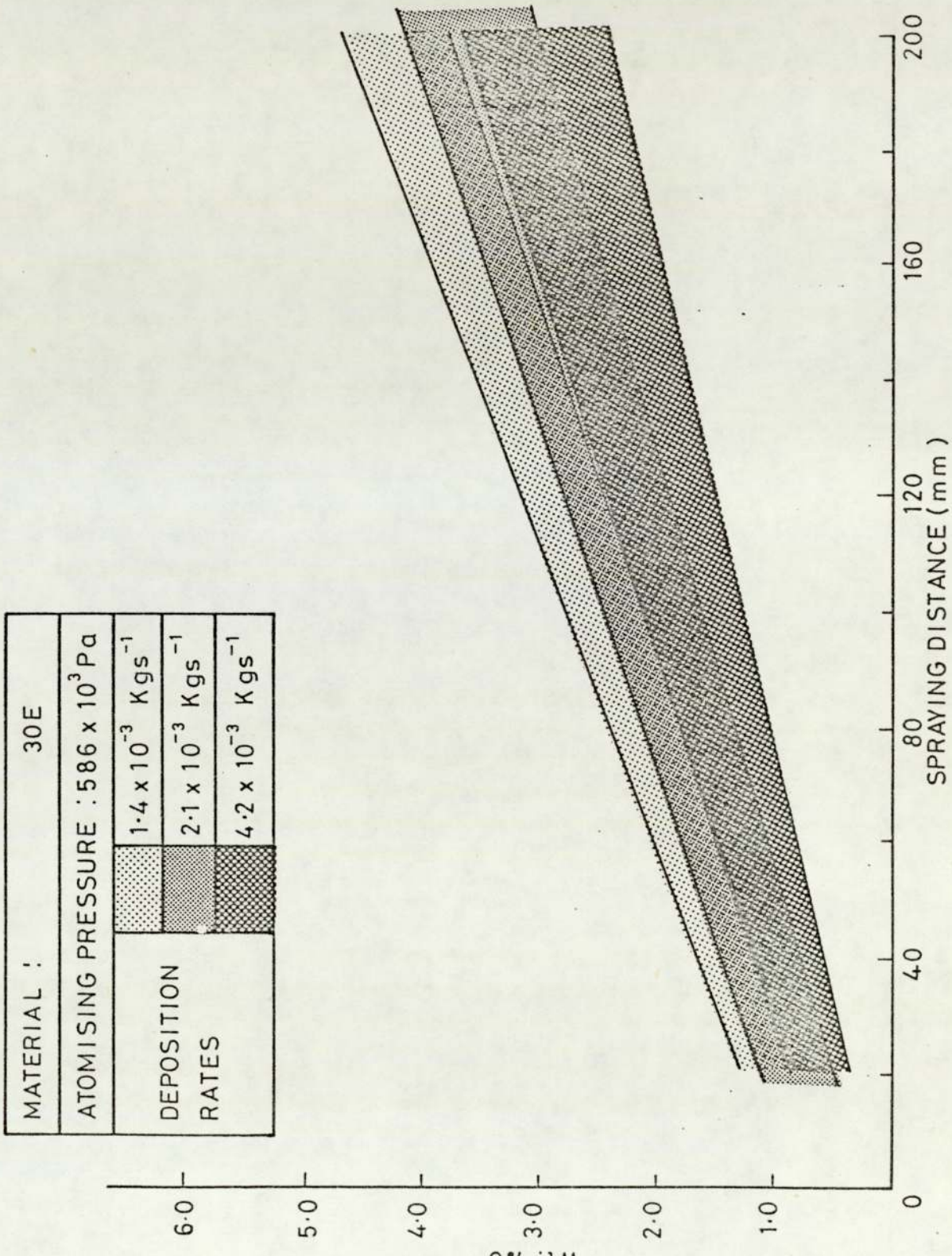

FIGURE 61 Relationship between spraying distance and wt% O content of 65E coatings at deposition rates of 1.4 - 4.2 x 10^{-3} Kg s^{-1}

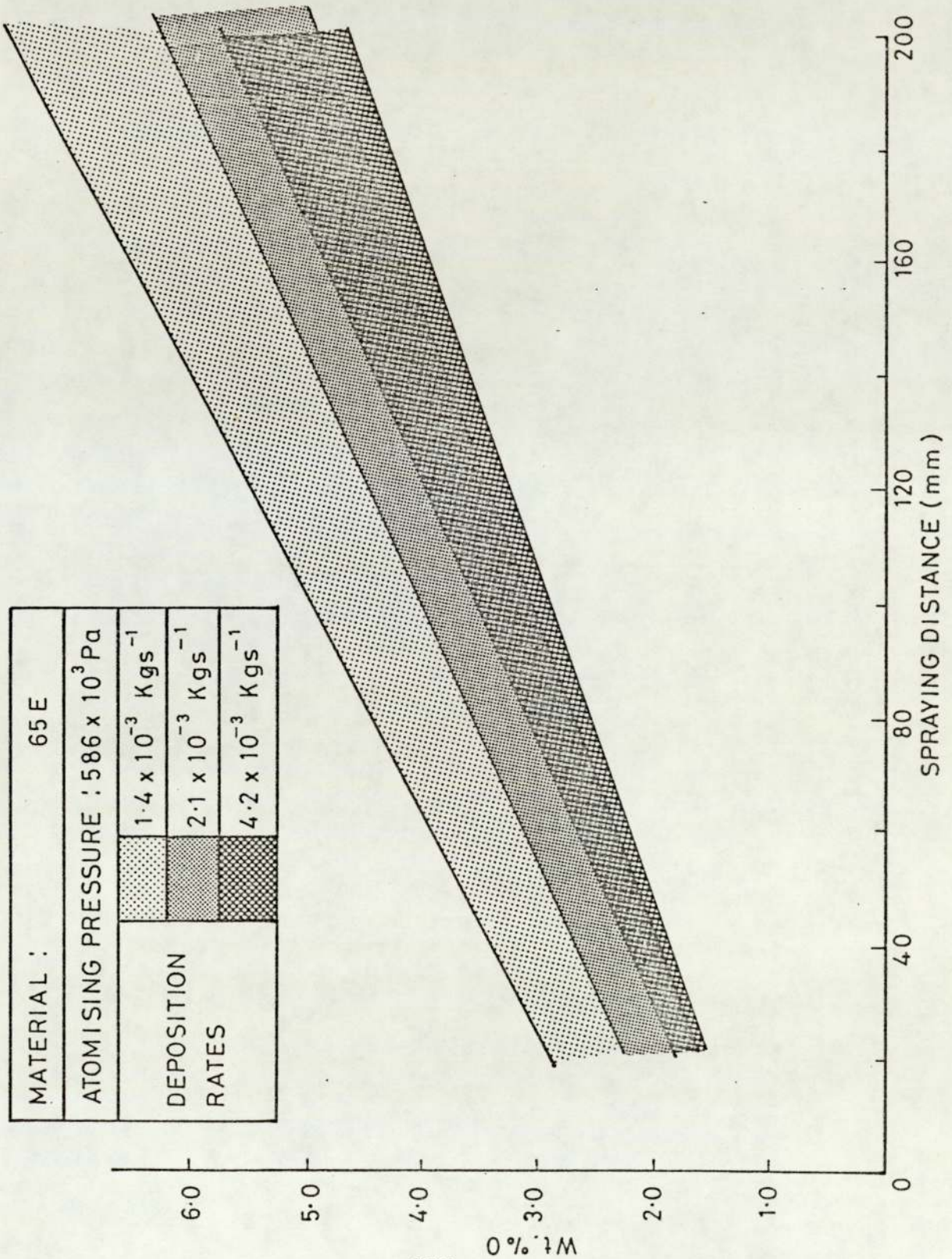

FIGURE 62 Relationship between spraying distance and wt% O content of 60E coatings at deposition rates of 1.4 - 4.2 x 10^{-3} Kg s^{-1}

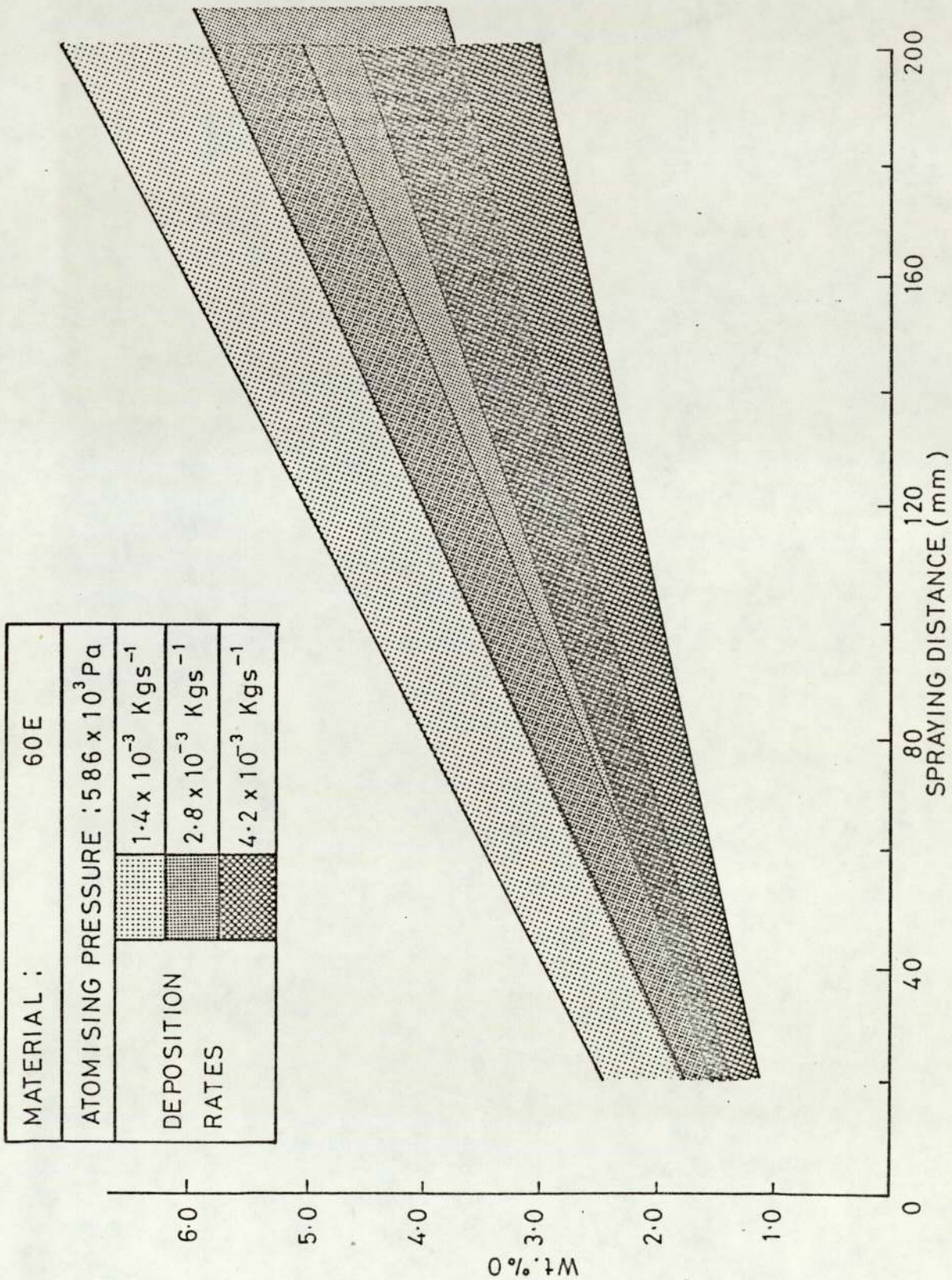

FIGURE 63 Relationship between atomising pressure and wt% O content of 30E, 60E and 65E coatings

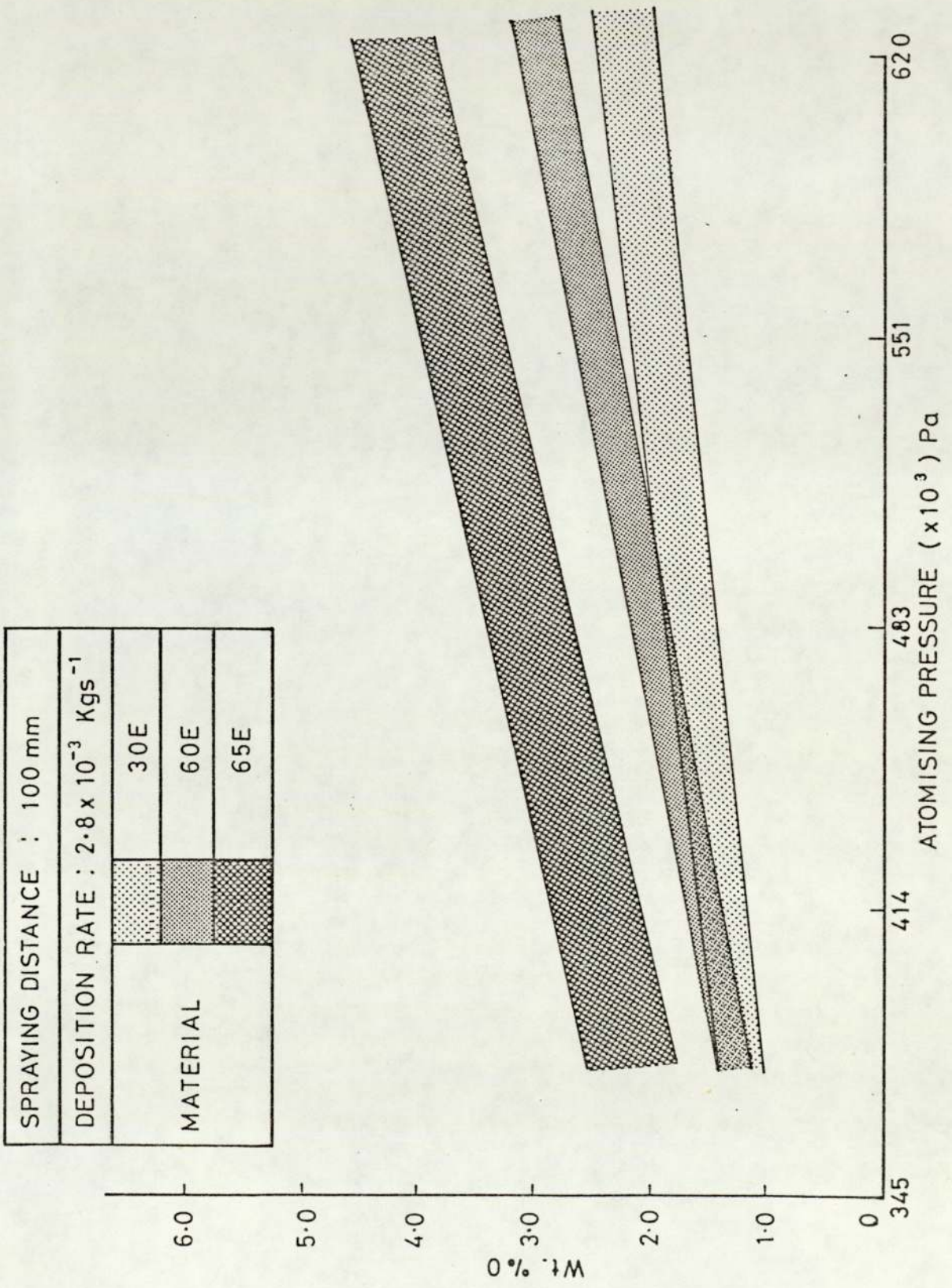

FIGURE 64 Relationship between arc voltage and wt% O content of 30E, 60E and 65E coatings

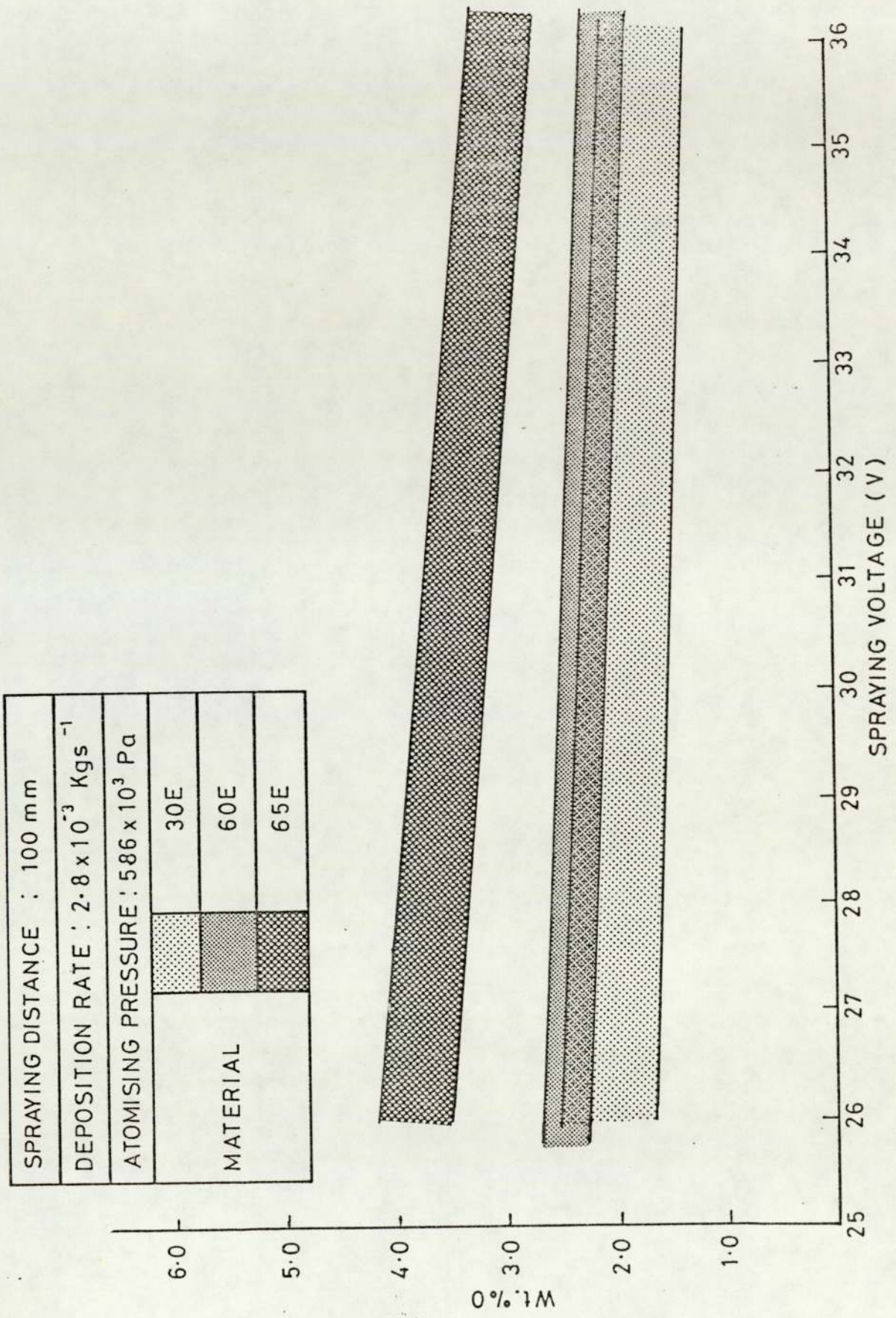

TABLE 12

GRADIENT (m) AND INTERCEPT (c) VALUES OF FIGURES 60 TO 64.

Variable: Spraying Distance

Material	Condition	m	c
30E	586 x 10^3Pa 29/26 v 1.4 x 10^{-3} Kgs^{-1}	0.02	0.6
30E	586 x 10^3Pa 29/26 v 2.1 x 10^{-3} Kgs^{-1}	0.01	0.9
30E	586 x 10^3Pa 29/26 v 4.2 x 10^{-3} Kgs^{-1}	0.01	0.7
65E	586 x 10^3Pa 29/26 v 1.4 x 10^{-3} Kgs^{-1}	0.02	1.8
65E	586 x 10^3Pa 29/26 v 2.1 x 10^{-3} Kgs^{-1}	0.02	1.3
65E	586 x 10^3Pa 29/26 v 4.2 x 10^{-3} Kgs^{-1}	0.02	0.9
60E	586 x 10^3Pa 32/29 v 1.4 x 10^{-3} Kgs^{-1}	0.02	1.4
60E	586 x 10^3Pa 32/29 v 2.8 x 10^{-3} Kgs^{-1}	0.01	1.4
60E	586 x 10^3Pa 32/29 v 4.2 x 10^{-3} Kgs^{-1}	0.01	1.3

Variable: Voltage

30E	586 x 10^3Pa 100 mm 2.8 x 10^{-3} Kgs^{-1}	-0.05	3.4
65E	586 x 10^3Pa 100 mm 2.8 x 10^{-3} Kgs^{-1}	-0.09	6.3
60E	586 x 10^3Pa 100 mm 2.8 x 10^{-3} Kgs^{-1}	-0.05	3.9

Variable: Atomising Pressure

30E	29/26 v 100 mm 2.8 x 10^{-3} Kgs^{-1}	0.03	-0.01
65E	29/26 v 100 mm 2.8 x 10^{-3} Kgs^{-1}	0.07	-1.6
60E	32/29 v 100 mm 2.8 x 10^{-3} Kgs^{-1}	0.05	-1.2

Increases in spraying distance and atomising pressure induced an increase in oxygen content, higher voltages and deposition rates had the reverse effect. It was expected that a certain amount of scatter would exist due to the small sample size and the inhomogeneity of the coating structure. The scatter bands obtained in practice were not excessive, and the results provided the information required.

4.4 Shear Adhesion Strength and Residual Stress

4.4.1 Preliminary Study

The results of the preliminary study are summarised in Table 13. The complete results are in Appendix IV. Statistical analysis of the results showed that there was an effect on shear adhesion strength at 0.5% significance level due to deposit and substrate materials singly and combined and due to collar width. Collar thickness or the action of slitting the collar before testing had no significant effect on shear adhesion strength.

The degree of error associated with the various collar dimensions examined is given in Table 13. The largest error occurred when using the 5 mm x 4 mm size of collar and the smallest error occurred with the 5 mm x 2 mm size. The latter size then was taken as the standard for the remainder of the study, it was also decided not to perform the operation of slitting the collars longitudinally as this action proved to have no effect on shear adhesion strength.

TABLE 13

SHEAR TEST VALIDATION RESULTS

A

Substrate		MILD STEEL				ALUMINIUM			
	W	W = 10mm		W = 5mm		W = 10mm		W = 5mm	
Coating	t	Av shear strength (Tonnes)	Av shear stress (MPa)	Av shear strength (Tonnes)	Av shear stress (MPa)	Av shear strength (Tonnes)	Av shear stress (MPa)	Av shear strength (Tonnes)	Mean shear stress (MPa)
CARBON STEEL	t=4 (mm)	9.7	119.1	5.7	139.4	4.7	57.2	2.7	67.3
	t=2 (mm)	8.7	106.9	5.8	143.3	3.9	48.1	2.5	60.6
ZINC	t=4 (mm)	2.0	25.3	1.1	28.4	2.0	25.1	1.3	34.1
	t=2 (mm)	1.7	20.9	1.2	30.0	2.3	28.1	1.4	33.9
ALUMIN - IUM	t=4 (mm)	4.2	51.1	2.4	60.0	3.5	43.1	1.9	51.4
	t=2 (mm)	4.3	52.0	2.2	36.0	3.8	47.1	2.0	50.1
Al-BRONZE	t=4 (mm)	6.8	84.0	4.3	105.0	6.0	73.8	3.4	85.0
	t=2 (mm)	6.1	74.6	3.7	91.7	5.5	68.0	2.5	61.5

B

Collar Dimension (mm)	Average % Error (Range/mean) x 100
10 x 4	25%
10 x 2	19%
5 x 4	38%
5 x 2	18%

Fractography studies revealed that for each of the materials deposited onto a mild steel substrate, fracture occurred through the coating near to the interface, as illustrated in Fig. 65. For the aluminium substrate, fracture occurred (in most cases) at the interface, with partial failure through the substrate with deposits of steel and aluminium bronze; fracture was through the coating with deposits of aluminium and zinc.

4.4.2 Main Study

Shear adhesion strength and circumferential residual stress results obtained from the engineering steel deposits are recorded in Appendix V. These results are summarised and illustrated in a graphical form, see Figs. 66 to 75.

Tensile circumferential residual stresses were found to be present in all coatings examined, whatever the deposition conditions. The most highly stressed coatings were of 60E, closely followed by 30E. Coatings of 65E generally gave very low levels of tensile residual stress and under many deposition conditions the conclusion was that the coating was unstressed.

It is apparent that a decrease in range or increase in deposition rate generally increases both the adhesion strength and the residual stress in a coating. A reduction in atomising pressure or increase in arc voltage has the same effect. In the majority of shear test pieces fracture occurred at the interface, however in certain cases, which involved spraying

FIGURE 65 : Cohesive failure, aluminium bronze coating/mild steel substrate

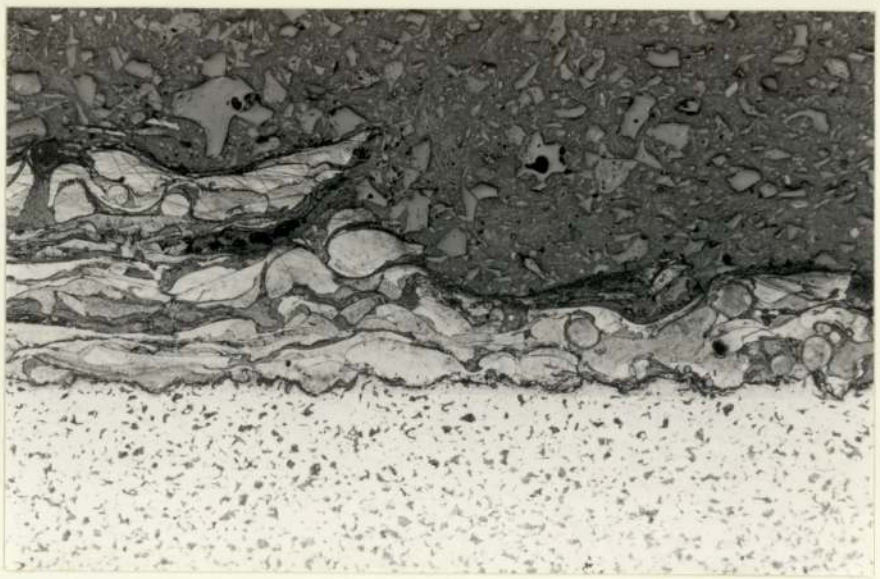

FIGURE 66 Relationship between shear adhesion strength and spraying distance of 30E coatings at deposition rates of 1.4 - 4.2 x 10^{-3} Kg s^{-1}

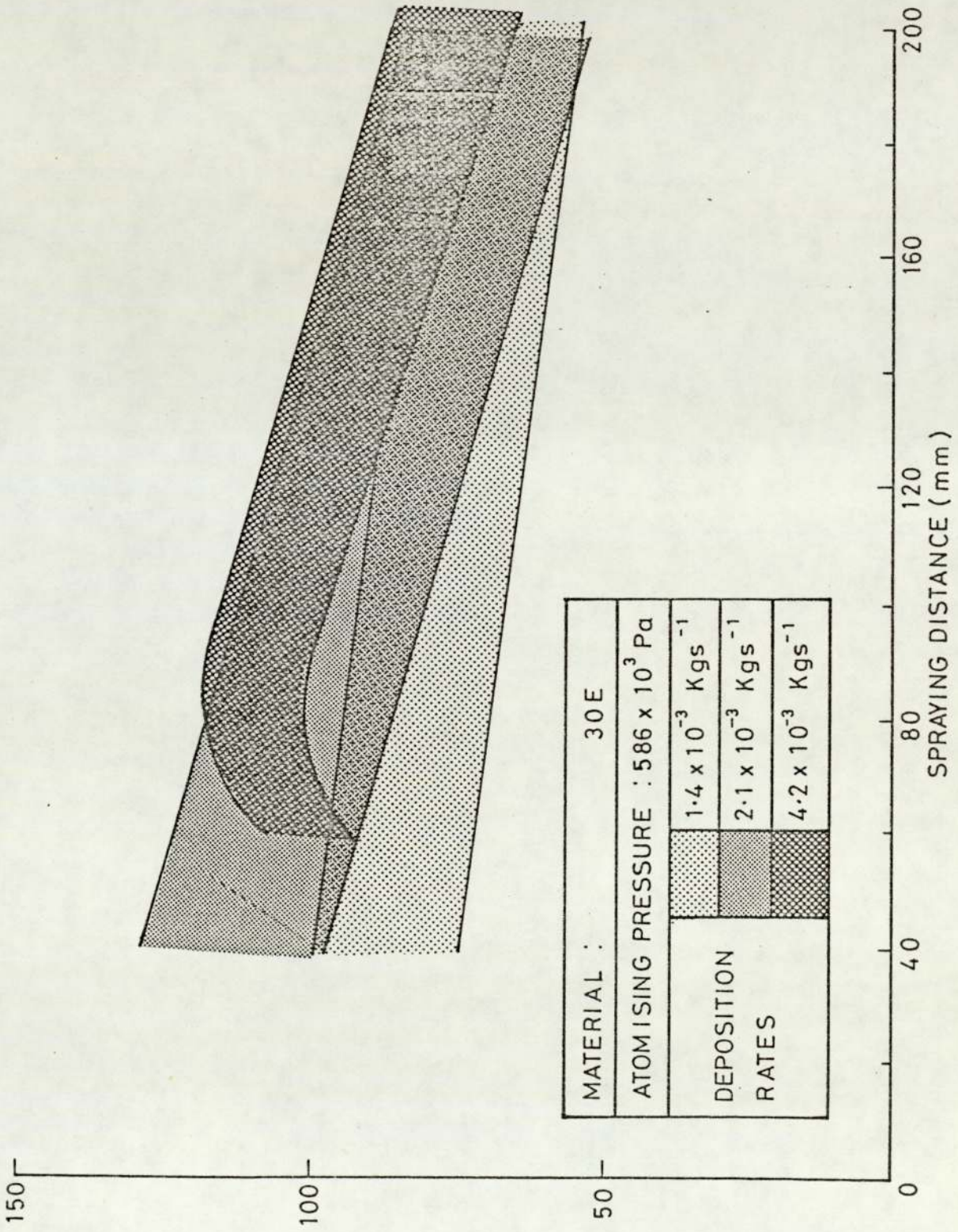

FIGURE 67 Relationship between circumferential residual shrinkage stress and spraying distance of 30E coatings at deposition rates of 1.4 - 4.2 x 10^{-3} Kg s^{-1}

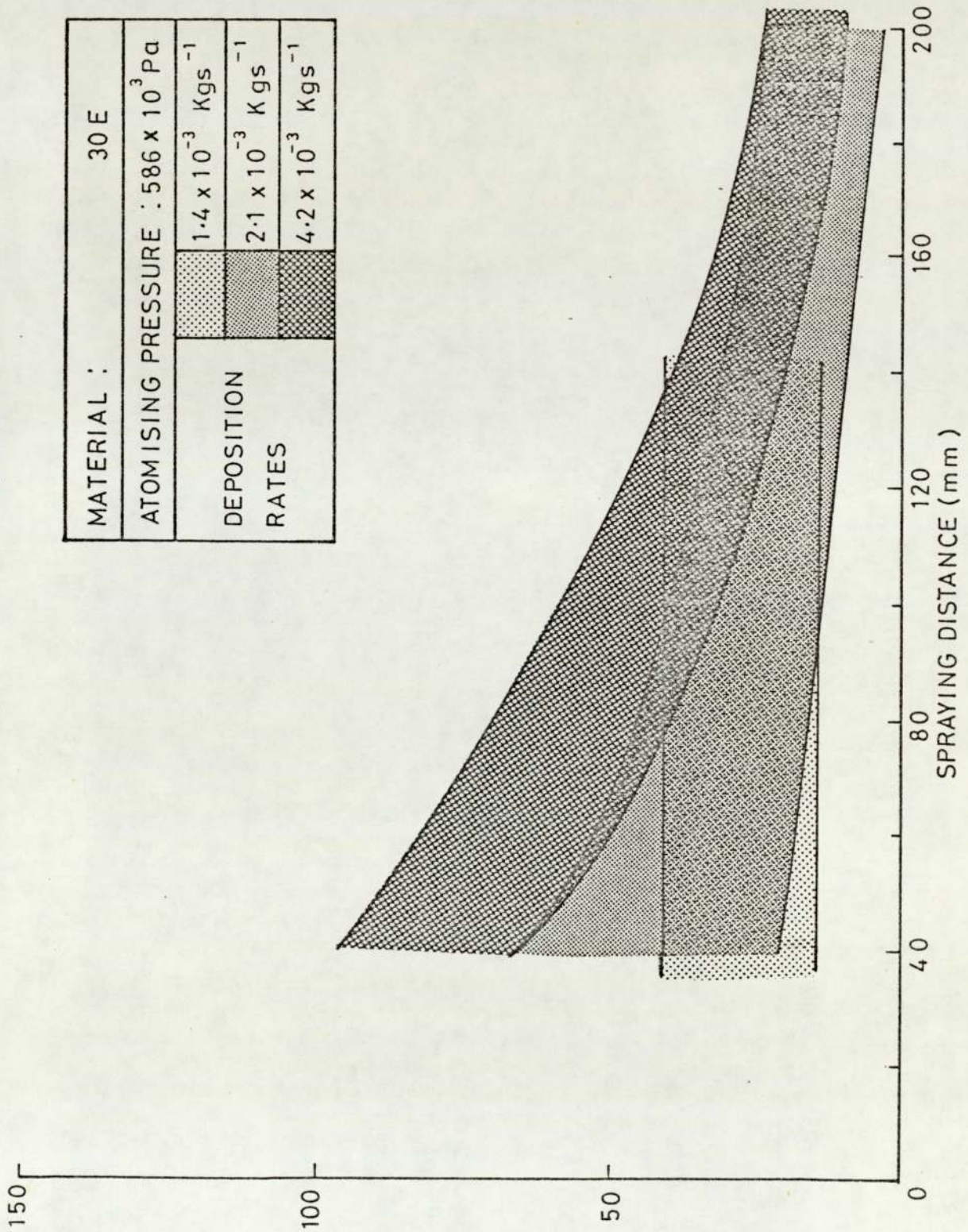

FIGURE 68 Relationship between shear adhesion strength and spraying distance of 60E coatings at deposition rates of $1.4 - 4.2 \times 10^{-3}$ Kg s^{-1}

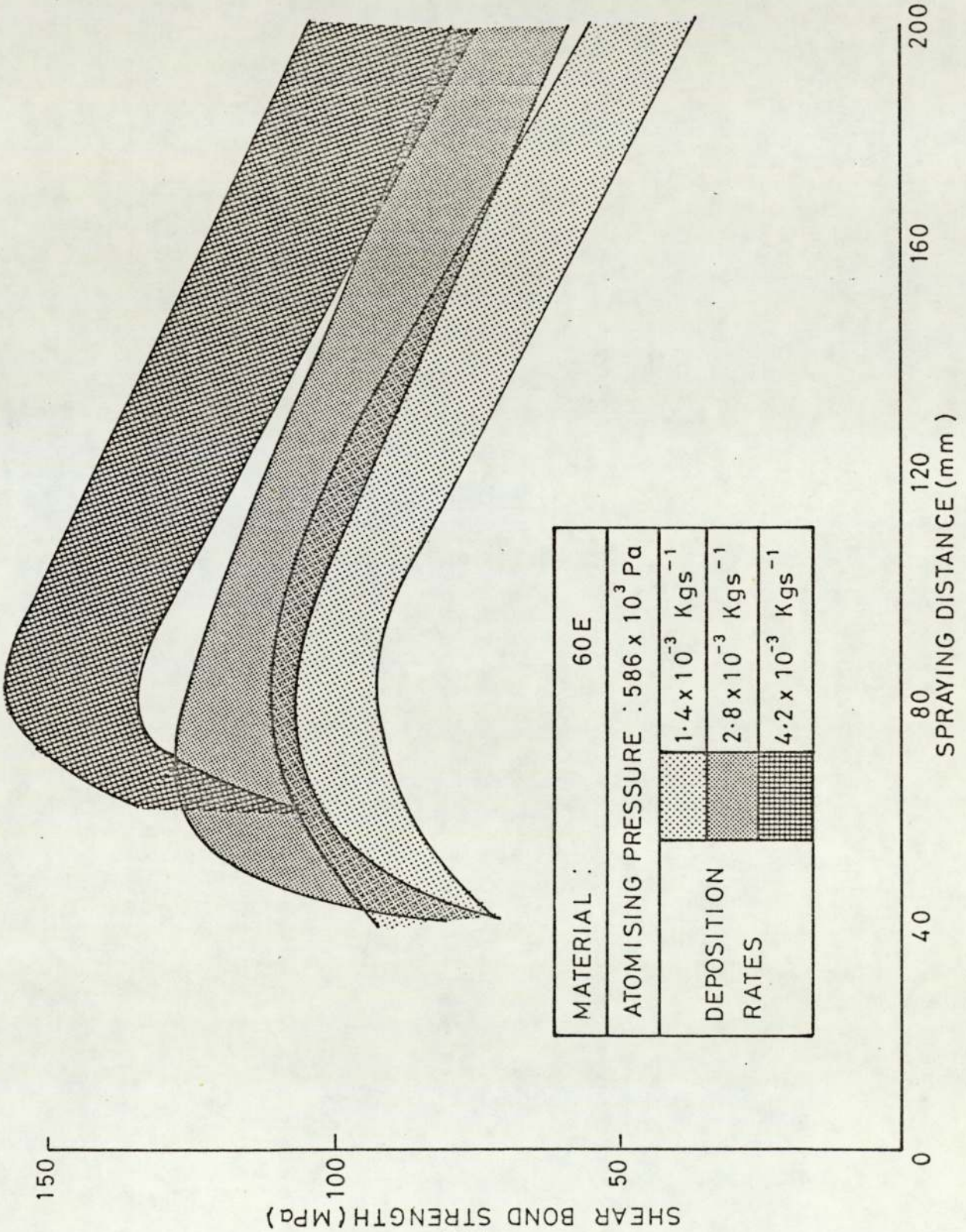

FIGURE 69 Relationship between circumferential residual shrinkage stress and spraying distance of 60E coatings at deposition rates of 1.4 - 4.2 x 10^{-3} Kg s^{-1}

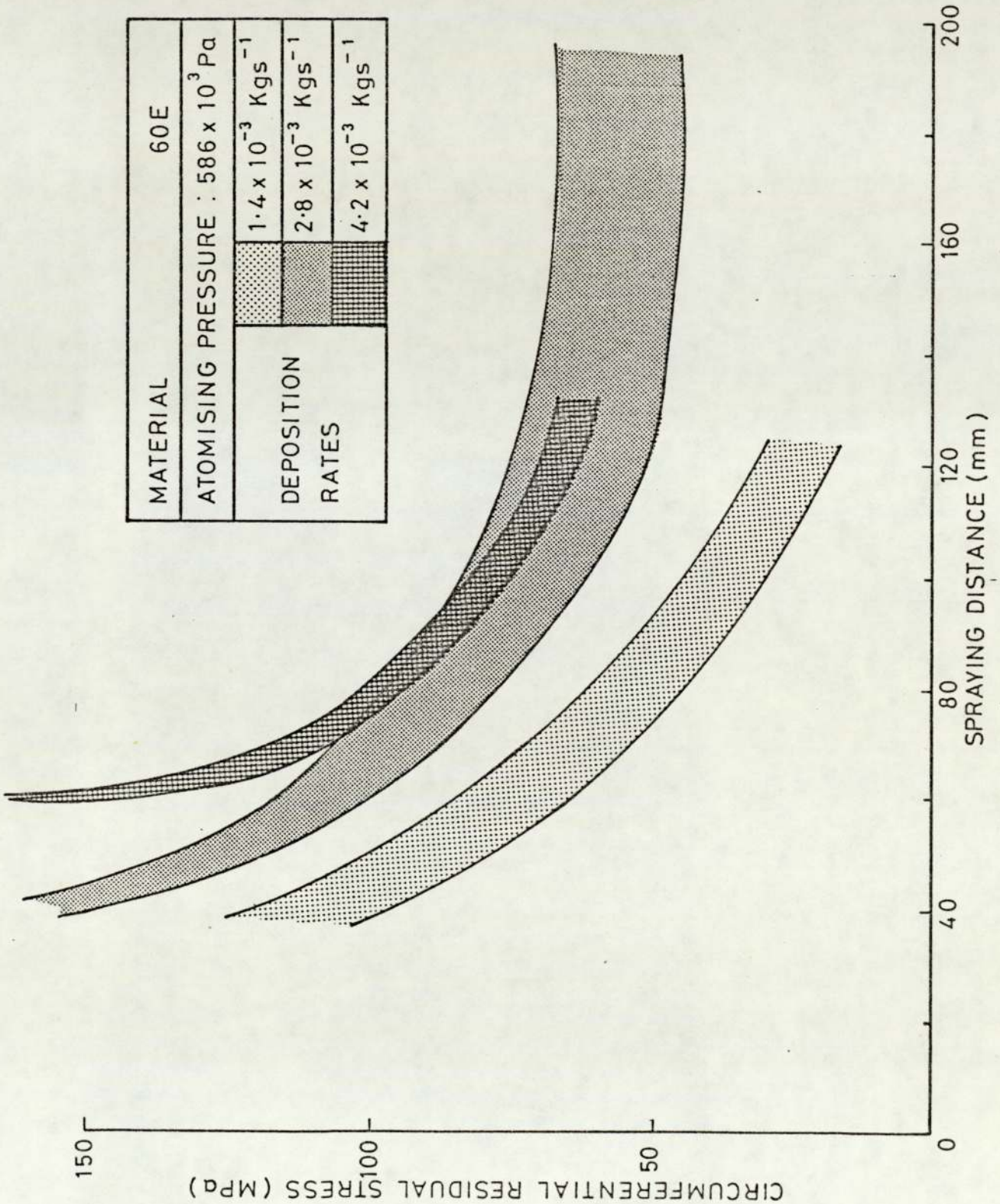

FIGURE 70 Relationship between shear adhesion strength and spraying distance of 65E coatings at deposition rates of 1.4 - 4.2 x 10^{-3} Kg s^{-1}

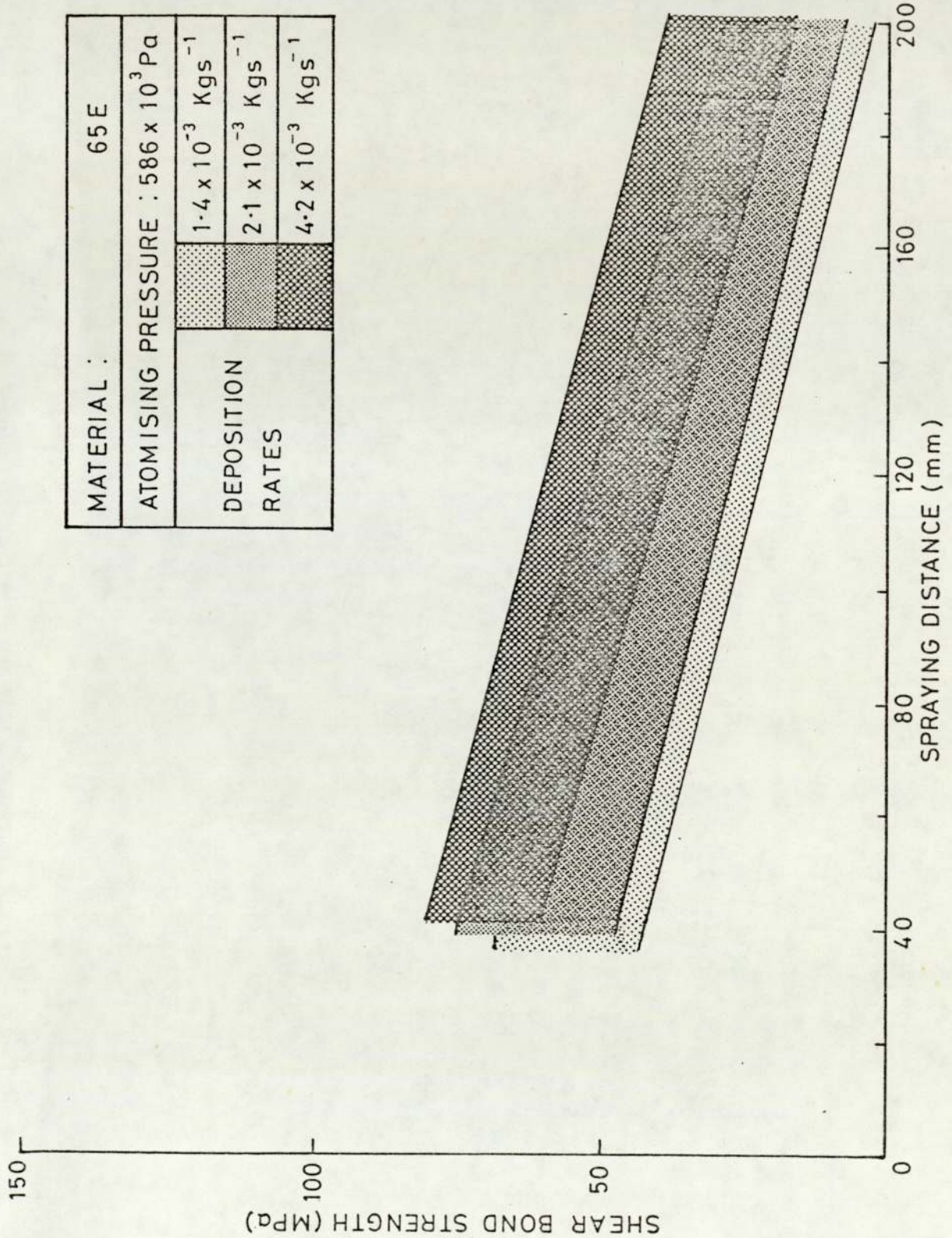

FIGURE 71 Relationship between circumferential residual shrinkage stress and spraying distance of 65E coatings at deposition rates of 1.4 - 4.2 x 10^{-3} Kg s^{-1}

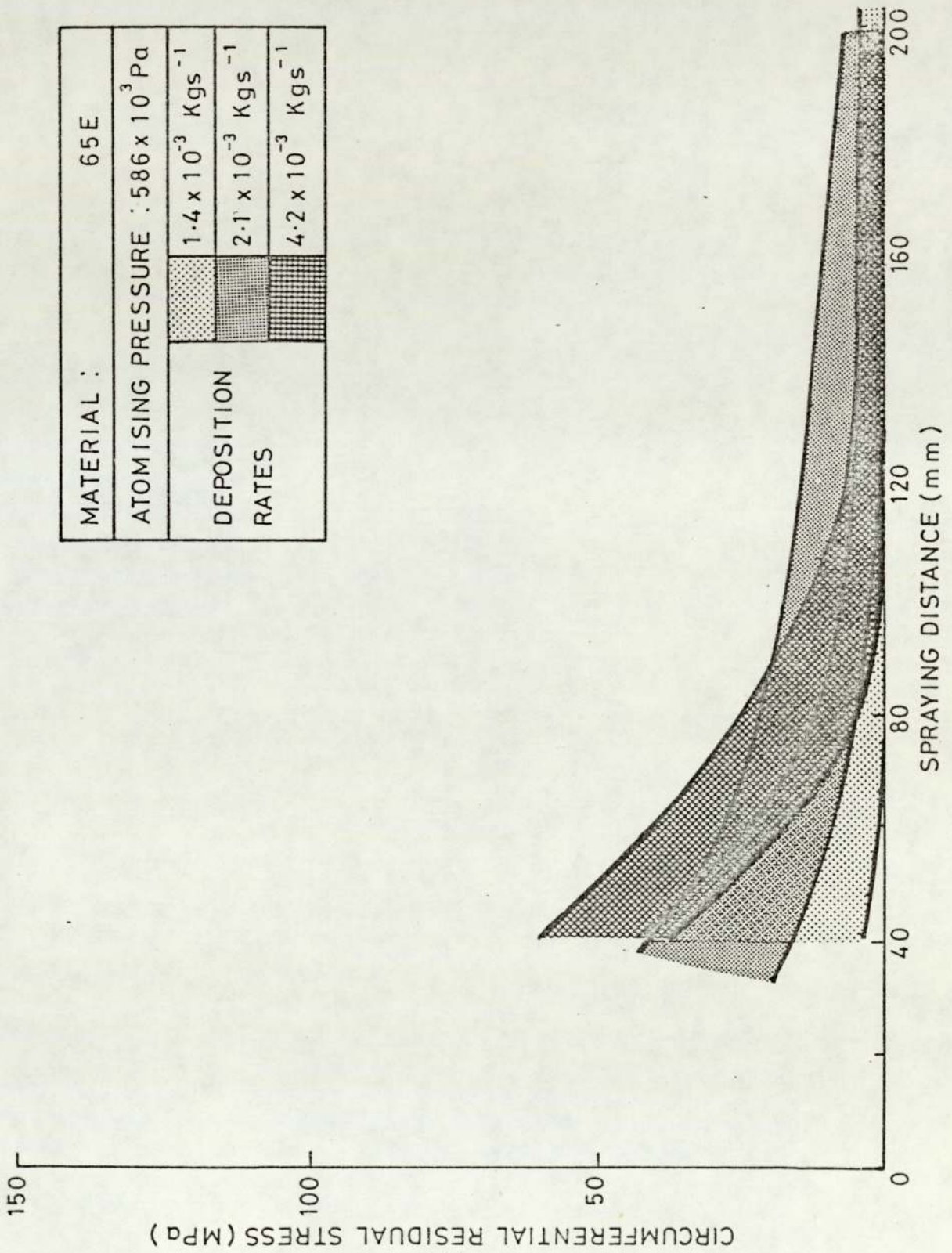

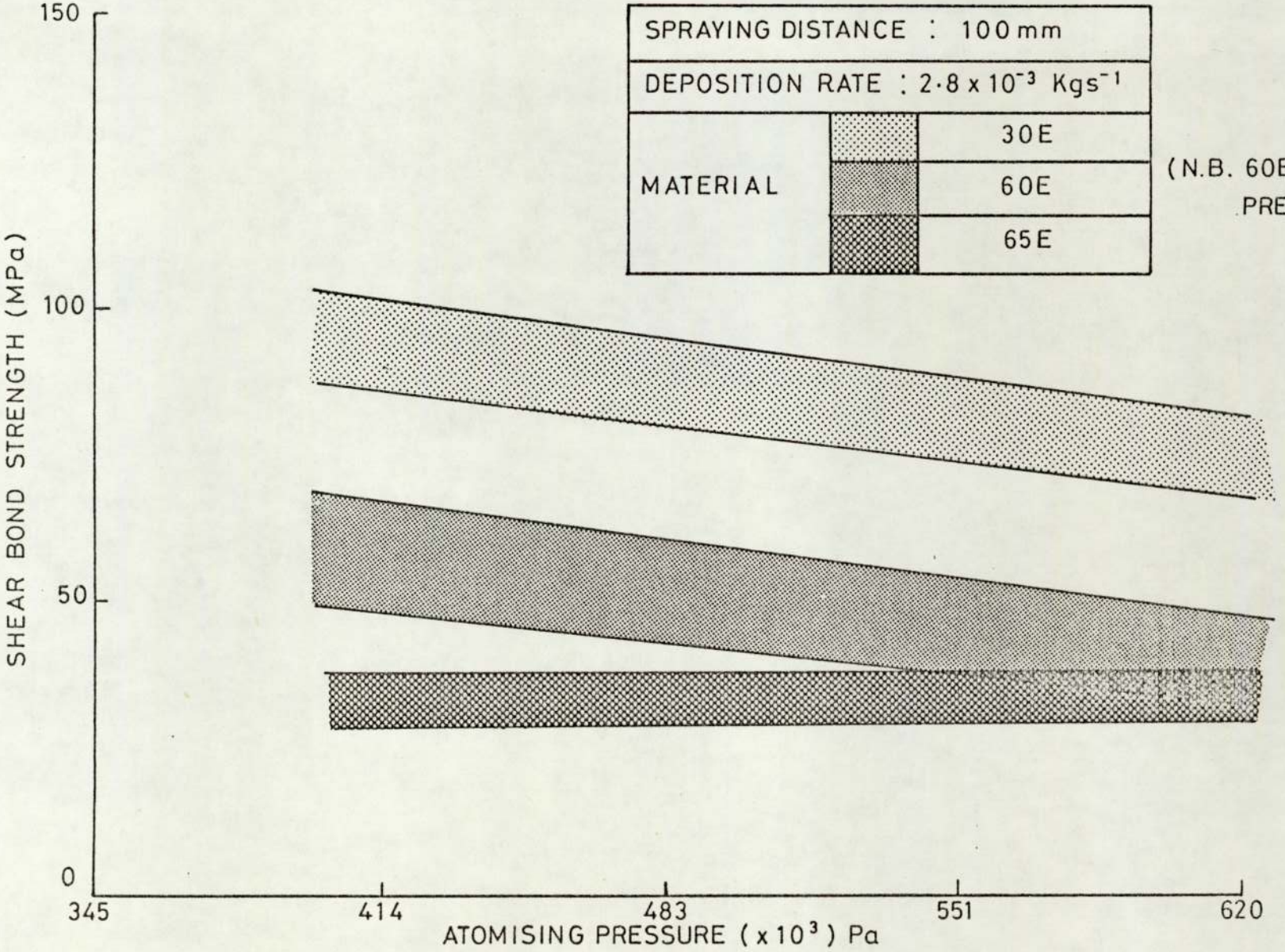

FIGURE 72 Relationship between shear adhesion strength and atomising pressure of 30E, 60E and 65E coatings

FIGURE 73 Relationship between circumferential residual shrinkage stress and atomising pressure of 30E, 60E and 65E coatings

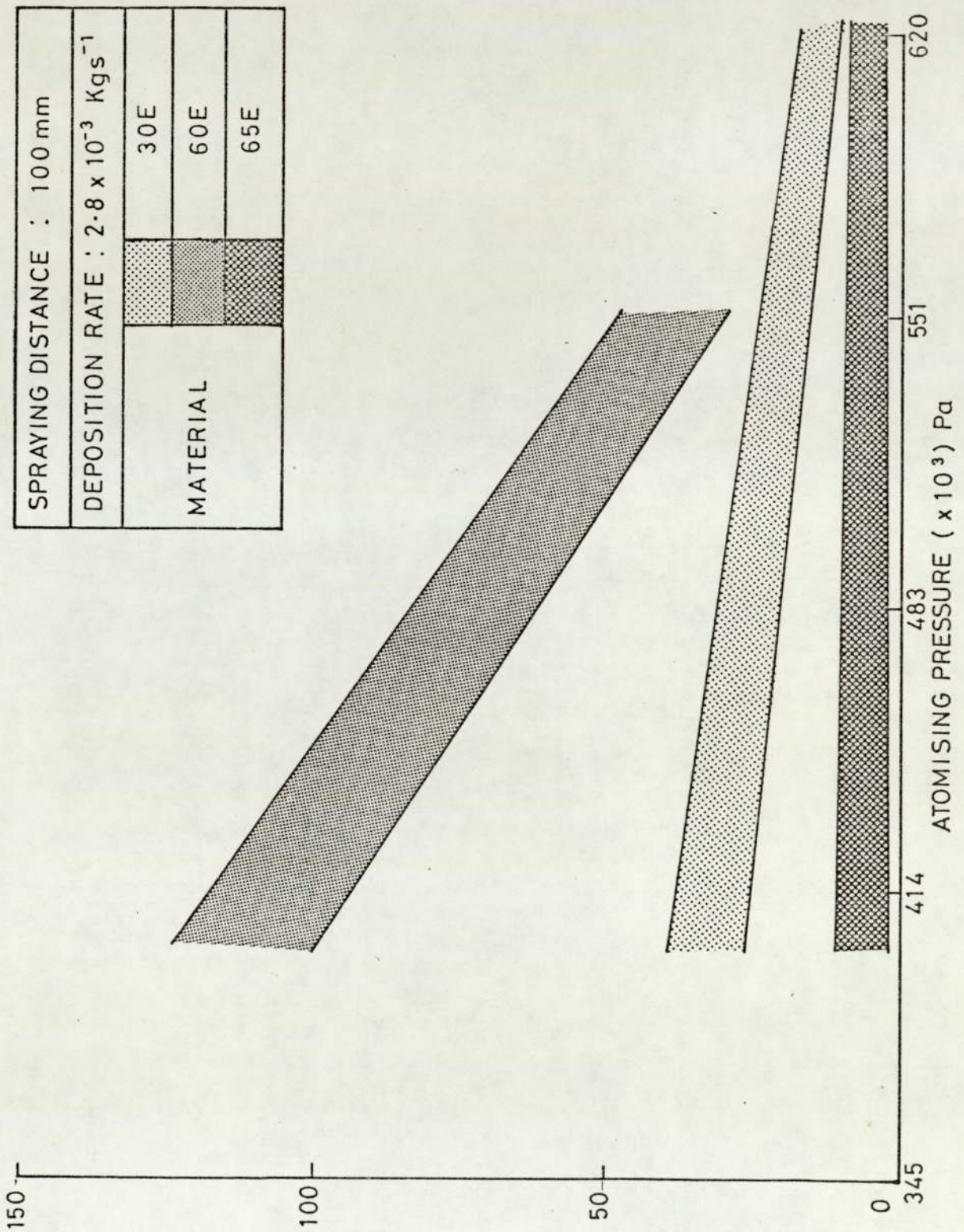

FIGURE 74 Relationship between shear adhesion strength and arc voltage of 30E, 60E and 65E coatings

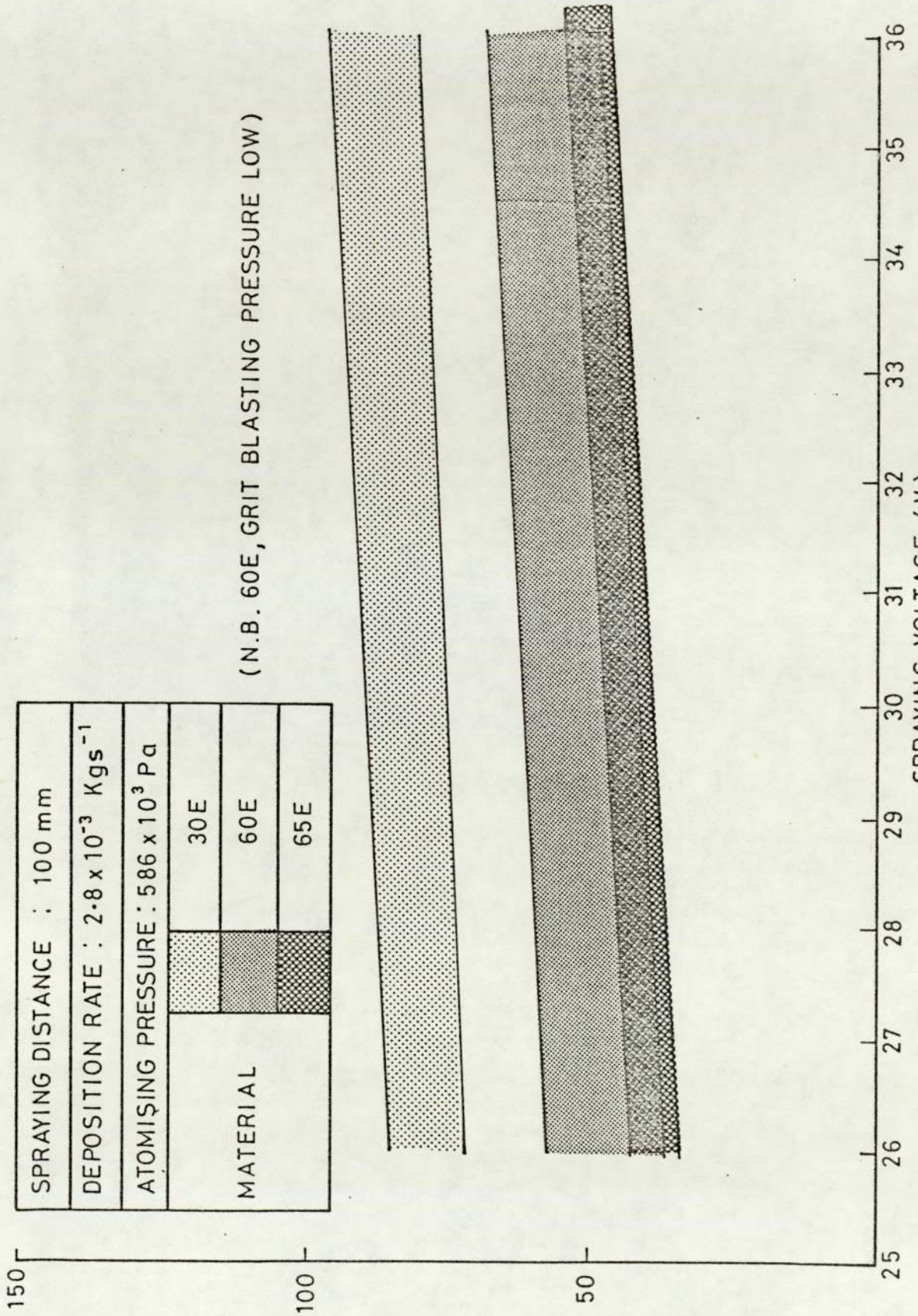

FIGURE 75 Relationship between circumferential residual shrinkage stress and arc voltage of 30E, 60E and 65E coatings

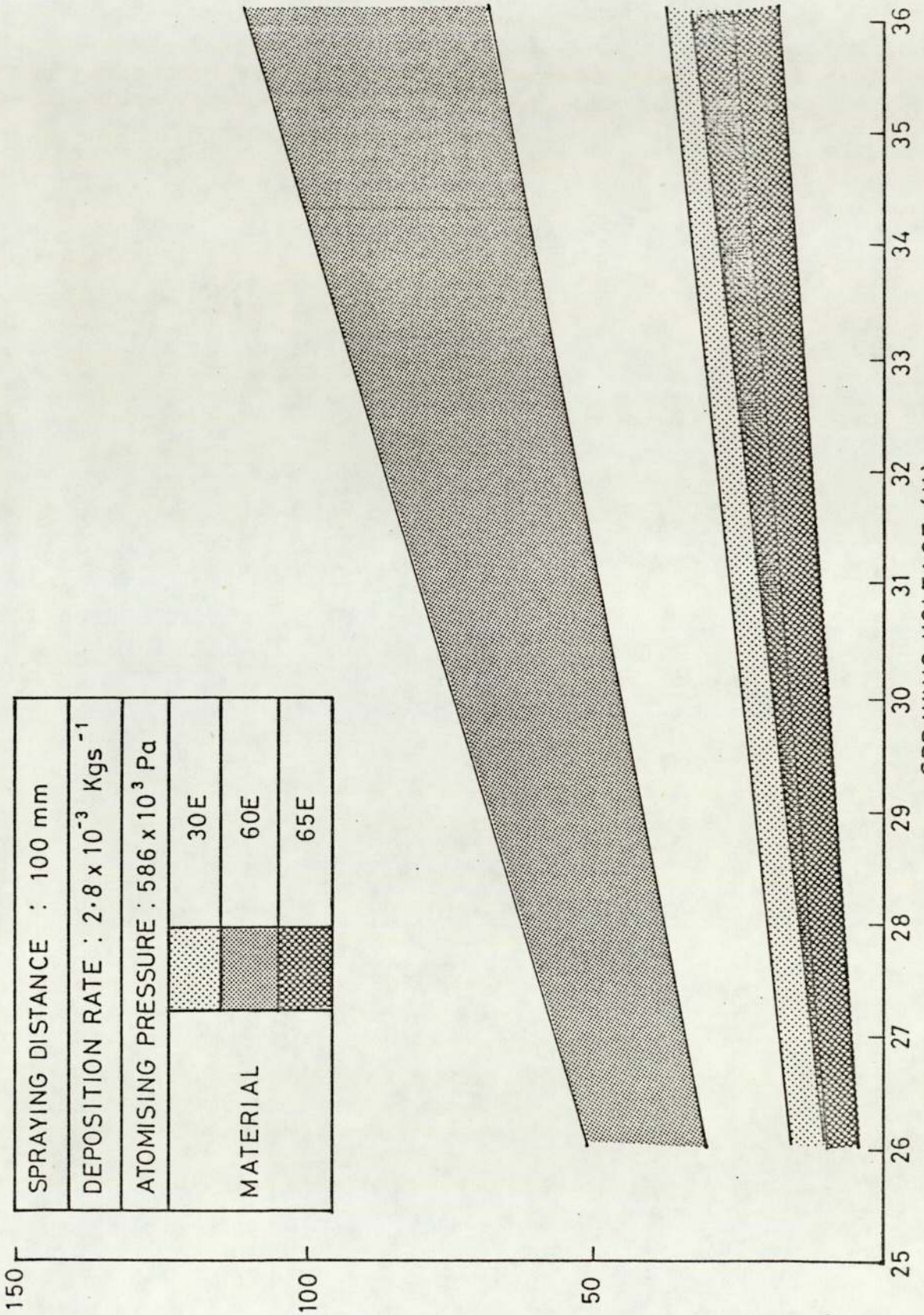

parameters which induced large residual stresses, fracture moved to a position some distance within the coating, see Figs. 76 and 77. This was accompanied by a reduction in adhesion strength, as exhibited by both 60E and 30E coatings, see Figs. 66 and 68.

Fracture, when cohesive, generally propagated by an inter-lamellar rather than trans-lamellar mechanism. This mode of fracture was also observed in tensile specimens, see Fig. 78, metallic lamellae appear to have been plucked from surrounding lamellae or oxide.

In the control testpieces, which had received a stress relieving heat treatment, no significant level of residual stress was detected, thus endorsing the testing technique, the results are presented in Appendix VI.

4.5 Fracture Stress and Young's Modulus

Tensile elastic modulus and tensile fracture stress results for 30E and 65E are presented in Table 14. The mean values are presented in Table 15, and include data obtained by Farrow [67] for 60E, for comparative purposes.

The low carbon steel (30E) exhibits the highest modulus followed by 60E then 65E. The tensile strength of 30E is the highest followed by 65E then 60E.

FIGURE 76 : Adhesive Failure During Shear Testing

A

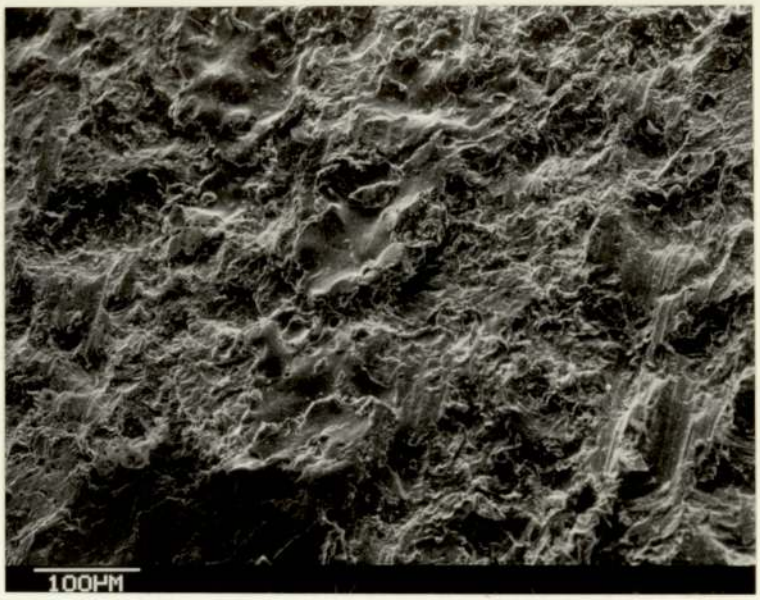

B

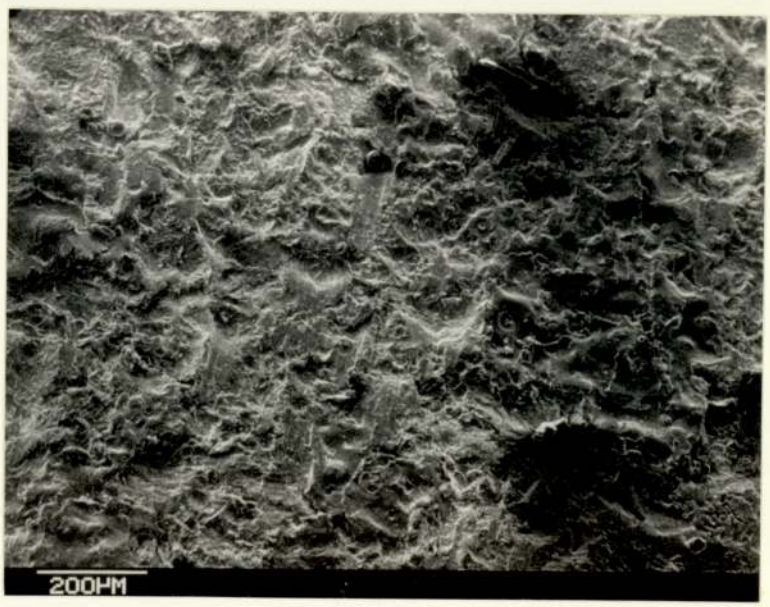

FIGURE 77 : 60E, Cohesive Failure During Shear Testing

A

B

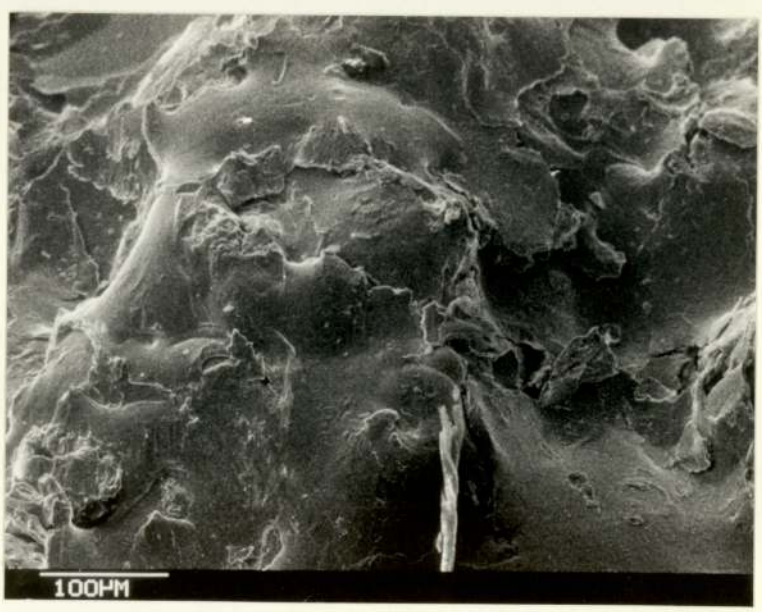

FIGURE 78 : Fracture Face : Tensile Specimen

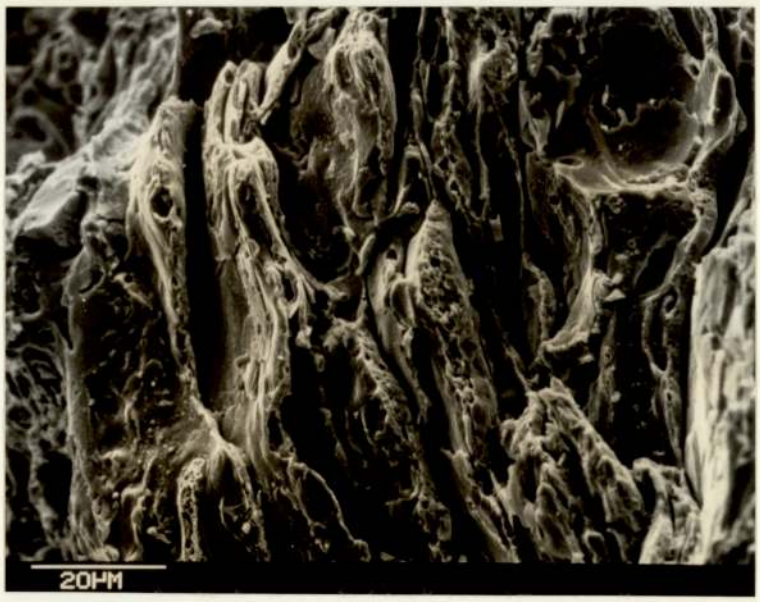

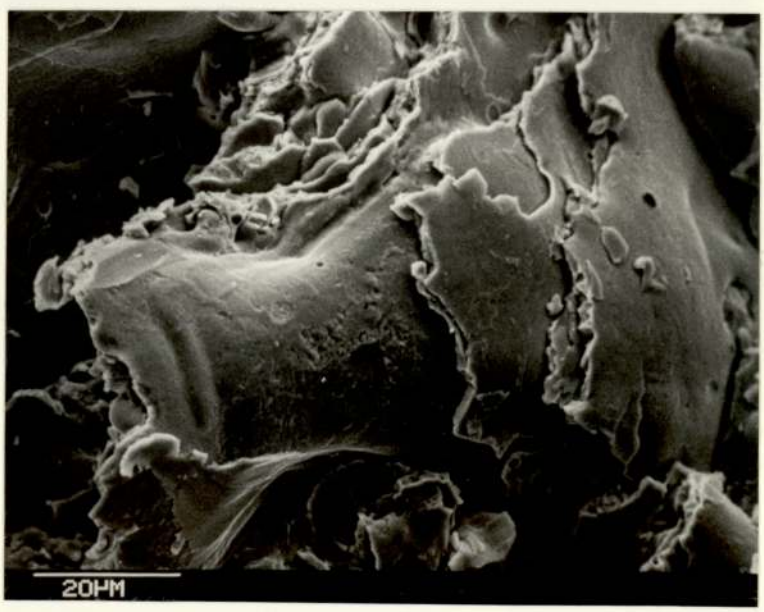

TABLE 14

ELASTIC MODULUS AND FRACTURE STRENGTH FOR 30E AND 65E

Test-piece	E Strain gauge No.1 (GPa)	E Strain gauge No.2 (GPa)	Fracture stress (MPa)
30E No. 1	118	121	203
30E No. 2	120	118	205
30E No. 3	122	122	232
65E No. 1	90	94	187
65E No. 2	87	90	191
65E No. 3	104	93	167

TABLE 15

MEAN VALUES OF ELASTIC MODULUS AND FRACTURE STRENGTH FOR 30E, 60E AND 65E

Material	E (GPa)	σ_F (MPa)
30E	120	213
60E [67]	113	171
65E	93	182

4.6 Hardness

The results of surveys to determine the influence of spraying parameters on the macro-hardness of 30E, 65E and 60E coatings are presented in Tables 16 and 17.

In general, 60E exhibited macro-hardness which increased with increase in spraying distance and atomising pressure, and decrease in spraying voltage. These trends, however, were not as pronounced in 30E and 65E deposits.

The micro-hardness ranges of selected individual oxide and metallic lamella within each of the deposits, are presented in Table 18. Generally the micro-hardness of the lamellae remained relatively constant and was unrelated to spraying conditions. A lowering of micro-hardness was experienced however when using spraying conditions which involved small spraying distances, high voltages or low atomising pressures, see Fig. 79. This was reflected in macro-hardness, Figs. 80 to 83.

TABLE 16

MACRO-HARDNESS VARIATION OF 30E, 60E AND 65E COATINGS WITH DEPOSITION RATE AND SPRAYING DISTANCE

	DEPOSITION RATE ($Kg\ s^{-1}$)					
	1.4×10^{-3}		2.1×10^{-3}		4.2×10^{-3}	
Material	Sp.Dist. (mm)	$Hv_{30\ kg}$	Sp.Dist. (mm)	$Hv_{30\ kg}$	Sp.Dist. (mm)	$Hv_{30\ kg}$
30E	40	242	40	234	60	236
30E	80	256	80	277	100	260
30E	125	250	100	267	165	252
65E	45	300	40	249	65	252
65E	125	342	60	295	125	330
65E	195	344	195	320	195	323
60E	40	301	40	225	80	274
60E	60	298	125	300	125	302
60E	195	327	195	333	195	325

Controlled conditions:

Arc Voltage : 26-30 v

Atomising Pressure : 586×10^3 Pa

TABLE 17

MACRO-HARDNESS VARIATION OF 30E, 60E AND 65E COATINGS WITH ARC VOLTAGE AND ATOMISING AIR PRESSURE

Material	Voltage (v)	$Hv_{30\ kg}$	Atomising Pressure (Pa)	$Hv_{30\ kg}$
30E	29/25	261	586×10^3	261
30E	34/30	254	483×10^3	260
30E	40/36	238	414×10^3	255
65E	29/26	303	586×10^3	303
65E	34/30	296	483×10^3	256
65E	40/36	297	414×10^3	247
60E	29/26	318	551×10^3	287
60E	34/30	246	483×10^3	240
60E	40/35	217	414×10^3	224

Controlled conditions:

Spraying distance : 100 mm

Deposition Rate : 2.8×10^{-3} Kg s^{-1}

TABLE 18

MICRO-HARDNESSS RANGE OF OXIDE AND METALLIC LAMELLAE OF 30E, 60E AND 65E COATINGS

Material	Lamella Type	Hardness Range ($Hv_{100\ g}$)
30E	Metallic	260-420
30E	Oxide	270-490
65E	Metallic	560-760
65E	Oxide	610-660
60E	Metallic	400-660
60E	Oxide	780-1006

FIGURE 79 Variation of micro-hardness of metallic lamellae of 60E coating with spraying distance

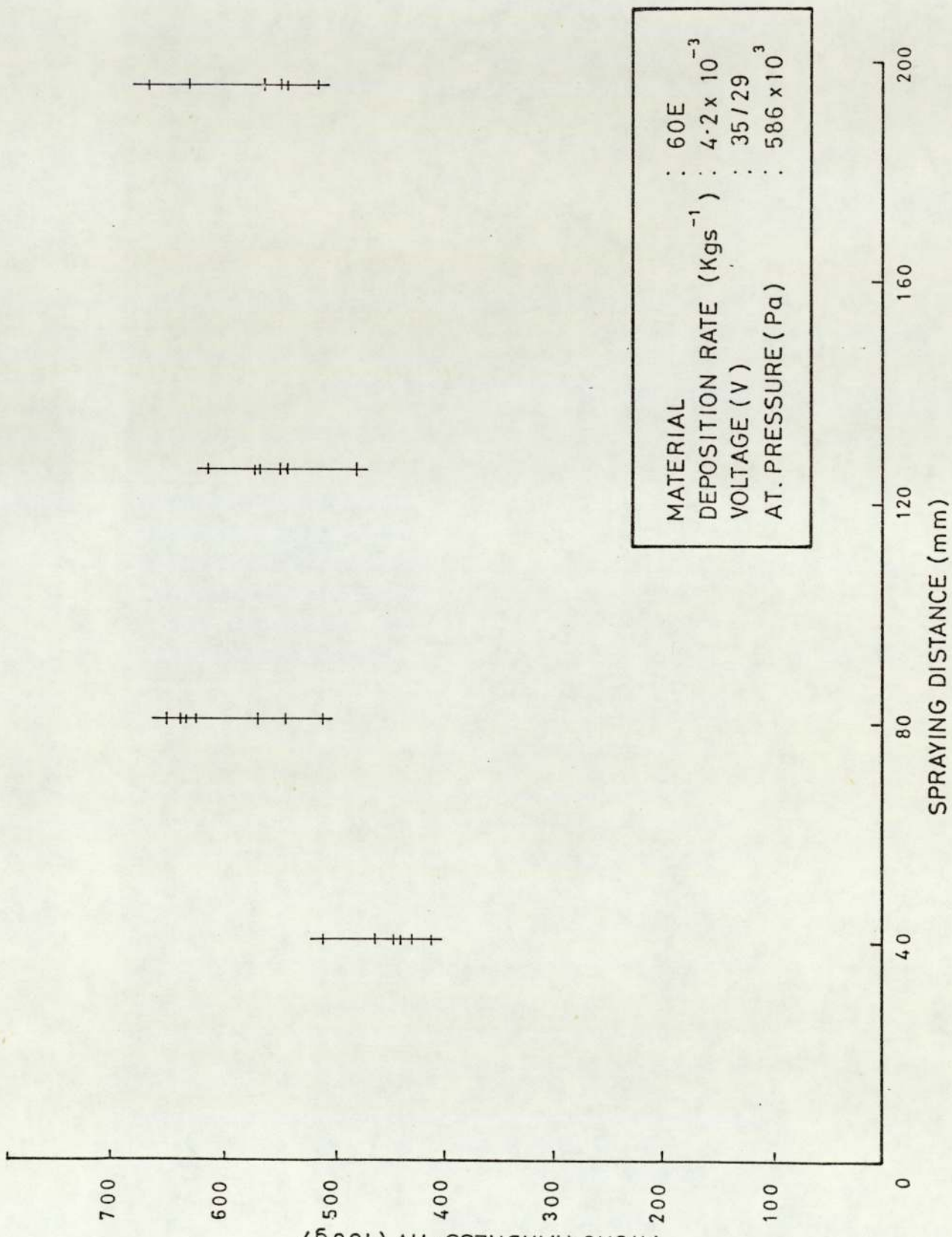

FIGURE 80 Variation of macro-hardness of 30E coatings with spraying distance

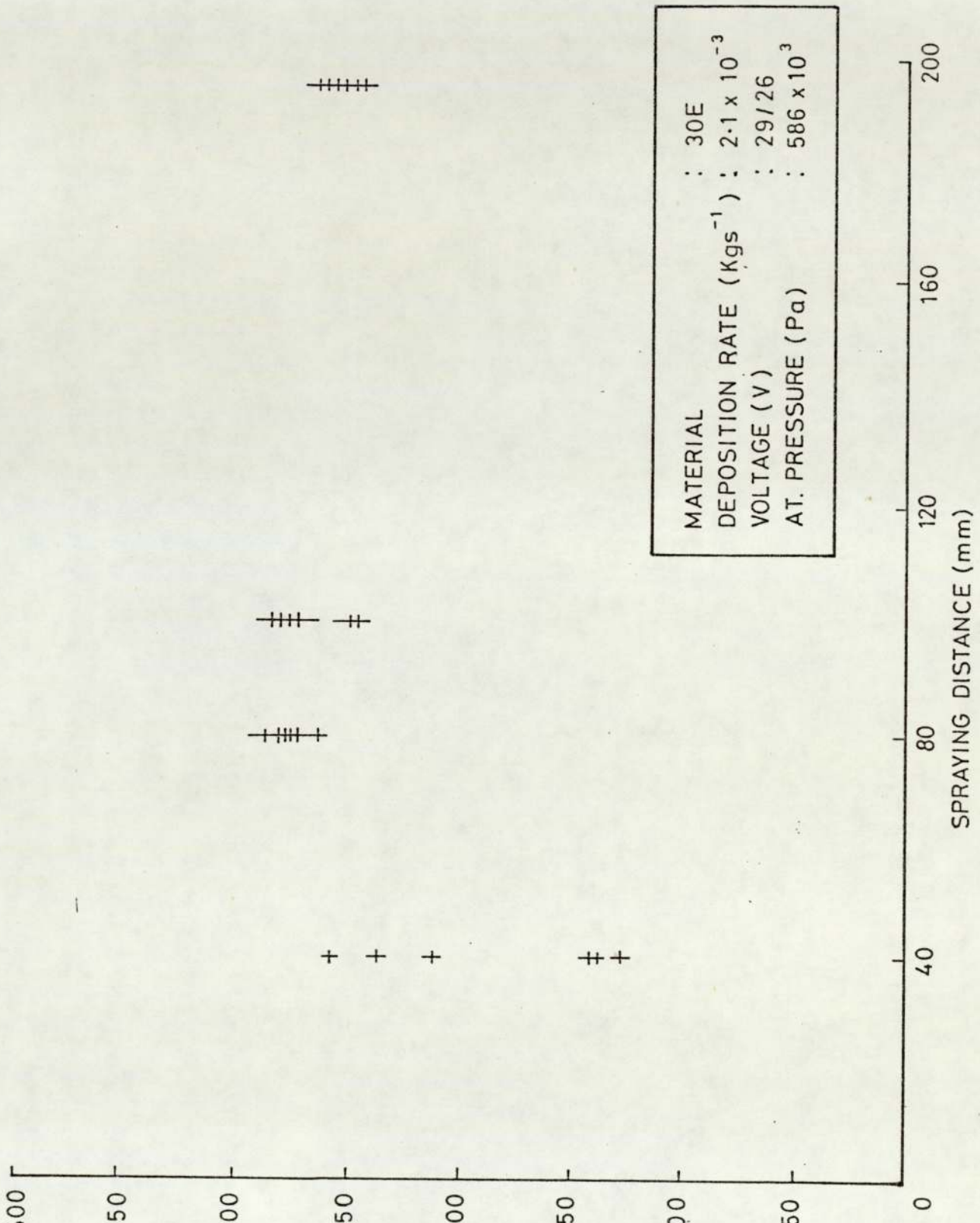

FIGURE 81 Variation of macro-hardness of 60E coating with spraying distance

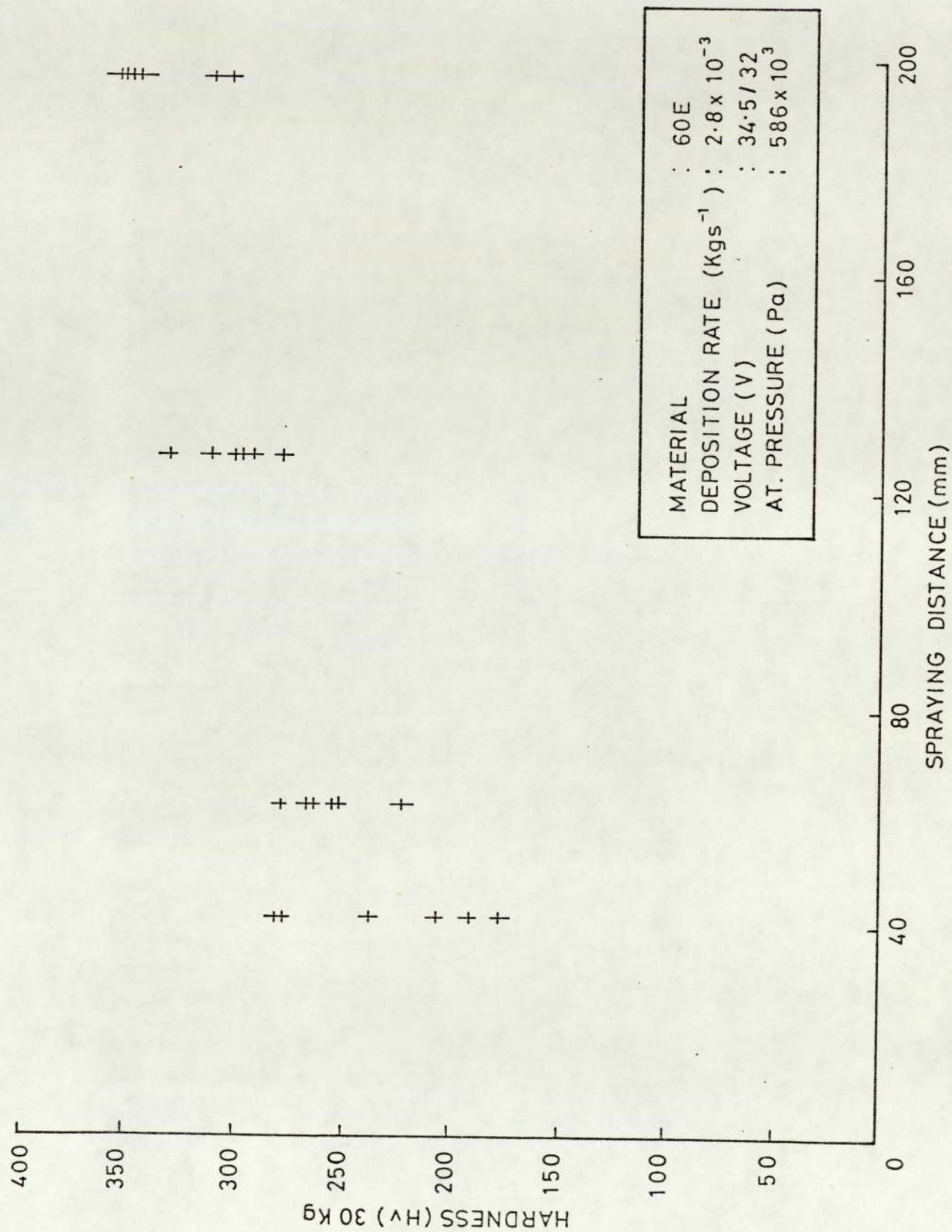

FIGURE 82 Variation of macro-hardness of 60E coating with atomising pressure

FIGURE 83 Variation of macro-hardness of 60E coating with arc voltage

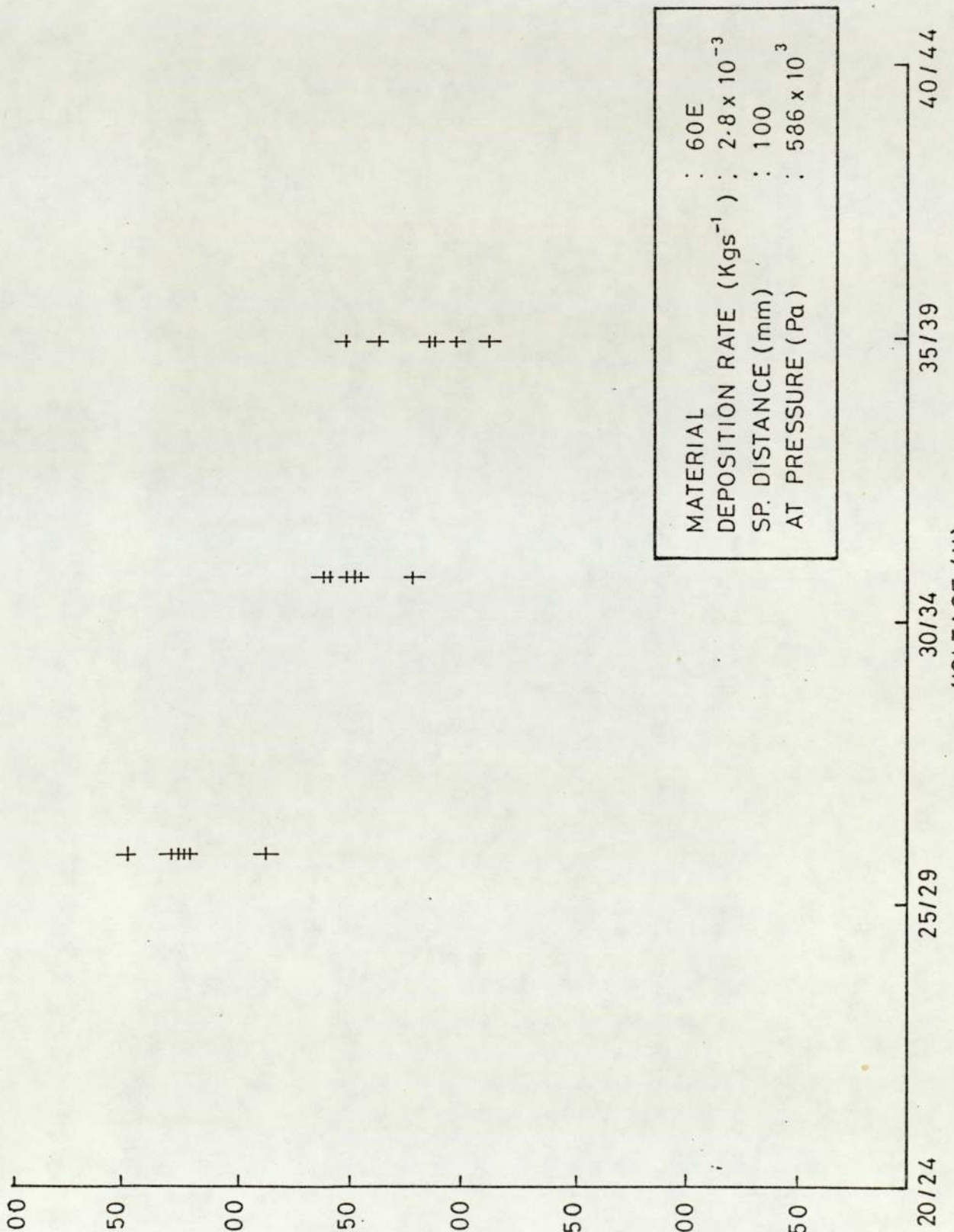

CHAPTER V - DISCUSSION

5.1 Coating Structure

The major feature of the microstructure of each steel was the fine-grained metallic lamellae separated by oxide lamellae, porosity and fissures. At higher magnifications of examination, the metallic lamellae were seen to contain finely dispersed oxides, nitrides and, in the case of chromium containing steels, chromium carbides. The carbides and nitrides, however, were difficult to resolve at magnifications up to x840. In the "as sprayed" form the oxides within metallic lamellae appeared as greyish/black specks or globules at high magnifications under an optical microscope.

Optical metallography of 30E revealed a fine-grained, mainly ferritic structure in the metallic lamellae, see Figs. 33A-D. Micro-hardness however was appreciably higher than would normally be expected for "equilibrium" ferrite. The unexpected micro-hardness of between 250 and 420 Hv is probably a consequence of the very small grain size, a conservative estimate is 0.5-5 μm, and the presence of low-carbon martensite.

Hall [102] and Petch [103] have shown that the tensile yield or flow stress of polycrystalline iron is related to grain diameter (d) by a linear relationship, of the form:-

$$\sigma_t = \sigma_{o,f} + k_f d^{-\frac{1}{2}} \qquad .....(1)$$

The variation of hardness (H) with grain diameter has also been shown to be represented by a similar equation (1) [104-107], the Petch equation:

$$H = H_o + k_H d^{-\frac{1}{2}} \qquad .....(2)$$

provided the hardness indentation is large enough to cover many grains.

Inokuti et al [108] examined the effect of solidification rates on the structure and hardness of iron which had approximately the same carbon content as 30E after deposition. Their results indicated that the critical cooling rate for the formation of martensite was 2×10^5 K s^{-1}. The hardness varied from 250-700 Hv, from a totally ferritic to a totally martensitic structure. Hardness data for solid state quenched ferrite-Fe [109,110], splat quenched ferrite-Fe [108] and splat quenched martensite [108] all obey the same Hall-Petch equation, as shown in Fig. 84. Grain sizes of 3-5 μm and martensite plate width of 0.3 - 0.5 μm were observed.

Certainly the cooling rates encountered in the spraying process which have been reported to be 10^4 - 10^7 K s^{-1}, see Section 2.4.3, are sufficient for the formation of low carbon martensite in 30E composition steel. Similar grain sizes were observed in all coatings and when related to hardness, also fit the Hall-Petch relationship.

The amount of nitrogen in solid solution, as explained in greater detail at a later stage, is expected to be high. This is another factor which may contribute to the hardness of metallic lamellae. Nitrogen in solution has been shown by a number of workers [111-113] to have a deleterious effect on the ductility of steel, by increasing hardness.

FIGURE 84 Hall-Petch plot/Iron

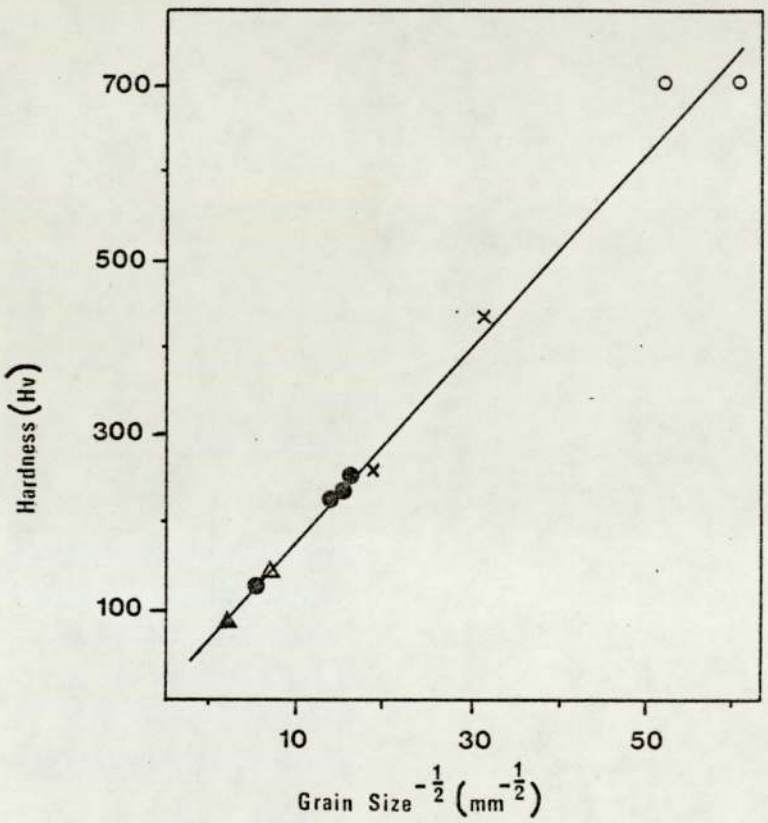

o splat quenched martensite (108)

● splat quenched ferrite (108)

△ solid quenched (109)

▲ solid quenched (110)

× arc sprayed 30E

Tschischewski [111] produced the diagram shown in Fig. 85, which illustrates the influence of nitrogen on the physical properties of steel. It is shown that increase in nitrogen increases the hardness and reduces the ductility. In conclusion the high hardness of metallic lamellae is probably due to a combination of the fine-grained structure, the formation of low carbon martensite and the solid solution hardening effect of nitrogen.

Annealing of selected samples of each composition of coating, using the treatments outlined in Section 2.6, generally promoted grain growth and the coalescence of lamellar oxides into a more spherical form, see Figs. 36-39. Specific to 30E coatings, however, was the formation and growth of iron nitride needles (Fe_4N) as the excess nitrogen came out of solid solution. Iron nitride at medium magnifications exhibited a fine acicular structure , Figs. 40-43. At higher magnifications, Fig. 44, the needles proved to be flattened crystals inclined at various angles to the sectioning plane. Koster [113] has shown that when nitrogen exists in the form of precipitated needles, the loss of ductility is not very marked, however in solid solution it has a significant effect on the mechanical properties of steel.

Optical metallography of 60E revealed a ferritic/martensitic structure, see Fig. 34. The micro-hardness of metallic lamellae ranged from 400 to 660 Hv, this also is higher than expected. A quenched 13% Chromium, wrought, low carbon steel has been shown to develop a hardness of 430 Hv [114], Fig. 86. The increase is probably also a consequence of the fine grain size and the influence of nitrogen. Nitrogen forms Cr_2N and a content of

FIGURE 85 Influence of nitrogen on the physical properties of steel

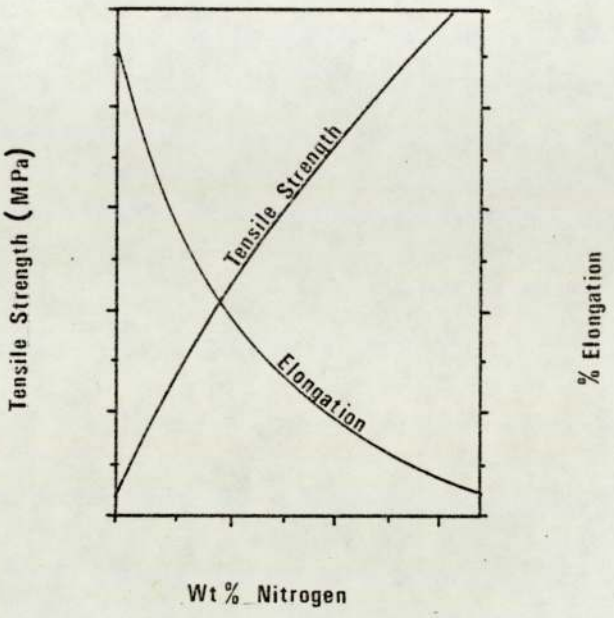

FIGURES 86 & 87 Effect of carbon and nitrogen on the tempering curve of a 12% Cr steel

FIGURE 86

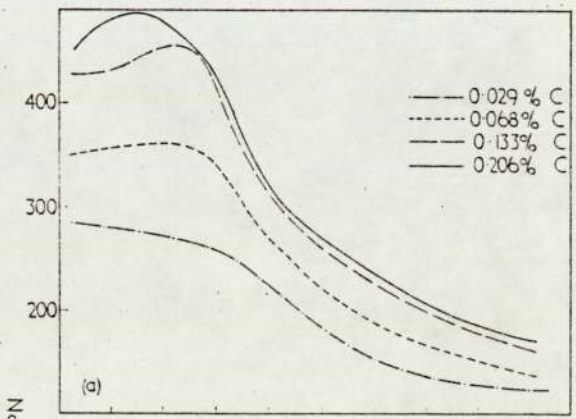

FIGURE 87

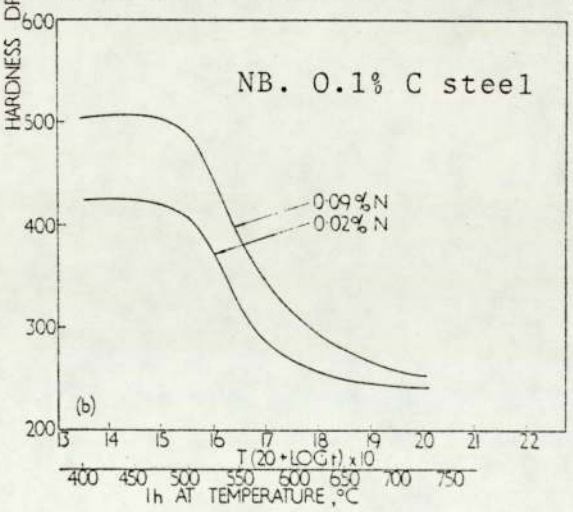

0.09 wt% has been shown to increase the hardness by 100 Hv [114], Fig. 87.

Optical metallography of 65E revealed a martensitic/austenitic structure. The formation of martensite and retention of austenite was not unexpected due to the soidification rates experienced and the high carbon content of the steel. The micro-hardness of metallic lamellae was in the range expected for an alloy martensite containing islands of retained austenite [115], 555-755 Hv, see Fig. 88. The volume fraction of austenite in a 65E coating was estimated to be 25% for a fixed set of spraying parameters. However, it is certain that the amount of austenite will vary with spraying parameters due to the direct influence on particle composition (in particular carbon content), size and thermal content and distribution.

X-ray diffractometry results endorse the findings from metallographic examination and hardness tests. A ferritic trace was produced for 30E, ferritic/martensitic for 60E, and martensitic/austenitic for 65E, Fig. 51. A number of reflections which could relate to oxides, nitrides and carbides were obtained, however identification of specific compounds proved difficult. In the majority of cases only the most intense line of the characteristic set of reflections was evident due to the small percentage of the particular compound present. Also in many instances the peaks were masked by coincidence with more intense peaks. Although individual compound identification was not possible, the nitrides observed in 60E and 65E coatings were probably of

FIGURE 88 The effect of alloying elements on the hardness of martensite

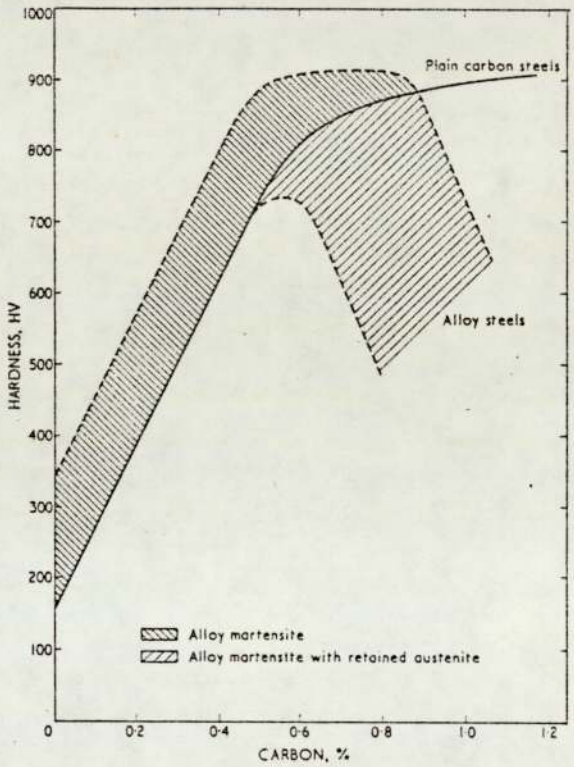

the type CrN, $(Cr, Fe)_2N$ which exist as fine particles which, even after annealing, are difficult to distinguish optically from the finely dispersed oxide particles, see Figs. 34 and 35.

Energy dispersive X-ray micro-analysis confirmed that the oxides in the coatings contained several, and varying amounts, of metallic elements, see Table 9. The oxides formed were complex and compositions of individual particles in a given coating differed considerably, especially in the more highly alloyed steels 60E and 65E. In all three types of coating typically 20-30% oxygen (determined by difference) was found in individual oxide particles. It seems likely that the oxides are spinels of manganese, iron and silicon in 30E with the added complication of the inclusion of chromium oxide in 60E and 65E.

Most of the oxide formed when spraying 30E is likely to be "straight" iron oxide due to the small amounts of other alloying elements present in the coating wires.

When iron is heated in air the formation of three types of oxide is possible, wüstite (FeO), magnetite (Fe_3O_4) and hematite (Fe_2O_3). Paidassi [116] and Pfeil [117,118] studied the oxidation of iron in the 970-1520 K region, the resultant oxide layers consisted mainly of FeO with some Fe_3O_4 and very little Fe_2O_3. However at temperatures below 840 K FeO, which was formed at a higher temperature, is unstable and decomposes to Fe_3O_4 and iron (Fe). This decomposition may however be influenced by the cooling rates experienced in the spraying process, as shown by Fischer et al [119,120,121]. The breakdown

products of wüstite, which is a non-stoichiometric compound more accurately represented as $Fe_{1-y}O$ where y is a measure of the concentration of vacancies [121], can be of wüstite of a low oxygen content.

Garber [47] differentiated between the three forms of oxide using hardness measurements. He showed that Fe_2O_3 is over 1000 Hv, Fe_3O_4 is of the order of 420-500 Hv and FeO is the softest at 270-350 Hv. The hardness of the oxides formed in 30E were in the range 270-490 Hv_{100g}, see Table 18. Assuming that the majority of the oxide present in 30E is iron oxide and neglecting the added complication of silicon and manganese oxides, then the results suggest the presence of Fe_3O_4 or the non-stoichiometric form of wüstite, or possibly a combination of the two. Matting and Steffens [34] are also of the opinion that the majority of oxide formed during the spraying of carbon steel is magnetite (Fe_3O_4).

5.1.1 Absorption of Gases in the Immediate Arc Region

Phenomena which occur at the arc position can be compared with those experienced in arc welding. The superheated condition of the molten metal and the presence of gas in the atomic and possibly ionised form promoted the absorption and reaction of relatively large amounts of gas. In open arc bare wire welding of iron, up to twenty times the expected equilibrium nitrogen content at that temperature and twenty eight times the equilibrium oxygen content has been recorded, see Section 2.4.1.1.

Approximate levels of oxygen expected in metal in the thermal spraying arc can be obtained by extrapolation of the relationships presented in Figs 60-64, the intercepts of which are shown in Table 12. These intercepts relate to the oxygen content within 30E, 60E and 65E at zero spraying distance. The predicted oxygen content of mild steel (30E) is approximately 0.6 wt% and alloyed steel 1.0 wt%, this is 2-3 times that measured in bare wire welding. Extrapolation of the relationship presented in Fig. 5 shows that this level of oxygen relates to the equilibrium content at 2200 K,which is the anticipated metal temperature in the arc zone. Welding results suggest that a similar high level of nitrogen could be exptected and metallographic studies of 30E have revealed large quantities of iron nitride needles. However, during this study only oxygen was measured and therefore this is only conjecture.

Although similar conditions exist in arc welding and spraying at the arc zone the deposition solidification rates experienced are vastly different. It is known that gases are often freely evolved during the solidification of a weld bead by the formation and transport of bubbles. This phenomenon must be greatly reduced at the solidification rates observed for sprayed droplets. In most instances droplet cooling rates in spraying are 10^4 times greater than weld bead cooling rates. This is conducive to the retention of even greater quantities of gas and it is not surprising that the spraying process retained larger quantities of gas than weld beads.

5.1.2 Transfer and Impact of Particles

Some researchers accept that the equilibrium saturation levels of absorbed gases are reached and even exceeded in the arc region [41,37,122]. If the saturation level is not reached, further absorption may occur during the transfer and impact stages. (This may be complicated by the falling temperature and reduction of the equilibrium saturation level.) Alternatively, there is also the consideration that if the saturation level has been reached at the arc temperature then, during transfer, a certain amount of desorption may be expected. High speed cimamatography [123] has recorded the regular bursting of molten steel particles during transfer. This is probably due to gas evolution, and it may be solely a consequence of the evolution of CO caused by the carbon removal reaction:-

$$C + O \rightarrow CO$$

which is referred to in greater detail in Section 5.2.

The absorption and/or desorption of gases during transfer will be influenced by the formation of an oxide layer around the particles. The cooling influence of the carrier gas on the particles is considered by some workers [124] to be sufficient to allow the formation of an oxide skin on the surface of particles whilst maintaining a liquid core.

The formation of an oxide skin was confirmed by a simple experiment. Particles were collected as the spray stream was directed into "Technical Vaseline", and the particles separated, sectioned and examined, Fig. 89. Certainly

FIGURE 89 Section through particles collected in "Technical Vaseline" during flight (60E)

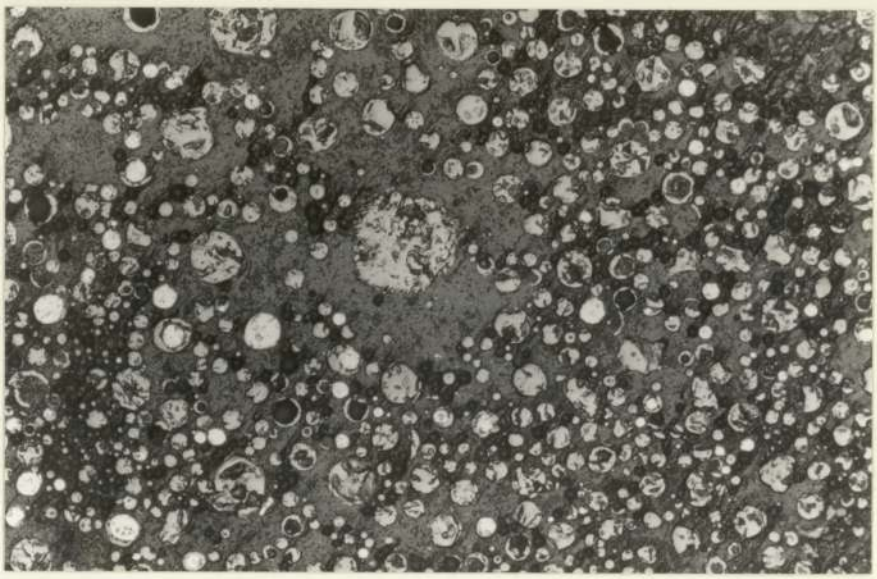

spherical oxide shells were also observed within all the deposits examined. The rates of absorption and desorption of the various gases are strongly affected by surface oxide films which normally act as a barrier to diffusion. This has been shown to occur in welding [41], see Section 2.4.1.1.

Most of the oxide however, as mentioned previously, was present in a lamellar form which extended between metallic lamellae. A particular lamella of oxide may consist partially of oxide formed during flight,which is plastically deformed on impact to form a lamella. The variation in oxide lamella thickness due to variations in parameters such as deposition rate (which does not affect the time available for oxidation during flight) however, suggests that oxidation is also influenced by conditions after impact. It is appropriate at this point to examine the time scale involved for the oxidation process during transfer and impact. The mean velocity of arc sprayed particles is generally considered to be in the region of 90 ms^{-1}. Crude estimates of particle velocity from films produced by high speed cinematography indicated this to be a realistic figure for the particular arc system used [123]. The spraying distances used in this study were in the range 40-195 mm. Thus depending on the spraying parameters the particles were exposed for oxidation for times in the range 4.4×10^{-4} - 2.2×10^{-3} seconds during transfer.

To calculate a realistic period of time likely to be available for oxidation to occur after deposition with the spraying parameters used during this study several assumptions had to be made:-

1. the particles are propelled to the substrate in a spray cone, the first assumption is that the particle concetration per unit volume within the spray cone is uniform, in reality this is not strictly correct. The concentration of particles increases towards the centre of the spray cone, see Fig. 90.

2. that the mean particle diameter is 50 μm, typical particle sizes are shown in Fig. 91, however it has been shown [125] that particle diameter can be increased and in fact doubled when using particularly small spraying distances, or higher arc voltages and low atomising pressures.

3. that lamella size and shape is constant, however this is dependent on the initial particle size which, as previously mentioned, can be variable. It is also dependent on flow characteristics of the material which is related to the thermal content or fluidity which can again be influenced by spraying parameters.

Bearing in mind these assumptions the time (t) available for oxidation after impact was calculated for two extreme cases:- (the calculations are presented in Appendix VII):

(i) using parameters which produced the greatest arrival rate per unit area of particles, that of small spraying distances and high deposition rates, t = 0.11 s;

FIGURE 90 Influence of spraying distance on the diameter of the spray cone

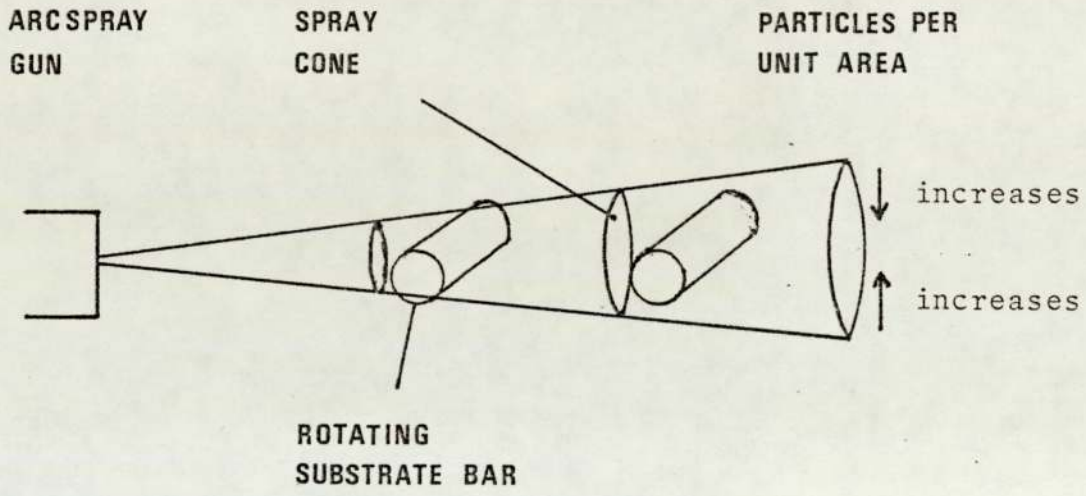

FIGURE 91 : Particles collected from Spray Stream (60E)

A

B

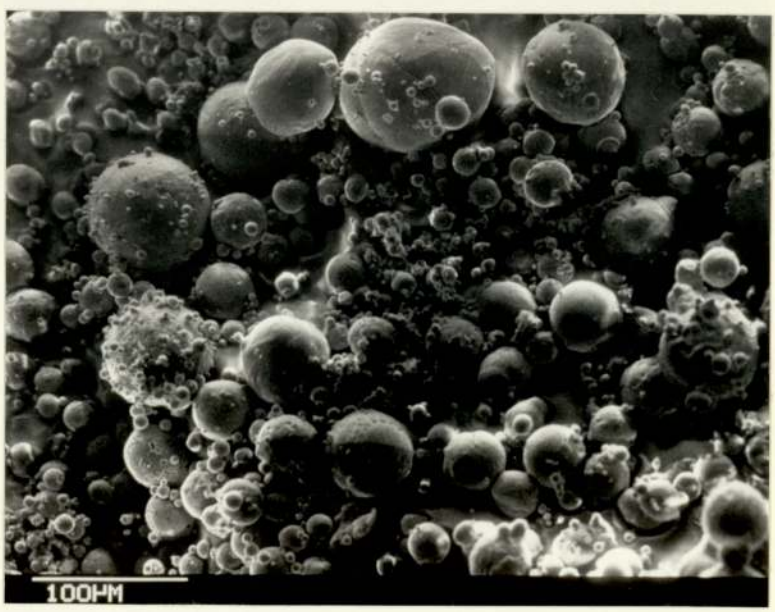

(ii) using parameters which produced the least arrival rate per unit area, that of large spraying distances and low deposition rates, t = 0.160 s.

Depending on the spraying parameters employed the particles can be exposed to the environment for up to 0.16 s after impact. It is evident that the time available for oxidation after impact is generally several orders of magnitude longer than that during flight. Oxidation will also be accelerated due to the exposure of a large active surface on impact. It is evident that the majority of oxidation should be expected after impact and certainly the metallographic examinations shown in Figs. 30-32 support this conclusion.

5.2 Elemental Loss During Spraying

It is clear from E.P.M.A. results that a high concentration of the alloying elements chromium, manganese and silicon exist within the oxides formed during spraying. It is inevitable then that the metallic ligaments within the coating are depleted in these elements. In a welding or steelmaking process this oxide or slag is removed during processing, and analysis of the finished product would show a net loss of these elements. The oxide formed during the spraying process however, is an integral part of the coating, and is not removed. Since analysis would record both elements in oxide and in metal, it might be assumed that there would be negligible difference in alloying content between wrought and sprayed material. However, results show a definite loss

of elements, which is controlled to a great extent by spraying parameters. This loss can only be accounted for by evaporative mechanisms during spraying.

The vaporization and oxidation of elements during arc welding, steelmaking and spraying has been studied by a number of researchers [126-128, 131-139]. One of the principal steelmaking reactions leading to the removal of carbon from liquid iron is represented by:-

$$[C]_{Fe} + [O]_{Fe} \rightleftharpoons (CO)_g \quad \text{(126-128)} \qquad \ldots\ldots\ldots(1)$$

where $[\ ]_{Fe}$ refers to a component in the liquid iron, $(\ )_g$ refers to a gaseous component. Carbon then, is removed by oxidation and forms a gaseous oxide. The reaction involves vigorous evolution and boiling and is responsible for slag/metal mixing.

In most steelmaking situations FeO is the principal source of oxygen for the oxidation reaction of the metal:-

$$(FeO) \rightleftharpoons (Fe^{2+})\ (O^{2-})$$
$$(O^{2-}) = [O]_{Fe} + 2e$$

Clearly such a reaction involving the release of two electrons has to be balanced by a similar reaction consuming electrons to maintain electrical neutrality (e.g. $2Fe^{3+} + 2e \rightarrow 2Fe^{2+}$). The oxygen in solution can then react via reaction (1) to produce carbon monoxide. Since both temperature and composition change with time, the activities of iron oxide and

hence oxygen transferred will be a complex function of the process variables.

Manganese and silicon are readily oxidised and form stable oxides, the oxidation of these elements has been studied in detail [126-128]. The oxidation reactions for silicon and manganese are both quite strongly exothermic. For example the reactions:-

$$[Si]_{Fe} + (O_2)_g \rightleftharpoons \langle SiO_2 \rangle_s$$

and $$[Mn]_{Fe} + (\tfrac{1}{2}O_2)_g \rightleftharpoons \langle MnO \rangle_s$$

the enthalpies are -745 kJ and -399 kJ respectively, where < > refer to pure solid constituents.

From examination of the oxygen potential diagram shown in Fig. 28, it is evident that chromic oxide is more stable than ferrous oxide and that it is formed at oxygen potentials similar to those required to form the oxides of manganese and silicon [126]. This suggests that the behaviour of chromium should be similar to that of manganese and silicon and it should oxidise in preference to iron. A variety of oxides have been reported to be formed by chromium oxidation [126]. In the early literature the divalent oxide CrO was considered to be the only product of oxidation of chromium containing iron. Later it was proposed that the chromite spinel; $FeO \cdot Cr_2O_3$, was formed in equilibrium with 0.2 to 3.0 percent of chromium in the metal. A distorted spinel structure was identified with chromium in the range 3.0 - 9.0 percent and Cr_3O_4 was stated to be the equilibrium phase at higher concentrations. More recent work has confirmed the

existence of the spinel phase, but the evidence now suggests that at high chromium contents the equilibrium phase is Cr_2O_3.

The equilibrium equations for the formation of these oxides are given as:-

$$Fe + 3Cr + 4O \rightleftharpoons FeOCr_2O_3 \text{ (s)}$$

and $$2Cr + 3O \rightleftharpoons Cr_2O_3 \text{ (s)}$$

Rates of evaporation of alloying elements from iron at high temperatures have been studied by a number of investigators [131-137]. The ratio of the concentration of each metal in the fume produced, to its concentration in the alloy, has been shown [135] to increase in the order:-

$$Fe\ [130] < Cr\ [130] < Si\ [129]^* < Mn\ [130]$$

which is the order of increasing vapour pressure of the metals. Up to 80% elemental loss due to vaporization has been recorded during MIG arc plasma welding [136]. An increase in fume formation rate has been shown to be induced by increasing current or voltage. This is related to the increased energy (i.e. temperature of the arc) due to the current. (The formation of more fume produced by more rapid droplet detachment is balanced by a reduced transfer time). It is also related to the increased arc length due to increases in voltages which promote an increase in transfer time.

* Few papers have been published describing work related to the vapour pressure of silicon and results may be unreliable.

The mechanism of fume formation has been explained to be one of vaporization, condensation and oxidation[135]. Fume is produced by two mechanisms. The first is simply vaporization of the metal or compound from the vicinity of the arc and subsequent condensation of that species outside the arc zone. Oxidation may follow. The second is enhanced vaporization due to the formation of a more volatile oxide on the surface of the molten metal, followed by condensation and perhaps further oxidation. The conclusion is that the total volume of fume generation is the sum of that due to elemental vaporization and oxide vaporization. It is felt that manganese loss is strictly attributed to elemental vaporization[135], silicon to SiO formation[133], and chromium to elemental and Cr_2O_3 vaporization[138].

Results of the study of the effect of variation of spraying parameters on the loss of the four major elements, carbon, manganese, silicon and chromium, see Figs.52-59, prove that variation in spraying parameters which alter particle flight and impacting conditions also influence elemental loss.

It is useful at this point to consider the influence of the various spraying parameters on the production of the spray droplets:-

(i) Spraying distance: the diameter of the spray cone increases with increase in spraying distance. The closer the proximity of the substrate to the arc gun then the greater the impacting particle density, see Fig.90. As mentioned previously, the particle concentration per unit volume increases towards the centre of the cone, smaller distances will further increase the impacting particle density.

An increase in spraying distance will increase the time available for reaction/elemental loss during flight and after impact. As calculated earlier the time of flight ranges from 4.4×10^{-4} - 2.2×10^{-3} s for spraying distances from 40 mm - 195 mm and exposure time after impact ranges from 1.1×10^{-2} - 1.6×10^{-1} s.

Particle size has been observed to [125] decrease with increase in spraying distance, sharply initially then more gradually. Although this effect was reported as only significant at short spraying distances, it is certainly illustrated metallographically in Figs. 30 and 31. Smaller particles will expose a larger total surface area for reaction in a given volume of coating. An increase in spraying distance then should increase elemental loss.

(ii) Deposition rate: there is a direct relationship between deposition rate and the time interval between two particles impacting at the same position. If the rate of deposition is doubled then the time interval if halved. The transfer time however should be unaffected. Thus an increase in deposition rate should decrease elemental loss.

(iii) Atomising air pressure: a reduction in air pressure reduces the effectiveness of atomisation and the average particle size increases. A large particle size reduces the overall surface area available for reaction and elemental loss should decrease.

(iv) Arc voltage: controls the melting energy of the arc and therefore the thermal input to the particles, it also has a pronounced effect on particle size, see Fig. 32. Thus, an increase in voltage has two conflicting effects with regard to elemental loss:

(a) the electrical energy input to the arc is increased, particles are therefore in a state of higher thermal energy, which should increase the rate of elemental loss,

(b) the particles produced are larger and as such will expose a smaller total surface area per unit volume of metal for reaction, which should decrease elemental loss.

In general the results indicate that a loss of 10-50% of each element could occur depending on the spraying parameters employed. James [33] carried out research on similar materials and determined typical carbon losses during arc spraying as 20-30% which could be increased to 60% using spraying conditions which induced higher thermal input to the spray droplets. Manganese losses of 50% and chromium of 10-18% were also recorded. The results obtained in the present study are in reasonable agreement with the results of James, except for the much larger chromium losses recorded. The differences may be attributed to the quite different spraying conditions used in each research programme.

The results of the bulk analysis study agree with the previously postulated theory. Increased spraying distances and atomising pressures,and reduction in deposition rates, generally promoted a greater elemental loss in all materials. The results also indicated that an increase in voltage either had no effect or slightly increased the loss of chromium, silicon and manganese in 30E and 65E materials. In contrast however, an increase in voltage resulted in a greater retention of these elements in 60E, although it must be emphasised that the retention of manganese and silicon was only marginal.

The explanation for the contrasting results with regard to the influence of voltage may be due to the conflicting effects on the thermal content and particle size that variation in voltage induces. The loss of chromium, manganese and silicon in 30E and 65E appears to be dominated by thermal effects. Alternatively the loss of these elements from 60E appears to be mainly influenced by particle size. It is possible that the formation of a more complete oxide film is occurring during transfer of 60E material which acts as a barrier to prevent or at least slow down elemental loss. An increase in spraying distance only marginally increases carbon loss which is unaffected by atomising air pressure. The carbon content slightly reduces with increase in voltage in 60E, and reduces by a significant amount in 65E. It is apparent then that carbon loss is dominated by changes in arc conditions, and is only marginally affected by conditions outside this region.

5.3 Oxygen Content of 30E, 60E and 65E, and the Variation with Spraying Parameters

In general, using almost identical spraying conditions, coatings of the more highly alloyed steels 60E and 65E contained a larger amount of total oxygen than those of 30E. Classical [140] quantitative work on the rates of scaling, however, indicates that the alloying elements commonly used in steel manufacture have a progressive effect, the rate of scaling decreasing gradually as the amount of alloying element is increased. Recent research has shown, however, that in practice, this may not necessarily be correct. The rate and temperature at which the formation of iron oxide layers proceeds on mild steel and complex oxide layers on several low chromium alloy steels has been studied by Pinder [141]. He concludes that below 870 K there is only a minor difference in overall scaling kinetics of mild steel and low chromium alloy steels. Between 870 and 970 K the rate of formation increases dramatically, and above 970 K the scaling kinetics of all steels studied fell within the same scatter band, see Fig. 92. The increase in rate of formation of oxide within the low chromium alloy steels is attributed to the formation and growth of a complex spinel layer, see Fig. 93.

This work is generally based on the formation of oxide films, the thickness of which can approach millimetres, and oxidation times as long as twenty four hours. Under these conditions the diffusion of the alloying elements through the preformed oxide layer limits their effect on the rate of growth. However, in the spraying process the final oxide thickness is of the order of a few microns and oxidation takes place in hundredths of a second. Under these conditions it may be the affinity of

FIGURE 92 Weight gain rate for mild steel and low chromium alloy steels (141)

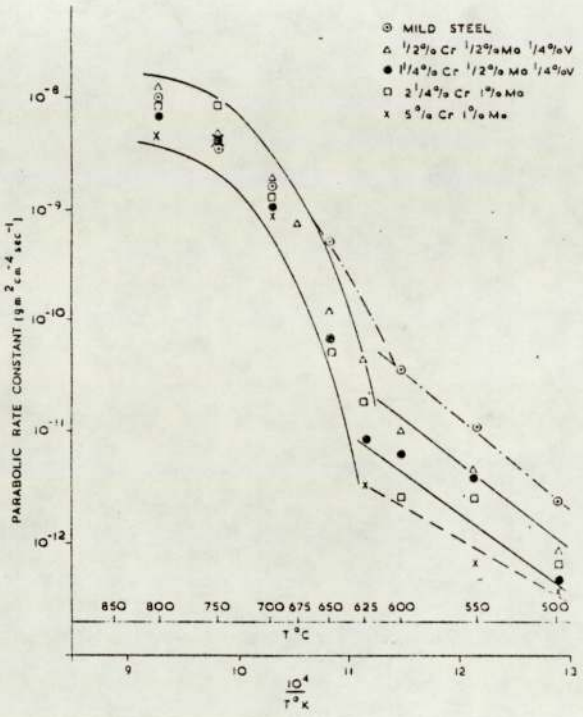

FIGURE 93 Complex spinel layer thickening rate on low chromium alloy steels (141)

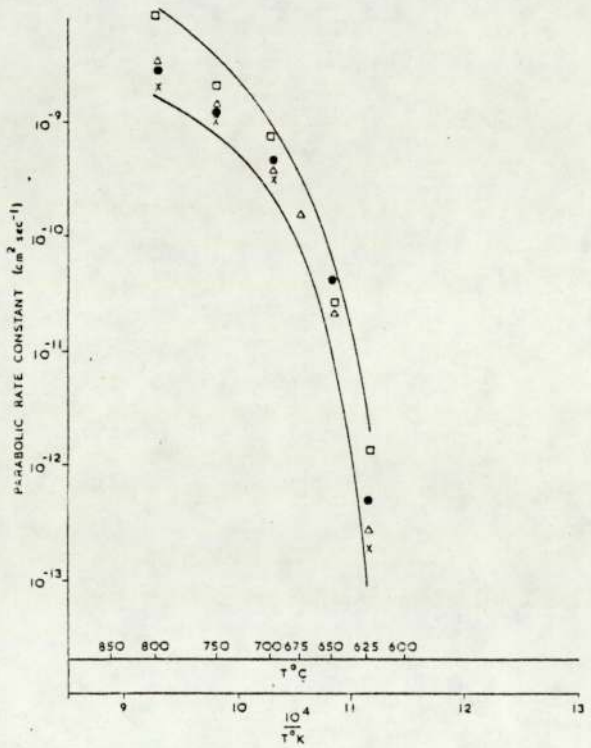

the alloying elements at the surface of the sprayed droplets that controls the relative degree of oxidation rather than the diffusion of these elements through a pre-existing oxide film.

Marginally more oxide was detected in 65E than 60E. A possible explanation for this involves the combination of two effects. The first, as mentioned in the previous section, is the likely formation of a complete and protective oxide film around certain lamellae of 60E which would reduce further oxidation. The chromium content of 65E is too low for this type of mechanism to occur. Alternatively or additionally the greater amount of manganese in 65E, which also has a high affinity for oxygen, may explain the increase.

The results presented in Figs. 60-64 show that spraying parameters which generally promoted a greater elemental loss, (i.e. increase in spraying distance and atomising pressure, and decrease in deposition rate), also increased the amount of oxide present within the structure. The explanations for this trend may be based on the same arguments as those used in the previous section. It is clear that direct relationships exist between spraying parameters and the oxygen content of the deposit when expressed in total wt%.

An increase in voltage only slightly decreases the amount of oxide present which is due to the conflicting effects mentioned in the previous section. The higher thermal input produced by increase in voltage increases the reactivity of the droplets. It also may increase the fluidity of the droplets so that on impact the larger spread exposes a greater surface area for reaction. Both effects may promote the formation of oxide. Counteracting this is the larger particle size produced by

higher voltages which reduces the effective area for oxidation. In this case it is the latter mechanism that is dominant.

5.4 Adhesion and Residual Stress

The preliminary study proved that the shear adhesion test was reliable and reproducible. The collar dimensions chosen from the results of the study gave consistency of results in the main programme of work, and a scatter band of less than 20% when using a triplicate testing procedure. This is significantly less than would be expected from the widely used adhesively bonded tensile test for coating adhesion. As expected, the most significant factors controlling the adhesive bond strength were substrate and coating material and width (w) of the ring of coating. Coating thickness was not highlighted as a significant factor with regard to the four coating materials used in the preliminary study. It is evident from review of published information, however, that in certain materials it can influence the magnitude and distribution of residual stress in a coating which can, as results show, ultimately affect adhesion strength.

The main study proved that the test was sensitive to small changes in spraying parameters. An additional useful feature of test-piece design was that circumferential residual stress in the collar of coating could be determined, after performing the shear test. The technique of slitting the rings of coating and using the increase in diameter to estimate the circumferential residual stress proved to be very successful. The test was reproducible, scatter was of the same order as that experienced with shear adhesion strength results and as such was quite acceptable. The same orders of magnitude of stresses

were reported by Szieslo [75], see Section 2.6, for similar materials. The method of slitting did not appear to affect results, values of residual stress did not vary from the normal observed scatter when slit either by spark machining or fracture. The extra process operation of spark machining may, then, have been proved to be unnecessary.

The six shear adhesion strength control specimens, which had received a stress relieving heat treatment before shear testing and slitting, all registered negligible residual stress, see Appendix VI . This confirms that the actual shear testing and/or slitting procedure did not cause plastic deformation (which would have affected residual stress measurement).

The survey of published literature revealed the importance of peak temperatures and temperature distribution within the coating and substrate relative to the development of residual stresses. It is useful at this point to examine the effect of spraying parameters on the thermal cycle of the deposit and/or substrate.

Factors which increase heat input to the substrate/coating composite are:-

(i) a reduction in spraying distance or increase in deposition rate which increases the number of impacting particles per unit area. A reduction in spraying distance also minimises thermal losses from particles by convection and radiation during transfer. There is also the possibility of direct thermal input to the deposit by radiation from the

arc, although this is likely to be small compared to the direct thermal input by the impinging particles.

(ii) an increase in particle size, produced by a reduction in atomising pressure or spraying distance, or an increase in arc-voltage. A given mass of metal in the form of large particles exposes a relatively smaller surface area to the environment, thermal losses due to radiation and convection should be reduced, therefore more heat is carried to the substrate/existing coating.

(iii) an increase in thermal input to the particles at the arc zone produced by higher arc voltages, which increases the energy of the arc.

Specific to the shear test-pieces, in most cases, a layer of about 25 μm thickness was deposited on a substrate area of 2.4×10^3 mm^2 during each two second spray cycle, although the final thickness and contact area was controlled by spraying parameters. A significant consideration with respect to heat treansfer is that the volume of substrate is one thousand times greater than that of the coating. The total thermal input to the deposit, because of the spraying procedure (2 second spray 5 second cool, under a compressed air jet) and the relative sizes of coating and substrate, was minimal. This was illustrated by the fact that the test-pieces could be handled directly after spraying. The heat dissipated

from the impinging particles is removed at extremely fast rates, the order of 10^4-10^5 K s^{-1}. These high rates are maintained by the formation of a thin disc of thickness 5-10 μm on impact. This exposes a large surface area for heat conduction away from the particle into either the substrate, during the first spray cycle, or into previously deposited coating layers. Solidification and further cooling is accelerated by convection due to the large throughput of compressed air.

The thermal input from the first impinging particles will raise the temperature of the substrate surface several hundred degrees. However there was no metallographic evidence suggesting a temperature above 1220 K (to form austenite) had been reached. The expansion of the substrate surface is restrained by the cooler inner bulk of the substrate. It is possible that the temperature at the surface of the substrate is sufficiently high to allow plastic deformation to take place. On cooling a residual tensile stress would develop in the core, this has also been proposed by Keshtvartzi [71].

The total thermal input to the substrate by the first impinging particles is likely to be small, and will reduce after each spraying cycle as the substrate will be insulated by previously deposited layers. The thermal distribution after spraying is likely to be similar to that proposed by Keshtvartzi, see Section 2.6., and is shown in Fig. 9. The level of the bulk temperature (T) in the coating is related to the thermal content of the impinging particles.

Each of the three coating materials; independent of spraying conditions, exhibited a tensile circumferential residual stress, manifested in the ring diameter increasing when slit. Spraying parameters which increased thermal input to the spray droplets or coating, increased the magnitude of residual stress, see Figs. 66-75. The build up of a residual tensile stress is largely a result of the coating shrinkage onto an unyielding substrate. A schematic representation of this event is shown in Fig. 94. As the temperature of the coating falls, the magnitude of the circumferential tensile stress increases due to further contraction of the coating onto the substrate. The higher the bulk temperature of the coating after spraying, the greater the magnitude of residual stress.

A very crude estimate of the temperature difference required between substrate and coating, to develop the stresses measured, can be obtained from the equation:-

$$\Delta\sigma = E \Delta T \alpha$$

α = coefficient of thermal expansion, $13.47 \times 10^{-6} K^{-1}$

E = modulus, 112×10^{3} MPa

σ = stress developed in coating

ΔT = change in temperature.

To produce the maximum level of stress recorded during the study (170 MPa), the coating would be required to cool the equivalent of approximately 120 degrees more than the substrate, T = the equivalent of 120 degrees.

The evidence points to the fact that thermal input to the coating ring controls the formation of residual stress within the sprayed ring deposits.

FIGURE 94 Temperature and stress distribution in shear test-pieces during and after spraying

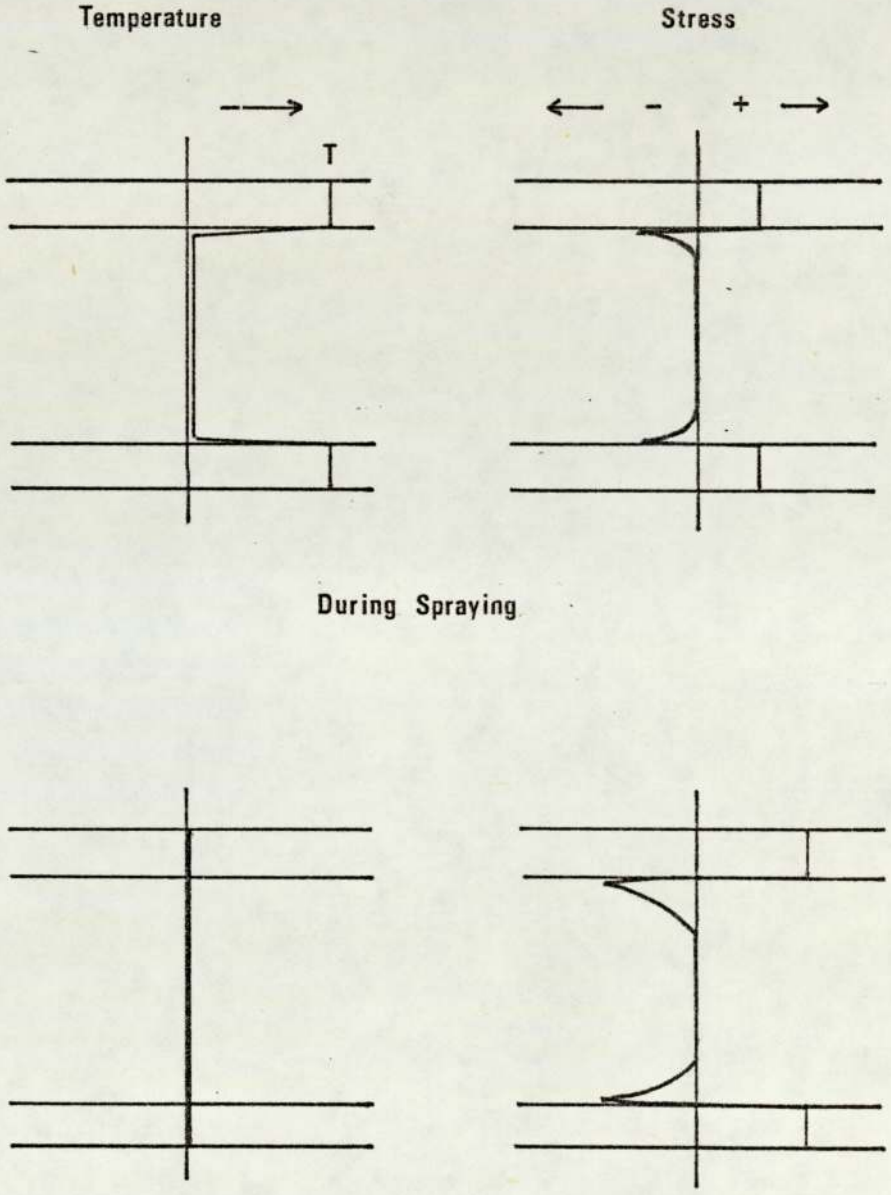

The magnitude of residual stress was also material dependent, see Figs. 66-75. The least stressed coating was the high carbon steel 65E. This has also been observed by Szieslo [75] and Harris [76], it is generally considered that this is associated with the volume expansion due to the martensitic transformation counteracting shrinkage during solidification. However, another contributing factor may be the yielding of the relatively large amount of retained austenite (25 wt%) as the shrinkage stress is building up. The other two materials 30E and 60E were more highly stressed than 65E, 60E was the most highly stressed. These trends were also observed for similar test-pieces by Haddleton [68].

The contraction process and the development of tensile residual stress has been reported by Haddleton, who provided evidence that the residual stress contributed to the "adhesion" of a sprayed ring to a substrate. He concluded that a possible 35% of the shear adhesion strength of 60E was due to residual stress. It is obvious from this study, however, that the magnitude of stress is related to spraying parameters and therefore the contribution to the apparent adhesion strength, as measured in a collar type test-piece, will vary.

Study of Figs. 66-75 shows that an increase in adhesive bond strength is generally associated with an increase in circumferential residual shrinkage stress. Metallographic examination revealed only localised evidence of a metallurgical bond between single particles and the substrate. This is in agreement with work performed by Farrow [66] who

observed the localised welding of 60E particles to a mild steel substrate as the exception rather than the rule. Specific to these material combinations and this type of test-piece, the mechanism of adhesion must be due to a combination of mechanical interlocking and residual shrinkage stress. An increase in adhesion generally requires the impact of particles of a greater thermal and kinetic energy content. The improved adhesion is produced not only by the formation of larger shrinkage stresses, but also by the promotion of more complete flow around surface features due to the increase in particle fluidity, which improves mechanical interlocking.

Several exceptions to these arguments were noted. The first relates to the results presented in Figures 72-75. The curves illustrate the variation of shear adhesion strength and circumferential residual stress with atomising air pressure and arc voltage. Although residual stress increased in the expected manner there was no corresponding increase in adhesion strength. However, experimental records proved that the grit blasting surface treatment of the substrate prior to spraying, was performed inadvertently at an exceptionally low air pressure. Thus the surface was not prepared to the standard required, which was reflected in poor adhesion strength results.

The second set was at reduced spraying distances for all deposition rates of 60E and the highest deposition rate of 30E, see Figures 66 and 68. These spraying conditions induced the highest circumferential residual stresses but were reflected in a relatively lower adhesion strength.

However, fracture did not occur at the interface between coating and substrate, unlike all the other specimens, but at some distance within the coating, that is, cohesive failure. The magnitude of circumferential residual stress developed was found to be close to that of the fracture stress of the sprayed material. Metallurgical examination, see Figure 30, revealed the presence of micro-cracking within the coating.

Thus a possible explanation for the reduction in shear adhesion strength is that micro-cracks formed during spraying result in a coating fracture strength lower than the coating to substrate adhesion strength. Fracture during the shear test has propagated through the coating rather than continuing at the interface. This type of failure may also be accentuated by an increase in the overall coating to substrate adhesion strength by improved mechanical interlocking due to the favourable deposition conditions involved. The relationship between mean shear adhesion strength and the respective mean circumferential residual stress for the three coating materials is illustrated graphically in Figure 95. Results which have been omitted are:-

(i) those which were obtained from test-pieces which had failed cohesively, which would involve a different fracture mechanism, and

(ii) those results obtained from test-pieces which were prepared using low surface preparation air pressures, which would lower the contribution to adhesion strength by mechanical interlocking.

FIGURE 9.5 Relationship between shear adhesion strength and circumferential residual shrinkage stress

●:65E

■:30E

▲:60E

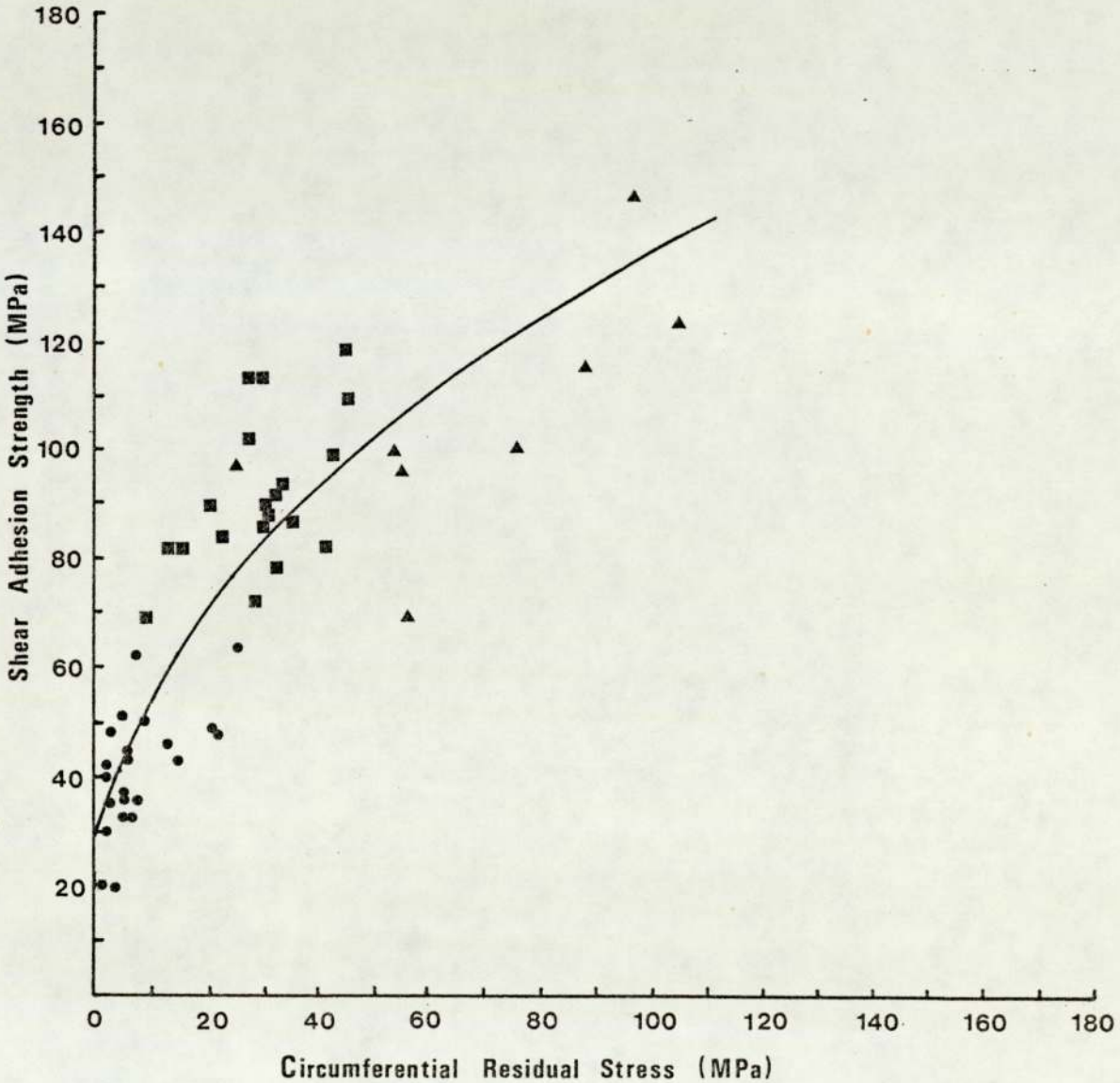

N.B. Each point is a mean of three experimental values.

In conclusion, an increase in the developed circumferential residual stress is generally beneficial to the shear adhesion strength of a coating. It increases the load required to remove a coating collar from its substrate to a limit when the magnitude of residual stress approaches that of the fracture stress of the coating. At that position cohesive failure begins to occur, which is reflected in a lowering of adhesion strength, see Figures 66 and 68.

A further exception was that the mode of fracture when shear testing steel coatings sprayed onto steel substrates during the preliminary study, was mainly cohesive. Most of the failures in the main body of work with similar materials, were adhesive. The high shear strengths (140 MPa) recorded during the preliminary study lead to an explanation. In the main test programme the samples approaching this high level of shear strength also exhibited cohesive failure. The test-pieces used in the preliminary study were not sprayed by the author and the spraying schedule was not monitored, however it seems likely that production involved a higher thermal input than the majority of test-pieces produced for the main programme.

The magnitude and "signs" of the residual stresses determined for the particular thickness of coating used in this study appear to contradict the results obtained by Harris et al, see Section 2.6 (although more recent work has indicated that a stress pattern opposite to that originally reported may exist, there is no published information at the present). At a similar thickness of coating, using a layer removal

method, they detected the presence of compressive stresses in 30E material. However, as highlighted in section 2.6, the influence of factors other than coating thickness have to be taken into account. In this particular comparison the contradictory results are probably due to the difference in thermal mass of the substrate. Although the same substrate material was used, the shear adhesion test-pieces were prepared on a solid mild steel bar, the dimensions of which were massive compared to the volume of coating, also, a spraying schedule was used to keep thermal input to substrate and coating to a minimum. Thus, the substrate acted as a restraint to any dimensional changes of the coating.

In contrast, the substrates used in the work of Harris et al, were mild steel tubes of wall thickness, 2 mm. Each tube was coated along the entire length to a thickness of 3 mm, with no recorded intermediate cooling stages. Thus the thermal input was considerable. The substrate would expand significantly as the coating was deposited. On cooling to room temperature, the shrinkage of the substrate may have been greater than that of the coating, introducing compressive stresses into the latter. Similar occurrences are discussed by Keshtvartzi [71].

5.5 Mechanical Properties

5.5.1 Tensile Strength and Young's Modulus

A coating may be regarded as a composite of lamellar and particulate oxide and porosity in a metallic lamellar matrix and exists somewhere in between the two classical composite structures, continuous and discontinuous, see Figure 96 [142].

FIGURE 96 Comparison of typical sprayed coating with classical composite structures

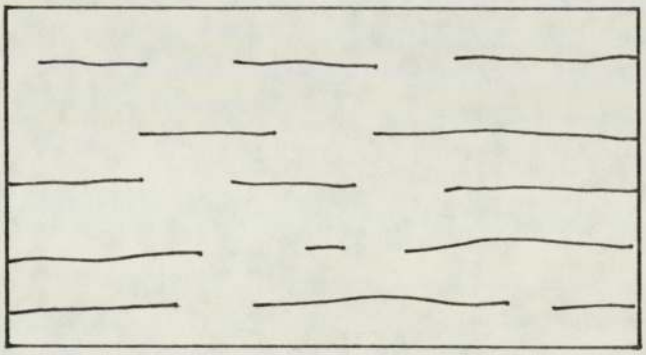

a; CONTINUOUS

b; TYPICAL SPRAYED COATING

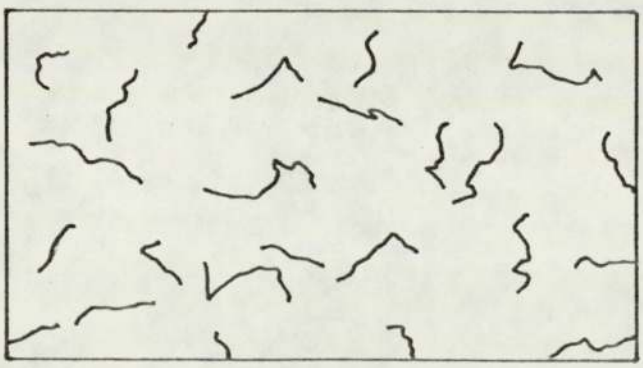

c; DISCONTINUOUS

Most metal oxides are brittle, and when fractured in tension give very little elongation at a fracture stress in the region of 6 MPa [78]. A tensile modulus of about 20 GPa has been reported [79].

Tylecote [78] found no adhesion between iron oxide and iron at room temperature after being formed at temperatures between 770 and 1470 K and cooled. Instead he observed a definite gap between oxide and metal, which was attributed to differential contraction. Metallographic examination by the writer suggested that oxide was bonded to the metallic lamellae, only a few gaps were observed. This is presumably due to the very thin films of oxide being able to accommodate the strain caused by the difference in coefficient of thermal expansion between metal and oxide. Coating fracture was generally observed to follow a path along the metal/oxide, and oxide/oxide interfaces, Figures 77 and 78. Some trans-metallic lamellar fracture was also visible, Figure 78. This suggests that a bond exists between metal and oxide although this must be weaker than the cohesive strength of the metallic lamellae. However, the degree of influence the mechanical properties of the individual pieces of oxide have on the bulk properties of the sprayed material is debatable.

The three main factors controlling the tensile strength and Young's modulus of a deposit are:-

(i) the total volume proportion occupied by oxide and porosity,

(ii) the presence of stress raising defects,

(iii) the degree of adhesion of oxide to oxide, oxide to metal and metal to metal in the structure.

Several models were tested in an attempt to quantitatively relate coating structure to Young's Modulus. The first requirement is a value to represent the volume of oxide within a coating relative to the specific spraying parameters used for the production of the blank for the tensile test-pieces. It has been shown that a range of oxides of complex nature exist in each coating. It was considered beyond the scope of this investigation to use the sophisticated analysis techniques necessary to fully characterise the oxides. Thus a precise calculation of the volume of oxide is not possible with the information available. However it is considered that assuming all the oxides were of the Fe_3O_4 type would lead to only a small error in the volume estimation.

The volume percent (V) of oxide was calculated as follows:-

Consider 100 g material which contains x g of oxide and 7.5% porosity then:-

$$\text{Volume of oxide} = \frac{x}{P_{oxide}} \text{ ccs} \qquad \ldots\ldots(1)$$

$$\text{Volume of matrix} = \frac{100-x}{P_{matrix}} \text{ ccs} \qquad \ldots\ldots(2)$$

$$\text{Volume of porosity} = 0.075\ ((1) + (2)) \qquad \ldots\ldots(3)$$

$$\text{Total volume} = (1) + (2) + (3)$$

$$\text{Therefore \% vol. oxide} = \frac{(1)}{(1) + (2) + (3)} \times 100$$

The wt% O, wt% oxide and % volume of oxide are presented in Table 19.

The analyses all assume 7.5% by volume inherent porosity which is considered by other authors and from measurements taken by the writer to be realistic for arc-sprayed materials; see Appendix VIII.

Analysis A

An extreme case in which the sprayed material is considered as a composite of oxide, metal and porosity.

Using composite theory and allowing for 7.5% porosity by volume, the modulus (E_c) of the composite was calculated using:-

$E_c = E_o C_o + E_m C_m$

E_o = modulus of oxide (20 MPa)

E_m = modulus of metal (210 MPa)

C_o = volume fraction of oxide

C_m = volume fraction of metal (taking into account porosity)

The results are presented in Table 20, however care must be taken when interpreting these results. Classic composite theory [142] applied to this structure assumes that the strength of the bond between oxide and metallic lamella is greater than the strength of the metallic lamella, this, as mentioned previously, is clearly not the case. If this was to occur, then during a tensile test, fracture would be expected through metallic, or at the very least, through oxide lamellae. Fractography reveals, see Fig. 78,

that the majority of cracks propagate through the interface between oxide and metallic lamellae, and fracture across lamellae is the exception rather than the rule, which leads to the conclusion that this bond is the weakest point. In fact the bond strength of the oxide must in general be lower than its fracture stress of 7 MPa [78].

However, this analysis is used only for comparative purposes and is not intended to represent the system.

Analysis 2

The other extreme is to consider the oxides as having zero strength and acting as voids, similar to the position of flake graphite in cast iron [83-88], as a void it is considered to transmit zero stress.

Values of modulus (E_v) are recorded in Table 20.

Analysis 3

Analyses 1 and 2 do not take into consideration the stress concentration effect which would be experienced in this type of structure, see Section 2.7.1 and 2.7.2. In this analyses modulii are calculated using the equation:

$$E_s = E(1-\varepsilon)^{3.4} \qquad (90)$$

which was derived for sintered steels. This equation involves a factor which takes into account the stress concentration effect produced by voids, cracks, unbonded areas, and oxides.

TABLE 19

VOLUME OF OXIDE WITHIN 30E, 60E AND 65E

Material	wt% O	wt% oxide	Vol.% oxide (± 1%)
30E	2.0	7.3	9.8
60E	2.8	10.2	13.5
65E	3.4	12.3	16.26

Using Density of Fe_3O_4 : 5180 Kg m^{-3}

TABLE 20

COMPARISON OF YOUNG'S MODULUS OF 30E, 60E AND 65E

Material	E_c (GPa)	E_v (GPa)	E_s (GPa)	E_A (GPa)
30E	175.6	173.7	110.1	120.2
60E	168.6	165.9	94.2	112.5
65E	163.3	160.1	82.6	93.5

E : Young's Modulus

E_c : calculated from composite theory

E_v : assuming oxide is a void

E_s : sintered powder theory

E_A : actual modulus

Values of modulus E_s are recorded in Table 20.

In the second and third analyses the oxides are treated as pores or voids, however it must be realised that although the adhesive strength of the oxide is probably relatively weak, the hardness is relatively high and, unlike graphite in cast iron, it will impart some strength to the structure, if only by interface friction during testing.

Analyses 1 and 2 produce values of modulus higher than the actual values determined, this is to be expected as they take no account of the stress concentration effects due to pore or oxide shape, size and distribution. The third analysis produced modulus values which are nearest to the actual experimentally measured modulus. The theoretical values are on average 13 GPa less than the measured modulii. The equation is particularly applicable because of the similarities in structure of a sintered and sprayed steel. The minimum defect radius, which acts as a stress raising point, was observed by Farrow [91] to be of the order of 0.4 μm or less. Defects of similar size are associated with sprayed coatings, see Figure 29.

The actual modulus of a coating is, as expected, greater than values calculated using McAdams equation, because the analysis assumes the oxides to be voids. These results, and previously discussed evidence, suggests that the oxides possess a certain degree of adhesion and contribute to the mechanical properties of the coating.

The factor 3.4 used in McAdams relationship is a stress distribution factor related to the matrix. Values of modulus experimentally determined were consistently higher than those calculated using this formula. A stress distribution factor of 2.9 is more representative for a sprayed steel.

Direct relationships of the kind $y = mx + c$ exist between spraying distance, atomising pressure or arc voltage and wt% oxygen within each coating. The approximate modulus of a sprayed steel can be determined from the following expression:

$$E_{sc} : E\left[1 - (K_2 (mx + c) + K_1)\right]^{2.9}$$

where E : Young's modulus of the wrought steel

E_{sc}: Modulus of sprayed coating

x : spraying distance, atomising pressure or arc voltage.

m and c : constants from Table 2

K_1 : fractional porosity

K_2 : conversion factor from wt% oxide to volume % oxide (expressed as a fraction).

The sprayed steels did not exhibit yielding. Fracture occurs at less than 50% of the yield stress of wrought mild steel and at a value significantly less than that of comparable sintered steels. In this respect they differ from sintered steels, which exhibit ductile fracture. The reason is probably linked to the method of formation, which induces a larger amount of weakly bonded areas, so reducing the fracture stress of the coating well below the yield stress of the metallic particles.

There is a distinct contrast between mechanisms of formation of the solid mass by the two processes. Particles which form a sprayed material, have only micro-seconds in the molten/plastic state for diffusion or localised welding, which is additionally hindered by the presence of oxides. This is in contrast to the sintering process in which diffusion and agglomeration of the clean, active particles is promoted over a period of time at steady high temperature. It is reasonable to expect a lower fracture stress in a coating and, since interlamellar fracture occurs long before the yield point of the metallic lamallae is reached, this also explains the lack of yielding.

It might be expected that the tensile strength of sprayed material would follow the same trends shown by sintered material, yield stress/fracture stress increasing with increase in density[91], interestingly 60E, which inherently involves more oxide than 65E, exhibits a slightly lower fracture stress.

This phenomenon may be explained by the argument put forward by Tylecote [78] and Steffens [54]. They each decided that the adherence of oxide on iron is reduced by the influence of individual elements such as chromium, silicon and manganese. The most susceptible of the materials to this effect would be 60E the most highly alloyed. Alternatively a more likely explanation is a weakening action produced by the oxides formed in 60E which, unlike in the other coatings, are considerably harder than the metallic matrix.

5.5.2 Hardness of Deposits

The size of the indentation produced in a coating by the indentor of a hardness machine is not only related to the hardness exhibited by discrete particles but also to the inter-particle adhesive strength, and porosity. This is illustrated by the fact that all three materials 30E, 60E and 65E exhibit lower macro-hardness than the micro-hardness of individual particles within each of the materials. The macro-hardness is low due to the presence of weak inter-particle bonds which initiate fracture/delamination during the indentation process, e.g. the macro-hardness of 60E can be as low as 230 Hv, whilst the minimum particle hardness is 400 Hv and the maximum 1000 Hv.

Macro-hardness results then are only useful as a comparative, not an absolute property, and care must be exercised when applying values in engineering fields.

The most striking aspect of the micro-hardness measurements is the range of values recorded in one coating, see Table 18 and Figure 79. Apart from the obvious differences between

the hardness of metal and oxide, this occurs because of the variation of chemistry (as shown by energy dispersive micro-analysis) and structure of individual particles due to the wide range of temperature, reaction and solidification conditions.

The micro-hardness of the oxides of 65E and 30E is similar to that of the metallic lamellae within each material, it falls within the range of hardness recorded for metallic lamella of 65E and is slightly harder than metallic lamellae of 30E, Table 18.

It is unlikely that oxide hardness alone will affect the macro-hardness of either of these materials. However the weak interparticle bonds induced by oxide may be a factor which reduces overall hardness. Using the effect of variations in spraying distance, on the macro-hardness of 30E, as an illustration, Figure 80, results obtained for 65E and 30E indicate that macro-hardness generally remains constant for changes in spraying parameters, or oxide content. The exception occurred when parameters were used which induced a significantly larger thermal input to the deposit, such as small spraying distances. Under these conditions a tempering effect is probably occurring reducing the overall micro- and macro-hardness, See Tables 16 and 17 and Figures 79 and 80.

In contrast to the coating materials discussed above, the micro-hardness of oxide formed in 60E is significantly harder than that of the metallic lamella, Table 18, and as expected this influences macro-hardness. Spraying conditions which induce larger amounts of oxide considerably increase the overall macro-hardness, Figs. 81-83.

Any reduction in macro-hardness due to higher thermal inputs (as observed in 65E and 30E) is masked by the effect of oxide, but is illustrated by a reduction in micro-hardness, see Fig. 79.

The major factors controlling macro-hardness then are oxide content and thermal input to the deposit. The micro-hardness is controlled by individual particle chemistry and structure, which may be modified by thermal input.

CHAPTER VI - CONCLUDING SUMMARY

6.1 Coating Structure

The micro- and macro-structure of each coating was synonomous with a material which had been superheated in the presence of air, atomised into fine particles, splat quenched and oxidised. A very fine grain size was developed within the coatings of the order of less than a micron up to five microns. The mild steel (30E) exhibited a mainly ferritic structure, the 13% chromium, low carbon steel (60E) a ferritic/martensitic structure and the 1% carbon, 2% chromium steel (65E) a martensitic/austenitic structure.

6.2 Coating Composition and Physico-chemical Aspects of the Spray Material

The interpolated oxygen content of droplets of mild steel leaving the arc zone corresponds to the theoretical equilibrium oxygen content at 2200 K, the temperature the metal is expected to reach in this region. The oxides formed in 30E coatings were identified by micro-hardness as of the type $Fe_{1-y}O$ or Fe_3O_4 or a combination of the two. The oxides formed in the more highly alloyed steels were of a more complex spinel type. Metallographic examination of mild steel coatings also revealed the presence of nitrogen.

Most of the oxide present in a coating forms after particle impact. The time of exposure of a droplet to air is 100-200 times greater than that during flight, which is typically 4.4×10^{-4} - 2.2×10^{-3} s. Oxidation is accelerated by the large surface area exposed by the spreading of drops on impact and the fracture of pre-existing oxide films to expose unreacted metal.

Spraying parameters which increased the rate of particle impact per unit area, and mean particle size, and/or reduced the thermal content of the impinging particles, reduced the amount of oxidation. Under conditions giving least oxidation the total oxygen contents were 0.9 wt% for 30E, 1.9 wt% for 60E and 2.0 wt% for 65E; under conditions giving the greatest oxidation the figures were 3.4 wt% for 30E, 4.3 wt% for 60E and 6.8wt% for 65E. The greater level of oxygen in the alloy steels is attributed to the alloying additions of manganese, chromium and silicon which have a greater affinity for oxygen than iron.

The high temperature involved in the formation of the spray stream produces "loss" of alloying elements. Carbon is lost by oxidation with the formation of carbon monoxide. Manganese, silicon and chromium are vaporized in an elemental or oxide form. Parameters which promoted an increase in the degree of oxidation also induced a greater elemental loss. Most of the carbon loss occurred in the arc zone and was influenced to a large extent by arc voltage. Manganese, chromium and silicon losses were influenced to a lesser extent by arc voltage and to a greater extent by parameters independent of the arc such as spraying distance and atomising pressure. With parameters giving the least loss of alloying elements, the losses of elements from 30E, 60E and 65E were respectively, 0%, 20% and 30% carbon; 20%, 25%, 30% silicon; 25%, 70%, 30% manganese; and from 60E and 65E were respectively 15% and 5% chromium. Under conditions giving the greatest loss of elements the losses of elements from 30E, 60E and 65E were 40%, 50% and 45% carbon; 45%, 80% and 60% silicon; 45%, 85% and 51% manganese; and from 60E and 65E 50% and 45% chromium.

6.3 Coating Mechanical Properties

The tensile properties of sprayed steel, fracture strength and elastic modulus, are shown to be directly related to oxide content, porosity and the associated influence of stress raising defects. The equation which gives the closest prediction of elastic modulus is that proposed by McAdam, of the type:-

$$E_s = E(1-\varepsilon)^n \qquad \text{where } n = 2.9$$

Direct relationships of the kind $y = mx + c$ exist to define the oxygen content of a coating (wt%) in terms of spraying distance, atomising pressure or arc voltage. It is possible to substitute in the McAdam equation to give:-

$$E_{sc} = E\left[1 - (K_2(mx+c) + K_1)\right]^{2.9}$$

The tensile fracture strength of a coating is less than 50% of the equivalent wrought steel and even significantly less than that of the equivalent sintered steel. In all tests there was no evidence of yielding, and generally, cracks propagated at metal/oxide and oxide/oxide interfaces. Fracture occurs at a stress well below the yield stress of metallic lamellae. The highest tensile strength (213 MPa) and lowest oxide content (7.3 wt%) was exhibited by 30E. The tensile strength of 65E (182 MPa), which has a higher oxide content (12.3 wt%) than 60E (10.2 wt%), was higher than 60E (171 MPa). This is probably due to much higher oxide hardnesses of 60E compared to the hardness of the metallic lamellae.

Macro-hardness measurements on a coating are unreliable due to the "collapse" of the structure under the indentor. The values measured (234-277 for 30E, 217-333 for 60E and 247-344, Hv 30 kg, for 65E) fell well below the micro-hardness of the individual structural constituents. The average micro-hardnesses of metallic lamellae were independent of changes in spraying parameters except for those giving the largest thermal input, which produced softening. The micro-hardnesses of oxides in 30E and 65E were of the same magnitude as the metallic lamellae and as such, did not influence macro-hardness. The oxides in 60E coatings were significantly harder (780-1010 Hv 100 g) than the metallic lamellae (400-660 Hv 100 g) and an increase in the proportion of oxide resulted in an increase in macro-hardness. The high micro-hardness of individual metallic lamellae in 30E (260-420 Hv 100g) and 60E is a combined consequence of the extremely fine grain size and the effect of nitrogen in solid solution. The hardness of metallic lamellae in 65E (560-760 Hv 100 g) is consistent with that of a quenched high carbon steel containing about 25% retained austenite.

6.4 Adhesion Strength

The shear test developed by the preliminary study proved to be a reliable and reproducible method of assessing the adhesion strength of arc sprayed steel coatings and was sensitive to small changes in spraying parameters. The change in collar diameter after splitting proved to be a reliable method of estimating circumferential residual stress in a coating. Spark machining or fracture of the collar were equally successful.

The shear adhesion strength of 65E ranged from 19-62 MPa, that of 60E ranged from 31-146 MPa and that of 30E, 68-119 MPa. It was significantly influenced by the residual circumferential, shrinkage stress developed in the sprayed ring. The adhesion strength is highest with the deposition of the highest energy (thermal and kinetic) spray particles. This is due to the more complete flow and thus interlocking of particles around surface features on the substrate and increased shrinkage of the ring on cooling.

All coating materials developed a tensile circumferential residual stress. Parameters which increased the net thermal input to the deposit increased the residual stress. The lowest residual stress was developed in 65E (1-24 MPa). This is probably a consequence of stress relief by yielding of the austenite, and the volume expansion due to the martensite transformation. Shrinkage stress during cooling is not always beneficial to the adhesion of a coating, under certain conditions it may reach levels which cause micro-cracking of the coating. The stress applied during shear testing then promotes premature cohesive failure.

APPENDIX I

ANALYSIS OF A BI-METALLIC ELEMENT WITH DIFFERENT TEMPERATURE GRADIENT ACROSS EACH METAL

When each of two metals, a substrate and a coating, assumed bonded together, is subjected to a temperature change, a strain pattern is developed which due to the difference between the coefficients of thermal expansion of the two metals produces interfacial stresses.

If subscripts s and c refer to the substrate and the coating respectively and

b = width of the element,

t = thickness,

T_c = change of temperature for the coating,

$T_s = f(y) = T_U + \frac{T_L - T_U}{t_s} y$ change of temperature of substrate,

T_U = change of temperature of the substrate at the interface,

T_L = change of temperature of the substrate at the free face,

σ = stress,

ε = strain,

α = coefficient of thermal expansion,

p = force,

M = moment,

E = modulus of elasticity,

C = constant,

$m = E_c/E_s$,

$h = t_c/t_s$ and

R = radius of curvature.

Provided ideal elasticity is assumed, it follows that

$$\left.\begin{aligned} \varepsilon_c &= C_c = \frac{\sigma_c}{E_c} + \alpha_c T_c \\ \varepsilon_s &= C_c + \frac{C_s}{t_s} y = \frac{\sigma_s}{E_s} + \alpha_s T_s \end{aligned}\right\} \quad (1)$$

From equation (1)

$$\left.\begin{aligned} \sigma_c &= E_c C_c - E_c \alpha_c T_c \text{ for } y = 0 \text{ and} \\ \sigma_s &= E_s C_c + E_s \frac{C_s}{t_s} y - E_s \alpha_s T_s \end{aligned}\right\} \quad (2)$$

Since there are no external forces acting on the element except P_c and P_s the summation of forces has to be equal to zero. Therefore

$$\Sigma P = 0 \qquad \text{and}$$

$$\sigma_c b t_c + b \int_0^{t_s} \sigma_s dy = 0 \quad (3)$$

Substitution of equation (2) into equation (3) and integration yields

$$C_c(E_c t_c + E_s t_s) + E_s t_s C_s/2 - E_c \alpha_c T_c t_c - E_s \alpha_s t_s \int_0^{t_s} \frac{T_s}{t_s} dy = 0$$

Substitution of $m = E_c/E_s$ and $h = t_c/t_s$ and defining

$\int_0^{t_s} \frac{T_s}{t_s} dy = T_{av}$ results in

$$C_c(mh+1) + C_s/2 - mh\alpha_c T_c - \alpha_s T_{av} = 0 \quad (5)$$

Eliminating the moment, $M = 0$ and

$$b \int_0^{t_s} \sigma_s y \, dy = 0, \text{ or} \quad (6)$$

$$E_s C_c t_s^2/2 + E_s C_s t_s^2/3 - E_s \alpha_s t_s^2 \int_0^{t_s} \frac{T_s}{t_s^2}\, y\, dy = 0,$$

and $$C_c + \frac{2}{3} C_s - 2\alpha_s T_m = 0, \qquad (7)$$

where $$T_m = \int_0^{t_s} \frac{T_s}{t_s^2}\, y\, dy$$

Solution of equations (5) and (7) simultaneously for C_c and C_s and substitution in equation (2) result in

$$\sigma_c = \frac{E_c}{4mh+1} (4\alpha_s T_{av} - 6\alpha_s T_m - \alpha_c T_c), \text{ and}$$

$$\sigma_s = \frac{E_s}{4mh+1} \Big[2(2mh\alpha_c T_c + \alpha_s(2T_{av} - 3T_m)) - \alpha_s T_s (4mh+1) + 6(2\alpha_s T_m (mh+1) - mh\alpha_s T_c - \alpha_s T_{av}) \frac{y}{t_s} \Big] \qquad (9)$$

The radius of curvature is given as

$$\frac{1}{R} = \frac{\sigma_c - \sigma_s(t_s)}{t_s} = \frac{C_c - (C_c + C_s)}{t_s} = -\frac{C_s}{t_s}, \text{ or}$$

$$\frac{1}{R} = \frac{-6(2\alpha_s T_m (mh+1) - mh\alpha_s T_c - \alpha_s T_{av})}{t_s (4mh+1)} \qquad (10)$$

Integration of $T_{av} = \int_0^{t_s} \frac{T_s}{t_s}\, dy$ and $T_m = \int_0^{t_s} \frac{T_s}{t_s^2}\, y\, dy$ results in

$$T_{av} = \frac{T_U + T_L}{2}, \text{ and} \qquad (11)$$

$$T_m = \frac{T_U + 2T_L}{6} \qquad (12)$$

$$T_s = T_U + \frac{T_L - T_U}{t_s} y \qquad (13)$$

APPENDIX II Unbalanced Bridge Circuit

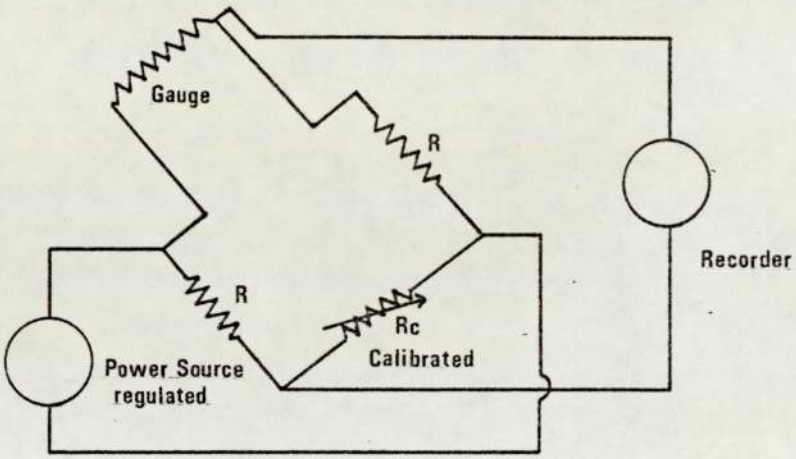

APPENDIX III

ELEMENTAL ANALYSIS OF 30E (wt%)

Spraying Conditions	Carbon	Manganese	Silicon
@ Deposition Rate of 1.4×10^{-3} Kg s^{-1}			
45 mm	0.05	1.01	0.64
125 mm	0.05	0.80	0.50
@ Deposition Rate of 2.1×10^{-3} Kg s^{-1}			
40 mm	0.07	1.00	0.67
100 mm	0.08	1.05	0.64
195 mm	0.06	0.88	0.58
@ Deposition Rate of 4.2×10^{-3} Kg s^{-1}			
80 mm	0.08	1.09	0.70
165 mm	0.09	1.11	0.68
29/26 v	0.06	0.89	0.61
34/30 v	0.07	0.87	0.55
40/34 v	0.05	0.80	0.58
585×10^3 Pa	0.06	0.89	0.56
483×10^3 Pa	0.06	0.94	0.58
414×10^3 Pa	0.06	1.00	0.56

APPENDIX III (Cont'd)

ELEMENTAL ANALYSIS OF 60E (wt%)

Spraying Conditions	Carbon	Chromium	Manganese	Silicon
@ Deposition Rate of 1.4×10^{-3} Kg s^{-1}				
40 mm	0.16	10.90	0.10	0.25
125 mm	0.15	8.14	0.06	0.13
195 mm	0.13	6.84	0.06	0.11
@ Deposition Rate of 2.8×10^{-3} Kg s^{-1}				
40 mm	0.15	10.80	0.08	0.30
80 mm	0.14	10.46	0.09	0.17
195 mm	0.13	8.97	0.07	0.12
@ Deposition Rate of 4.2×10^{-3} Kg s^{-1}				
60 mm	0.13	10.83	0.06	0.33
125 mm	0.12	10.20	0.07	0.24
195 mm	0.13	9.71	0.05	0.18
31/26 v	0.18	9.49	0.06	0.22
35/31 v	0.16	10.00	0.06	0.27
39/35 v	0.16	10.70	0.08	0.25
551×10^3 Pa	0.18	10.08	0.07	0.24
483×10^3 Pa	0.19	10.90	0.07	0.24
414×10^3 Pa	0.18	11.49	0.11	0.36

APPENDIX III (Cont'd)

ELEMENTAL ANALYSIS OF 65E

Spraying Conditions	Carbon	Chromium	Manganese	Silicon
@ Deposition Rate of 1.4×10^{-3} Kg s^{-1}				
45 mm	0.73	1.68	1.19	0.31
125 mm	0.71	1.26	0.90	0.23
195 mm	0.62	1.06	0.80	0.18
@ Deposition Rate of 2.8×10^{-3} Kg s^{-1}				
65 mm	0.73	1.65	1.19	0.33
125 mm	0.74	1.25	0.99	0.22
195 mm	0.68	1.02	0.83	0.23
@ Deposition Rate of 4.2×10^{-3} Kg s^{-1}				
65 mm	0.78	1.42	1.25	0.34
125 mm	0.79	1.35	0.99	0.25
195 mm	0.77	1.03	0.86	0.22
29/26 v	0.73	1.50	0.95	0.26
34/29 v	0.67	1.55	0.96	0.25
40/35 v	0.60	1.46	0.90	0.26
585×10^3 Pa	0.73	1.50	0.95	0.26
483×10^3 Pa	0.73	1.45	0.95	0.25
414×10^3 Pa	0.71	1.50	1.02	0.28

APPENDIX IV

SHEAR ADHESION STRENGTH (MPa) RESULTS FOR PRELIMINARY STUDY

Coating		Carbon Steel		Zinc		Aluminium		Aluminium Bronze	
		t_2	t_1	t_2	t_1	t_2	t_1	t_2	t_1
CARBON STEEL SUBSTRATE	w_1	121	132	23	23	54	53	71	95
		91	117	20	27	51	47	78	81
		109	78	20	27	52	57	75	80
			149		23		47		79
	w_2	154	179	28	22	59	57	99	131
		115	134	32	35	58	52	92	83
		161	84	30	21	45	61	84	113
			160		35		70		92
ALUMINIUM SUBSTRATE	w_1	42	57	25	21	51	46	65	77
		44	54	27	27	44	44	80	83
		58	61	31	29	46	45	59	63
			57		23		37		72
	w_2	56	75	37	35	52	51	66	101
		63	65	30	35	49	47	52	87
		63	65	35	35	49	52	66	55
			65		30		55		96

t_1 = 4 mm w_1 = 10 mm

t_2 = 2 mm w_2 = 5 mm

‖ Denotes non-split collars

APPENDIX V

SHEAR ADHESION STRENGTH, RESIDUAL STRESS AND Wt % O RESULTS

MATERIAL: 30E	SPRAYING DISTANCE : Variables		DEPOSITION RATE : 1.4×10^{-3} kgs^{-1}		
	ARC VOLTAGE: 29/26 v		ATOMISING PRESSURE: 586×10^{3} Pa		
Variable	Shear Adhesion strength (MPa)	σ circ (MPa)	wt% O	Position of fracture	Slitting Method
40 mm	90	44	1.54	I	CR
40 mm	93 (93)	22 (33)	1.15	I	CR
40 mm	95	33	1.40	I	SM
60 mm	86	33	-	I	CR
60 mm	86 (86)	36 (34)	-	I	SM
80 mm	64	14	2.19	I	CR
80 mm	71 (71)	19 (27)	1.84	I	SM
80 mm	81	47	1.80	I	CR
125 mm	91	36	3.22	I	CR
125 mm	82 (82)	47 (41)	2.57	I	CR
125 mm	73	41	2.91	I	SM
CODE	I	: Interfacial Failure			
	PC	: Partial Cohesive Failure			
	C	: Cohesive Failure			
	CR	: Cracked			
	SM	: Spark Machined			
		Mean Values in Brackets			

MATERIAL: 30E	SPRAYING DISTANCE : Variable		DEPOSITION RATE : 2.1×10^{-3} kgs^{-1}		
	ARC VOLTAGE : 29/26 v		ATOMISING PRESSURE : 586×10^{3} Pa		
40 mm	123	22	1.51	PC	CR
40 mm	117 (119)	67 (44)	1.61	I	CR
40 mm	117	44	1.49	I	SM
60 mm	93	39	1.47	I	CR
60 mm	103 (99)	44 (42)	1.41	I	CR
60 mm	100	44	1.80	I	SM
80 mm	103	17	1.82	I	CR
80 mm	119 (113)	39 (29)	1.30	I	SM
80 mm	117	30	1.46	I	SM
100 mm	103	22	2.41	I	SM
100 mm	98 (102)	44 (27)	1.90	I	CR
100 mm	103	14	2.09	I	CR
125 mm	81	-	-	I	-
125 mm	80 (84)	-	-	I	-
125 mm	90	-	-	I	-
145 mm	70	-	-	I	-
145 mm	65 (69)	-	-	I	-
145 mm	71	-	-	I	-
165 mm	95	14	2.60	I	CR
165 mm	90 (89)	29 (20)	2.47	I	SM
165 mm	82	18	2.57	I	SM
195 mm	65	3	4.10	I	SM
195 mm	70(68)	14 (8)	) 3.11) 2.98	I	CR

MATERIAL: 30E	SPRAYING DISTANCE : Variable		DEPOSITION RATE : 4.2×10^{-3} Kgs^{-1}		
	ARC VOLTAGE : 31/28 v		ATOMISING PRESSURE : 586×10^{3} Pa		
Variable	Shear Adhesion Strength (MPa)	σ circ (MPa)	wt% O	Position of fracture	Slitting Method
60 mm	100	78	0.83	C	SM
60 mm	94 (100)	58 (71)	0.90	PC	SM
60 mm	105	78	0.94	C	CR
80 mm	117	41	1.70	I	SM
80 mm	103 (109)	55 (46)	2.04	I	CR
80 mm	106	41	1.60	I	SM
100 mm	114	12	2.00	I	CR
100 mm	109 (113)	34 (28)	1.85	I	SM
100 mm	114	37	2.17	I	SM
125 mm	89	33	-	I	SM
125 mm	89 (89)	28 (30)	-	I	CR
165 mm	69	25	2.29	I	SM
165 mm	87 (83)	15 (23)	2.08	I	CR
165 mm	93	30	2.08	I	SM

MATERIAL: 30E	SPRAYING DISTANCE : 100 mm		DEPOSITION RATE : 2.8×10^{-3} Kgs^{-1}		
	ARC VOLTAGE : Variable		ATOMISING PRESSURE : 586×10^{3} Pa		
Variable	Shear Adhesion Strength (MPa)	σ circ (MPa)	wt% O	Position of fracture	Slitting Method
29/26v	80	17	2.01	I	SM
29/26v	85 (81)	11 (14)	2.37	I	CR
29/26v	78	14	2.01	I	SM
34/30v	71	50	2.50	I	CR
34/30v	79 (77)	25 (32)	1.49	I	SM
34/30v	82	22	2.33	I	SM
40/34	82	25	2.18	I	CR
40/34	81 (87)	28 (30)	1.34	I	SM
40/34	98	36	1.76	I	SM

MATERIAL: 30E	SPRAYING DISTANCE : 100 mm		DEPOSITION RATE : 2.8×10^{-3} Kgs^{-1}		
	ARC VOLTAGE : 29/26v		ATOMISING PRESSURE : Variable		
414×10^{3}Pa	86	28	1.52	I	SM
414×10^{3}Pa	102 (91)	35 (33)	1.20	I	SM
414×10^{3}Pa	86	36	1.63	I	CR
483×10^{3}Pa	86	33	1.94	I	SM
483×10^{3}Pa	89 (84)	28 (29)	1.44	I	SM
483×10^{3}Pa	78	25	2.00	I	CR
586×10^{3}Pa	80	17	2.01	I	SM
586×10^{3}Pa	85 (81)	11 (14)	2.37	I	CR
586×10^{3}Pa	78	14	2.01	I	SM

MATERIAL: 60E	SPRAYING DISTANCE : Variable		DEPOSITION RATE : 1.4×10^{-3} Kgs^{-1}		
	ARC VOLTAGE : 34/32 v		ATOMISING PRESSURE : 586×10^{3} Pa		
Variable	Shear Adhesion Strength (MPa)	σ circ (MPa)	wt% O	Position of Fracture	Slitting Method
40 mm	91	108	2.18	C	SM
40 mm	70 (80)	120(114)	2.20 2.86	C	CR
60 mm	100	65	2.43	I	SM
60 mm	87 (98)	77 (76)	2.44	PC	SM
60 mm	106	85	2.24	I	CR
80 mm	108	62	4.10	I	SM
80 mm	98 (100)	49 (53)	2.85	PC	SM
80 mm	92	49	3.99	I	CR
125 mm	98	28	3.76 3.57	I	CR
125 mm	95 (96)	21 (24)	4.11 4.40	I	SM
125 mm	96	23	4.72 5.10	I	SM
195 mm	31 (31)	-	-	I	-
195 mm	31	-	-	I	-

MATERIAL: 60E	SPRAYING DISTANCE : Variable		DEPOSITION RATE : 2.8×10^{-3} Kgs^{-1}		
	ARC VOLTAGE : 35/31 v		ATOMISING PRESSURE : 586×10^{3} Pa		
Variable	Shear Adhesion Strength (MPa)	σ circ (MPa)	wt% O	Position of Fracture	Slitting Method
40 mm	71	156	2.37	C	SM
40 mm	79 (73)	165 (164)	1.68	C	SM
40 mm	69	170	1.69	C	CR
60 mm	125	100	2.12	I	CR
60 mm	123 (122)	100 (105)	1.97	PC	SM
60 mm	117	115	) 2.00) 2.39	I	SM
80 mm	124	77	2.35	I	SM
80 mm	112 (115)	95 (88)	2.51	I	CR
80 mm	111	93	2.46	I	SM
80 mm	123	-	2.79	I	-
80 mm	106	-	-	I	-
125 mm	98	57	2.95	I	SM
125 mm	100 (95)	52 (54)	3.06	I	CR
125 mm	86	52	) 3.50) 3.12	I	SM
195 mm	60	67	) 3.61) 3.60	I	CR
195 mm	66 (68)	52 (58)	) 3.23) 3.78	I	SM
195 mm	77	54	) 4.40) 5.79	I	SM

MATERIAL: 60E	SPRAYING DISTANCE : Variable		DEPOSITION RATE : 4.2×10^{-3} Kgs^{-1}		
	ARC VOLTAGE : 35/29 v		ATOMISING PRESSURE : 586×10^{3} Pa		
Variable	Shear Adhesion Strength (MPa)	σ circ (MPa)	wt% O	Position of Fracture	Slitting Method
60 mm	132	158	1.52	C	SM
60 mm	111 (114)	153 (166)	2.33	C	SM
60 mm	101	188	) 2.29) 2.23	C	CR
80 mm	155	98	2.41	I	CR
80 mm	149 (146)	98 (97)	2.46	I	SM
80 mm	133	95	2.48	I	SM
125 mm	117	67	2.69	I	SM
125 mm	125 (121)	65 (65)	2.85	I	SM
125 mm	120	62	2.35	I	CR
195 mm	77	-	3.35	I	-
195 mm	111 (87)	-	3.70	I	-
195 mm	74	-	4.50	I	-

MATERIAL: 60E	SPRAYING DISTANCE : 100 mm		DEPOSITION RATE : 3.2×10^{-3} Kgs^{-1}		
	ARC VOLTAGE : Variable		ATOMISING PRESSURE : 586×10^{3} Pa		
Variable	Shear Adhesion Strength (MPa)	σ circ (MPa)	wt% O	Position of Fracture	Slitting Method
39/35 v	47	108	2.02	I	CR
39/35 v	68 (56)	98 (89)	2.30	I	SM
39/35 v	54	62	2.20	I	CR
35/31 v	50	85	2.14	I	CR
35/31 v	55 (46)	85 (77)	2.25	I	SM
35/31 v	34	62	2.30	I	SM
31/26 v	51	31	2.69	I	CR
31/26 v	59 (56)	39 (41)	2.47	I	CR
31/26 v	57	52	2.60	I	SM

MATERIAL: 60E	SPRAYING DISTANCE : 100 mm		DEPOSITION RATE : 3.2×10^{-3} Kgs^{-1}		
	ARC VOLTAGE : 32/27 v		ATOMISING PRESSURE : Variable		
414×10^{3} Pa	66	98	1.44	I	CR
414×10^{3} Pa	67 (63)	103 (106)	1.60	I	CR
414×10^{3} Pa	58	118	1.66	I	SM
483×10^{3} Pa	61	44	1.80	I	CR
483×10^{3} Pa	46 (45)	90 (69)	2.07	I	CR
483×10^{3} Pa	41	72	2.05 1.94	I	SM
551×10^{3} Pa	48	34	2.41	I	CR
551×10^{3} Pa	55 (46)	36 (37)	2.67	I	CR
551×10^{3} Pa	37	41	2.37	I	CR

MATERIAL: 65E	SPRAYING DISTANCE : Variable		DEPOSITION RATE : 1.4×10^{-3} Kgs^{-1}		
	ARC VOLTAGE: 29/26 v		ATOMISING PRESSURE : 586×10^{3} Pa		
Variable	Shear Adhesion Strength (MPa)	σ circ (MPa)	wt% O	Position of Fracture	Slitting Method
45 mm	63	15	2.70	I	SM
45 mm	61 (62)	6 (7)	2.78	I	CR
45 mm	63	1	3.31	I	SM
65 mm	51	4	-	I	CR
65 mm	51 (48)	4 (3)	-	I	SM
65 mm	41	0	-	I	SM
85 mm	40	9	-	I	SM
85 mm	28 (32)	1 (5)	-	I	CR
85 mm	29	4	-	I	SM
125 mm	30	0	4.49	I	CR
125 mm	33 (30)	4 (2)	4.82	I	SM
125 mm	28	1	4.74	I	SM
195 mm	18	0	6.90	I	SM
195 mm	22 (20)	4 (1)	6.17	I	SM
195 mm	20	0	7.36	I	CR

MATERIAL: 65E	SPRAYING DISTANCE : Variable		DEPOSITION RATE : 2.1×10^{-3} Kgs^{-1}		
	ARC VOLTAGE : 29/26 v		ATOMISING PRESSURE : 586×10^{3} Pa		
40 mm	52	22	2.37	I	SM
40 mm	46 (47)	28 (21)	2.62	I	CR
40 mm	44	13	2.64	I	SM
60 mm	49	9	2.06	I	SM
60 mm	50 (50)	6 (9)	2.55	I	CR
60 mm	51	13	2.18	I	SM
80 mm	49	17	2.88	I	SM
80 mm	37 (43)	17 (14)	2.84	I	CR
80 mm	44	9	2.61	I	SM
100 mm	35	6	3.26	I	CR
100 mm	58 (43)	2 (6)	3.43	I	SM
100 mm	54	11	3.08	I	SM
100 mm	38	-	-	I	-
100 mm	34	-	-	I	-
100 mm	41	-	-	I	-
125 mm	49	15	3.79	I	CR
125 mm	46 (44)	4 (6)	3.74	I	SM
125 mm	37	0	3.93	I	SM
165 mm	40 (40)	2 (2)	3.80 3.97 4.08	I	CR
195 mm	18	4	5.43	I	CR
195 mm	10 (19)	4 (4)	6.24	I	SM
195 mm	30	4	6.13	I	SM

MATERIAL: 65E	SPRAYING DISTANCE: Variable		DEPOSITION RATE : 4.2×10^{-3} Kgs^{-1}		
	ARC VOLTAGE: 30/26 v		ATOMISING PRESSURE: 586×10^{3} Pa		
Variable	Shear Adhesion Strength (MPa)	σ circ (MPa)	wt% O	Position of Fracture	Slitting Method
45 mm	-	-	1.99	-	-
45 mm	-	-	1.90	-	-
45 mm	-	-	2.10	-	-
65 mm	65	19	-	I	CR
65 mm	59 (63)	28 (24)	-	I	CR
65 mm	66	26	-	I	CR
85 mm	59	4	-	I	SM
85 mm	50 (51)	4 (4)	-	I	CR
85 mm	45	4	-	I	SM
125 mm	49	0	3.35	I	SM
125 mm	39 (42)	4 (2)	3.96	I	SM
125 mm	38	2	3.95	I	CR
195 mm	24	2	5.77	I	SM
195 mm	42 (35)	2 (3)	5.52	I	CR
195 mm	38	4	5.97	I	SM

MATERIAL: 65E	SPRAYING DISTANCE : 100 mm		DEPOSITION RATE : 2.8×10^{-3} Kgs^{-1}		
	ARC VOLTAGE : Variable		ATOMISING PRESSURE : 586×10^{3} Pa		
Variable	Shear Adhesion Strength (MPa)	σ circ (MPa)	wt% O	Position of Fracture	Slitting Method
40/36 v	50	17	3.12	I	SM
40/36 v	49 (49)	28 (20)	3.18	PC	CR
40/36 v	49	15	2.99	I	SM
34/30 v	48	13	3.05	I	SM
34/30 v	48 (46)	9 (12)	3.77	I	SM
34/30 v	43	13	3.69	I	SM
29/26 v	37	4	3.86	I	SM
29/26 v	34 (37)	4 (5)	3.69	I	SM
29/26 v	41	6	4.26	I	SM

MATERIAL: 65E	SPRAYING DISTANCE : 100 mm		DEPOSITION RATE : 2.8×10^{-3} Kgs^{-1}		
	ARC VOLTAGE : 29/26 v		ATOMISING PRESSURE : Variable		
414×10^{3} Pa	36	7	2.15	I	SM
414×10^{3} Pa	29 (33)	2 (6)	2.47	I	SM
414×10^{3} Pa	33	9	2.81	I	SM
483×10^{3} Pa	32	9	2.57	I	SM
483×10^{3} Pa	38 (35)	2 (7)	3.29	I	SM
483×10^{3} Pa	35	11	3.51	I	SM
586×10^{3} Pa	37	4	3.86	I	SM
586×10^{3} Pa	34 (37)	4 (5)	3.69	I	SM
586×10^{3} Pa	41	6	4.26	I	SM

APPENDIX VI

RESIDUAL STRESS RESULTS FOR STRESS RELIEVED SPECIMENS

Material	Spraying Distance (mm)	Deposition Rate ($Kg\ s^{-1}$)	Arc Voltage (v)	Atomising Pressure (Pa)	Splitting Method	σ_{circ} (MPa)
60E	100	2.8×10^{-3}	34/31	586×10^{3}	SM	3
60E	100	2.8×10^{-3}	34/31	586×10^{3}	CR	8
60E	195	2.8×10^{-3}	34/31	586×10^{3}	CR	3
30E	100	3.5×10^{-3}	29/26	586×10^{3}	SM	6
30E	100	3.5×10^{-3}	29/26	586×10^{3}	CR	0
30E	195	3.5×10^{-3}	29/26	586×10^{3}	CR	0

APPENDIX VII

Calculation of oxidation times after particle impact.

Assuming:-

a) Diameter of spray cone (d) :-

(i) At a spraying distance of 40 mm; d = 37 mm

(ii) At a spraying distance of 195 mm; d = 180 mm

b) Deposition rates:-

(i) 4.2×10^{-3} Kg s^{-1}

(ii) 1.4×10^{-3} Kg s^{-1}

c) Mean spray particle diameter:-

(i) 50 µm

d) Lamella diameter (D):-

(i) 200 µm

e) Density of spray wire:-

(i) 7700 Kg m^{-3}

Calculation (i) using spraying distance of 40 mm and deposition rate of 4.2×10^{-3} Kg s^{-1}.

$$\text{Volume of material deposited in 1 second} = \frac{\text{Mass deposited in 1 second}}{\text{Density}}$$

$$= \frac{4.2 \times 10^{-3}}{7700}$$

$$= 5.45 \times 10^{-7} \text{ m}^3 \quad \ldots\ldots(1)$$

The diameter of spray particle is 50×10^{-6} m

$\therefore$ Volume of particle = $6.55 \times 10^{-14} \text{m}^3$ ...(2)

The number of particles produced per second (N_1) is (1) ÷ (2),

$$N_1 = \frac{5.45 \times 10^{-7}}{6.55 \times 10^{-14}} = 8.32 \times 10^6 \quad \ldots\ldots(3)$$

Consider substrate rotated at surface speed (v_s) of 0.2 ms^{-1}.

In one second N_1 particles will be spread over a substrate area (A_s) of:-

$$A_s = d \times v_s = 0.037 \times 0.2 \quad \ldots\ldots(4)$$
$$= 7.4 \times 10^{-3} \ m^2$$

The particle density (N_2) after 1 second is (3) ÷ (4),

$$N_2 = \frac{N_1}{A_s} = \frac{8.32 \times 10^6}{7.40 \times 10^{-3}} = 1.12 \times 10^9 \text{ particles per } m^2$$

Each particle generates a surface area of A_L :-

$$A_L = \frac{\pi D^2}{4} = 3.14 \times 10^{-8} \ m^2 \quad \ldots\ldots(6)$$

Taking into account substrate rotates 2.5 times in 1 second then the number of particles (N_3) which impact at the same position in one second is:-

$$(5) \times (6)$$

$$N_3 = (N_2 \times A_L)\ 2.5 = 88. \quad \ldots\ldots(7)$$

The average time (t_{av}) between two particles being deposited at the same position is:-

$$t_{av} = 0.011 \text{ s}$$

Calculation (ii), the same method was used to determine (t_{av}) for a deposition rate of 1.4×10^{-3} Kg s^{-1} at a spraying distance of 180 mm with the result,

$$t_{av} = 0.16 \text{ s}$$

APPENDIX VIII

POROSITY DETERMINATIONS IN 65E, 60E AND 30E

Material	Spraying Conditions	Density gm/cm^3	* % Porosity
65E	40 mm, 2.1 x 10^{-3} Kg s^{-1} 29/26 v, 585 x 10^3 Pa	7.016	6.15
65E	125 mm, 2.1 x 10^{-3} Kg s^{-1} 29/26 v, 585 x 10^3 Pa	6.511	5.12
65E	195 mm, 2.1 x 10^{-3} Kg s^{-1} 29/26 v, 585 x 10^3 Pa	6.023	4.89
65E	40/35 v, 2.8 x 10^{-3} Kg s^{-1} 100 mm, 585 x 10^3 Pa	6.771	4.03
65E	414 x 10^3 Pa, 2.8 x 10^{-3} Kg s^{-1} 100 mm, 29/26 v	6.849	6.69
60E	40 mm, 1.4 x 10^{-3} Kg s^{-1} 35/29 v, 585 x 10^3 Pa	6.565	11.73
60E	125 mm, 1.4 x 10^{-3} Kg s^{-1} 35/29 v, 585 x 10^3 Pa	6.153	8.97
60E	195 mm, 1.4 x 10^{-3} Kg s^{-1} 35/29 v, 585 x 10^3 Pa	5.895	5.27
60E	40/35 v, 2.8 x 10^{-3} Kg s^{-1} 100 mm, 585 x 10^3 Pa	6.822	8.44
60E	414 x 10^3 Pa, 2.8 x 10^{-3} Kg s^{-1} 100 mm, 35/29 v	6.972	9.84
30E	40 mm, 2.1 x 10^{-3} kg s^{-1} 29/26 v, 585 x 10^{-3} Pa	6.940	12.67
30E	100 mm, 2.1 x 10^{-3} Kg s^{-1} 29/26 v, 585 x 10^{-3} Pa	7.028	8.14
30E	195 mm, 2.1 x 10^{-3} Kg s^{-1} 29/26 v, 585 x 10^{-3} Pa	6.444	9.60
30E	40/35 v, 2.8 x 10^{-3} Kg s^{-1} 100 mm, 585 x 10^3 Pa	6.822	13.74
30E	414 x 10^3 Pa, 2.8 x 10^{-3} Kgs^{-1} 100 mm, 29/26 v.	6.972	10.76

* Corrected for oxide content

REFERENCES

1. Anonymous, Flame spraying by the electric arc process, Welding and Metal Fabrication, Vol. 44, 185-189, 1976

2. Bailey, J.C., Thermal spraying of metals and ceramics, Engineering Designer, (March/April), 21-24, 1981

3. Smart, R.F., Arc plasma sprayed metals and plastics, Practical Metallic Composites, March, E19-26, 1974

4. Steffens, H.D., Metallurgical changes in the arc spraying of steel, British Welding Journal, Vol. 13, 597-605, 1966

5. Matting, A., Metal spraying from gas flame to plasma jet, British Welding Journal, Vol. 13, 526-532, 1966

6. Lavin, P.A., The leap from conventional to high energy plasma spraying, Design with Thermal Spraying in the 80's (Association of Metal Sprayers), Paper 4, 1982

7. Machin, R.F., Metal Spraying, Engineering, Vol. 214, 1-7, 1974

8. Kretzschmar, E., Methods of testing sprayed and ceramic coatings, Surfacing Journal, Vol. 8-9, 2-9, 1977

9. Dini, J.W., Johnson, H.R., Techniques for quantitavely measuring the adhesion of coatings, Metal Finishing, Vol. 75, 42-46, 1977

10. Sprayed unfused metal coatings for engineering purposes, B.S. 4761, 1971

11. Protection of iron and steel by aluminium and zinc against atmospheric corrosion, B.S. 2569, Part I, 1968

12. Protection of iron and steel against corrosion and oxidation at elevated temperatures, B.S. 2509, Part II, 1965

13. Specifications for sprayed and fused metal coatings for engineering purposes, B.S. 4950, 1973

14. Böhme, D., Modification of a known and development of a new testing method for the determination of the adhesive strength of thermally sprayed coatings. Advances in surface coating technology. International Conference, 13-15 Feb., 87-97, 1978

15. Endoh, M., Shinmen, S., Shinmen, S., Influences of principle factors of pre-treatment on surface roughness on mild steel substrate and adhesive strength of zinc sprayed coatings. 8th International Thermal Spraying Conference, 492-502, 1976

16. Berndt, C.C., McPherson, R., A fracture mechanics approach to the adhesion of flame and plasma sprayed coatings. 9th International Thermal Spraying Conference, 310-316, 1980

17. Jacobson, R., Measurement of the adhesion of thin films, Thin Solid Films, Vol. 34, 191-199, 1976

18. Baxter, C.F.G., Reiter, H., Mechanism of adhesion of plasma sprayed aluminium to metallic substrates, Metals Technology, Vol. 6, 111-114, 1979

19. Catherall, J.A., Kortegas, K.E., Measurement of bond strength of flame sprayed deposits, Metal Construction and British Welding Journal, Vol. 4, 11-13, 1972

20. Kitahara, S., Atsushi, H., A study of the bonding mechanism of sprayed coatings. Journal of Vacuum Science and Technology, Vol. 11, 747-752, 1974

21. Determination of the adhesive shear strength in shear test, DIN 50161, 1977

22. Fletcher, R.K., The selection of spray coating materials for engineering applications, Surfacing Journal, Vol. 6-7, 6-8, 1975

23. Stanton, W.E., The mechanical properties of sprayed metals for engineering, Seventh International Metal Spraying Conference, 157-164, 1973

24. Hoff, I., Experience and new prospects in the automotive industry, Design with Thermal Spraying in the 80's; (Association of Metal Sprayers), Paper 3, 1982

25. Marantz, D.R., The basic principles of electric arc spraying, Science and Technology of Surface Coating, (A Nato advanced study Institute), April, 308-321, 1972

26. Blake, P.D., Jordan, M.F., Nitrogen absorption during the arc melting of iron, Journal of the Iron and Steel Institute, Vol. 209, 197-200, 1971

27. Steffens, H.D., Metallurgical changes in the arc spraying of steel, British Welding Journal, Vol. 13, 597-605, 1966

28. Uda, M., Wada, T.W., Solubility of nitrogen in arc-melted and levitation melted iron and iron alloys, Transactions of the National Research Institute for Metals, Vol. 10, 21-23, 1968

29. Cobine, J.D., The nature of the arc, Welding Research Council Bulletin Series, No. 2, 1949

30. Christensen, N., Chipman, J., Slag-metal interactions in arc welding, Welding Research Council Bulletin Series, No. 15, 1953

31. Christensen, N., Gjermundsen, K., Measurements of temperature outside and in the weld pool in submerged arc welding, U.S. Dept. of Army, European Research Office, Report No. AD273091, 1962

32. Belton, G.R., Moore, T.J., Tankins, E.S., Slag-metal reactions in submerged arc welding, Welding Journal, 42, 289-295, 1963

33. James, D.H., The properties and applications of arc sprayed coatings. Transactions of the Institute of Metal Finishing, 60, 49-53, 1982

34. Matting, A., Steffens, H.D., Adhesion and layer formation for arc and flame spraying, Metalloberfache, Vol. 17, 583-593, 905-922, 1213-1227, 1963

35. Howden, D.G., The behaviour of hydrogen in arc weld pools. Weld Pool Chemistry and Metallurgy, (International Conference Welding Institute), Paper 3, 205-209, 1980

36. Salter, G.R., Milner, D.R., Gas absorption from arc atmospheres, British Welding Journal, Vol. 7, 89-100, 1960

37. Howden, D.G., Milner, D.R., Hydrogen absorption in arc melting, British Welding Journal, Vol. 10, 304-316, 1963

38. Smithells, C.J., Impurities in metals, Chapman and Hall, 1930

39. Elliot, J.F., Gleiser, M., Ramakrishna, V., Thermochemistry of steelmaking, Pergamon Press, Oxford, 1963

40. Kobayashi, T., Kuwana, T., Kikuchi, Y., Kiguchi, R., Nitrogen absorption of alloy steel welds in an air atmosphere, I.I.I.W., Doc. XII-461-68, 1969

41. Uda, M., Ohno, S., Effect of surface active elements on nitrogen content of iron under arc melting, Transactions of National Research Institute of Metals, Vol. 15, 20-28, 1973

42. McPherson, R., The relationship between the mechanism of formation, microstructure and properties of plasma sprayed coatings. Thin Solid Films, Vol. 83, 297-310, 1981

43. Dallaire, S., Influence of temperature on the bonding mechanism of plasma sprayed coatings, Thin Solid Films, Vol. 95, 237-244, 1982

44. Worthington, A.M., A study of splashes, MacMillan, New York, 1963

45. Zaat, J.H., Thermal spraying research and development tendencies in 1980, 9th International Thermal Spraying Conference, The Hague, 1-13, 1980

46. Pfeil, L.B., The oxidation of iron and steel at high temperatures, Journal of the Iron and Steel Institute, Vol. 70, 501-548, 1929

47. Garber, S., Fundamental aspects of scale on mild steel strip, Journal of the Iron and Steel Institute, Vol. 192, 153-160, 1959

48. Paidassi, J., The kinetics of the air oxidation of iron in the range 700-1250°C, Acta Metallurgica, Vol. 6, 184-194, 1958

49. Apps, R.L., The bond strength of flame-sprayed coatings, Surfacing Journal, Vol. 4-5, 1-5, 1974

50. Kniewald, D., Contributions to the problems of preliminary treatment of surfaces by means of blasting and its influence on the properties of sprayed metal coatings. Eigth International Thermal Spraying Conference, 482-491, 1976

51. Apps, R.L., Further investigations into metal spraying, CIT Memo 130, Cranfield Institute of Technology, March, 1-14, 1974

52. Crane, L.W., Johnston, C.L., James, D.H., Effect of processing parameters on the shear adhesion strength of arc-sprayed deposits, Tenth International Thermal Spraying Conference, 46-50, 1983

53. Stanton, W.E., Private communication, Unpublished results

54. Marynowski, C.W., Halden, F.A., Farley, E.P., Variables in plasma spraying, Electro-chemical Technology, Vol. 3, 109-115, 1965

55. Herpol, G.A., Tavernier, E., Surface preparation and its relationship to weakness of a coating, British Welding Journal, Vol. 13, 683-689, 1966

56. Matting, H.A., Becker, K., Investigations of flame spraying processes, Schweissen und Schneiden, Vol. 6, 127-141, 1954

57. Ballard, W.E., Metal spraying and the flame deposition of plastics and ceramics, Griffin, London, 1963

58. Cottrell, A., An introduction to metallurgy, Arnold, 2nd Edition, 1976

59. Matting, H.A., Raabe, W., The formation of sprayed metal layers, Schweissen und Schneiden, Vol. 8, 369-374, 1956

60. Lancaster, J.F., The metallurgy of welding, brazing and soldering, George Allen and Unwin Ltd., Second edition, 1970

61. Gierstein, S.B., Document 1.350.67, International Institute of Welding, 1967

62. Stanton, W.E., The behaviour of aluminium in sprayed metal coating. Corrosion Prevention and Control, Vol. 25, 221-223, 1978

63. Matting, A., Steffens, H.D., Fatigue tests on metal sprayed steel samples. Härt. Techn. Mitt., 221-223, 1967

64. Birchon, D., Effect of molybdenum deposit on adhesion and fatigue of ferritic steels. Metallurgica, Vol. 58, 273-284, 1958

65. Overs, M.P., Fretting wear and fretting fatigue of arc sprayed coatings containing iron, nickel and chromium at elevated temperatures. Ph.D. Thesis, University of Bath, 1981

66. Farrow, R., Crane, L.W., Fracture mechanics approach to the testing of sprayed coatings, S.E.R.C. Report, Unpublished Results, The University of Aston in Birmingham, 1983

67. Stanton, W.E., Wear resistance and internal stress evaluation in gas and arc sprayed deposits. Seventh International Spraying Conference, 1-14, 1970

68. Haddleton, F.W., A study of adhesion in sprayed metal coatings, Undergraduate Thesis, Unpublished results, The University of Aston in Birmingham, 1982

69. Lee, D., A finite element modelling of the low pressure plasma deposition process, temperature analysis, Institute of Mechanical Sciences, Vol. 25, 543-551, 1983

70. Lee, D., A finite element modelling of the low pressure plasma deposition process, stress analysis, Institute of Mechanical Sciences, Vol. 25, 553-563, 1983

71. Keshtvartzi, A., The effect of plasma sprayed molybdenum coatings on the fatigue properties of steel, Ph.D. Thesis, University of Bath, 1977

72. Ingham, H.S., Composite Engineering Laminates, MIT Press, 1969

73. Keshtvartzi, A., Reiter, H., The effect of flame sprayed coatings on the fatigue behaviour of high strength steels. Tenth International Thermal Spraying Conference, 222-225, 1983

74. Barbinok, V.A., Residual stresses in plasma coatings deposited on the internal surface of a ring, Welding Production, Vol. 28, 11-13, 1981

75. Szieslo, U., Residual stresses within thermal sprayed layers. Tenth International Thermal Spraying Conference, 222-225, 1983

76. Harris, S.J., Cobb, R.C., James, D.H., Influence of wire composition and other process variables on the internal stress of arc sprayed steel coatings. Tenth International Thermal Spraying Conference, 245-249, 1983

77. Drazkiewicz, T., Compressive strength of sprayed metal coatings, Second International Metal Spraying Conference, 1-16, 1958

78. Tylecote, R.F., Adherence of oxides on metals, Journal of the Iron and Steel Institute, Vol. 196, 135-141, 1960

79. Dankov, P.D., Churaev, P.V., Proceedings of the Academy of Sciences of the U.S.S.R., Vol. 73, 1221-1224, 1950

80. Peters, F.K., Engell, H.J., Die Haftfestigkeit von zunderschichten auf stahl, Archiva Fur Das Eisenhütten-Wesen, Vol. 30, 275-282, 1959

81. Rigby, G.R., Reversible thermal expansion from theoretical considerations, Transactions of the British Ceramics Society, Vol. 50, 175-183, 1951

82. Cleaves, H.E., Hiegel, J.M., Properties of high purity iron, Journal of Research National Bureau of Standards, Vol. 28, 643-667, 1942

83. Capyto, J.W., Pels, A.R., What controllable density means to the design engineering. Powder Metallurgy, Vol. 3, 17-23, 1967

84. Morgan, V.T., Techniques for the evaluation of powders III. Observations on compacts, Powder Metallurgy, Vol. 7, 44-65, 1961

85. Meyersberg, G., The internal mechanisms of cast iron, Iron and Steel, Vol. 17, 243-247, 1944

86. Thum, A., Ude, H., Die elastizität und die schwingungsfestigkeit des Gubeisens. Die Giesserei, Vol. 16, 501-515, 1929

87. Thum, A., Die elastizität und die schwingungsfestigkeit des Gubeisens. Die Giesserei, Vol. 16, 1164-1174, 1929

88. Schwartz, H.A., Junge, C.H., Young's modulus of elasticity and some related properties of graphitic materials. Proceedings of the American Society for the Testing of Materials, Vol. 41, 816-824, 1941

89. Pohl, D., On the fatigue strength of sintered iron, Powder Metallurgy International, Vol. 1, 26-28, 1969

90. McAdam, G.D., Some relations of powder characteristics to the elastic modulus and shrinkage of sintered ferrous compacts, Journal of the Iron and Steel Institute, Vol. 168, 346-358, 1951

91. Farrow, R.J., Mechanical properties of sintered low alloy steels, M.Sc. Thesis, University of Aston in Birmingham, 1981

92. Donovan, M., Influence of spraying parameters on quality, Surfacing Journal, Vol. 13, 26-29, 1982

93. Private conversation with delegate, 10th International Thermal Spraying Conference, 1982

94. Hatfield, W.H., Thirkell, G.L., Season cracking, Journal of the Institute of Metals, Vol. 22, 67-91, 1919

95. Ford, H., Mechanical methods for the measurement of internal stress, Symposium on internal stress in metals and alloys. The Institute of Metals, Paper 1072, 3-12, 1948

96. Mackowiak, J., Physical chemistry for metallurgists, George Allen and Unwin Ltd., 1965

97. Personal communication, Technical Director, Metallisation Ltd., 1984

98. Powder diffraction file, JCPOS, Pennsylvania 19081, 1978

99. Miller, R.L., Volume fraction analysis of phases in textured alloys, Transactions of the American Society of Metals, Vol. 61, 592-597, 1968

100. Jatczak, C.F., Larson, J.A., Shin, S.W., Retained austenite and its measurement, SAE Fatigue Design and Evaluation Committee, September 1979

101. Miller, R.L., A rapid X-ray method for the determination of retained austenite. Transactions of the American Society of Metals, Vol. 57, 892-899, 1964

102. Hall, E.O., The deformation and ageing of mild steel, Proceedings of the Physical Society, B64, 747-753, 1951

103. Petch, N.J., The cleavage strength of polycrystals, Journal of the Iron and Steel Institute, Vol. 174, 25-28, 1953

104. Hall, E.O., Variation of hardness of metals with grain size, Nature, Vol. 173, 948-949, 1954

105. Jindal, P.C., Armstrong, R.W., The dependence of the hardness of cartridge brass on grain size, Transactions of the American Metallurgical Society, Vol. 239, 1856-1857, 1967

106. Douthwaite, R.M., Relationship between the hardness, flow stress and grain size of metals. Journal of the Iron and Steel Institute, Vol. 208, 265-268, 1970

107. Farrell, K., Loh, B.T.M., Hardness-flow stress, grain size relationships in iron, Journal of the Iron and Steel Institute, Vol. 209, 915-917, 1971

108. Inokuti, Y., Duflas, F., Cantor, B., Martensite morphology in rapidly solidified pure iron, Phase Transformations, Institution of Metallurgists, Spring Residential Conference, Series 3, Vol. 2, 17-19, 1979

109. Bibby, M.J., Gordon-Parr, J., The martensitic transformation in pure iron. Journal of the Iron and Steel Institute, Vol. 202, 100-104, 1964

110. Inokuti, Y., Cantor, B., The formation of martensite in splat quanched Fe-Mn and Fe-Ni-C alloys, Journal of Materials Science, Vol. 12, 946-958, 1977

111. Tschischewski, N., The occurrence and influence of nitrogen in steel, Journal of the Iron and Steel Institute, Vol. 92, 47-98, 1915

112. Hodge, J.C., The welded boiler drums of the U.S. Navy Scout Cruisers, Journal of the American Welding Society, April, 11-14, 1931

113. Koster, W., The effect of quenching and drawing below A_1 Point upon the physical properties of iron/nitrogen alloys, Metals and Alloys, Vol. 1, 571-575, 1930

114. Irvine, K.J., Crowe, D.J., Pickering, F.B., The physical metallurgy of 12% chromium steels, Journal of the Iron and Steel Institute, Vol. 195, 386-405, 1960

115. Irvine, K.J., Pickering, F.B., Garstone, J., The effect of composition on the structure and properties of martensite, Journal of the Iron and Steel Institute, Vol. 196, 66-81, 1960

116. Paidassi, J., The kinetics of the air oxidation of iron in the range 700-1250°C. Acta Metallurgica, Vol. 6, 184-194, 1958

117. Pfeil, L.B., The oxidation of iron and steel at high temperatures, Journal of the Iron and Steel Institute, Vol. 119, 501-547, 1929

118. Pfeil, L.B., The constitution of scale, Journal of the Iron and Steel Institute, Vol. 123, 237-258, 1931

119. Fischer, W.A., Hoffmann, A., Shimada, R., Der wüstitzerfall unterlab 570°C in gegenwart von eisen. Archiva Fur Das Eisenhütten-Wesen, Vol. 27, 521-529, 1956

120. Fischer, W.A., Hoffmann, A., Der wüstitzerfall in gegenwart von metallischem eisen nach abschrecken auf temperaturen unterhalb 570°C. Archiva Fur Das Eisenhütten-Wesen, Vol. 29, 107-113, 1958

121. Engell, H.J., Unterbuchungen, über thermodynamik und zusammensetzung des wüstits, Archiva Fur Das Eisenbütten-Wesen, Vol. 28, 109-115, 1957

122. Krivenko, L.F., Slutskaya, T.M., Effects of alloying elements on the residual nitrogen content of the weld metal after open arc welding, Automatic Welding, Vol. 20, 12-13, 1967

123. High speed cine film. Surface metallurgy research group, visual aid. The University of Aston in Birmingham, 1982

124. Krasnischenkow, L., Schtschirjetskij, M., On the problem of the formation of sprayed metal coatings, Journal of Technical Physics, Vol. 25, 791-795, 1955

125. Clifuentes, L., Harris, S.J., James, D.H., Composition and microstructure of arc-sprayed 13% Cr steel coatings, Thin Solid Films, Vol. 118, 515-526, 1984

126. Bodsworth, C., The physical chemistry of iron and steel manufacture, 2nd edition, Longman Group Ltd., 1972

127. Ward, R.G., The physical chemistry of iron and steelmaking, Edward Arnold Ltd., 1962

128. Sharp, J.D., Electric Steelmaking, Iliffe Books Ltd., London, 1966

129. Nesmeyanov, N., Vapour pressure of the elements, Macmillan, London, 1963

130. Hultgren, R., Orr, R.L., Anderson, P.D., Selected values of Thermodynamic properties of metals and alloys, John Wiley & Sons Inc., 1963

131. Ohno, R., Ishida, T., Rate of evaporation of manganese, copper, tin, chromium and sulphur from molten iron under vacuum, Journal of the Iron and Steel Institute, Vol. 206, 904-908, 1968

132. Howden,D.G., Mass transfer of metal vapour and anode temperatures in arc melting, The Welding Journal, Vol. 48, 125s-132s, 1969

133. Heile, R.F., Hill, D.C., Particulate fume generation in arc welding processes, The Welding Journal, Vol. 54, 201s-214s, 1975

134. Ward, R.G., Evaporative losses during vacuum induction melting of steel, Journal of the Iron and Steel Institute, Vol. 201, 11-15, 1963

135. Gray, C.N., Hewitt, P.J., Hicks, R., The prediction of fume compositions in stainless steel inert metal gas welding, Weld pool chemistry and metallurgy, The Welding Institute, International Conference, Paper 39, 197-203, 1980

136. Corderoy, D.J.H., Wallwork, G.R., Gas/weld metal reactions in MIG arc plasma welding, Weld pool chemistry and metallurgy, The Welding Institute, International Conference, Paper 12, 147-153, 1980

137. Gray, C.N., Hewitt, D.J., The effect of oxygen on the rate of fume formation in metal inert gas welding arcs, Weld pool chemistry and metallurgy, The Welding Institute, International Conference, Paper 27, 167-176, 1980

138. Fryburg, G.C., Kohl, F.J., Stearns, C.A., Enhanced oxidative vaporisation of Cr_2O_3 and chromium by oxygen atoms, Journal of the Electrichemical Society, Vol. 121, 952-959, July 1974

139. Benz, R., Scheidler, G.P., Metal-gas reactions in arc plasma spraying of Ag, Cu, Ni, Ti, TiC, W, Zn, and Ar, Zeitschcrift Für Metallkunde, Vol. 91, 182-188, 1970

140. Pfeil, L.B., Winterbottom, A.B., The constitution and formation of scale on ferrous alloys, Dept. of Scientific and Industrial Research, Review of oxidation and scaling of heated solid metals, Section II, 18-30, 1935.

141. Pinder, L.W., Oxidation Kinetics and Scale Morphology of Mild Steel and Low Chromium Alloy Steels in N_2/20% O_2 Between 500 and 850°C. Central Electricity Generating Board, Scientific Services Dept., 1977

142. Flinn, R.A., Trojan, P.K., Engineering Materials and their applications, Houghton Muffin Co., Boston, 1975

143. Safai, S., Herman, H., Micro-structural Investigation of Plasma-Sprayed Aluminium Coatings. Thin Solid Films, Vol. 45, 295-307, 1977

ACKNOWLEDGEMENTS

The author would like to acknowledge the invaluable guidance received throughout the duration of this research from Mr. L.W. Crane (supervisor) and Mr. D.H. James (industrial advisor). Thanks are also due to, the Staff and Research Students of the Department of Metallurgy and Materials Engineering for their technical advice, Mrs. H. Howell for all typing, Mrs. J. Hopkins and Miss L.J. Hopkins for help in preparation of this thesis.

Finally the author would like to express his gratitude to his parents for their support and encouragement.